

Development and Application of Efficient Computational Methods for Molecular Spectroscopy in Finite Magnetic Fields

Zur Erlangung des akademischen Grades eines

Doktors der Naturwissenschaften

(Dr. rer. nat.)

von der KIT-Fakultät für Chemie und Biowissenschaften
des Karlsruher Instituts für Technologie (KIT)
genehmigte

Dissertation

von

M.Sc. Ansgar Iring Pausch

1. Referent: Prof. Dr. Wim Klopper
 2. Referent: Prof. Dr. Florian Weigend
- Tag der mündlichen Prüfung: 18.07.2022

*„Daran erkenn’ ich den gelehrten Herrn!
Was ihr nicht tastet, steht euch meilenfern,
Was ihr nicht fasst, das fehlt euch ganz und gar,
Was ihr nicht rechnet, glaubt ihr, sei nicht wahr,
Was ihr nicht wägt, hat für euch kein Gewicht,
Was ihr nicht münzt, das, meint ihr, gelte nicht.“*
– Mephistopheles

Johann Wolfgang von Goethe, Faust II

Abstract

Molecular spectroscopy is an important tool for the characterization of chemical compounds. Various types of spectroscopy use the effects induced by external magnetic fields, such as nuclear magnetic resonance, electron paramagnetic resonance, or magnetic circular dichroism. Their theoretical description is typically achieved through quantum chemical methods in combination with linear perturbation theory, as the magnetic fields used in such experiments are small compared to the electromagnetic forces responsible for the formation of the chemical bond.

Beyond the linear effects captured by this approach lies a rich and fascinating world of chemistry waiting to be explored. Entirely new types of chemical bonding, spin-phase transitions, and color changes of aromatic compounds are just some of the non-linear effects induced by the presence of a magnetic field. Their theoretical description requires a finite field approach, in which the magnetic field is explicitly used in the corresponding Hamiltonian operator. Such an approach can be used for an accurate description of the effects induced by arbitrarily strong magnetic fields. This allows for the prediction of spectroscopic properties for molecules in the vicinity of interstellar objects exhibiting very strong magnetic fields, such as magnetic white dwarfs or neutron stars. In these cases, molecular spectroscopy can be used to verify the existence of small molecules in such extreme environments.

The theoretical description of a finite field approach requires highly efficient computational methods, the development and application of which is the subject of this thesis. First, the theoretical framework for the quantum chemical description of molecular spectroscopy is introduced. Several well-established methods are adapted for the use in finite magnetic fields, including density functional theory (DFT), approximate coupled cluster theory (CC2), and the *GW*/BSE method. An efficient implementation of these methods is developed and carefully tested. Selected applications include calculations on the magnetic circular dichroism spectrum of an organometallic complex, predicting the change of color induced by moderately strong magnetic fields for tetracene with UV/Vis spectroscopy, and the investigation of rotational-vibrational spectra for diatomic molecules in strong magnetic fields.

Zusammenfassung

Molekülspektroskopie ist ein wichtiges Werkzeug für die Charakterisierung chemischer Substanzen. Verschiedene Arten von Spektroskopie verwenden die Effekte, die durch Magnetfelder hervorgerufen werden, wie etwa Kernspinresonanz, Elektronenspinresonanz oder Magnetocirculardichroismus. Ihre theoretische Beschreibung erfolgt typischerweise durch quantenchemische Methoden in Kombination mit linearer Störungstheorie, da die Magnetfelder in solchen Experimenten klein sind, verglichen mit den für die chemische Bindung verantwortlichen, elektromagnetischen Kräften.

Jenseits der linearen Effekte, die durch einen solchen Ansatz beschrieben werden, liegt eine vielfältige, faszinierende Chemie, die darauf wartet erforscht zu werden. Neue Arten chemischer Bindung, Spinphasenübergänge und Farbveränderungen aromatischer Verbindungen sind nur einige der nicht-linearen Effekte, die durch Magnetfelder hervorgerufen werden. Ihre theoretische Beschreibung erfordert einen Ansatz, in dem ein finites Feld explizit im Hamiltonoperator auftaucht. Solch ein Ansatz kann für eine korrekte Beschreibung von beliebig starken Magnetfeldern verwendet werden. Dadurch wird die Vorhersage spektroskopischer Eigenschaften von Molekülen in der Nähe interstellarer Objekte mit extrem starken Magnetfeldern ermöglicht, wie etwa magnetische Weiße Zwerge oder Neutronensterne. In solchen Fällen kann Molekülspektroskopie verwendet werden, um die Existenz kleiner Moleküle nachzuweisen.

Die theoretische Beschreibung eines finiten Feldes erfordert hocheffiziente, rechnergestützte Methoden, deren Entwicklung und Anwendung Thema dieser Arbeit sind. Zunächst werden hierfür die theoretischen Grundlagen für die quantenchemische Beschreibung von Molekülspektroskopie eingeführt. Einige verbreitete Methoden der Quantenchemie werden adaptiert, inklusive der Dichtefunktionaltheorie (DFT), genähertem Coupled-Cluster (CC2), sowie der *GW*/BSE-Methode. Eine effiziente Implementierung wird entwickelt und getestet. Ausgewählte Anwendungen werden vorgestellt, inklusive Rechnungen an Magnetocirculardichroismusspektren eines organometallischen Komplexes, die Vorhersage der Farbveränderung von Tetracen im Magnetfeld mithilfe der UV/Vis-Spektroskopie, sowie die Untersuchung von Schwingungsrotationsspektren zweiatomiger Moleküle in starken Magnetfeldern.

Danksagung

Für die Bereitstellung des spannenden Promotionsthemas, zahlreichen wissenschaftlichen Diskussionen und Hilfestellungen sowie die exzellente Betreuung möchte ich meinem Doktorvater, Prof. Dr. Wim Klopper, herzlich danken. Prof. Dr. Florian Weigend danke ich für die Übernahme des Koreferats dieser Arbeit sowie ebenfalls für diverse hilfreiche Diskussionen, insbesondere im Zusammenhang der Implementierungen in das TURBOMOLE Programmpaket.

Für unzählige hilfreiche Gespräche, eine hervorragende Zusammenarbeit im Rahmen von drei Publikationen und die Übernahme der Korrektur dieser Arbeit gilt mein besonderer Dank Dr. Christof Holzer. Ebenfalls danken möchte ich Dr. Yannick Franzke, sowohl für diverse Hilfestellungen bei der Programmierarbeit, als auch für die Übernahme der Korrektur dieser Arbeit. Meinem Bürokollegen Florian Rehak möchte ich für ein stets entspanntes Miteinander danken. Den Mitgliedern der Gruppe für Theoretische Chemie am KIT gilt darüber hinaus mein besonderer Dank. Für viele wertvolle Diskussionen „zwischen Tür und Angel“ möchte ich dabei insbesondere Dr. Angela Bihlmeier, PD Dr. Michael Harding und PD Dr. Sebastian Höfener danken. Für die hervorragende Arbeitsatmosphäre, vielen Krökelrunden und den Zusammenhalt auch während der Pandemie danke ich allen Mitgliedern der Gruppe.

Ein für mich besonders wichtiger Aspekt waren die vielen Studierenden, die ich im Laufe meiner Promotion begleiten durfte: Anja Appenzeller, Melina Dilanas, Melanie Gebele, Xenia Kraft und Laurenz Monzel, mit dem ich gleich in mehreren Projekten zusammenarbeiten konnte. Ihnen allen gilt mein Dank, denn ohne ihre Mithilfe wäre diese Arbeit nicht möglich gewesen.

Eine Promotionszeit ist stressig und fordert einige Entbehrungen. Alleine schafft das niemand, deswegen gilt mein Dank allen Menschen, die mich in den letzten Jahren auf diesem Weg begleitet haben. Meinen Freunden, die auch in den weniger einfachen Zeiten immer an meiner Seite standen. Meinen Eltern, die mich ermutigt haben diesen Weg zu gehen. Zuletzt möchte ich dem Fonds der chemischen Industrie sowie der Studienstiftung des deutschen Volkes für die finanzielle Unterstützung dieser Arbeit im Rahmen von Promotionsstipendien danken.

Contents

Abstract	ii
Zusammenfassung	iii
Danksagung	iv
I. Introduction	1
1. Introduction	3
II. Theory	7
2. A Brief Introduction Into Classical Electrodynamics	9
2.1. Notation	10
2.1.1. Atomic Units	10
2.1.2. Linear Algebra	10
2.2. Basic Principles of Classical Electrodynamics	11
2.2.1. Maxwell's equations	11
2.2.2. Electric Scalar and Magnetic Vector Potential	11
2.2.3. Gauge problem and gauge fixing	12
2.3. Moving Charged Particle in an Electromagnetic Field	13
2.3.1. Principle of Minimal Coupling and Lorentz force	13
2.3.2. Cyclotron Rotation	15
3. Quantum-Mechanical Description of Molecules in External Magnetic Fields	16
3.1. Notation	17
3.1.1. Operators	17
3.1.2. Dirac notation	17

3.2.	Born–Oppenheimer Approximation	18
3.2.1.	Born–Oppenheimer Ansatz	18
3.2.2.	Adiabatic Approximations	19
3.3.	Construction of the Electronic Hamiltonian	21
3.3.1.	Hydrogen-like Atom	21
3.3.2.	Many-Electron Systems	24
3.4.	Construction of the Nuclear Hamiltonian	25
4.	Electronic Wave Function: Construction and Symmetry	29
4.1.	Notation	30
4.2.	Phase of the Electronic Wave Function	30
4.2.1.	Global Phase	30
4.2.2.	Gauge Transformation	31
4.3.	Ansatz for the Electronic Wave Function	32
4.3.1.	Two-Component Wave Functions	32
4.3.2.	Linear Combination of Atomic Orbitals	32
4.4.	Basic Concepts of Symmetry	34
4.5.	Spin Symmetry	34
4.5.1.	Spin Operator	34
4.5.2.	Squared Spin Operator	36
4.5.3.	Spin Projection Operator	36
4.6.	Time-reversal symmetry	36
4.6.1.	Time-Reversal Operator	36
4.6.2.	Magnetic Operator	37
4.7.	Spatial Symmetry	38
4.7.1.	Molecular Point Groups in Static Magnetic Fields	38
4.7.2.	Properties and Identification of Magnetic Point Groups	40
5.	Quantum Chemical Methods for Electronic Ground States	43
5.1.	Notation	44
5.2.	Hartree–Fock Theory	44
5.2.1.	Basic Concept and Symmetry Classification	44
5.2.2.	Generalized Hartree–Fock	46
5.2.3.	Construction of the Fock Matrix	47
5.2.4.	Resolution of the Identity Approximation	49
5.3.	<i>Post</i> Hartree–Fock Methods	50
5.3.1.	Electron Correlation	50

5.3.2.	Møller–Plesset Perturbation Theory	51
5.3.3.	Approximate Coupled Cluster Theory	52
5.4.	Kohn–Sham Density Functional Theory	53
5.4.1.	Basic Concept and Symmetry Classification	53
5.4.2.	Density Functional Theory in External Magnetic Fields	54
5.4.3.	Spin-Noncollinear Kohn–Sham Density Functional Theory	56
5.4.4.	Hybrid and Range-Separated Hybrid Functionals	58
5.5.	<i>Post</i> Kohn–Sham: The <i>GW</i> Method	59
6.	Quantum Chemical Methods for Electronic Excitations	61
6.1.	Linear Response Theory	62
6.1.1.	Basic Concept	62
6.1.2.	Time-Dependent Hartree–Fock Theory	63
6.1.3.	Approximate Coupled Cluster Theory	64
6.1.4.	Time-Dependent Density Functional Theory	64
6.1.5.	Bethe-Salpeter Equation	68
6.2.	Calculation of Optical Spectra	69
6.2.1.	Electronic Transition Dipole Moments	69
6.2.2.	UV/Vis Spectroscopy	70
6.2.3.	Magnetic Circular Dichroism Spectroscopy	71
7.	Semi-classical Approach for the Nuclear Equation of Motion	73
7.1.	Nuclear Equations of Motion	74
7.1.1.	Hamilton’s Equations of Motions	74
7.1.2.	Lagrangian Equations of Motions	75
7.2.	Berry Curvature	77
7.2.1.	General Properties and Connection to Charge Distribution	77
7.2.2.	Approximation through Mulliken Charge Matrix	78
III.	Implementation	81
8.	Implementation of Quantum Chemical Methods in Finite Magnetic Fields	83
8.1.	Implementation into TURBOMOLE	84
8.2.	Electronic Ground States	85
8.2.1.	General Outline of SCF Procedure	85
8.2.2.	Coulomb and Exchange Potentials	88

8.2.3.	Exchange-Correlation Potential	90
8.2.4.	Efficiency Increase for SCF Procedure	91
8.2.5.	Canonical Orthogonalization	92
8.2.6.	Spin Zeeman Scaling	93
8.2.7.	Squared Spin Operator	94
8.2.8.	Ground State Properties and Expectation Values	94
8.3.	Molecular Gradients and Geometry Optimization	95
8.3.1.	General Outline	95
8.3.2.	Geometry Optimization in External Magnetic Fields	97
8.4.	<i>Post</i> Hartree–Fock Methods and Electronic Excitations	99
9.	Efficient Integral Evaluation	100
9.1.	Calculation of Shell-Pair Quantities	101
9.2.	Overlap Integrals	102
9.2.1.	Horizontal Recurrence Relations	102
9.2.2.	Translational Recurrence Relations	103
9.2.3.	Obara–Saika Recurrence Relations	103
9.2.4.	Molecular Gradient	105
9.3.	Kinetic Energy Integrals	106
9.3.1.	Evaluation of Integrals	106
9.3.2.	Molecular Gradient	109
9.4.	Nuclear Attraction Integrals	110
9.4.1.	Basic Integral	110
9.4.2.	Complex Molecular Boys Function	111
9.4.3.	Obara–Saika Recurrence Relations	113
9.4.4.	Molecular Gradient	116
9.5.	Electron Repulsion Integrals	118
9.5.1.	Four-Center Integrals	118
9.5.2.	Molecular Gradient	120
9.5.3.	Three-Center Integrals	122
10.	Assessment of Accuracy and Efficiency	125
10.1.	Molecules Used for Benchmark Calculations	126
10.2.	Accuracy of the RI Approximation	126
10.2.1.	Computational Methods	126
10.2.2.	Electronic Ground States	128
10.2.3.	Electronic Excitations	130

10.3. Accuracy of Linear Response Methods	131
10.4. Efficiency of the Implementation	131
10.4.1. Assessment of Efficiency	131
10.4.2. Computational Methods	132
10.4.3. Comparison to Field-Free Calculations	132
10.4.4. OpenMP Parallelization	133
11. Berry Curvature: Implementation and Connection to Partial Charges	135
11.1. Implementation of Numerical Evaluation	136
11.2. Partial Charges in the Limit of a Vanishing Field	138
11.2.1. Computational Details	138
11.2.2. Charge Distribution and Sum Rule	139
11.2.3. Partial Charges and Basis Set Dependence	142
IV. Selected Applications	145
12. Magnetic Circular Dichroism Spectroscopy	147
12.1. Comparison to Perturbative Approach	148
12.1.1. Computational Details	148
12.1.2. <i>p</i> -Benzoquinone	149
12.1.3. Tetrachloro- <i>p</i> -Benzoquinone	150
12.2. Comparison to Experiment: The ZnDiNTAP Molecule	151
12.2.1. Computational Details	151
12.2.2. Choice of Basis Set	152
12.2.3. Choice of Density Functional	153
12.2.4. Comparison to Experimental Spectrum	154
13. Absorption Spectroscopy in Moderately Strong Magnetic Fields	156
13.1. Influence of Magnetic Field on Electronic Excitations	157
13.1.1. Computational Details	157
13.1.2. Small and Medium-Sized Molecules	157
13.1.3. Electronic Excitations of Pyrazine	160
13.2. UV/Vis Spectroscopy and Color Change of Tetracene	161
13.2.1. Computational Details	161
13.2.2. UV/Vis Spectrum in Absence of Magnetic Field	162
13.2.3. Influence of External Magnetic Field	165

13.2.4. Prediction of Color Change	167
14. Rotational-Vibrational Spectroscopy in Strong Magnetic Fields	169
14.1. Computational Details	170
14.2. Rovibrational Spectrum of Molecular Hydrogen	170
14.2.1. Potential Energy Surface	170
14.2.2. Molecular Rotations and Vibrations	173
14.2.3. Rotational-Vibrational Spectra in Strong Magnetic Fields	174
14.3. Rovibrational Spectrum of Lithium Hydride	177
14.3.1. Infrared Spectroscopy in Strong Magnetic Fields	177
14.3.2. Potential Energy Surface	178
14.3.3. Molecular Rotations and Vibrations	179
14.3.4. Rotational-Vibrational Spectra in Strong Magnetic Fields	181
14.3.5. Mulliken Charge Approximation	183
15. Geometry Optimization of Helium Clusters in Strong Magnetic Fields	184
15.1. Helium Dimer and Perpendicular Paramagnetic Bonding	185
15.1.1. Computational Details	185
15.1.2. Perpendicular Paramagnetic Bonding	185
15.1.3. Geometry Optimization of Different Electronic States	187
15.2. Helium Clusters: Structure and Symmetry	189
15.2.1. Computational Details	189
15.2.2. Geometry Optimization of Helium Clusters	189
V. Conclusion and Outlook	191
16. Conclusion and Outlook	193
A. Appendix	197
A.1. Abbreviations and Acronyms	197
A.1.1. Abbreviations in Mathematics	197
A.1.2. Abbreviations in Chemistry	197
A.1.3. Abbreviations in Quantum Chemistry	197
A.1.4. Orbital-Related Acronyms	198
A.1.5. Quantum Chemical Methods	198
A.1.6. Abbreviations for Basis Sets	199

Bibliography	200
List of Figures	220
List of Tables	222
Permissions to Print	223
List of Publications	224

Part I.

Introduction

1. Introduction

Magnetism has fascinated humanity for all of history.^[1] Countless ancient civilizations are known to have come in contact with magnetism in the form of magnetic ores found in nature.^[2-4] By the 12th century, the magnetic compass was already in use for navigation purposes in the western world and later experiments carried out in the 16th century proved the earth itself to be magnetic.^[5] The advent of modern natural sciences in the early 19th century brought some clarity to the questions surrounding magnetism, intimately connecting it to the phenomenon of electricity. Among others, the groundbreaking works of André-Marie Ampère, Jean-Baptiste Biot, Félix Savart, and Michael Faraday laid the foundation for the theory of electromagnetism later formalized by James Clerk Maxwell in form of his famous equations.^[1] Scientific discoveries of the early 20th century proved that electromagnetic phenomena were responsible for the nature of the chemical bond, with moving electrons exhibiting magnetic fields.^[6] Finally, the theory of quantum mechanics was able to unify these discoveries into a powerful tool capable of predicting molecular properties.^[7, 8]

Compared to the electromagnetic forces present in molecules, magnetic fields found on earth are relatively small. The geomagnetic field (ca. $50 \mu\text{T}$) is able to redirect magnetized matter such as compass needles.^[9] Magnetic ores (ca. 0.5 T) exhibit magnetic fields strong enough to naturally attract ferromagnetic materials in their close vicinity.^[10] In laboratories, magnets are used for various purposes, including the investigation of the interaction between matter and magnetism. Several spectroscopic methods rely on the presence of external magnetic fields, including nuclear magnetic resonance (NMR), electron paramagnetic resonance (EPR), and magnetic circular dichroism (MCD) spectroscopy (usually up to 21 T).^[11, 12] Even the strongest non-destructive magnetic fields currently created on earth (ca. 150 T) display only a small fraction of the electromagnetic forces present in molecules.^[13, 14]

Future endeavours will very likely push the limit of humanity's capabilities even further, making larger and larger magnetic fields experimentally accessible. But even now, gazing upon the stars reveals the existence of magnetic fields magnitudes stronger than anything currently obtainable on earth. Elsewhere in the universe, interstellar

objects such as magnetic white dwarfs (up to 10^5 T) and neutron stars (up to 10^{11} T) exhibit field strengths strong enough to compete with the electromagnetic interactions responsible for the formation of chemical bonds.^[15–18] As a result, entirely new types of chemical bonding may be induced by these extreme environments.^[19]

Molecular quantum mechanics, also known as quantum chemistry, allows for the description of the physical interaction between magnetism and matter.^[20, 21] The inclusion of a magnetic field in the corresponding calculations is facilitated through its inclusion in the molecular Hamiltonian operator.^[14] Using this approach, the effects of arbitrarily weak or strong magnetic fields may be calculated, enabling an accurate prediction of molecular properties both in earth-like conditions and in the vicinity of, for instance, magnetic white dwarfs. For molecular spectroscopy in weak magnetic fields (NMR, EPR, MCD), the use of perturbation theory is very common, and considerable effort has gone into the development of computational methods for a great variety of chemical applications.^[22–31] For the quantum chemical calculation of molecular properties in finite magnetic fields, substantial progress has been made in recent years.^[32–38] Applications include the investigation of bonding mechanisms in strong magnetic fields,^[19] molecular geometries,^[34, 38] spin-phase transitions,^[37] and anapole moments.^[39] Furthermore, calculations in finite magnetic fields have been used in an astrophysical context for the interpretation of atomic spectra measured on magnetic white dwarfs.^[14, 40–43]

Having established the general concepts for chemical bonding in magnetic fields as well as the computational methods for molecular spectroscopy in the context of perturbation theory, all key ingredients for a more general investigation of molecular spectroscopy in magnetic fields are now formally available. As such, recent years have seen an increasing amount of research, in which quantum chemical calculations have been carried out for molecular spectroscopy using finite magnetic fields.^[44–49] Such an approach has several advantages. While yielding identical results to perturbation theory in weak magnetic fields, using finite fields enables us to go beyond just linear effects, giving us a glimpse of the rich and fascinating chemistry waiting to be revealed through experimental means. Furthermore, these methods can be used for the verification of the existence of small molecules in the vicinity of magnetic white dwarfs.^[50, 51] However, the disadvantage is that this approach is associated with considerable computational cost, which, in the past, limited its application to a handful of small systems.

Thus, the central aim of this thesis is the development and application of efficient computational methods for molecular spectroscopy in finite magnetic fields. This requires three separate steps:

1. The derivation of theoretical methods for the description of molecular properties in finite magnetic fields.
2. The efficient and parallel implementation of these methods.
3. The application to different types of molecular spectroscopy in magnetic fields.

Therefore, this thesis is structured into three main parts. First, the theoretical framework is laid out (chapters 2–7). Second, an efficient implementation is discussed (chapters 8–11). Finally, selected applications are examined (chapters 12–15). The individual chapters are arranged in the following manner:

- Chapters 2 and 3 build the theoretical foundation of this work. The former introduces the classical description of electromagnetism and charged particles in magnetic fields. The latter expands this to a quantum-mechanical description for molecules in finite magnetic fields.
- In chapter 4, the electronic wave function for molecular systems in external magnetic fields is examined. Both its gauge origin invariant construction and its (spin-)symmetry are considered. The discussions on spatial symmetry contained in this chapter follow research carried out in the context of this thesis, published in Ref. [52].
- Chapters 5 and 6 introduce methods of modern quantum chemistry for electronic ground states and electronic excitations, respectively. Their adaption for the inclusion of external magnetic fields remains the central focus throughout. Some of these methods have been adapted for this thesis, and the results have been published in Refs. [53], [54], and [55].
- Chapter 7 concludes the theoretical part of this thesis, presenting a semi-classical approach for the description of nuclear motion in strong magnetic fields. A central quantity appearing within this context, the Berry curvature tensor, is introduced.
- In chapters 8 and 9, the efficient implementation of quantum-chemical methods in finite magnetic fields is discussed. Most importantly, the relevant adaptations to a program already capable of calculating these quantum chemical methods in the absence of a field are highlighted. Part of this implementation has previously been presented by the author in Ref. [56].

- Chapter 10 is focused on the assessment of the accuracy and efficiency of quantum chemical methods in strong magnetic fields. Particularly the resolution of the identity approximation is examined. This chapter contains results previously published in Refs. [53], [54], and [56].
- In chapter 11, an implementation of a numerical scheme for the calculation of the Berry curvature tensor is discussed. The computation of partial charges derived from this tensor in the limit of a vanishing magnetic field is introduced and their basis set dependence is tested.
- Chapter 12 presents the first application of this thesis: MCD spectroscopy in weak magnetic fields. Results computed using the finite field implementation are first compared to those obtained from a perturbative approach. The capability of the implementation carried out in this work is highlighted by examining the MCD spectrum of an organometallic complex and comparing it to experimental data. The results of this chapter were published in Ref. [54].
- In chapter 13, the non-linear effects induced by moderately strong magnetic fields on optical spectroscopy are investigated. For electronic excitations, the influence of magnetic fields up to 10,000 T is examined for a set of 36 small to medium-sized molecules. For the tetracene molecule, the influence on the absorption spectrum in the ultraviolet and visible region (UV/Vis spectroscopy) is investigated, predicting the change of color this molecule is expected to undergo in moderately strong magnetic fields. These results were published in Ref. [53].
- In chapter 14, rotational-vibrational spectroscopy for diatomic molecules in strong magnetic fields is examined. The complex coupling patterns which result from the magnetic field are characterized and the canonical ensemble of spectra is examined. The results discussed here were obtained in the context of this thesis and presented in Ref. [57].
- Chapter 15 contains the final application presented of this thesis. The equilibrium geometry of helium clusters in strong magnetic fields is investigated, examining how well the methods implemented here perform for the description of the perpendicular paramagnetic bonds responsible for their formation.

The thesis is concluded and summarized in chapter 16, also giving an outlook on the future of quantum chemical calculations in finite magnetic fields.

Part II.

Theory

2. A Brief Introduction Into Classical Electrodynamics

In this work, both a semi-classical and a fully quantum-mechanical description of molecules and their properties in the presence of external electromagnetic fields is considered. For both cases, it is vital to understand the fundamental concepts responsible for the dynamics of moving charged particles in external fields. These concepts have been known since at least the 19th century, when James Clerk Maxwell formalized them the context of what is today known as classical electrodynamics.

Thus, after a short section introducing the notation used in this work, Maxwell's equations are presented. A convenient description of electromagnetic fields through their respective potentials is established and the equations of motion governing their dynamics are re-cast in the framework of magnetic vector and electric scalar potentials. The gauge problem, which is a direct consequence of using the vector and scalar potentials, is introduced. The Coulomb gauge, which is commonly employed for semi-classical calculations and consistently used throughout this work, is presented and explicit forms for the electric scalar and the magnetic vector potentials are derived. In particular, the explicit form for a homogeneous, static magnetic field as well as its unphysical dependence on a gauge origin is discussed.

This chapter concludes with a classical description of the mechanics describing the motion of a moving charged particle in an electromagnetic field. The principle of minimal coupling is introduced, yielding a gauge-invariant form for the momentum of a particle in an electromagnetic field. Lagrangian mechanics is used in order to derive the well-known form of the Lorentz force. The Hamiltonian of this system is derived, which forms the basis for the quantum-mechanical description of the Hamiltonian operator in the next chapter. Finally, the motion of a moving charged particle in an external, homogeneous, static magnetic field is considered. The resulting cyclotron rotation is discussed, building the basis for discussions about molecular dynamics in strong magnetic fields in chapter 14.

2.1. Notation

2.1.1. Atomic Units

Atomic units are used throughout this work, unless explicitly stated otherwise. It is defined by setting the reduced Planck's constant \hbar , the elementary charge e , the mass of an electron m_e , the Bohr radius a_0 , and Coulomb's constant $(4\pi\epsilon_0)^{-1}$ equal to unity:^[58]

$$\hbar = e = m_e = a_0 = 4\pi\epsilon_0 = 1. \quad (2.1.1)$$

2.1.2. Linear Algebra

Vectors, matrices, and tensors are denoted by bold letters. Upright letters as subscripts are used as descriptors. Italic and general Greek letters as subscripts denote the elements of matrices and vectors, while the first three letters of the Greek alphabet specifically are used as subscripts for Cartesian tensors, with $\alpha, \beta, \gamma \in \{x, y, z\}$. Following this notation, the Kronecker delta δ_{ij} and Levi-Civita symbol $\epsilon_{\alpha\beta\gamma}$

$$\delta_{ij} = \begin{cases} 1 & \text{if } i = j \\ 0 & \text{if } i \neq j \end{cases} \quad (2.1.2)$$

$$\epsilon_{\alpha\beta\gamma} = \begin{cases} 1 & \text{if } (\alpha, \beta, \gamma) \text{ is a cyclic permutation of } (x, y, z) \\ -1 & \text{if } (\alpha, \beta, \gamma) \text{ is a noncyclic permutation of } (x, y, z) \\ 0 & \text{otherwise} \end{cases} \quad (2.1.3)$$

define elements of a matrix and a Cartesian tensor of third rank, respectively.^[59] The Einstein summation convention for repeated indices^[60]

$$\sum_{i=M}^N A_i B_i := A_i B_i \quad (2.1.4)$$

is used throughout this work. Regardless of this, the sum sign may be given in certain instances in order to avoid ambiguities in the lower or upper bound M and N .

2.2. Basic Principles of Classical Electrodynamics

2.2.1. Maxwell's equations

The fundamental equations governing the laws of classical electrodynamics are known as Maxwell's equations.^[61] They form relations between electric fields \mathbf{E} and magnetic fields \mathbf{B}

$$\nabla \cdot \mathbf{E} = 4\pi\rho, \quad (2.2.1)$$

$$\nabla \cdot \mathbf{B} = 0, \quad (2.2.2)$$

$$\nabla \times \mathbf{E} = -\frac{\partial \mathbf{B}}{\partial t}, \quad (2.2.3)$$

$$\nabla \times \mathbf{B} = \frac{1}{c_0^2} \frac{\partial \mathbf{E}}{\partial t} + \frac{4\pi}{c_0^2} \mathbf{j}, \quad (2.2.4)$$

which also involve the charge density ρ and the current density \mathbf{j} of a system. The variable t denotes time, c_0 the speed of light in vacuum and ∇ is the nabla symbol. Equations (2.2.1) and (2.2.2) are known as Gauss's law and Gauss's law for magnetism, respectively. They signify that the flux of an electric field is proportional to the charge density, while magnetic fields only appear in closed loops. The Maxwell–Faraday equation (2.2.3) states that time-dependent magnetic fields induce electric fields, while the Ampère–Maxwell equation (2.2.4) implies that time-dependent electric fields as well as an electric currents induce magnetic fields.

An additional condition used in classical electromagnetism is that the electric charge is conserved, also known as continuity equation,^[62]

$$\nabla \cdot \mathbf{j} = -\frac{\partial \rho}{\partial t}, \quad (2.2.5)$$

which implies that the current density is related to the charge density directly through the velocity \mathbf{v} of the charges:

$$\mathbf{j} = \rho \mathbf{v}. \quad (2.2.6)$$

2.2.2. Electric Scalar and Magnetic Vector Potential

Maxwell's equations may be simplified by working with potentials instead of the fields themselves. Indeed, the magnetic and electric fields are related to a magnetic vector

potential \mathbf{A} and an electric scalar potential φ through

$$\mathbf{B} = \nabla \times \mathbf{A}, \quad (2.2.7)$$

$$\mathbf{E} = -\nabla\varphi - \frac{\partial\mathbf{A}}{\partial t}, \quad (2.2.8)$$

which automatically solve Gauss's law for magnetism (2.2.2) and the Maxwell–Faraday equation (2.2.3) by construction.^[61] Reinserting these definitions for \mathbf{B} and \mathbf{E} into Gauss's law (2.2.1) and the Ampère–Maxwell equation (2.2.4) yields the following equations of motions (EOM):

$$\nabla^2\varphi + \frac{\partial}{\partial t}(\nabla \cdot \mathbf{A}) = -4\pi\rho, \quad (2.2.9)$$

$$\nabla^2\mathbf{A} - \frac{1}{c_0^2}\frac{\partial^2\mathbf{A}}{\partial t^2} = -\frac{4\pi}{c_0^2}\mathbf{j} + \nabla\left(\nabla \cdot \mathbf{A} + \frac{1}{c_0^2}\frac{\partial\varphi}{\partial t}\right). \quad (2.2.10)$$

These EOM only possess four degrees of freedom compared to the six degrees of freedom contained in the original formulation of Maxwell's equations.

2.2.3. Gauge problem and gauge fixing

The magnetic vector potential and electric scalar potential are not uniquely defined. Using a transformed magnetic vector potential $\mathbf{A}' = \mathbf{A} + \nabla\Lambda$ and a transformed electric scalar potential $\varphi' = \varphi + C$, with Λ being an arbitrary scalar field and C being a constant, is equally valid and fulfills all conditions imposed onto the two potentials. Such a shift from one valid form of a potential to another is called a gauge transformation. Typically, this freedom of choice in the determination of the potentials is restricted by choosing a gauge. The gauge of φ can be chosen such that the potential vanishes at large distances. The gauge of \mathbf{A} is restricted by introducing an additional restriction to its divergence $\nabla \cdot \mathbf{A}$.^[61]

One choice of gauge for the magnetic vector potential is the Coulomb gauge,

$$\nabla \cdot \mathbf{A} = 0, \quad (2.2.11)$$

which simplifies the EOM in eq. (2.2.9) and (2.2.10) significantly:^[62]

$$-\nabla^2\varphi = 4\pi\rho, \quad (2.2.12)$$

$$-\nabla^2\mathbf{A} + \frac{1}{c_0^2}\left[\frac{\partial^2\mathbf{A}}{\partial t^2} + \nabla\frac{\partial\varphi}{\partial t}\right] = \frac{4\pi}{c_0^2}\mathbf{j}. \quad (2.2.13)$$

From this, an explicit form for the electric scalar and magnetic vector potentials can be derived:^[63]

$$\varphi(\mathbf{r}, t) = \int \frac{\rho(\mathbf{r}', t)}{|\mathbf{r} - \mathbf{r}'|} d\mathbf{r}', \quad (2.2.14)$$

$$\mathbf{A}(\mathbf{r}, t) = \nabla \times \int \frac{\mathbf{B}(\mathbf{r}', t)}{4\pi|\mathbf{r} - \mathbf{r}'|} d\mathbf{r}'. \quad (2.2.15)$$

In the case of a static, homogeneous magnetic field, eq. (2.2.15) further simplifies to

$$\mathbf{A}(\mathbf{r}) = \frac{1}{2} \mathbf{B} \times \mathbf{r}, \quad (2.2.16)$$

which is also sometimes referred to as the symmetric gauge. The magnetic vector potential in the symmetric gauge exhibits the unphysical behaviour of diverging at infinity. For a finite volume, however, the symmetric gauge is generally a reasonable description for a magnetic field in the case of magnetostatic conditions.

It should be noted that the Coulomb gauge is not complete and additional constraints have to be included. In the case of the symmetric gauge, for instance, this leads to a dependence of the magnetic vector potential on the gauge origin \mathbf{O} of the system, leading to an infinite number of equally valid magnetic vector potentials:^[62]

$$\mathbf{A}^{\mathbf{O}}(\mathbf{r}) = \frac{1}{2} \mathbf{B} \times (\mathbf{r} - \mathbf{O}). \quad (2.2.17)$$

While this unphysical dependence of the magnetic vector potential on the gauge origin is not problematic, it is crucial that all observable quantities are gauge origin independent.

2.3. Moving Charged Particle in an Electromagnetic Field

2.3.1. Principle of Minimal Coupling and Lorentz force

Having introduced a way to describe electromagnetic fields through their vector and scalar potentials, it is now possible to understand the dynamics of a moving charged particle in an external field. The Lagrangian of a system,

$$\mathcal{L} = T - V, \quad (2.3.1)$$

is defined through its kinetic energy T and potential energy V . The trajectory of a particle with charge q can be described through its position vector of \mathbf{r} . Its velocity is $\mathbf{v} = \dot{\mathbf{r}}$, where one dot over a variable is used to describe a time-derivative, while two dots over a variable denote a second derivative with respect to time. The kinetic and potential energies of the particle,

$$T = \frac{1}{2}m\dot{\mathbf{r}}^2, \quad (2.3.2)$$

$$V = q\varphi - q\mathbf{A} \cdot \dot{\mathbf{r}}, \quad (2.3.3)$$

and thus also the Lagrangian, can be constructed in a straightforward manner known as minimal coupling. The canonical momentum of the particle

$$\mathbf{p} := \frac{\partial \mathcal{L}}{\partial \dot{\mathbf{r}}_\alpha} = m\dot{\mathbf{r}} + q\mathbf{A} \quad (2.3.4)$$

contains the magnetic vector potential and is therefore a gauge-dependent quantity. The kinetic momentum

$$\boldsymbol{\pi} = \mathbf{p} - q\mathbf{A}, \quad (2.3.5)$$

however, must remain gauge invariant as it corresponds to an observable quantity. The Euler-Lagrange equation

$$\frac{d}{dt} \frac{\partial \mathcal{L}}{\partial \dot{\mathbf{r}}} = \frac{\partial \mathcal{L}}{\partial \mathbf{r}} \quad (2.3.6)$$

can then be used in order to construct an EOM for the moving charged particle in the external electromagnetic field. Identifying the left-hand side (lhs) of the equation as force and re-inserting the magnetic and electric field from their definitions in eq. (2.2.7) and (2.2.8) on the right-hand side (rhs), the fundamental force of electrodynamics

$$\mathbf{F}_L = q[\mathbf{E} + \mathbf{v} \times \mathbf{B}], \quad (2.3.7)$$

the Lorentz force, is obtained.

In the context of Hamiltonian mechanics, the Hamiltonian of the system

$$\mathcal{H} = \mathbf{p} \cdot \dot{\mathbf{r}} - \mathcal{L} = T + V \quad (2.3.8)$$

can be constructed from the Lagrangian and the canonical momentum of the system. For the moving charged particle in an external, electromagnetic field the Hamiltonian thus becomes

$$\mathcal{H} = \frac{\boldsymbol{\pi}^2}{2m} + q\varphi. \quad (2.3.9)$$

Since the Hamiltonian corresponds to the energy of the system ($\mathcal{H} = E$), it contains the kinetic momentum instead of the gauge-dependent canonical momentum. Using Hamiltonian mechanics, the same EOM that could be constructed from Lagrangian mechanics through eq. (2.3.6) or Newtonian mechanics using the definition of the Lorentz force (2.3.7) is obtained.

2.3.2. Cyclotron Rotation

Using the EOM introduced in the last section, the effects of magnetostatic conditions on a moving charged particle may be considered. A particle of charge q and mass m can be put into an external, homogeneous, static magnetic field pointed in the z -direction: $\mathbf{B} = (0, 0, B_z)^\top$ and $\mathbf{E} = \mathbf{0}$. Given an initial velocity in a direction perpendicular to the external magnetic field, the charged particle starts to rotate in a circular motion often referred to as the cyclotron rotation. The frequency of this rotation is called the cyclotron frequency,^[64]

$$\omega_C = \frac{qB_z}{m}, \quad (2.3.10)$$

and it is only dependent on the magnitude of the magnetic field as well as the charge and mass of the particle.

3. Quantum-Mechanical Description of Molecules in External Magnetic Fields

In this chapter, the dynamics of electronic and nuclear motions in molecules is considered in a fully quantum-mechanical framework. This requires the solution of the time-dependent molecular Schrödinger equation and therefore the construction of the molecular Hamiltonian operator.

After a short introduction of quantum-mechanical notation used throughout this work, the Born–Oppenheimer approximation for molecules in external magnetic fields is carefully introduced. The molecular Schrödinger equation is separated into the electronic and nuclear Schrödinger equations using the Born–Oppenheimer ansatz. Subsequently, the Born–Huang adiabatic approximation and the Born–Oppenheimer adiabatic approximation are introduced, thereby neglecting different contributions to the electronic Schrödinger equation, following the nomenclature introduced in Ref. [65]. The construction of an adiabatic potential energy hypersurface is presented, including its dependence on the external magnetic field.

Using a fully relativistic approach and considering the nonrelativistic limit, an explicit form for the electronic Hamiltonian operator is derived for hydrogen-like atoms. Through the principle of minimal coupling introduced in chapter 2, the external magnetic field is conveniently described through the magnetic vector potential. An expression for the electronic Hamiltonian is given for the case of static, homogeneous magnetic fields. This result is generalized to many-electron systems, distributing the different contributions into field-free, paramagnetic and diamagnetic parts.

Finally, the Hamiltonian operator for nuclear motions in the external field is derived. The dependence on the Born–Oppenheimer potential energy hypersurface is hereby considered as well as the dependence of the nuclear kinetic energy on the external magnetic field through the principle of minimal coupling. Effective screened charges are introduced through the Berry connection which is shown to naturally enter the expression for the effective kinetic energy of nuclear motion in a Born–Oppenheimer potential energy hypersurface.

3.1. Notation

3.1.1. Operators

In quantum mechanics, any physical quantity may be represented by use of an operator, which allows for a convenient way to translate the concepts introduced in the context of classical mechanics (chapter 2) into the framework of quantum mechanics. In this work, the operator representation of a scalar O is written as \hat{O} . Similarly, the representation of a vector \mathbf{r} is written as $\hat{\mathbf{r}}$. For multiplicative operators, the operator sign may sometimes be omitted.

3.1.2. Dirac notation

In order to simplify the notation of quantum mechanics, the Dirac notation is employed. If a wave function Ψ is defined by certain characteristic integer numbers p or q , the Bra- and Ket-vectors representing Ψ_p and Ψ_q can be written as:

$$\langle p| \rightarrow \Psi_p^*, \quad (3.1.1)$$

$$|q\rangle \rightarrow \Psi_q. \quad (3.1.2)$$

The combination of a Bra- and a Ket-vector is called a Bracket and it implies an integration over the entire Hilbert space over which the wave functions are defined,

$$\langle p|q\rangle = \langle q|p\rangle^* = \int \Psi_p^* \Psi_q d\tau, \quad (3.1.3)$$

where τ is a representation of the volume associated with this Hilbert space. Using the Dirac notation, the expectation value of an operator \hat{O} is written as

$$\langle p|\hat{O}|q\rangle := \langle p|\hat{O}q\rangle = \langle \hat{O}^\dagger p|q\rangle. \quad (3.1.4)$$

Observable quantities are represented by Hermitian operators $\hat{A} = \hat{A}^\dagger$ and as a result, all expectation values of observable quantities become real-valued

$$\langle p|\hat{A}|q\rangle \in \mathbb{R}, \quad (3.1.5)$$

even though both operators and wave functions are generally complex-valued.

3.2. Born–Oppenheimer Approximation

3.2.1. Born–Oppenheimer Ansatz

The nonrelativistic time-dependent Schrödinger equation for a molecular system,

$$\hat{H}^{\text{mol}}\Psi^{\text{mol}}(\mathbf{R}, \mathbf{r}, t) = i\frac{\partial}{\partial t}\Psi^{\text{mol}}(\mathbf{R}, \mathbf{r}, t), \quad (3.2.1)$$

is the central EOM in the context of quantum chemistry.^[7, 8] It can be constructed by identifying the molecular Hamiltonian operator \hat{H}^{mol} as the representation of the classical Hamiltonian \mathcal{H} containing all relevant physical interactions between the N_{el} electrons and the N_{nuc} nuclei constituting the molecule. The solution of this EOM is given by the time-dependent molecular wave function $\Psi^{\text{mol}}(\mathbf{R}, \mathbf{r}, t)$ which describes the simultaneous motion of all electrons and nuclei contained within the molecular system. The wave function is dependent on the time coordinate t as well as all position vectors of both the electrons \mathbf{r}_i and the nuclei \mathbf{R}_I .

This problem can be simplified significantly by realizing that due to differences in mass, the electronic and nuclear movements happen on a different time scale. The Born–Oppenheimer (BO) ansatz^[66, 67] therefore decouples their movements by approximating the molecular wave function in an infinite series of products between nuclear and electronic wave functions:

$$\Psi^{\text{mol}}(\mathbf{R}, \mathbf{r}, t) \approx \Psi_p^{\text{nuc}}(\mathbf{R}, t)\Psi_p^{\text{el}}(\mathbf{R}, \mathbf{r}, t). \quad (3.2.2)$$

While this ansatz does not correspond to an exact separation of the center-of-mass motion in an external magnetic field, it should be noted that such an exact separation is generally not possible for molecules in external magnetic fields.^[68–72] Considering the two time scales separately also leads to a separation of variables for the respective wave functions. From the perspective of an electron in state p described by the electronic wave function Ψ_p^{el} , the nuclei appear to be fixed. One possibility is to consider the electronic wave function for clamped nuclei and let it be only parametrically dependent on the nuclear position vectors \mathbf{R}_I .^[67] From the perspective of a nucleus, on the other hand, the electronic movements happen instantaneously. Thus the nuclear wave function corresponding to state p does not need to depend on the electronic coordinates \mathbf{r}_i at all.

Reinserting the BO ansatz in eq. (3.2.2) into the time-dependent Schrödinger equation

(3.2.1) and focusing on the movements of the electrons yields

$$\hat{H}^{\text{mol}}\Psi_p^{\text{el}}(\mathbf{R}, \mathbf{r}, t) = i\frac{\partial}{\partial t}\Psi_p^{\text{el}}(\mathbf{R}, \mathbf{r}, t), \quad (3.2.3)$$

where it is beneficial to separate the molecular Hamiltonian

$$\hat{H}^{\text{mol}} = \hat{H}^{\text{nuc}} + \hat{H}^{\text{el}} \quad (3.2.4)$$

into an electronic Hamiltonian in the presence of clamped nuclei and a nuclear Hamiltonian. Both of these operators are constructed as representation of their classical counterparts using

$$\hat{H}^{\text{el}} = \hat{T}^{\text{el}} + \hat{V}^{\text{el}}, \quad (3.2.5)$$

$$\hat{H}^{\text{nuc}} = \hat{T}^{\text{nuc}} + \hat{V}^{\text{nuc}}. \quad (3.2.6)$$

For moving charged particles in external magnetic fields, the classical Hamiltonian was derived in section 2.3.1 and given in eq. (2.3.9). The external magnetic field is contained in the kinetic energy operators for the electrons \hat{T}^{el} and the nuclei \hat{T}^{nuc} through the principle of minimal coupling and an explicit form of both operators will be derived later in this chapter.

3.2.2. Adiabatic Approximations

Let the electronic wave functions corresponding to states p and q be represented by $|p\rangle$ and $|q\rangle$, respectively. Projecting eq. (3.2.3) onto $\langle q|$ then leads to several important realizations. Firstly, since the electronic wave functions form an orthonormal set, the electronic Hamiltonian takes on a diagonal form:

$$\langle q|\hat{H}^{\text{el}}|p\rangle = \langle q|\hat{T}^{\text{el}}|p\rangle \delta_{pq} + \langle q|\hat{V}^{\text{el}}|p\rangle \delta_{pq}. \quad (3.2.7)$$

Secondly, as the operator representing the nuclear potential energy \hat{V}^{nuc} is a multiplicative operator, it is also diagonal in the basis of electronic wave functions:

$$\langle q|\hat{V}^{\text{nuc}}|p\rangle = V_{\text{NN}}\delta_{pq}. \quad (3.2.8)$$

Thirdly, the nuclear kinetic energy, even in the absence of an external magnetic field, is generally not diagonal in the basis of electronic wave functions. However, the coupling of different electronic states through the nuclear kinetic energy can be neglected using

the Born–Huang adiabatic approximation^[65, 73–75]

$$\langle q | \hat{T}^{\text{nuc}} | p \rangle \approx T_{\text{N}} \delta_{pq}, \quad (3.2.9)$$

which only leaves the diagonal terms. The spectral decomposition of these diagonal terms contains a sum over all electronic states and thus any term in $\langle p | \hat{T}^{\text{nuc}} | p \rangle$ couples the electronic state p to all other electronic states. Fully decoupling all electronic states thus requires that

$$\langle q | \hat{T}^{\text{nuc}} | p \rangle \approx 0, \quad (3.2.10)$$

which is referred to as Born–Oppenheimer adiabatic approximation.^[65, 76]

Within the BO adiabatic approximation, it is sufficient to solve the time-dependent electronic Schrödinger equation

$$\hat{H}^{\text{el}} \Psi_p^{\text{el}}(\mathbf{R}, \mathbf{r}, t) = i \frac{\partial}{\partial t} \Psi_p^{\text{el}}(\mathbf{R}, \mathbf{r}, t), \quad (3.2.11)$$

for each electronic state p individually as they are fully decoupled. For static systems, the time-independent electronic Schrödinger equation

$$\hat{H}^{\text{el}} \Psi_p^{\text{el}}(\mathbf{R}, \mathbf{r}) = E_p^{\text{el}} \Psi_p^{\text{el}}(\mathbf{R}, \mathbf{r}), \quad (3.2.12)$$

replaces its time-dependent counterpart, introducing the electronic energy E_p^{el} . Both eqs. (3.2.11) and (3.2.12) must be solved separately for each set of nuclear coordinates \mathbf{R} . This results in a potential energy hypersurface (PES) in the coordinate space of all $3N_{\text{nuc}}$ nuclear coordinates. For electronic state p , the PES is constructed using the BO potential energy

$$E_p^{\text{BO}}(\mathbf{R}) = E_p^{\text{el}} + V_{\text{NN}}, \quad (3.2.13)$$

which in the context of quantum chemistry is also often referred to as total electronic energy. Nonadiabatic effects can then, in principle, also be included. One common approximation aiming at recovering nonadiabatic effects is the diagonal Born–Oppenheimer correction (DBOC)^[77, 78], which in the absence of an external magnetic field reads

$$E_p^{\text{DBOC}} = \langle p | \hat{T}^{\text{nuc}} | p \rangle \quad (3.2.14)$$

and contains only the diagonal terms of the nuclear kinetic energy. In the presence of an external magnetic field, the DBOC takes a somewhat different form which converges into the expression given in eq. (3.2.14) for zero-fields. An explicit form for the DBOC in external magnetic fields is presented later in this chapter.

3.3. Construction of the Electronic Hamiltonian

3.3.1. Hydrogen-like Atom

The aim of this section is to construct the nonrelativistic electronic Hamiltonian operator. As a central result, we will obtain a Hamiltonian operator of the form

$$\hat{H}^{\text{el}} = \hat{H}_{\text{field-free}}^{\text{el}} + \hat{H}_{\text{paramagnetic}}^{\text{el}} + \hat{H}_{\text{diamagnetic}}^{\text{el}}, \quad (3.3.1)$$

which contains a field-free part, a paramagnetic part which depends linearly on the external magnetic field, and a diamagnetic part with a quadratic field-dependence. In the paramagnetic part, the magnetic field is coupled with angular motion and thus contains both the angular momentum and the spin of an electron. Therefore, the derivation of an explicit form of the nonrelativistic electronic Hamiltonian operator requires casting the time-independent electronic Schrödinger equation presented in eq. (3.2.12) in a fully relativistic picture, which naturally introduces the electron spin. In a subsequent step, the nonrelativistic limit is considered, resulting in a spin-dependent two-component framework, which is used throughout this work.

The relativistic equivalent of the electronic Schrödinger equation is the four-component Dirac equation. For hydrogen-like atoms it reads^[79, 80]

$$\begin{pmatrix} \hat{V}_{\text{Ne}} & c_0 \boldsymbol{\sigma}_\alpha \hat{\pi}_\alpha \\ c_0 \boldsymbol{\sigma}_\alpha \hat{\pi}_\alpha & \hat{V}_{\text{Ne}} - 2c_0^2 \end{pmatrix} \begin{pmatrix} \Psi_{\text{L}} \\ \Psi_{\text{S}} \end{pmatrix} = E^{\text{el}} \begin{pmatrix} \Psi_{\text{L}} \\ \Psi_{\text{S}} \end{pmatrix}, \quad (3.3.2)$$

containing the Pauli matrices $\boldsymbol{\sigma}_\alpha$ representing the electron spin in three Cartesian directions. They are traceless 2×2 matrices which are typically cast as

$$\boldsymbol{\sigma}_x = \begin{pmatrix} 0 & 1 \\ 1 & 0 \end{pmatrix}, \quad \boldsymbol{\sigma}_y = \begin{pmatrix} 0 & -i \\ i & 0 \end{pmatrix}, \quad \boldsymbol{\sigma}_z = \begin{pmatrix} 1 & 0 \\ 0 & -1 \end{pmatrix}. \quad (3.3.3)$$

Thus, the wave function Ψ^{el} solving the Dirac equation is a four-component vector consisting of a so-called large component Ψ_{L} and a small component Ψ_{S} , both of which contain two spin components. The Dirac equation presented in eq. (3.3.2) has electronic and positronic solutions and is shifted in such a way that its electronic solutions align with those of the electronic Schrödinger equation in eq. (3.2.12), with negative energy solutions corresponding to bound states.

The diagonal of eq. (3.3.2) contains the shifted potential energy of the system, where

\hat{V}_{Ne} describes the attractive interaction between nucleus and electron. On the off-diagonal, the kinetic energy is represented using the Pauli matrices as well as the kinetic momentum operator $\hat{\boldsymbol{\pi}}$ with an explicit form

$$\hat{\boldsymbol{\pi}} = \hat{\mathbf{p}} + \hat{\mathbf{A}} \quad (3.3.4)$$

derived from the principle of minimal coupling^[81] as presented in the context of classical mechanics in eq. (2.3.5). It contains the canonical momentum operator $\hat{\mathbf{p}} = -i\nabla$ and the magnetic vector potential operator $\hat{\mathbf{A}}$. In the case of a static, homogeneous magnetic field in the Coulomb gauge, it can be written in a form resembling the symmetric gauge in eq. (2.2.16):

$$\hat{\mathbf{A}}^{\mathbf{O}}(\mathbf{r}) = \frac{1}{2}\mathbf{B} \times \hat{\mathbf{r}}^{\mathbf{O}}. \quad (3.3.5)$$

As discussed before, the gauge origin of this system \mathbf{O} has no physical meaning and can be arbitrarily chosen. One convenient choice mostly used in this work is the origin of the Cartesian coordinate system. The electron coordinate $\mathbf{r}^{\mathbf{O}} = (\mathbf{r} - \mathbf{O})$ in eq. (3.3.5) directly references this gauge origin.

Having cast the relativistic Dirac equation, the nonrelativistic limit can be derived by realizing that the two equations contained in eq. (3.3.2) are coupled. Using the lower equation, the small component of the wave function can be written as a function of the large component by

$$\Psi_{\text{S}} = \hat{Y} \frac{\boldsymbol{\sigma}_{\alpha} \hat{\boldsymbol{\pi}}_{\alpha}}{2c_0} \Psi_{\text{L}}, \quad (3.3.6)$$

where the coupling operator \hat{Y} can be conveniently written out in terms of a Taylor expansion

$$\hat{Y} = \left(1 + \frac{E^{\text{el}} - \hat{V}_{\text{Ne}}}{2c_0^2} \right)^{-1} = 1 - \frac{E^{\text{el}} - \hat{V}_{\text{Ne}}}{2c_0^2} + \dots \quad (3.3.7)$$

which is, of course, an infinite series. In the nonrelativistic limit where $c_0 \rightarrow \infty$, the series can be stopped after the zeroth order term

$$\hat{Y} \approx 1, \quad (3.3.8)$$

which is considered as the nonrelativistic limit. Substituting the small component in such a way, eq. (3.3.2) yields

$$\left[\hat{V}_{\text{Ne}} + \frac{(\boldsymbol{\sigma}_{\alpha} \hat{\boldsymbol{\pi}}_{\alpha})^2}{2} \right] \Psi_{\text{L}} = E^{\text{el}} \Psi_{\text{L}}, \quad (3.3.9)$$

where by comparison with eq. (3.2.12), the large component can be identified as the electronic wave function $\Psi_L = \Psi_{\text{el}}$. It is important to realize that the nonrelativistic Schrödinger equation presented in eq. (3.3.9) is still a two-component equation as it directly references the Pauli matrices. As a consequence, the solutions must also be two-component wave functions.

Finally, an explicit form of the electronic Hamiltonian operator for a hydrogen-like atom in a static, homogeneous, external magnetic field can be derived from eq. (3.3.9). Using the Dirac identity,

$$(\boldsymbol{\sigma}_\alpha \hat{a}_\alpha)(\boldsymbol{\sigma}_\alpha \hat{b}_\alpha) = (\hat{a}_\alpha \hat{b}_\alpha) \boldsymbol{\sigma}_0 + i \varepsilon_{\alpha\beta\gamma} \hat{a}_\alpha \hat{b}_\beta \boldsymbol{\sigma}_\gamma, \quad (3.3.10)$$

with the zeroth-component Pauli matrix $\boldsymbol{\sigma}_0 = \mathbf{I}_2$ being introduced as the two-component identity matrix, and the definition of the magnetic vector potential in eq. (3.3.5), we write:

$$(\boldsymbol{\sigma}_\alpha \hat{\pi}_\alpha)^2 = \hat{\boldsymbol{\pi}}^2 + \boldsymbol{\sigma}_\alpha B_\alpha. \quad (3.3.11)$$

The squared kinetic momentum operator $\hat{\boldsymbol{\pi}}$,

$$\hat{\boldsymbol{\pi}}^2 = \hat{\mathbf{p}}^2 + \mathbf{B} \cdot (\hat{\mathbf{r}}^{\mathbf{O}} \times \hat{\mathbf{p}}) + \frac{1}{4} [\mathbf{B}^2 (\hat{\mathbf{r}}^{\mathbf{O}})^2 - (\mathbf{B} \cdot \hat{\mathbf{r}}^{\mathbf{O}})^2], \quad (3.3.12)$$

contains the canonical momentum operator, a paramagnetic term which scales linearly with the external magnetic field \mathbf{B} , and diamagnetic contributions scaling quadratically with the field. Introducing the gauge origin dependent canonical angular momentum operator $\hat{\mathbf{I}}^{\mathbf{O}} = \hat{\mathbf{r}}^{\mathbf{O}} \times \hat{\mathbf{p}}$, and gathering all terms on the lhs of eq. (3.3.9), the electronic Hamiltonian operator can be divided into four different parts:

$$\hat{H}^{\text{el}} = \hat{H}_0^{\text{el}} + \hat{H}_{\text{BL}}^{\text{el}} + \hat{H}_{\text{BS}}^{\text{el}} + \hat{H}_{\text{BD}}^{\text{el}}. \quad (3.3.13)$$

Firstly, the field-free Hamiltonian \hat{H}_0^{el} does not reference the external field and contains both the kinetic and potential energy contributions also present in the absence of a field. Secondly, the two paramagnetic contributions are known as the orbital Zeeman term $\hat{H}_{\text{BL}}^{\text{el}}$ and the spin Zeeman term $\hat{H}_{\text{BS}}^{\text{el}}$. Thirdly, all diamagnetic contributions are contained in $\hat{H}_{\text{BD}}^{\text{el}}$. Explicit forms for all contributions to the electronic Hamiltonian

can be written out as:

$$\hat{H}_0^{\text{el}} = \frac{\hat{\mathbf{p}}^2}{2} + \hat{V}_{\text{Ne}}, \quad (3.3.14)$$

$$\hat{H}_{\text{BL}}^{\text{el}} = \frac{1}{2} \mathbf{B} \cdot \hat{\mathbf{l}}^{\text{O}}, \quad (3.3.15)$$

$$\hat{H}_{\text{BS}}^{\text{el}} = \frac{1}{2} \boldsymbol{\sigma}_{\alpha} B_{\alpha}, \quad (3.3.16)$$

$$\hat{H}_{\text{BD}}^{\text{el}} = \frac{1}{8} [\mathbf{B}^2 (\hat{\mathbf{r}}^{\text{O}})^2 - (\mathbf{B} \cdot \hat{\mathbf{r}}^{\text{O}})^2]. \quad (3.3.17)$$

It should be stressed again that even in the nonrelativistic case, the two-component form of the electronic Hamiltonian directly referencing the electron spin is retained through the inclusion of the spin Zeeman term.

3.3.2. Many-Electron Systems

An expansion of the electronic Hamiltonian operator for many-electron systems is straightforward. For a molecular system, henceforth all quantities referencing electrons are written with subscripts i, j and all quantities referencing nuclei with subscripts of I, J . The electronic Hamiltonian for a molecule in an external magnetic field can be divided into the same four contributions presented in eq. (3.3.14) – (3.3.17), that is, a field-free Hamiltonian, the two paramagnetic orbital and spin Zeeman terms and a diamagnetic part:^[14]

$$\hat{H}_0^{\text{el}} = \sum_i^{N_{\text{el}}} \frac{\hat{\mathbf{p}}_i^2}{2} - \sum_I^{N_{\text{nuc}}} \sum_i^{N_{\text{el}}} \frac{Z_I}{|\mathbf{R}_I - \mathbf{r}_i|} + \sum_{i < j}^{N_{\text{el}}} \frac{1}{|\mathbf{r}_i - \mathbf{r}_j|}, \quad (3.3.18)$$

$$\hat{H}_{\text{BL}}^{\text{el}} = \frac{1}{2} \sum_i^{N_{\text{el}}} \mathbf{B} \cdot \hat{\mathbf{l}}_i^{\text{O}}, \quad (3.3.19)$$

$$\hat{H}_{\text{BS}}^{\text{el}} = \frac{1}{2} \sum_i^{N_{\text{el}}} \boldsymbol{\sigma}_{\alpha}(i) B_{\alpha}, \quad (3.3.20)$$

$$\hat{H}_{\text{BD}}^{\text{el}} = \frac{1}{8} \sum_i^{N_{\text{el}}} [\mathbf{B}^2 (\hat{\mathbf{r}}_i^{\text{O}})^2 - (\mathbf{B} \cdot \hat{\mathbf{r}}_i^{\text{O}})^2]. \quad (3.3.21)$$

Here, Z_I refers to the nuclear charge of nucleus I . It is important to realize that all contributions stemming from an external magnetic field in eq. (3.3.19) – (3.3.21) are one-electron contributions. The interaction between two electrons is strictly contained in the field-free operator.

Examining the field-dependent contributions to the Hamiltonian individually reveals the effects a magnetic field has on a molecular system. Negative energy contributions stabilize a physical system while positive contributions destabilize it. A wave function solving the electronic Schrödinger equation is therefore chosen such that it minimizes the energy. The orbital Zeeman term in eq. (3.3.19) should thus minimize the total angular momentum of the system by maximizing its angular momenta and aligning them anti-parallel to the external field. The same is true for the spin Zeeman term, which favors an antiparallel orientation of the total electron spin with respect to the external field. The diamagnetic contribution is always positive and destabilizes the system. It can be minimized by contracting the molecule, leading to smaller values in the electron coordinates \mathbf{r}_i .

The total electronic energy also depends on the nuclear repulsion potential

$$V_{\text{NN}} = \sum_{I < J}^{N_{\text{nuc}}} \frac{Z_I Z_J}{|\mathbf{R}_I - \mathbf{R}_J|} \quad (3.3.22)$$

which in the BO adiabatic approximation is merely a constant. On the resulting PES of an electronic state p spanned by the nuclear coordinates \mathbf{R}_I , a local minimum

$$\frac{\partial E_p^{\text{BO}}(\mathbf{R})}{\partial R_{I\alpha}} = 0 \quad \forall R_{I\alpha} \quad (3.3.23)$$

corresponds to an equilibrium structure if the related Hessian is positive-definite. This remains strictly true for a molecular system in an external magnetic field, although the PES itself is, of course, field-dependent. Since an infinitesimal change in the external field results only in an infinitesimal change in the hypersurface, one might consider a field-dependent PES $E_p^{\text{BO}}(\mathbf{R}, \mathbf{B})$ in which the magnetic field vector \mathbf{B} is simply a variable. Such a PES can have equilibrium geometries at any field strength, but a global minimum may exist at only a certain field strength which does not necessarily need to be the zero-field.

3.4. Construction of the Nuclear Hamiltonian

Having constructed the electronic Hamiltonian and BO potential energy hypersurface, it is now possible to derive an explicit form for a nuclear Hamiltonian operator. Throughout this entire section, the Einstein summation convention is not used. Starting from the molecular time-dependent Schrödinger equation in eq. (3.2.1), and using the

BO ansatz in eq. (3.2.2) for the molecular wave function yields

$$\sum_p \hat{H}^{\text{mol}} \Psi_p^{\text{nuc}}(\mathbf{R}, t) \Psi_p^{\text{el}}(\mathbf{R}, \mathbf{r}) = \sum_p i \frac{\partial}{\partial t} \Psi_p^{\text{nuc}}(\mathbf{R}, t) \Psi_p^{\text{el}}(\mathbf{R}, \mathbf{r}), \quad (3.4.1)$$

thereby separating electronic and nuclear motions. Within the BO picture, electronic movement occurs instantaneously while nuclei move along the PES. From the perspective of the nuclei, it is sufficient to solve the time-independent electronic Schrödinger equation in eq. (3.2.12) for each (relevant) point of the hypersurface. Thus, the electronic wave function Ψ_p^{el} is not a function of time in eq. (3.4.1). Using the Dirac notation for electronic states and projecting the Schrödinger equation on state $\langle q |$ results in

$$\sum_p \langle q | \hat{H}^{\text{mol}} | \Psi_p^{\text{nuc}} \rangle = i \frac{\partial}{\partial t} \Psi_q^{\text{nuc}}, \quad (3.4.2)$$

where the orthonormality condition for the electronic wave function was used on the rhs of eq. (3.4.1).^[82]

As previously discussed, the molecular Hamiltonian can be partitioned into the electronic and nuclear components

$$\hat{H}^{\text{mol}} = \hat{T}^{\text{nuc}} + \hat{V}^{\text{nuc}} + \hat{H}^{\text{el}} \quad (3.4.3)$$

and then reinserted into eq. (3.4.2) in order to separate the nuclear Schrödinger equation into two parts. The first part references the time-independent electronic Schrödinger equation with clamped nuclei which results in a contribution corresponding to the BO PES:

$$\sum_p \langle q | \hat{H}^{\text{el}} + \hat{V}^{\text{nuc}} | \Psi_p^{\text{nuc}} \rangle = E_q^{\text{BO}}(\mathbf{R}) \Psi_q^{\text{nuc}}. \quad (3.4.4)$$

The second part consists of the nuclear kinetic energy contribution which had previously been neglected for electronic motions. Using the Born–Huang approximation in order to neglect non-diagonal terms, the kinetic energy contribution to the nuclear motion can be written as

$$\sum_p \langle q | \hat{T}^{\text{nuc}} | \Psi_p^{\text{nuc}} \rangle = \langle q | \hat{T}^{\text{nuc}} | \Psi_q^{\text{nuc}} \rangle, \quad (3.4.5)$$

where the nuclear kinetic energy operator in an external magnetic field is derived similarly to its electronic counterpart from the principle of minimal coupling:

$$\hat{T}^{\text{nuc}} = \sum_I^{N_{\text{nuc}}} \frac{1}{2M_I} \hat{\Pi}_I^2, \quad (3.4.6)$$

$$\hat{\Pi}_I = \hat{\mathbf{P}}_I - Z_I \hat{\mathbf{A}}(\mathbf{R}_I). \quad (3.4.7)$$

This kinetic energy does not describe the effective motion of nuclei for a molecule in an external magnetic field.^[72] This would be the case if bare nuclei with charges Z_I were moving in an external magnetic field, which is not what the BO picture suggests. If we imagine, for instance, the nuclear motion of a hydrogen molecule, most of the nuclear charge is screened by the electrons in its vicinity. The principle of minimal coupling leads to a Lorentz force for moving charged particles and should thus only effect the effective charges Z_I^{eff} as screened by the electrons which are adapting adiabatically to the nuclear movement on the PES. The effective nuclear kinetic energy \hat{T}^{nuc} therefore has to include the adiabatic screening charges from the electrons in addition to the minimal coupling for bare nuclei as contained in \hat{T}^{nuc} .

Applying the operator $\hat{\Pi}_I^2$ contained in the nuclear kinetic energy on the BO ansatz results in the following expression^[83]

$$\hat{\Pi}_I^2(\Psi_q^{\text{nuc}} \Psi_q^{\text{el}}) = \Psi_q^{\text{el}}(\hat{\Pi}_I^2 \Psi_q^{\text{nuc}}) + 2(\hat{\mathbf{P}}_I \Psi_q^{\text{el}}) \cdot (\hat{\Pi}_I \Psi_q^{\text{nuc}}) + (\hat{\mathbf{P}}_I^2 \Psi_q^{\text{el}}) \Psi_q^{\text{nuc}}, \quad (3.4.8)$$

which can be derived by using the product rule for the canonical nuclear momentum operator $\hat{\mathbf{P}}_I = -i\nabla_I$. Inserting eq. (3.4.8) into the expression for the nuclear kinetic energy in eq. (3.4.5) in the Born–Huang approximation yields^[82]

$$\langle q | \hat{T}^{\text{nuc}} | \Psi_q^{\text{nuc}} q \rangle = \sum_I^{N_{\text{nuc}}} \frac{1}{2M_I} \left[\hat{\Pi}_I^2 + 2\hat{\chi}_I \cdot \hat{\Pi}_I + \hat{\Delta}_I \right] \Psi_q^{\text{nuc}}, \quad (3.4.9)$$

where the two quantities $\hat{\chi}_I$ and $\hat{\Delta}_I$ have been introduced

$$\hat{\chi}_I = \langle q | \hat{\mathbf{P}}_I | q \rangle \quad (3.4.10)$$

$$\hat{\Delta}_I = \langle q | \hat{\mathbf{P}}_I^2 | q \rangle, \quad (3.4.11)$$

known as the geometric vector potential and geometric scalar potential, respectively. The geometric vector potential also naturally arises from a gauge transformation of the electronic wave function in the BO picture and is sometimes referred to as Berry

connection or Berry potential.^[83–86]

Rewriting eq. (3.4.9) results in a convenient form,

$$\langle q | \hat{T}^{\text{nuc}} | \Psi_q^{\text{nuc}} \rangle = \sum_I^{N_{\text{nuc}}} \frac{1}{2M_I} \left[(\hat{\Pi}_I + \hat{\chi}_I)^2 + \hat{\Delta}_I - \hat{\chi}_I^2 \right] \Psi_q^{\text{nuc}}, \quad (3.4.12)$$

in which the nuclear kinetic energy is separated into an effective operator containing the Berry connection and into another part corresponding to the DBOC energy contribution:

$$\hat{T}_q^{\text{eff}} = \sum_I^{N_{\text{nuc}}} \frac{1}{2M_I} \left[\hat{\mathbf{P}}_I - Z_I \hat{\mathbf{A}}(\mathbf{R}_I) + \hat{\chi}_I \right]^2, \quad (3.4.13)$$

$$E_q^{\text{DBOC}} = \sum_I^{N_{\text{nuc}}} \frac{1}{2M_I} \left[\hat{\Delta}_I - \hat{\chi}_I^2 \right]. \quad (3.4.14)$$

The subscripts q have been kept in order to reference the explicit dependence on electronic state q in the quantities presented in eq. (3.4.12). For the effective nuclear kinetic energy \hat{T}_q^{eff} in eq. (3.4.13) this stems from the Berry connection operator which includes an explicit dependence on the electronic state its referencing. It is included in \hat{T}_q^{eff} to screen the bare nuclear charges such that the Lorentz force only effects the effective nuclear charges Z_I^{eff} . Since the distribution of electrons is different for all non-degenerate electronic states, the screening on the nuclear charges will also be different.

Finally, neglecting the DBOC contribution, the nuclear Schrödinger equation in the BO adiabatic approximation reads

$$\left[\hat{T}_q^{\text{eff}} + E_q^{\text{BO}} \right] \Psi_q^{\text{nuc}} = i \frac{\partial}{\partial t} \Psi_q^{\text{nuc}}, \quad (3.4.15)$$

and thus can only be solved if the BO PES is known for the relevant region of the nuclear motion. In the absence of an external field, the magnetic vector potential is zero and no Lorentz force is induced on the moving nuclei. The Berry connection also vanishes in the absence of an external field as eq. (3.4.10) suggests if real-valued electronic wave functions are inserted. The presence of the Berry connection therefore seems to be intrinsically linked to the existence of magnetic fields, even though it bears no actual dependence on the magnetic field itself. It appears in the calculation of a variety of magnetic properties, such as rotational g factors, but generally also has to be considered in the vicinity of conical intersections of the PES.^[87–89]

4. Electronic Wave Function: Construction and Symmetry

Having established the Born-Oppenheimer approximation for molecules in external magnetic fields and how to construct the electronic and nuclear Schrödinger equations, it is time to examine their solutions. Since the nuclear Schrödinger equation requires a solution to the time-independent electronic Schrödinger equation for each relevant point of the potential energy surface, it is necessary to focus on the solution to the electronic Schrödinger equation first.

In this chapter, the electronic wave function for a molecular system in a static, homogeneous, external magnetic field is closely examined. After establishing a more convenient notation, the properties of the exact electronic wave function are thoroughly investigated. Both the global phase as well as a phase introduced by an external magnetic field are considered. Due to the appearance of the Pauli matrices in the electronic Hamiltonian, a two-component spinor form for the wave function is suggested. The linear combination of atomic orbitals ansatz is discussed and how a phase correction eliminates gauge origin dependencies of observable quantities. The resulting London atomic orbitals (LAOs) are used throughout this work.

The remaining part of this chapter is concerned with the symmetry of the exact electronic wave function in an external magnetic field. Firstly, the spin symmetry is introduced and compared to the spin symmetry of wave functions in the absence of fields. Secondly, the time-reversal and magnetic symmetries are investigated. Lastly, spatial symmetry is considered in the framework of molecular point groups in magnetic fields – magnetic point groups. The investigation of magnetic point groups and their properties was carried out in the context of this work and published in Ref. [52]. The results are presented here, including a discussion of general properties of magnetic point groups and the introduction of a flow chart, which can be used to conveniently identify magnetic point groups. All of these findings are utilized in the next chapter in order to classify approximate wave functions by which symmetries are retained.

4.1. Notation

The majority of this work is concerned with electronic structure theory in external magnetic fields, both for static and dynamic systems. Therefore, the short-hand notation $\hat{H} := \hat{H}^{\text{el}}$ is used for the electronic Hamiltonian operator and $\Psi := \Psi^{\text{el}}$ for the electronic wave function. For the electronic Hamiltonian operator \hat{H} , we assume that the effects of an external, static, homogeneous magnetic field \mathbf{B} are included through the separation presented in eq. (3.3.18)–(3.3.21). Furthermore, the electronic wave function Ψ_p in this chapter is referring to a bound electronic state p and is considered as an exact solution to the time-independent electronic Schrödinger equation (3.2.12). Continuum wave functions, for which the Born-Oppenheimer ansatz presented in section 3.2.1 is not valid,^[67] are not considered in this work.

Most (but unfortunately not all) properties assigned to Ψ_p in this chapter also apply to approximate wave functions such as the ones presented in chapter 5. Whenever any of the properties discussed in this chapter does not apply to an approximate wave function, it will be addressed.

4.2. Phase of the Electronic Wave Function

4.2.1. Global Phase

Solutions to the time-independent electronic Schrödinger equation are not unique. In fact, any phase-shifted wave function

$$\Psi'_p = e^{i\Phi}\Psi_p \quad (4.2.1)$$

with $0 \leq \Phi < 2\pi$ has the exact same physical properties as Ψ_p .^[83] This can easily be verified by calculating the expectation value over any operator \hat{O}

$$\langle p' | \hat{O} | p' \rangle = \langle p | e^{-i\Phi} \hat{O} e^{i\Phi} | p \rangle = \langle p | \hat{O} | p \rangle \quad (4.2.2)$$

and realizing that the phase factor cancels out exactly. If possible without loss of generality, we choose this phase factor to belong to the set $\Phi \in \{0, \pi\}$ by requiring the wave function to be real-valued.

4.2.2. Gauge Transformation

The magnetic vector potential \mathbf{A} has been introduced in the context of classical electrodynamics in section 2.2.3, thereby establishing the gauge problem. In the Coulomb gauge ($\nabla \cdot \mathbf{A} = 0$), an explicit form for the magnetic vector potential was derived for static, homogeneous magnetic fields in eq. (2.2.17). A gauge transformation from a magnetic vector potential \mathbf{A} with gauge origin \mathbf{O} to another magnetic vector potential \mathbf{A}' with gauge origin \mathbf{O}' corresponds to

$$\mathbf{A}'(\mathbf{r}) = \mathbf{A}(\mathbf{r}) - \nabla\Lambda(\mathbf{r}), \quad (4.2.3)$$

where the gauge factor Λ may be written as

$$\Lambda(\mathbf{r}) = \mathbf{A}(\mathbf{O}') \cdot \mathbf{r}. \quad (4.2.4)$$

Any physical quantity containing the magnetic vector potential, such as the electronic Hamiltonian derived in section 3.3.2, must then also be gauge transformed, which may be expressed through a similarity transformation:^[90]

$$\hat{H}' = e^{-i\Lambda(\mathbf{r})} \hat{H} e^{i\Lambda(\mathbf{r})}. \quad (4.2.5)$$

Since the gauge origin has no physical meaning, no observable quantity must depend on it. Both \hat{H} and \hat{H}' thus correspond to the same physical problem and their solutions $|p\rangle$ and $|p'\rangle$ must lead to identical electronic energies E_p :

$$\langle p' | \hat{H}' | p' \rangle = \langle p | \hat{H} | p \rangle = E_p \quad (4.2.6)$$

Inserting eq. (4.2.5) into eq. (4.2.6) leads to the realization that the gauge transformed wave functions $|p\rangle$ and $|p'\rangle$ are linked through a phase factor

$$\Psi'_p = e^{-i\Lambda(\mathbf{r})} \Psi_p, \quad (4.2.7)$$

which results in a gauge origin invariant electronic energy.^[71] However, as a consequence the wave function itself becomes dependent on the gauge origin. Furthermore, the complex phase factor now contains vital information and thus the global phase Φ can, in general, not be chosen such that the wave function becomes real-valued. As a consequence, electronic wave functions for molecules in external magnetic fields are generally complex-valued.

4.3. Ansatz for the Electronic Wave Function

4.3.1. Two-Component Wave Functions

The electronic Hamiltonian operator for a molecule in an external magnetic field depends on the two-component Pauli matrices through the spin Zeeman term given in eq. (3.3.20). Consequently, the electronic wave function must be expressed in terms of a two-component spinor

$$\Psi_p = \begin{pmatrix} \varphi_p^\alpha \\ \varphi_p^\beta \end{pmatrix}, \quad (4.3.1)$$

separating the wave function into two parts corresponding to generalized spin components denoted by $\sigma \in \{\alpha, \beta\}$.^[91] If certain spin symmetries apply, these two generalized spin components may be decoupled, which is discussed in more detail in section 4.5.

4.3.2. Linear Combination of Atomic Orbitals

For molecular systems, it is generally not possible to find analytic solutions to the time-independent Schrödinger equation. The electronic wave function can be represented in terms of a linear combination of basis functions ξ_μ through

$$\varphi_p^\sigma = C_{\mu p}^\sigma \xi_\mu(\mathbf{r}), \quad (4.3.2)$$

where the matrix \mathbf{C}^σ contains the expansion coefficients corresponding to the generalized spin component σ . A fixed set of basis functions ξ_μ is referred to as a basis set. If a basis represents the electronic wave function exactly, it is complete. However, this generally requires an infinite amount of basis functions. In practice, we use truncated basis sets in order to approximate the electronic wave function. For electronic wave functions of molecular systems, a common approach is to choose atom-centered one-electron wave functions called orbitals as basis functions. For this choice, eq. (4.3.2) is then referred to as the linear combination of atomic orbitals (LCAO) ansatz.^[92–95]

Let us consider the electronic wave function of an atomic system for which the LCAO ansatz was chosen. All atomic orbitals are then centered at the nucleus and thus a single point in space. If the gauge origin \mathbf{O} of the magnetic vector potential is also centered at the atom, the phase factor in eq. (4.2.7) vanishes and the electronic wave function can be chosen to be real-valued without loss of generality. This choice of gauge is known as the natural gauge origin.^[23, 96] Any other choice of gauge corresponds

to a gauge transformation and results in a complex-valued electronic wave function. For molecular systems, no natural gauge can be formulated in the LCAO ansatz. Starting from a set of real-valued basis functions χ_μ , the gauge transformation of atomic orbitals (AOs) corresponding to different atoms, each centered at \mathbf{R}^μ , is written as

$$\xi_\mu(\mathbf{r}) = \exp\left(-\frac{i}{2}\varepsilon_{\alpha\beta\gamma}B_\alpha(R_\beta^\mu - O_\beta)r_\gamma\right)\chi_\mu(\mathbf{r}) \quad (4.3.3)$$

and incorporates the correct field-induced phase into the electronic wave function.^[20, 21, 97] As a consequence, the electronic wave function generally becomes complex-valued and dependent on the gauge origin. This choice of basis function is typically referred to as London atomic orbital (LAO) or alternatively gauge-including atomic orbital (GIAO). For historical reasons, the term LAO is mostly used in the context of calculations in strong magnetic fields, while the term GIAO is mostly used for perturbative approaches.

An atomic orbital χ_μ can be expressed in terms of a Gaussian-type orbital (GTO)

$$\chi_\mu(\mathbf{r}) = N_\mu(x - R_x^\mu)^{a_x^\mu}(y - R_y^\mu)^{a_y^\mu}(z - R_z^\mu)^{a_z^\mu} \exp(-\zeta_\mu|\mathbf{r} - \mathbf{R}^\mu|^2), \quad (4.3.4)$$

where N_μ is a normalization constant, \mathbf{a}^μ is a vector containing integers corresponding to the type of orbital χ_μ is representing, with $|\mathbf{a}^\mu| = 0$ being s -type orbitals, $|\mathbf{a}^\mu| = 1$ being p -type orbitals and so forth. The exponents ζ_μ were pre-optimized for certain basis sets and are held fixed for the entirety of a calculation. In order to further increase efficiency of quantum chemical calculations, certain subsets of GTOs in a basis may additionally be contracted with fixed prefactors.^[98–100]

It should be noted that the necessity for LAOs is somewhat of a consequence of using a truncated basis. The LAO phase factor in eq. (4.3.3) is similar to that of a plane wave, which implies that a magnetic field induces oscillations in the electronic wave function. A complete basis would be sufficiently flexible to introduce these oscillations intrinsically and could therefore be chosen to be real-valued without loss of generality.^[101, 102] In small magnetic fields, if a large basis is used and all atoms are close to the gauge origin, the error of neglecting the LAO phase factors may become small, although it never vanishes. Historically, this has led to a considerable amount of research in which a solution to the gauge problem was approximated via a multitude of methods.^[23, 103–111] Recent advances in quantum chemistry have been trying to rectify this by consistently using LAOs, both in the strong-field regime^[19, 32–35, 37, 38, 112] as well as for perturbative^[113–121] approaches.

4.4. Basic Concepts of Symmetry

An exact electronic wave function has to exhibit the same symmetry as the physical system it describes. Let $\hat{\Omega}$ represent a constant of motion:

$$[\hat{H}, \hat{\Omega}] = 0. \quad (4.4.1)$$

The electronic wave function must then either be an eigenfunction to $\hat{\Omega}$ or, in the case of degeneracies, it can be chosen such that it becomes an eigenfunction satisfying

$$\hat{\Omega}\Psi_p = \omega\Psi_p, \quad (4.4.2)$$

where ω is a so-called good quantum number describing the system.^[122-124] It is then possible to construct a projection operator $\hat{\Omega}^R$ corresponding to a symmetry transformation with respect to the preserved quantity. Any such projection operator must also commute with the Hamiltonian operator and can be inserted into the time-independent Schrödinger equation from the left to yield

$$\hat{H}\hat{\Omega}^R\Psi_p = E_p\hat{\Omega}^R\Psi_p. \quad (4.4.3)$$

Consequently, a projection operator corresponding to a symmetry transformation may at most introduce a phase factor

$$\hat{\Omega}^R\Psi_p = e^{i\Phi}\Psi_p \quad (4.4.4)$$

as a symmetry-projected wave function describes an identical state of the system with an identical electronic energy. The following sections describe symmetry properties of the electronic wave function describing a molecule in a static, homogeneous, external magnetic field.

4.5. Spin Symmetry

4.5.1. Spin Operator

In a two-component nonrelativistic framework, the wave function is expressed in terms of spinors as previously shown in eq. (4.3.1). The Hamiltonian operator may similarly be cast in terms of a two-component matrix with elements corresponding to

the generalized spin components of the spinor:

$$\hat{H} = \begin{pmatrix} \hat{H}^{\alpha\alpha} & \hat{H}^{\alpha\beta} \\ \hat{H}^{\beta\alpha} & \hat{H}^{\beta\beta} \end{pmatrix}. \quad (4.5.1)$$

The electron spin is represented by the Pauli matrices to which it is related via

$$\hat{\mathbf{S}}_\alpha = \frac{1}{2} \boldsymbol{\sigma}_\alpha \quad (4.5.2)$$

and the generalized spin components can be expressed through either a parallel orientation with respect to the electron spin (α) or an antiparallel orientation (β). In the absence of an external field, where a molecular system is described through $\hat{H} = \hat{H}_0$, the electron spin can always be chosen such that the generalized spin components are aligned to the z -axis. As a consequence, the spin in this direction becomes a constant of motion which results in

$$[\hat{H}_0, \hat{\mathbf{S}}_z] = 0 \quad (4.5.3)$$

$$\hat{\mathbf{S}}_z \Psi_p = S_z \Psi_p \quad (4.5.4)$$

which can be used in order to decouple the electron spin in the two-component representation of \hat{H} , resulting in

$$\hat{H} = \begin{pmatrix} \hat{H}^{\alpha\alpha} & 0 \\ 0 & \hat{H}^{\beta\beta} \end{pmatrix}. \quad (4.5.5)$$

In external magnetic fields, this is generally not possible as the spin Zeeman term references the Pauli matrices directly and thus

$$[\hat{H}_S, \hat{\mathbf{S}}_z] \neq 0. \quad (4.5.6)$$

If, however, the external magnetic field is aligned with the z -axis, $\mathbf{B} = (0, 0, B_z)^\top$, then \hat{H}_S and $\hat{\mathbf{S}}_z$ commute and the electronic Hamiltonian can be decoupled as shown in eq. (4.5.5).

4.5.2. Squared Spin Operator

In the presence of an external magnetic field, the electronic Hamiltonian commutes with the squared spin operator

$$[\hat{H}, \hat{\mathbf{S}}^2] = 0 \quad (4.5.7)$$

regardless of the spin orientation and therefore the exact electronic wave function is always an eigenfunction of $\hat{\mathbf{S}}^2$:

$$\hat{\mathbf{S}}^2 \Psi_p = S(S + 1) \Psi_p. \quad (4.5.8)$$

4.5.3. Spin Projection Operator

The spin projection operator $\hat{S}^R(\theta, \mathbf{R})$ describes a rotation of the electron spin around an axis represented by the unit vector \mathbf{R} about an angle of θ . Such a symmetry transformation must be expressed through a phase factor which takes the form of^[123]

$$\hat{S}^R(\theta, \mathbf{R}) = \exp\left(\frac{i\theta}{2} R_\alpha \sigma_\alpha\right). \quad (4.5.9)$$

A rotation about 2π or 360° around any axis does not result in an identical spinor, but instead reverses its sign

$$\hat{S}^R(0, \mathbf{R}) \Psi_p = -\hat{S}^R(2\pi, \mathbf{R}) \Psi_p \quad (4.5.10)$$

and only a rotation about 4π or 720° results in an identical spinor, which constraints the rotational angle to $0 \leq \theta < 4\pi$.^[91, 123]

4.6. Time-reversal symmetry

4.6.1. Time-Reversal Operator

The time-reversal operator $\hat{\mathbf{T}}$ describes the effects of moving a system backwards in time instead of forwards. It can be written as

$$\hat{\mathbf{T}} = -i\sigma_y \hat{K} \quad (4.6.1)$$

and is thus represented through an antihermitian two-component matrix and therefore does not correspond to any good quantum numbers.^[91, 123] The time-reversal operator includes the complex conjugation operator

$$\hat{K}\Psi_p = \Psi_p^*, \quad (4.6.2)$$

which is also antihermitian and only has an effect on complex-valued wave functions. The electronic Hamiltonian operator for a molecule in a static, homogeneous, external magnetic field does not commute with the time-reversal operator

$$[\hat{H}, \hat{\mathbf{T}}] \neq 0 \quad (4.6.3)$$

due to the presence of the field-dependent terms.^[125] The corresponding electronic wave function is therefore also not time-reversal symmetric. As a consequence, Kramers symmetry^[126] cannot be invoked for spinors in the presence of magnetic fields:

$$\begin{pmatrix} \varphi_p^\alpha \\ \varphi_p^\beta \end{pmatrix} \neq \begin{pmatrix} -\varphi_p^{\beta*} \\ \varphi_p^{\alpha*} \end{pmatrix}. \quad (4.6.4)$$

4.6.2. Magnetic Operator

The magnetic operator $\hat{\mathbf{M}}$ can be expressed as a combination of a spin rotation about an angle of π and the time-reversal operation:^[123]

$$\hat{\mathbf{M}}(\mathbf{R}) = \hat{\mathbf{T}}\hat{S}^R(\pi, \mathbf{R}) = iR_\alpha \boldsymbol{\sigma}_\alpha \hat{\mathbf{T}}. \quad (4.6.5)$$

Despite its name, the electronic Hamiltonian operator for a molecule in a static, homogeneous, external magnetic field does not commute with the magnetic operator

$$[\hat{H}, \hat{\mathbf{M}}] \neq 0. \quad (4.6.6)$$

Electronic wave functions for molecules in external magnetic fields are thus also not invariant with respect to the time-reversal and magnetic operations. In practice, it is therefore necessary to choose an ansatz for the electronic wave function which is not invariant with respect to either operations.^[124, 127]

4.7. Spatial Symmetry

4.7.1. Molecular Point Groups in Static Magnetic Fields

The results of this section were derived in collaboration with Gebele and Klopper in the context of this work and published in Ref. [52]. This section contains the main results presented therein, including some additional background on the combined description of spin and spatial symmetry. For the sake of brevity, the mathematical proofs contained in Ref. [52] are omitted here.

The incorporation of spatial symmetry into the electronic wave function requires a group theoretical approach. In contrast to field-free calculations, the symmetry of the external magnetic field has to be considered in addition to the molecular symmetry of the system. The spatial symmetry of a molecular system can be described through symmetry operations \hat{O}_i which map the system onto itself. In three-dimensional space (\mathbb{R}^3), this is possible through reflections, rotations and their combinations, with the complete set of symmetry operations forming a group. Both the operator representations of all symmetry operations \hat{O}_i as well as their matrix representations in \mathbb{R}^3 , \mathbf{O}_i , form homomorphic groups. A symmetry operation will transform the position vector of a nucleus \mathbf{R}_I according to

$$\mathbf{O}_i \mathbf{R}_I = \mathbf{R}'_I, \quad (4.7.1)$$

where \mathbf{R}'_I is the position vector of a nucleus of an identical atom and isotope. Similarly, the magnetic field is transformed as

$$\det(\mathbf{O}_i) \mathbf{O}_i \mathbf{B} = \mathbf{B}, \quad (4.7.2)$$

since its represented by an axial vector as demonstrated in eq. (2.2.7).^[128] It should be noted that the spatial symmetry of a molecular system depends both on the nuclear configuration and the magnetic field vector and we can thus obtain different symmetries for different points on the BO PES represented by $E_p^{\text{BO}}(\mathbf{R}, \mathbf{B})$ as introduced in section 3.3.2. Consequently, the symmetry of the electronic wave function is also dependent on the reference point of the BO PES. Most notably, the symmetry of the electronic wave function is also dependent on the orientation of the external magnetic field with respect to the molecule. Molecular rotations about an axis not aligned with the magnetic field vector will therefore generally change the molecular symmetry and the corresponding symmetry of the electronic wave function.

Following the rules laid out in eqs. (4.7.1)–(4.7.2), only the following symmetry operations can exist in static, external, magnetic fields:^[52, 128]

- the rotation about an n -fold axis parallel to the field (\hat{C}_n)
- the reflection at a mirror plane perpendicular to the field ($\hat{\sigma}$)
- the rotation-reflection about an n -fold axis (\hat{S}_n)

In passing, we note that the inversion (\hat{i}) is not listed since it is identical to the \hat{S}_2 operation. For each symmetry operation, a projection operator can be introduced, writing $\hat{O}_C^R(\theta, \mathbf{R})$ for a rotation about an angle of θ around a rotation axis represented by unit vector \mathbf{R} , \hat{O}_σ^R for a reflection and $\hat{O}_S^R(\theta, \mathbf{R})$ for a rotation-reflection. Such projection operators corresponding to each symmetry operation may at most introduce a phase factor to the electronic wave function according to eq. (4.4.4). For a rotation of the molecular system about a C_1 axis, no phase is introduced:

$$\hat{O}_C^R(0) \Psi_p = \hat{O}_C^R(2\pi) \Psi_p \quad (4.7.3)$$

However, if the spin rotation is taken into account as discussed in section 4.5.3, the electronic wave function transforms according to

$$\hat{S}^R(0, \mathbf{R}) \hat{O}_C^R(0, \mathbf{R}) \Psi_p = -\hat{S}^R(2\pi, \mathbf{R}) \hat{O}_C^R(2\pi, \mathbf{R}) \Psi_p \quad (4.7.4)$$

and thus the operation \hat{C}_1 may be represented by a symmetry operation labeled \hat{E}' .^[129, 130] Only for a rotation about an angle of 4π , no phase is introduced into the wave function,

$$\hat{S}^R(0, \mathbf{R}) \hat{O}_C^R(0, \mathbf{R}) \Psi_p = \hat{S}^R(4\pi, \mathbf{R}) \hat{O}_C^R(4\pi, \mathbf{R}) \Psi_p, \quad (4.7.5)$$

and therefore the symmetry operation $\hat{C}_{1/2}$ is labeled identity (\hat{E}), which in the context of group theory takes the role of the neutral element.^[131] This procedure is not strictly necessary if the spin variable can be decoupled, that is, if $[\hat{H}, \hat{S}_z] = 0$ and the electronic Hamiltonian can be expressed as presented in eq. (4.5.5). Since the decoupled electronic wave functions then no longer directly reference the electron spin, the \hat{C}_1 operation does not need to include a rotation of the spin and can then be used as the neutral element and labeled identity (\hat{E}). Those groups which include the operation \hat{E}' are called double groups and their use is strictly necessary if working with two-component spinors.^[130]

4.7.2. Properties and Identification of Magnetic Point Groups

Point groups which can exist in magnetic fields are denoted as magnetic point groups. They exhibit a number of properties,^[132] which were mathematically proven in collaboration with Gebele in the context of this work:^[52, 128]

- All magnetic point groups are subgroups of $C_{\infty h}$
- The magnetic point group of a system is a subgroup of the molecular point group in the absence of a field
- All magnetic point groups are Abelian

As a consequence of the first two points, the magnetic point group of a system can be identified by examining the cross-section between its molecular point group in the absence of a field and $C_{\infty h}$.^[132] Alternatively, eqs. (4.7.1)–(4.7.2) can be examined for a molecular system in order to identify its magnetic point group. These considerations can be condensed into a flow chart as shown in fig. 4.7.1, which can be used to easily identify magnetic point groups.

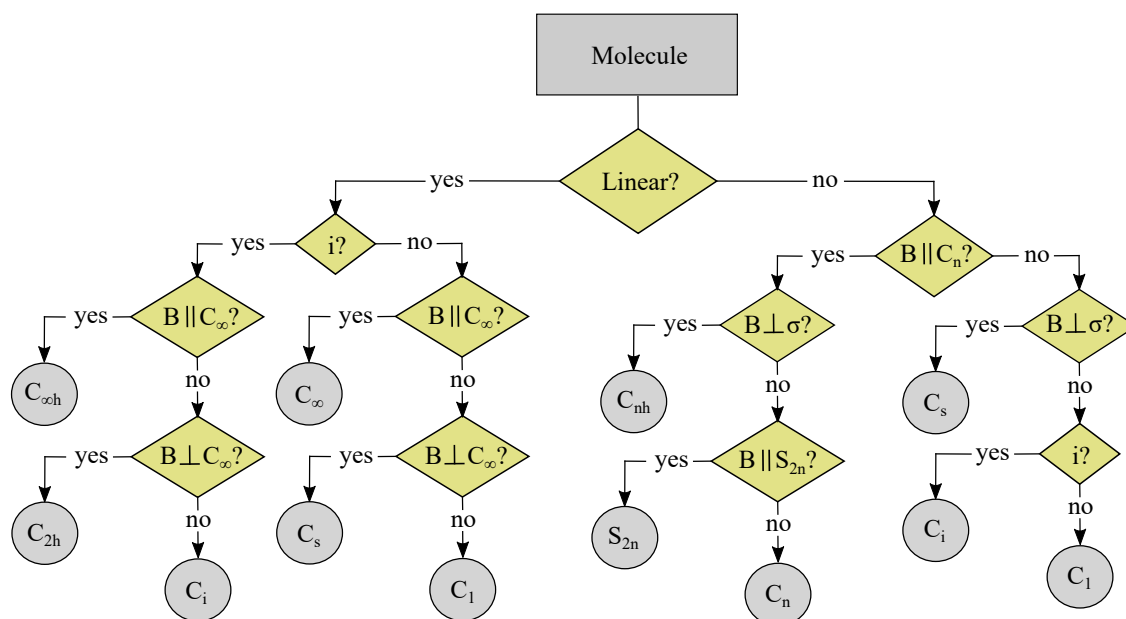


Figure 4.7.1.: Flow chart to identify the Schoenflies symbols of molecular point groups in static external magnetic fields. The symmetry operations inversion (i), rotation about an n -fold axis (C_n), reflection (σ) and rotation-reflection about a $2n$ -fold axis (S_{2n}) have to be considered, including their relative position to the external magnetic field. Reprinted with permission from Ref. [52] and originally modeled after Ref. [128].

For linear molecules, this results in two point groups which can not be found in the absence of a magnetic field: C_∞ and $C_{\infty h}$.^[90, 133] The character tables for the double groups corresponding to these two point groups were constructed using Schur's lemma for this thesis and first published in Ref. [52]. It should be noted that character tables are not unique. In this work, the conventions of Altmann and Herzog^[130] were chosen to construct the additional character tables, since they are missing in their otherwise exhaustive list.

The character table for the double group C_∞ is shown in table 4.7.1:

Table 4.7.1.: Character table of the double group C_∞ . Reprinted with permission from Ref. [52].

C_∞	E	$C_\infty(\phi)$
$A = \Sigma$	+1	+1
$E_1 = \Pi$	+1	$+\varepsilon_1^*$
	+1	$+\varepsilon_1$
$E_2 = \Delta$	+1	$+\varepsilon_2^*$
	+1	$+\varepsilon_2$
$E_3 = \Phi$	+1	$+\varepsilon_3^*$
	+1	$+\varepsilon_3$
E_n	+1	$+\varepsilon_n^*$
	+1	$+\varepsilon_n$
$E_{1/2}$	+1	$+\varepsilon_{1/2}$
	+1	$+\varepsilon_{1/2}^*$
$E_{3/2}$	+1	$+\varepsilon_{3/2}$
	+1	$+\varepsilon_{3/2}^*$
$E_{5/2}$	+1	$+\varepsilon_{5/2}$
	+1	$+\varepsilon_{5/2}^*$
$E_{7/2}$	+1	$+\varepsilon_{7/2}$
	+1	$+\varepsilon_{7/2}^*$
$E_{n+1/2}$	+1	$+\varepsilon_{n+1/2}$
	+1	$+\varepsilon_{n+1/2}^*$

$\varepsilon_k = \exp(ik\phi), \quad 0 < \phi < 2\pi, \quad n = 4, 5, 6, \dots$

The character table for the double group $C_{\infty h}$ is presented in table 4.7.2. Following the general conventions of designating irreducible representations, the subscript g (short for *gerade*) is used for irreducible representations with a positive sign in their inversion character, while u (short for *ungerade*) is used for negative signs. Other compilations of these character tables do not seem to follow this convention.^[134]

4. Electronic Wave Function: Construction and Symmetry

Table 4.7.2.: Character table of the double group $C_{\infty h}$. Reprinted with permission from Ref. [52].

$C_{\infty h}$	E	$C_{\infty}(\phi)$	I	σ_h	$S_{\infty}(\phi)$
$A_g = \Sigma_g$	+1	+1	+1	+1	+1
$E_{1g} = \Pi_g$	+1	$+\varepsilon_1^*$	+1	-1	$-\varepsilon_1^*$
	+1	$+\varepsilon_1$	+1	-1	$-\varepsilon_1$
$E_{2g} = \Delta_g$	+1	$+\varepsilon_2^*$	+1	+1	$+\varepsilon_2^*$
	+1	$+\varepsilon_2$	+1	+1	$+\varepsilon_2$
$E_{3g} = \Phi_g$	+1	$+\varepsilon_3^*$	+1	-1	$-\varepsilon_3^*$
	+1	$+\varepsilon_3$	+1	-1	$-\varepsilon_3$
E_{ng}	+1	$+\varepsilon_n^*$	+1	$(-1)^n$	$(-1)^n \varepsilon_n^*$
	+1	$+\varepsilon_n$	+1	$(-1)^n$	$(-1)^n \varepsilon_n$
$A_u = \Sigma_u$	+1	+1	-1	-1	-1
$E_{1u} = \Pi_u$	+1	$+\varepsilon_1^*$	-1	+1	$+\varepsilon_1^*$
	+1	$+\varepsilon_1$	-1	+1	$+\varepsilon_1$
$E_{2u} = \Delta_u$	+1	$+\varepsilon_2^*$	-1	-1	$-\varepsilon_2^*$
	+1	$+\varepsilon_2$	-1	-1	$-\varepsilon_2$
$E_{3u} = \Phi_u$	+1	$+\varepsilon_3^*$	-1	+1	$+\varepsilon_3^*$
	+1	$+\varepsilon_3$	-1	+1	$+\varepsilon_3$
E_{nu}	+1	$+\varepsilon_n^*$	-1	$(-1)^{n+1}$	$(-1)^{n+1} \varepsilon_n^*$
	+1	$+\varepsilon_n$	-1	$(-1)^{n+1}$	$(-1)^{n+1} \varepsilon_n$
$E_{1/2,g}$	+1	$+\varepsilon_{1/2}$	+1	+i	$-i \varepsilon_{1/2}$
	+1	$+\varepsilon_{1/2}^*$	+1	-i	$+i \varepsilon_{1/2}^*$
$E_{3/2,g}$	+1	$+\varepsilon_{3/2}$	+1	+i	$-i \varepsilon_{3/2}$
	+1	$+\varepsilon_{3/2}^*$	+1	-i	$+i \varepsilon_{3/2}^*$
$E_{5/2,g}$	+1	$+\varepsilon_{5/2}$	+1	+i	$-i \varepsilon_{5/2}$
	+1	$+\varepsilon_{5/2}^*$	+1	-i	$+i \varepsilon_{5/2}^*$
$E_{7/2,g}$	+1	$+\varepsilon_{7/2}$	+1	+i	$-i \varepsilon_{7/2}$
	+1	$+\varepsilon_{7/2}^*$	+1	-i	$+i \varepsilon_{7/2}^*$
$E_{n+1/2,g}$	+1	$+\varepsilon_{n+1/2}$	+1	+i	$-i \varepsilon_{n+1/2}$
	+1	$+\varepsilon_{n+1/2}^*$	+1	-i	$+i \varepsilon_{n+1/2}^*$
$E_{1/2,u}$	+1	$+\varepsilon_{1/2}$	-1	-i	$+i \varepsilon_{1/2}$
	+1	$+\varepsilon_{1/2}^*$	-1	+i	$-i \varepsilon_{1/2}^*$
$E_{3/2,u}$	+1	$+\varepsilon_{3/2}$	-1	-i	$+i \varepsilon_{3/2}$
	+1	$+\varepsilon_{3/2}^*$	-1	+i	$-i \varepsilon_{3/2}^*$
$E_{5/2,u}$	+1	$+\varepsilon_{5/2}$	-1	-i	$+i \varepsilon_{5/2}$
	+1	$+\varepsilon_{5/2}^*$	-1	+i	$-i \varepsilon_{5/2}^*$
$E_{7/2,u}$	+1	$+\varepsilon_{7/2}$	-1	-i	$+i \varepsilon_{7/2}$
	+1	$+\varepsilon_{7/2}^*$	-1	+i	$-i \varepsilon_{7/2}^*$
$E_{n+1/2,u}$	+1	$+\varepsilon_{n+1/2}$	-1	-i	$+i \varepsilon_{n+1/2}$
	+1	$+\varepsilon_{n+1/2}^*$	-1	+i	$-i \varepsilon_{n+1/2}^*$

$$\varepsilon_k = \exp(ik\phi), \quad 0 < \phi < 2\pi, \quad n = 4, 5, 6, \dots$$

5. Quantum Chemical Methods for Electronic Ground States

Since an exact solution to the electronic Schrödinger equation for molecular systems is generally not possible, approximations have to be introduced. Most of modern quantum chemistry is concerned with finding a good compromise between accuracy and computational effort, leading to a wide variety of different quantum chemical methods. The adaptation of these methods for the inclusion of external magnetic fields shall be the main focus of this chapter.

Two types of approaches for approximating the electronic Schrödinger equation are presented in this work. Firstly, wave function-based methods in which the many-electron wave function is approximated through various means. This includes the Hartree–Fock method and subsequent corrections which are commonly referred to as *post* Hartree–Fock methods, such as Møller–Plesset perturbation theory up to second order (MP2) and the approximate coupled cluster singles and doubles (CC2) method. For all methods, particular care is taken of an appropriate description of the wave function’s symmetry as described in the last chapter. The resolution of the identity approximation is introduced, which was derived for external magnetic fields in the context of this work and published in Ref. [56].

Secondly, Kohn–Sham density functional theory is introduced in which the electronic Schrödinger equation is approximately solved by modeling a noninteracting reference system and describing the non-classical electron interaction as a functional of the electron density and its derivatives. The existence of an external magnetic field induces currents and their inclusion in the exchange-correlation functional is thoroughly discussed, which was worked out in collaboration with Holzer and presented in Ref. [55]. The chapter concludes with the introduction of the *post* Kohn–Sham method *GW*, in which quasiparticle energies are used to replace the functional-dependent and generally physically meaningless Kohn–Sham orbital energies. The derivation of *GW* for molecules in external magnetic fields was carried out in collaboration with Holzer and Klopper and first presented in Ref. [53].

5.1. Notation

In this chapter, the many-electron wave function Ψ is approximated through one-electron wave functions ψ , also often referred to as orbitals. For general orbitals, we use the subscripts p, q, r, s , for occupied orbitals i, j, k, l and for unoccupied (virtual) orbitals a, b, c, d . These subscripts are strictly different from the designations p, q used previously in order to describe electronic states.

Within the context of quantum chemical methods, electron repulsion is represented through four-center integrals. In this work, the Mulliken notation

$$(\mu\nu|\kappa\lambda) = \iint \xi_\mu(\mathbf{r})^* \xi_\nu(\mathbf{r}) \frac{1}{|\mathbf{r} - \mathbf{r}'|} \xi_\kappa(\mathbf{r}')^* \xi_\lambda(\mathbf{r}') \, d\mathbf{r} \, d\mathbf{r}' \quad (5.1.1)$$

is consistently employed. In the context of the resolution of the identity (RI) approximation, an auxiliary basis denoted P, Q, R is introduced, which must not be confused with the similar, but lower case letter subscripts for general orbitals.^[135, 136]

The resulting three- and two-center integrals are defined as

$$(\mu\nu|P) = \iint \xi_\mu(\mathbf{r})^* \xi_\nu(\mathbf{r}) \frac{1}{|\mathbf{r} - \mathbf{r}'|} \chi_P(\mathbf{r}') \, d\mathbf{r} \, d\mathbf{r}'; \quad (5.1.2)$$

$$(P|Q) = \iint \chi_P(\mathbf{r}) \frac{1}{|\mathbf{r} - \mathbf{r}'|} \chi_Q(\mathbf{r}') \, d\mathbf{r} \, d\mathbf{r}', \quad (5.1.3)$$

using the Mulliken notation. For auxiliary basis functions, real-valued GTOs χ can always be used even in the presence of magnetic fields.^[56, 137]

5.2. Hartree–Fock Theory

5.2.1. Basic Concept and Symmetry Classification

The Hartree–Fock (HF) method is one of the most widespread approaches to approximating the many-electron wave function Ψ .^[58, 138–141] For any electronic state such as the ground state of the system, here denoted as 0, a single Slater determinant consisting of an antisymmetric tensor product of one-electron wave functions,

$$\Psi_0(\mathbf{x}_1, \mathbf{x}_2, \dots, \mathbf{x}_N) \approx (N!)^{-1/2} \det[\psi_1 \psi_2 \dots \psi_N], \quad (5.2.1)$$

is used as the ansatz. In an iterative procedure often referred to as self-consistent field (SCF) method, the orbitals are variationally optimized by solving a set of coupled effective one-electron Schrödinger equations called canonical HF equations:

$$\hat{F}\psi_j = \varepsilon_j\psi_j. \quad (5.2.2)$$

The Fock operator \hat{F} serves as an effective Hamiltonian, while the orbital energies ε_j are used to characterize the stability of their respective orbitals. The sum of the orbital energies does not correspond to the total electronic energy of the system.

As previously discussed in sec. 4.4, the exact electronic wave function is an eigenfunction of any symmetry operator $\hat{\Omega}$. For approximated wave functions such as the Slater determinant in the Hartree–Fock method, this is not necessarily the case. It is, however, generally possible to force approximated wave functions to be eigenfunctions of any symmetry operator, which is equivalent to carrying out the SCF method under a variational constraint.^[122] If the approximated wave function is an eigenfunction of $\hat{\Omega}$, this does not change the energy, otherwise the additional constraint will lead to higher energies.

Let us consider the symmetry operations presented in secs. 4.5–4.7. For spatial symmetry, the Slater determinant is an exact eigenfunction of spatial symmetry operators. Without loss of generality, the spinors can thus be characterized as belonging to irreducible representations of the magnetic point group corresponding to the current nuclear configuration.

Approximate wave functions are generally not eigenfunctions to any spin, time-reversal or magnetic operator. As mentioned before, these symmetries can be included in forms of variational constraints, leading to different labels for the HF method. If the \hat{S}^2 -symmetry is preserved, the term restricted Hartree–Fock (RHF) is used. If only the \hat{S}_z -symmetry is retained, the method is labelled unrestricted Hartree–Fock (UHF). Finally, if no spin symmetry is enforced, the method is referred to as generalized Hartree–Fock (GHF).^[142] In combination with preserved symmetries in the time-reversal or magnetic operator, eight different labels may be assigned to the HF method as listed in table 5.2.1.^[123, 124, 143]

For molecules in static, external magnetic fields, time-reversal and magnetic symmetry are broken. Therefore, only the complex RHF, UHF and GHF methods should be applied. For closed-shell molecules where electrons can be paired, the complex RHF method can be used if the magnetic field is oriented along the z -axis. Since the spin Zeeman term in the electronic Hamiltonian favors unpaired spins, this restriction

Table 5.2.1.: Symmetry classification of Hartree–Fock wave functions as modeled after Ref. [123]. Instead of the acronyms suggested by Fukutome, the more common Stuber and Paldus designations^[143] are used.

Preserved symmetry	$\hat{\mathbf{T}}$	$\hat{\mathbf{M}}$	—
$\hat{\mathbf{S}}^2$	Real RHF	Complex RHF	
\hat{S}_z	Paired UHF	Real UHF	Complex UHF
—	Paired GHF	Real GHF	Complex GHF

generally leads to Slater determinants of excited states.^[32–34] Not preserving the $\hat{\mathbf{S}}^2$ symmetry, but aligning the magnetic field with the z -axis so that the \hat{S}_z symmetry can be retained leads to the complex UHF method.^[39] This is a common choice since the magnetic field can always be oriented along the z -axis without loss of generality, thereby reducing the computational effort significantly by separating the Hamiltonian and its corresponding wave function according to eq (4.5.5). We refer to those solutions which do not retain $\langle \hat{\mathbf{S}}^2 \rangle = S(S+1)$ with S being either an integer or half-integer as spin contaminated.

For general orientations of the magnetic field, however, only the complex GHF method can be used.^[37, 56] On the one hand, this approach has some advantages, particularly its compability with relativistic approaches as well as its correct description of triplet excitations in the framework of time-dependent HF, which will be discussed in more detail in chapter 6. On the other hand, the complex GHF approach can lead to symmetry-broken wave functions with lower energies than their UHF counterparts, most importantly in the context of molecular dissociation.^[124] Nevertheless, the complex GHF method is employed throughout this work.

5.2.2. Generalized Hartree–Fock

The complex GHF method can be derived from the general HF equations presented in eq. (5.2.2). Since the Fock operator does not commute with \hat{S}_z operator, it must take the general form from eq. (4.5.1). The one-electron wave functions must be expressed in terms of spinors as shown in eq. (4.3.1) and using the LCAO ansatz with LAOs in order to ensure gauge origin invariance. The resulting non-linear equations,

$$\begin{pmatrix} \mathbf{F}^{\alpha\alpha} & \mathbf{F}^{\alpha\beta} \\ \mathbf{F}^{\beta\alpha} & \mathbf{F}^{\beta\beta} \end{pmatrix} \begin{pmatrix} \mathbf{C}_j^\alpha \\ \mathbf{C}_j^\beta \end{pmatrix} = \varepsilon_j \begin{pmatrix} \mathbf{S} & \mathbf{0} \\ \mathbf{0} & \mathbf{S} \end{pmatrix} \begin{pmatrix} \mathbf{C}_j^\alpha \\ \mathbf{C}_j^\beta \end{pmatrix}, \quad (5.2.3)$$

are the complex two-component Roothaan–Hall equations. They represent a generalized eigenvalue problem with the overlap matrix $S_{\mu\nu} = \langle \mu | \nu \rangle$ constituting the metric. If LAOs are employed, the overlap matrix is hermitian.

The Fock matrix can be cast more conveniently using the Pauli matrices, defining $\boldsymbol{\sigma}_1 := \boldsymbol{\sigma}_x$, $\boldsymbol{\sigma}_2 := \boldsymbol{\sigma}_y$ and $\boldsymbol{\sigma}_3 := \boldsymbol{\sigma}_z$. In combination with $\boldsymbol{\sigma}_0$, the Fock matrix may be decomposed according to

$$\mathbf{F} = \mathbf{F}_m \otimes \boldsymbol{\sigma}_m, \quad (5.2.4)$$

with $m = \{0, 1, 2, 3\}$.^[37] These four contributions correspond to a spin-free ($\boldsymbol{\sigma}_0$) term as well as three terms representing the electron spin, each in one Cartesian component. They can be constructed individually as

$$\mathbf{F}_m = \mathbf{h}_m + \mathbf{V}_m[\mathbf{D}_m], \quad (5.2.5)$$

where \mathbf{h} is the one-electron part and \mathbf{V} the two-electron part of the Fock matrix. The two-electron part is a functional of the density matrix which can similarly be decomposed into a total electron density matrix \mathbf{D}_0 and three spin density matrices:

$$\mathbf{D} = \mathbf{D}_m \otimes \boldsymbol{\sigma}_m. \quad (5.2.6)$$

The two-component Roothaan–Hall equations are solved in an iterative procedure with an initial guess for the coefficient matrices \mathbf{C} from which the density matrices are constructed:

$$D_{\mu\nu}^{\sigma\sigma'} = C_{\mu j}^{\sigma} C_{\nu j}^{\sigma'*}. \quad (5.2.7)$$

For any set of density matrices, the Fock matrix can be constructed according to eq. (5.2.5). By transforming the Fock matrix into the molecular orbital (MO) basis and diagonalizing it, a new set of coefficients is obtained and the procedure is continued until the coefficients are converged.

5.2.3. Construction of the Fock Matrix

Having described an outline of the GHF method and SCF procedure, it is now necessary to focus on how the Fock matrix is constructed. Since the Fock operator acts as an effective one-electron Hamiltonian, it must contain all terms derived in sec. 3.3.2. According to eq. (5.2.5), it can be separated into a one-electron and a

two-electron part. The one-electron part must be decomposed as

$$h_{\mu\nu,0} = \langle \mu | \hat{h}_0 | \nu \rangle , \quad (5.2.8)$$

$$h_{\mu\nu,n} = \frac{1}{2} B_n \langle \mu | \nu \rangle , \quad (5.2.9)$$

with $n = \{1, 2, 3\}$ and $B_1 = B_x$, $B_2 = B_y$, $B_3 = B_z$, since only the spin Zeeman term contains an explicit reference to the Pauli matrices. All other one-electron contributions, including the canonical kinetic energy, electron-nuclear attraction, orbital Zeeman and the diamagnetic terms, are contained in the spin-free one-electron Hamiltonian operator:

$$\hat{h}_0 = \frac{\hat{\mathbf{p}}^2}{2} - \sum_I^{N_{\text{nuc}}} \frac{Z_I}{|\mathbf{R}_I - \mathbf{r}|} + \frac{1}{2} \mathbf{B} \cdot \hat{\mathbf{l}}^{\text{O}} + \frac{1}{8} [\mathbf{B}^2 (\hat{\mathbf{r}}^{\text{O}})^2 - (\mathbf{B} \cdot \hat{\mathbf{r}}^{\text{O}})^2] . \quad (5.2.10)$$

It should be stressed again that an external magnetic field only directly influences the one-electron part through its Hamiltonian, while all parts are indirectly impacted through the use of field-dependent LAOs.

The two-electron part \mathbf{V} consists of a classical Coulomb contribution \mathbf{J} and a purely quantum-mechanical term called exchange \mathbf{K} resulting from the Pauli exclusion principle embedded into the method through the use of Slater determinants. While the Coulomb contribution is repulsive, the exchange contribution represents an attractive potential between electrons of different spin, thus accounting for a lessened repulsion between electrons of different spin. Therefore, the exchange contribution is specifically spin-dependent and the two-electron potential is decomposed as

$$\mathbf{V}_0[\mathbf{D}_0] = \mathbf{J}_0[\mathbf{D}_0] - \mathbf{K}_0[\mathbf{D}_0] , \quad (5.2.11)$$

$$\mathbf{V}_n[\mathbf{D}_n] = -\mathbf{K}_n[\mathbf{D}_n] . \quad (5.2.12)$$

The individual elements of the Coulomb and exchange matrices are given by

$$J_{\mu\nu,0} = \sum_{\kappa\lambda} (\mu\nu | \kappa\lambda) D_{\lambda\kappa,0} , \quad (5.2.13)$$

$$K_{\mu\nu,m} = \sum_{\kappa\lambda} (\mu\lambda | \kappa\nu) D_{\lambda\kappa,m} , \quad (5.2.14)$$

and need four-center integrals contracted with density matrix elements for their construction. As such, calculating the exchange contribution is significantly more computationally demanding than the Coulomb contribution and is usually the most

time-consuming step of a HF calculation.

Finally, the total electronic energy can be computed from its individual contributions

$$E_{\text{GHF}} = E_{1e} + E_{\text{J}} + E_{\text{K}} + V_{\text{NN}}, \quad (5.2.15)$$

$$E_{1e} = T_e + V_{\text{Ne}} + E_{\text{BS}} + E_{\text{BL}} + E_{\text{BD}}, \quad (5.2.16)$$

through contraction with their respective density matrices. The field-dependent terms are all contained in the one-electron energy (E_{1e}) and labeled as their respective Hamiltonian operators in sec. (3.3.2).

5.2.4. Resolution of the Identity Approximation

In the HF method, the construction of the two-electron contribution to the Fock matrix is usually the most time-intensive step. More specifically, the construction of four-center integrals is extremely time-consuming as they are both the most abundant and computationally demanding integrals to be solved. Through the use of auxiliary basis functions, the integrals can be approximated through

$$(\mu\nu|\kappa\lambda) \approx \sum_{PQ} (\mu\nu|P)(P|Q)^{-1}(Q|\kappa\lambda), \quad (5.2.17)$$

which is called the resolution of the identity (RI) approximation.^[135, 144–148] This can significantly reduce the computational effort for the Coulomb matrix, for which eq. (5.2.17) can be directly inserted into eq. (5.2.13) to yield

$$J_{\mu\nu,0} \approx \sum_{\kappa\lambda} \sum_{PQ} (\mu\nu|P)(P|Q)^{-1}(Q|\kappa\lambda)D_{\lambda\kappa,0}. \quad (5.2.18)$$

This requires only the solution of two- and three-center integrals which formally reduces the scaling from $\mathcal{O}(N^4)$ to $\mathcal{O}(N^3)$. This is referred to as the RI- J approximation.^[136, 149] Unfortunately, the typically more computationally demanding exchange matrix cannot be treated equivalently, as μ and ν refer to the same electronic coordinate. Therefore, the auxiliary three-center quantities

$$B_{\mu\nu,Q} = \sum_P (\mu\nu|P)(P|Q)^{-1/2}, \quad (5.2.19)$$

$$B'_{Q,\kappa\lambda} = \sum_R (Q|R)^{-1/2}(R|\kappa\lambda) \quad (5.2.20)$$

are introduced, combined with a generally larger auxiliary basis set. The coefficient matrices \mathbf{C} are then used directly in order to construct the exchange matrix as

$$K_{\mu\nu}^{\sigma\sigma'} \approx \sum_{\kappa\lambda} \sum_Q \sum_j B_{\mu\lambda,Q} B'_{Q,\kappa\nu} C_{\lambda j}^{\sigma} C_{\kappa j}^{\sigma'*}. \quad (5.2.21)$$

While the RI- K approximation does not formally reduce the scaling of the HF method, it can still lead to significantly reduced computation times.^[149]

A detailed overview of the RI approximation in the context of external magnetic fields and LAOs was worked out in the context of this thesis and published in Ref. [56]. The working equations of both RI- J and RI- K for LAOs are identical to those constructed using AOs. Thus, the only differences between RI for quantum chemical calculations in the absence and presence of a magnetic field lie in the construction and processing of integrals. Since auxiliary basis functions can be chosen to be real-valued without loss of generality,^[137] the two-center integrals ($P|Q$) remain real-valued. Three-center integrals ($\mu\nu|P$) in the basis of LAOs are complex-valued; their computation is presented in sec. 9.5.3 of this work. Finally, the necessary steps for the implementation of the RI approximation in external magnetic fields are discussed in sec. 8.1.

5.3. Post Hartree–Fock Methods

5.3.1. Electron Correlation

The Hartree–Fock method reduced the many-electron wave function to a single Slater determinant consisting of one-electron wave functions. Using a mean-field description for the interaction between electrons, the generalized Hartree–Fock energy E_{GHF} and corresponding wave function for the electronic ground state $|\text{GHF}\rangle$ was obtained. However, the correlated movement of electrons was disregarded in this approach and we thus define the difference between the exact electronic energy and HF as the correlation energy

$$E_{\text{corr}} = E_{\text{exact}} - E_{\text{GHF}}, \quad (5.3.1)$$

which is always negative since HF is a variational method. While an exact calculation of the correlation energy is in principle possible, it is extremely time-consuming and cannot be carried out for systems containing more than a few electrons. However, a large number of approximations for the correlation energy are available, presenting different compromises between accuracy and computational effort. These methods are

called *post* Hartree–Fock methods since they typically require a HF reference wave function and can thus only be carried out after a successful HF calculation.

All of these *post* HF methods aim at improving the two-electron part of a HF calculation and as such, they generally do not reference one-electron terms such as the field-dependent contributions. Therefore, these methods only indirectly depend on an external magnetic field through the use of LAOs. A very short overview over two of these methods implemented in the context of this work is given here and the interested reader is referred to the literature.^[150–154]

5.3.2. Møller–Plesset Perturbation Theory

The correlation energy can be approximated using a perturbative approach. Treating the two-electron part as the external perturbation, the electronic energy and wave function can be expanded in a power series. If the GHF wave function is used as the unperturbed wave function, this approach is called generalized Møller–Plesset perturbation theory up to n -th order (GMP n). While GMP1 yields the GHF energy as a result, the first correction results from GMP2 which can be used to approximate the correlation energy: $E_{\text{corr}} \approx E_{\text{GMP2}}$.

In this work, GMP2 is used in combination with the RI approximation.^[155–157] Similar to RI- K , three-center integrals are calculated using LAOs and an auxiliary basis. This auxiliary basis, however, is typically chosen to be a lot larger than the basis used for RI- K . The three-center integrals are transformed to the MO basis,

$$B_{pq,Q} = \sum_{\mu\nu} B_{\mu\nu,Q} [C_{\mu p}^{\alpha*} C_{\nu q}^{\alpha} + C_{\mu p}^{\beta*} C_{\nu q}^{\beta}] , \quad (5.3.2)$$

$$B'_{Q,rs} = \sum_{\kappa\lambda} B'_{Q,\kappa\lambda} [C_{\kappa r}^{\alpha*} C_{\lambda s}^{\alpha} + C_{\kappa r}^{\beta*} C_{\lambda s}^{\beta}] , \quad (5.3.3)$$

and then used for the approximate construction of four-center integrals:

$$(pq|rs) \approx B_{pq,Q} B'_{Q,rs} . \quad (5.3.4)$$

This approach is denoted RI- C and can also be used for other *post* HF methods in which the four-center integrals are required.^[153, 154] Finally, the GMP2 energy can be calculated using the following expression:

$$E_{\text{GMP2}} = -\frac{1}{4} \sum_{ijab} \frac{|(ia|jb) - (ib|ja)|^2}{\varepsilon_a + \varepsilon_b - \varepsilon_i - \varepsilon_j} . \quad (5.3.5)$$

It should be noted that this approach is only well-defined if no degenerate Slater determinants exist ($\varepsilon_a + \varepsilon_b \neq \varepsilon_i + \varepsilon_j$), which is evident from eq. (5.3.5) considering the denominator. While extensions to the GMP2 method for degenerate orbitals do exist, they are not considered in this work. More detailed descriptions of the GMP2 approach can be found elsewhere in literature.^[150–152]

5.3.3. Approximate Coupled Cluster Theory

The approximate coupled cluster singles and doubles (CC2) method can be used to estimate the correlation energy, yielding results similar in quality to MP2.^[158] By constructing the wave function according to

$$|\text{CC2}\rangle = e^{\hat{T}_1 + \hat{T}_2} |\text{GHF}\rangle, \quad (5.3.6)$$

using a cluster operator consisting of single and double excitations and the GHF reference wave function, one obtains the two-component CC2 method.^[154] Single and double excitation manifolds are defined by μ_1 and μ_2 and the corresponding single and double excitation operators are given by

$$\hat{T}_n = \sum_{\mu_n} t_{\mu_n} \hat{\tau}_{\mu_n}, \quad (5.3.7)$$

with t_{μ_1} and t_{μ_2} being the cluster amplitudes $\hat{\tau}_{\mu_1}$ and $\hat{\tau}_{\mu_2}$ the excitation operators, respectively.^[159] By using the shorthand notation

$$\hat{H} = e^{-\hat{T}_1} \hat{H} e^{\hat{T}_1} \quad (5.3.8)$$

for a similarity transformation of the Hamiltonian using the single excitation operator, the cluster amplitudes are determined through the solution of the following equations:

$$\Omega_{\mu_1} = \langle \mu_1 | \hat{H} + [\hat{H}, \hat{T}_2] | \text{GHF} \rangle = 0, \quad (5.3.9)$$

$$\Omega_{\mu_2} = \langle \mu_2 | \hat{H} + [\hat{H}, \hat{T}_2] | \text{GHF} \rangle = 0. \quad (5.3.10)$$

These equations are solved in an iterative procedure, using RI-*C* with LAOs for the construction of four-center integrals.^[160, 161] While yielding comparable results to MP2 for ground-state energies, the CC2 method can also be used for the subsequent calculation of electronic excitations.^[158, 162, 163]

5.4. Kohn–Sham Density Functional Theory

5.4.1. Basic Concept and Symmetry Classification

Kohn–Sham density functional theory (DFT) is likely the most commonly used method in modern quantum chemistry.^[164–166] Although structurally very similar to the HF method, it does not rely on finding an approximation to the many-electron wave function Ψ . Instead, a noninteracting reference system is proposed, which is solved using a single Slater determinant consisting of one-electron wave functions often referred to as Kohn–Sham (KS) orbitals. In contrast to the orbitals used in HF theory, KS orbitals are generally not assigned any physical meaning, with a few exceptions such as Janak’s theorem.^[167–169]

The entire non-classical electronic interaction is then contained in a term called exchange-correlation (xc) energy E_{xc} , which is self-consistently optimized as a functional of the ground-state electron density. The noninteracting and fully interacting systems are smoothly linked via the density-fixed adiabatic connection and can in principle be exactly represented through the same electron density.^[170–175] Unfortunately, the exact xc functional is unknown, making the use of approximations necessary. In this work, two types of approximations for the xc functional are used. Firstly, the generalized gradient approximation (GGA), in which the xc energy is calculated as a functional of the electron density ρ_m and its gradient $\nabla\rho_m$:

$$E_{xc}^{\text{GGA}} = \sum_m \int f_{xc} [\rho_m(\mathbf{r}), \nabla\rho_m(\mathbf{r})] d\mathbf{r}. \quad (5.4.1)$$

Secondly, the *meta*-generalized gradient approximation (MGGA) in which the xc functional is additionally dependent on the kinetic energy density τ_m :

$$E_{xc}^{\text{MGGA}} = \sum_m \int f_{xc} [\rho_m(\mathbf{r}), \nabla\rho_m(\mathbf{r}), \tau_m(\mathbf{r})] d\mathbf{r} \quad (5.4.2)$$

The subscript m refers to (generalized) spin components of the electron density, its gradient and the kinetic energy density. These quantities are defined as

$$\rho_m(\mathbf{r}) = D_{\mu\nu,m} \xi_\mu(\mathbf{r}) \xi_\nu^*(\mathbf{r}), \quad (5.4.3)$$

$$\nabla\rho_m(\mathbf{r}) = D_{\mu\nu,m} [\{\nabla\xi_\mu(\mathbf{r})\} \xi_\nu^*(\mathbf{r}) + \xi_\mu(\mathbf{r}) \nabla\xi_\nu^*(\mathbf{r})], \quad (5.4.4)$$

$$\tau_m(\mathbf{r}) = \frac{1}{2} D_{\mu\nu,m} [\hat{\mathbf{p}} \xi_\mu(\mathbf{r})] \cdot [\hat{\mathbf{p}} \xi_\nu(\mathbf{r})]^*, \quad (5.4.5)$$

respectively. In the absence of fields, LAOs $\xi(\mathbf{r})$ are reduced to regular GTOs $\chi(\mathbf{r})$. Due to the similarity of Kohn–Sham DFT and the HF method, the one-electron density matrix \mathbf{D} may be defined as previously presented in eq. (5.2.6). The total electron density at any point in space with position vector \mathbf{r} is described by $\rho_0(\mathbf{r})$. Furthermore, the generalized spin density vector $\mathbf{s}(\mathbf{r}) = (\rho_1(\mathbf{r}), \rho_2(\mathbf{r}), \rho_3(\mathbf{r}))^\top$ may point in arbitrary directions at any point in space, which is referred to as spin-noncollinearity. All rotations in the spin manifold are allowed and the generalized spin density is defined as $s(\mathbf{r}) = |\mathbf{s}(\mathbf{r})|$.^[176, 177]

Spin-collinear Kohn–Sham DFT can be obtained by imposing additional spin constraints for the xc functional. The first option is to limit the spin density vector to a single component, typically the z -component: $\mathbf{s}(\mathbf{r}) = (0, 0, \rho_3(\mathbf{r}))^\top$. Then the two-component Fock matrix can be decoupled according to eq. (4.5.5) and the approach is labeled unrestricted Kohn–Sham (UKS) DFT. The second option is to assume that the spin density vanishes completely $s(\mathbf{r}) = 0$, leading to the restricted Kohn–Sham (RKS) approach.^[178–180] In this work, only spin-noncollinear KS DFT is used.

5.4.2. Density Functional Theory in External Magnetic Fields

Using Kohn–Sham DFT in external magnetic fields requires a few additional considerations compared to the field-free case. As already described in the previous section, the electron density and its related quantities need to be calculated using LAOs in order to avoid an unphysical dependence on the gauge origin. Furthermore, external magnetic fields are known to induce currents which the exact xc functional depends on, leading to current density functional theory (CDFT).^[181–185] Alternatively, the xc functional may also be chosen to be explicitly depend on the magnetic field.^[186–188] The physical current density \mathbf{j}_m in a quantum-mechanical context can be defined from its classical counterpart given in eq. (2.2.6) and may be expressed as

$$\mathbf{j}_m(\mathbf{r}) = \hat{\boldsymbol{\pi}}\rho_m. \quad (5.4.6)$$

Using the principle of minimal coupling, it may be separated into two contributions:

$$\mathbf{j}_m(\mathbf{r}) = \mathbf{j}_m^p(\mathbf{r}) + \mathbf{A}_m^{\text{xc}}(\mathbf{r})\rho_m(\mathbf{r}). \quad (5.4.7)$$

The first contribution is equivalent to the canonical current density,

$$\mathbf{j}_m^p(\mathbf{r}) = \hat{\mathbf{p}}\rho_m = \frac{i}{2}D_{\mu\nu,m}[\nabla\xi_\mu(\mathbf{r})\xi_\nu^*(\mathbf{r}) - \xi_\mu(\mathbf{r})\nabla\xi_\nu^*(\mathbf{r})], \quad (5.4.8)$$

and is typically referred to as paramagnetic current density, while the second contribution is field-dependent through the xc contribution to the magnetic vector potential, $\mathbf{A}_m^{\text{xc}}(\mathbf{r})$.^[181, 189] For electronic ground states, we require the physical current density to vanish at all points in space, $\mathbf{j}_m(\mathbf{r}) = 0$, and derive an explicit form for the xc contribution to the magnetic vector potential:

$$\mathbf{A}_m^{\text{xc}}(\mathbf{r}) = -\frac{\mathbf{j}_m^{\text{p}}(\mathbf{r})}{\rho_m(\mathbf{r})}. \quad (5.4.9)$$

Thus, the paramagnetic current density for electronic ground states vanishes in the absence of fields or relativistic effects such as spin orbit coupling.^[190, 191]

Several options on how to consider external magnetic fields in Kohn–Sham DFT now present themselves, three of which shall be briefly discussed here. Firstly, the xc energy may be approximated using GGA functionals which were derived for calculations in the absence of fields.^[46, 49, 54] No further alterations are made and the only difference between field-free and field-dependent calculations lies in the use of LAOs.

Secondly, if the xc energy is approximated through MGGA functionals, a dependency on the paramagnetic current density naturally arises.^[184, 185, 189, 192–194] The kinetic energy density $\tau_m(\mathbf{r})$ presented in eq. (5.4.5) depends on the canonical momentum operator $\hat{\mathbf{p}}$ which may be replaced via the physical momentum operator $\hat{\boldsymbol{\pi}}$ through the principle of minimal coupling. The resulting physical kinetic energy density $\tilde{\tau}_m(\mathbf{r})$ may then be expressed as

$$\tilde{\tau}_m(\mathbf{r}) = \tau_m(\mathbf{r}) - \frac{|\mathbf{j}_m^{\text{p}}(\mathbf{r})|^2}{2\rho_m(\mathbf{r})} \quad (5.4.10)$$

by inserting the expression for the xc contribution to the magnetic vector potential as previously derived in eq. (5.4.9). It should be noted that the physical kinetic energy density as shown in eq. (5.4.10) includes both paramagnetic and diamagnetic contributions. An alternative derivation of 5.4.10 through the Fermi hole curvature is possible, but a detailed description is omitted here and the interested reader is referred to the literature.^[195, 196] The use of the physical kinetic energy density in MGGA functionals is further convenient since the inhomogeneity parameter^[197, 198]

$$\tilde{z}_m(\mathbf{r}) = \frac{\tau_m^{\text{vW}}(\mathbf{r})}{\tilde{\tau}_m(\mathbf{r})} \quad (5.4.11)$$

is constrained, $0 \leq \tilde{z}_m(\mathbf{r}) \leq 1$,^[199] and thus iso-orbital regions where one KS orbitals or several of the same shape dominate the electron density are correctly represented.^[189]

Here, $\tau_m^{\text{vW}}(\mathbf{r})$ is the von Weizsäcker kinetic energy density:^[200]

$$\tau_m^{\text{vW}}(\mathbf{r}) = \frac{|\nabla \rho_m(\mathbf{r})|^2}{8\rho_m(\mathbf{r})} \quad (5.4.12)$$

Thirdly, new functionals which depend on the current density may be developed. One common approach is to include the current density via the gauge-invariant vorticity

$$\boldsymbol{\nu}_m(\mathbf{r}) = \nabla \times \frac{\mathbf{j}_m^{\text{p}}(\mathbf{r})}{\rho_m(\mathbf{r})}, \quad (5.4.13)$$

either by construction of entirely new functionals or by modification of existing ones.^[181, 182, 201–207] The inclusion of the vorticity can, however, lead to significant numerical instabilities.^[185, 193, 208] Only the first two approaches (modification of existing GGA and MGGA functionals) are considered in this work.

In passing, it should be noted that the xc scalar and vector potentials are defined through their functional derivatives

$$\varphi_m^{\text{xc}} = \frac{\delta E_{\text{xc}}}{\delta \rho_m(\mathbf{r})} = \frac{\delta f_{\text{xc}}}{\delta \rho_m(\mathbf{r})}, \quad (5.4.14)$$

$$\mathbf{A}_m^{\text{xc}}(\mathbf{r}) = \frac{\delta E_{\text{xc}}}{\delta \mathbf{j}_m^{\text{p}}(\mathbf{r})} = \frac{\delta f_{\text{xc}}}{\delta \mathbf{j}_m^{\text{p}}(\mathbf{r})}, \quad (5.4.15)$$

and may be treated as their classical counterparts described in sec. 2.2.^[193] The vorticity may then be identified as

$$\boldsymbol{\nu}_m(\mathbf{r}) = -\nabla \times \mathbf{A}_m^{\text{xc}}(\mathbf{r}) = -\mathbf{B}_m^{\text{xc}}(\mathbf{r}), \quad (5.4.16)$$

which is equivalent to an intrinsic magnetic field induced by the presence of an external magnetic field or, alternatively, relativistic effects such as spin orbit coupling.^[190, 191]

5.4.3. Spin-Noncollinear Kohn–Sham Density Functional Theory

Spin-noncollinear KS DFT is structurally very similar to GHF, which was introduced in detail in sec. 5.2. The total energy in KS DFT can be deconstructed as

$$E_{\text{DFT}} = E_{1e} + E_{\text{J}} + E_{\text{xc}} + V_{\text{NN}} \quad (5.4.17)$$

and the individual contributions are evaluated using KS orbitals constructed from a linear combination of LAOs. As in GHF theory, the field-dependent paramagnetic and

diamagnetic contributions are contained in the one-electron energy. The xc energy is approximated using any density functional and may also be field-dependent as described in sec. (5.4.2), for instance in the case of CDFT.

Here, we consider the general case of a spin-noncollinear approach using MGGA functionals. The xc potential energy matrix is defined as a functional derivative,

$$V_{\mu\nu,m}^{\text{xc}} = \frac{\delta E_{\text{xc}}}{\delta D_{\mu\nu,m}} = \int \frac{\delta f_{\text{xc}}}{\delta D_{\mu\nu,m}} \text{d}\mathbf{r}, \quad (5.4.18)$$

and consequently, the two-electron potential can be decomposed according to:^[46]

$$\mathbf{V}_0[\mathbf{D}_0] = \mathbf{J}_0[\mathbf{D}_0] + \mathbf{V}_0^{\text{xc}}[\mathbf{D}_0], \quad (5.4.19)$$

$$\mathbf{V}_n[\mathbf{D}_n] = \mathbf{V}_n^{\text{xc}}[\mathbf{D}_n]. \quad (5.4.20)$$

Using the chain rule of derivatives, \mathbf{V}^{xc} may be written as^[38]

$$V_{\mu\nu,m}^{\text{xc}} = \int \left[\frac{\partial f_{\text{xc}}}{\partial \rho_m} \frac{\partial \rho_m}{\partial D_{\mu\nu,m}} + \frac{\partial f_{\text{xc}}}{\partial \nabla \rho_m} \frac{\partial \nabla \rho_m}{\partial D_{\mu\nu,m}} + \frac{\partial f_{\text{xc}}}{\partial \tilde{\tau}_m} \frac{\partial \tilde{\tau}_m}{\partial D_{\mu\nu,m}} \right] \text{d}\mathbf{r}. \quad (5.4.21)$$

It should be noted that the approach for GGA functionals is equivalent, except that the last term can be omitted as GGA functionals do not depend on the kinetic energy density. For MGGA functionals, the physical kinetic energy density $\tilde{\tau}(\mathbf{r})$ can be constructed as shown in eq. (5.4.10). In this case, the derivative of the physical kinetic energy density with respect to a (spin-)density matrix element reads

$$\frac{\partial \tilde{\tau}_m}{\partial D_{\mu\nu,m}} = \frac{\partial \tau_m}{\partial D_{\mu\nu,m}} - \frac{\mathbf{j}_m^{\text{p}}}{\rho_m} \frac{\partial \mathbf{j}_m^{\text{p}}}{\partial D_{\mu\nu,m}} + \frac{|\mathbf{j}_m^{\text{p}}|^2}{2\rho_m^2} \frac{\partial \rho_m}{\partial D_{\mu\nu,m}}, \quad (5.4.22)$$

highlighting the paramagnetic and diamagnetic contributions according to eq. (5.4.9). Finally, rearranging the terms, the xc potential energy matrix can be calculated as

$$\begin{aligned} V_{\mu\nu,m}^{\text{xc}} = \int & \left[\left(\frac{\partial f_{\text{xc}}}{\partial \rho_m} + \frac{|\mathbf{j}_m^{\text{p}}|^2}{2\rho_m^2} \frac{\partial f_{\text{xc}}}{\partial \tilde{\tau}_m} \right) \xi_\mu(\mathbf{r}) \xi_\nu^*(\mathbf{r}) \right. \\ & + \frac{\partial f_{\text{xc}}}{\partial \nabla \rho_m} \{ [\nabla \xi_\mu(\mathbf{r})] \xi_\nu^*(\mathbf{r}) + \xi_\mu(\mathbf{r}) \nabla \xi_\nu^*(\mathbf{r}) \} \\ & + \frac{1}{2} \frac{\partial f_{\text{xc}}}{\partial \tilde{\tau}_m} [\nabla \xi_\mu(\mathbf{r})] \cdot [\nabla \xi_\nu(\mathbf{r})]^* \\ & \left. - \frac{i}{2} \frac{\mathbf{j}_m^{\text{p}}}{\rho_m} \frac{\partial f_{\text{xc}}}{\partial \tilde{\tau}_m} \{ [\nabla \xi_\mu(\mathbf{r})] \xi_\nu^*(\mathbf{r}) - \xi_\mu(\mathbf{r}) [\nabla \xi_\nu^*(\mathbf{r})] \} \right] \text{d}\mathbf{r}. \end{aligned} \quad (5.4.23)$$

The integral is evaluated over a three-dimensional grid and requires the knowledge of LAO $\xi_\mu(\mathbf{r})$ and its derivative $\nabla\xi_\mu(\mathbf{r})$ as well as the electron (spin-)density $\rho_m(\mathbf{r})$, its gradient $\nabla\rho_m(\mathbf{r})$, the kinetic energy density $\tau_m(\mathbf{r})$ and the paramagnetic current density $\mathbf{j}_m^p(\mathbf{r})$ on all individual points of the grid.

5.4.4. Hybrid and Range-Separated Hybrid Functionals

One significant problem with the approach described thus far is the incorrect description of the exchange functional's asymptotic behaviour.^[209–211] The exact exchange of HF theory, on the other hand, does not exhibit this problem. Motivated through the adiabatic connection,^[171–175] a fraction $0 < c^x < 1$ of HF exchange may therefore be included in the calculations.^[212] The resulting method is a hybrid between HF and KS DFT and the corresponding xc functionals which then typically include $(1 - c^x)$ are referred to as hybrid functionals. The energy within the hybrid DFT (HDFT) approach may be calculated as

$$E_{\text{HDFT}} = E_{1e} + E_J + E_{\text{xc}} + c^x E_K + V_{\text{NN}} \quad (5.4.24)$$

and the (spin-)density-matrix-dependent two-electron potential includes both the xc potential energy and the fraction of exact exchange:

$$\mathbf{V}_0[\mathbf{D}_0] = \mathbf{J}_0[\mathbf{D}_0] + \mathbf{V}_0^{\text{xc}}[\mathbf{D}_0] - c^x \mathbf{K}_0[\mathbf{D}_0], \quad (5.4.25)$$

$$\mathbf{V}_n[\mathbf{D}_n] = \mathbf{V}_n^{\text{xc}}[\mathbf{D}_n] - c^x \mathbf{K}_n[\mathbf{D}_n]. \quad (5.4.26)$$

The HDFT approach may be further enhanced to better describe long-range behaviour, which is particularly important for the calculation of Rydberg and charge-transfer (CT) excitations.^[213] This can be achieved by dividing the two-electron operator into a long-range and into a short-range part:^[214–216]

$$\frac{1}{r_{12}} = \frac{\text{erf}(\mu r_{12})}{r_{12}} + \frac{1 - \text{erf}(\mu r_{12})}{r_{12}} \quad (5.4.27)$$

The long-range operator is used for the calculation of exact exchange, whereas the short-range operator is modified for the use in the xc functional. Functionals using this ansatz are called range-separated hybrid (RSH) functionals. Both the hybrid and RSH DFT approach can be combined with GGA and MGGA functionals. The RI- K approximation may be used both for the exact exchange in hybrid DFT as well as for the screened exchange in RSH DFT.

5.5. Post Kohn–Sham: The *GW* Method

The systematic improvement of Kohn–Sham DFT is no trivial effort. While in principle an exact method, in practice it is necessary to introduce approximations to the xc functional as previously described in sec. 5.4.1 and 5.4.4. It is not uncommon to classify these approximations according to their relative accuracy using Jacob’s ladder, with each rung indicating a statistical improvement with respect to the computation of molecular properties.^[217–219] However, the semi-empirical nature of these approximations prevents the systematic improvement of KS DFT solely through the use of another type of functional.^[220–222] Another approach puts the focus on improving upon the drawbacks of KS DFT instead. Since KS orbitals are constructed for a noninteracting reference system using a variety of mostly semi-empirical methods, any subsequent calculation including them is affected by their extremely functional-dependent nature.^[167, 168] KS orbital energies may, however, be replaced by quasiparticle energies for subsequent calculations using the *GW* method. For a detailed description of *GW*, the interested reader is referred to the literature.^[223–227] Based on previous work on the description of *GW* in external magnetic fields for atomic systems,^[228, 229] a general approach capable of handling molecular systems was developed in the context of this work in collaboration with Holzer and Klopper, see Ref. [53]. The general outline of the eigenvalue-only self-consistent *GW* approach (ev*GW*)^[230] for molecules in finite magnetic fields is presented here.

Starting from self-consistently obtained KS orbitals $|p\rangle$ and their related energies $\varepsilon_p^{(0)}$, the quasiparticle energies ε_p are calculated in an iterative scheme according to

$$\varepsilon_p^{(n+1)} = \varepsilon_p^{(n)} + \langle p | \Sigma_c(\varepsilon_p^{(n)}) + \Sigma_x - V^{\text{xc}} | p \rangle. \quad (5.5.1)$$

Here, V^{xc} is the xc potential as used in the reference KS DFT calculation. The so-called exchange self-energy is defined as

$$\langle p | \Sigma_x | p \rangle = - \sum_k (pk | kp), \quad (5.5.2)$$

while the correlation self-energy $\langle p | \Sigma_c(\varepsilon_p) | p \rangle$ in turn depends on the quasiparticle energy, thus necessitating the use of an iterative procedure:

$$\langle p | \Sigma_c(\varepsilon_p) | p \rangle = \sum_k \sum_{m \neq 0} |(pk | \rho_m)|^2 D_{pkm}^+ + \sum_c \sum_{m \neq 0} |(cp | \rho_m)|^2 D_{pcm}^-, \quad (5.5.3)$$

where the correlation self-energy was approximated as a product of the one-electron Green's function G and the correlation contribution to the linearly screened potential W_c , hence giving rise to the method's name. The integrals containing the charge fluctuation ρ_m are computed as

$$(pq|\rho_m) = \sum_{ia} [(pq|ai)X_{ia}^m + (pq|ia)Y_{ia}^m], \quad (5.5.4)$$

while the matrices \mathbf{D}^\pm can be evaluated from

$$D_{pqm}^\pm = \frac{\varepsilon_p - \varepsilon_q \pm \omega_m}{(\varepsilon_p - \varepsilon_q \pm \omega_m)^2 + \eta^2}, \quad (5.5.5)$$

with η being a small positive number in order to avoid numerical instabilities. The (de-)excitation vectors \mathbf{X}^m and \mathbf{Y}^m as well as their respective excitation energies ω_m are obtained from the direct random-phase approximation (dRPA):^[231–233]

$$\begin{pmatrix} \mathbf{A} & \mathbf{B} \\ -\mathbf{B}^* & -\mathbf{A}^* \end{pmatrix} \begin{pmatrix} \mathbf{X} & \mathbf{Y}^* \\ \mathbf{Y} & \mathbf{X}^* \end{pmatrix} = \begin{pmatrix} \mathbf{X} & \mathbf{Y}^* \\ \mathbf{Y} & \mathbf{X}^* \end{pmatrix} \begin{pmatrix} \boldsymbol{\omega} & \mathbf{0} \\ \mathbf{0} & -\boldsymbol{\omega} \end{pmatrix}, \quad (5.5.6)$$

where the orbital rotation matrices \mathbf{A} and \mathbf{B} only contain diagonal contributions from quasiparticle energy differences and the Coulomb integrals representing the Hartree kernel:

$$A_{ia,jb} = (\varepsilon_a - \varepsilon_i)\delta_{ij}\delta_{ab} + (ia|bj); \quad (5.5.7)$$

$$B_{ia,jb} = (ia|jb). \quad (5.5.8)$$

The solution of the dRPA equations is the most time-consuming step of the GW method, which formally scales with $\mathcal{O}(N^6)$.^[223] Therefore, several approximations such as the analytic continuation GW (AC- GW)^[234–236] or the contour-deformation GW (CD- GW)^[230, 237, 238] approaches, both of which rely on the use of the RI- C approximation and, in their current formulation, assume Kramer's symmetry for KS spinors. Since Kramer's symmetry is broken in external magnetic fields, AC- GW and CD- GW should only be used with great care and in small magnetic fields, where the effects of the broken time-reversal symmetry are negligible.^[53] For the construction of both the KS reference orbitals as well as for all integrals used in the GW method, LAOs have to be employed in order to avoid dependencies on the gauge origin.

6. Quantum Chemical Methods for Electronic Excitations

In the previous chapter, several different approximations to the time-independent electronic Schrödinger equation for molecules in external magnetic fields have been discussed. This included the Hartree–Fock method and approximate coupled cluster theory as well as Kohn–Sham density functional theory and the GW method. Having found approximate solutions for the static case by using one of these methods, the propagation in time becomes possible by subsequently solving the time-dependent electronic Schrödinger equation. This allows for the description of the interaction between molecules and electromagnetic radiation, giving access to the physical description of most spectroscopic methods.

This chapter introduces linear response theory for molecules in static, external magnetic fields. In this approach, the influence of electromagnetic radiation on the molecular system is treated perturbatively, leading to a physical problem similar to the random phase approximation discussed in the context of the GW method.

Using linear response theory, time-dependent versions of the quantum chemical methods established in the last chapter are presented. The first method introduced is time-dependent Hartree–Fock, followed by a time-dependent version of approximate coupled cluster. Time-dependent density functional theory requires the additional evaluation of the exchange-correlation kernel, which is derived for MGGA functionals in the presence of magnetic fields. Finally, the Bethe-Salpeter equation is discussed, giving access to linear response theory for quasiparticles as generated by the GW method. The chapter concludes with the description on how quantum chemical calculations with any of these methods can be used for the simulation of optical spectra. This includes the computation of UV/Vis spectra for molecules in finite magnetic fields as well as the calculation of magnetic circular dichroism spectroscopy. Most of the results presented in this chapter were derived in collaboration with Holzer and Klopper and presented in Refs. [53], [54] and [55].

6.1. Linear Response Theory

6.1.1. Basic Concept

Approximate solutions to the static electronic Schrödinger equation (3.2.12) were discussed in great detail in the last chapter, introducing the wave function-based HF and CC2 methods as well as KS DFT and the GW method. These solutions may be propagated in time by solving the time-dependent electronic Schrödinger equation (3.2.12) at the same level of theory. While a propagation in the real-time domain is possible,^[239, 240] the most common approach for the solution of the time-dependent Schrödinger equation is linear response theory (LRT).^[177, 241–243] For molecules in static, external magnetic fields, both the real-time propagation^[46, 49] and the LRT approach^[44, 47, 53–55] have been carried out. The focus of this work is LRT, particularly in the context of the aforementioned HF, CC2, DFT, and GW methods. Their time-dependent (TD) counterparts are denoted TD-HF, TD-DFT and TD-CC2. For GW , the Bethe-Salpeter equation (BSE) has to be solved, leading to the expression GW/BSE for time-dependent cases.

In LRT, the interaction between a molecule as described using a quantum chemical method and electromagnetic radiation as described through classical field theory (sec. 2.2) is constructed in the framework of perturbation theory, using multipole expansions to represent the electromagnetic field.^[59] The time-dependent electromagnetic potentials (see: (eq. 2.2.14) and (2.2.15)) are expressed in the frequency domain through the use of a Fourier transformation. Thus, the linear response of the electronic wave function and electron density of a molecule may also be expressed in the frequency domain, with electronic excitations corresponding to resonance frequencies of the reference system.^[241, 243, 244]

The central equation of LRT can be written out as

$$\begin{pmatrix} \mathbf{A} & \mathbf{B} \\ \mathbf{B}^* & \mathbf{A}^* \end{pmatrix} \begin{pmatrix} \mathbf{X}_j \\ \mathbf{Y}_j \end{pmatrix} = \omega_j \begin{pmatrix} \mathbf{1} & \mathbf{0} \\ \mathbf{0} & -\mathbf{1} \end{pmatrix} \begin{pmatrix} \mathbf{X}_j \\ \mathbf{Y}_j \end{pmatrix} \quad (6.1.1)$$

for most quantum chemical methods. Depending on the reference method, eq. (6.1.1) is referred to as random phase approximation (RPA), Casida's equation, or Bethe-Salpeter equation.^[243] The vectors \mathbf{X}_j and \mathbf{Y}_j parametrize the j -th (de-)excitation and are further constrained through an additional normalization condition:

$$\mathbf{X}^\dagger \mathbf{X} - \mathbf{Y}^\dagger \mathbf{Y} = \mathbf{1}. \quad (6.1.2)$$

The excitation frequency ω_j is equivalent to the excitation energy in atomic units, and thus these two expressions are used interchangeably. It corresponds to the resonance of the reference system and is not directly dependent on the external perturbation. For different quantum chemical methods, only the orbital rotation matrices

$$A_{ia,jb}^{\sigma\sigma'\tau\tau'} = (\varepsilon_a^{\sigma'} - \varepsilon_i^\sigma) \delta_{ij} \delta_{ab} \delta_{\sigma\tau} \delta_{\sigma'\tau'} + K_{ia,jb}^{\sigma\sigma'\tau\tau'}, \quad (6.1.3)$$

$$B_{ia,jb}^{\sigma\sigma'\tau\tau'} = K_{ia,bj}^{\sigma\sigma'\tau\tau'}, \quad (6.1.4)$$

differ, here expressed in the two-component framework with explicit reference to the electron spin through $\sigma, \sigma', \tau, \tau' \in \{\alpha, \beta\}$. The orbital energies ε_p^σ contain an explicit reference to the electron spin, which can be omitted for two-component spinors as introduced in eq. (4.3.1). The coupling matrix \mathbf{K} is usually constructed in the AO basis and then transformed to the MO basis according to:

$$K_{pq,rs}^{\sigma\sigma'\tau\tau'} = K_{\mu\nu\kappa\lambda}^{\sigma\sigma'\tau\tau'} C_{\mu p}^{\sigma*} C_{\nu q}^{\sigma'} C_{\kappa r}^{\tau*} C_{\lambda s}^{\tau'}. \quad (6.1.5)$$

For the construction of the coupling matrix, LAOs are used in order to avoid any dependencies on the magnetic field. The explicit form given to the coupling matrix depends on the quantum chemical method.

6.1.2. Time-Dependent Hartree–Fock Theory

In the context of GHF, it might be more convenient to express the coupling matrix in terms of Pauli matrices instead of the generalized spin components of eq. (6.1.5). One element of the coupling matrix can be calculated as

$$\mathbf{K}_{\mu\nu\kappa\lambda,kl} = \frac{\delta^2 E_{\text{GHF}}}{\delta D_{\mu\nu,k} \delta D_{\kappa\lambda,l}} \quad (6.1.6)$$

and can therefore only contain two-electron contributions. This is convenient, as the coupling matrix may be expressed entirely in terms of two-electron integrals,

$$\mathbf{K}_{\mu\nu\kappa\lambda} = (\mu\nu|\kappa\lambda)\{\boldsymbol{\sigma}_0 \otimes \boldsymbol{\sigma}_0\} - (\mu\lambda|\kappa\nu)\{\boldsymbol{\sigma}_m \otimes \boldsymbol{\sigma}_m\}, \quad (6.1.7)$$

and is thus constructed similarly to the field-free case. The only difference lies in the use of LAOs for the calculation of four-center integrals, either directly or by using the RI approximation. For a more detailed description of TD-HF in static, external magnetic fields, the reader is referred to the literature.^[44]

6.1.3. Approximate Coupled Cluster Theory

The TD-CC2 method is the both the most accurate and time-consuming method for the computation of excitation energies presented in this work. Structurally very similar to the equation of motion coupled cluster singles and doubles (EOM-CCSD) method,^[112, 245] TD-CC2 approximates the double excitations and uses linear response theory.^[154] In this work, TD-CC2 is used as a reference to benchmark excitation energies obtained from the other methods.

In order to calculate excitation energies, the Jacobian matrix \mathbf{A} is constructed in the manifold spanned by the single (μ_1) and double (μ_2) excitations:

$$A_{\mu_1\nu_1} = \langle \mu_1 | [\hat{H} + [\hat{H}, \hat{T}_2], \hat{\tau}_{\nu_1}] | \text{GHF} \rangle \quad (6.1.8)$$

$$A_{\mu_1\nu_2} = \langle \mu_1 | [\hat{H}, \hat{\tau}_{\nu_2}] | \text{GHF} \rangle \quad (6.1.9)$$

$$A_{\mu_2\nu_1} = \langle \mu_2 | [\hat{H}, \hat{\tau}_{\nu_1}] | \text{GHF} \rangle \quad (6.1.10)$$

$$A_{\mu_2\nu_2} = \langle \mu_2 | [[\hat{F}, \hat{T}_2], \hat{\tau}_{\nu_2}] | \text{GHF} \rangle \quad (6.1.11)$$

Excitation energies are obtained either by solving for the left or right eigenvectors of the Jacobian,

$$\bar{\mathbf{C}}(\omega_j) \mathbf{A} = \omega_j \bar{\mathbf{C}}(\omega_j), \quad (6.1.12)$$

$$\mathbf{A} \mathbf{C}(\omega_j) = \omega_j \mathbf{C}(\omega_j), \quad (6.1.13)$$

both of which are required for subsequent calculation of properties. For a more detailed overview of TD-CC2, the reader is referred to the literature.^[154, 160, 162, 246]

6.1.4. Time-Dependent Density Functional Theory

Spin-noncollinear TD-DFT in the framework of LRT was originally introduced for applications considering relativistic effects such as spin orbit coupling.^[247–251] However, applications including the investigation of spiral and frustrated spin structures require a nonrelativistic spin-noncollinear approach.^[176, 177, 252–254] For the case of static, external magnetic fields, spin-noncollinear linear response TD-DFT was first presented in Ref. [47] in the framework of relativistic quantum chemistry. A nonrelativistic description was derived in the context of this work in collaboration with Holzer and Klopper for GGA and MGGA functionals as well as their corresponding hybrid and range-separated hybrid versions.^[54, 55]

The coupling matrix in TD-DFT is defined similarly to its TD-HF counterpart:

$$K_{\mu\nu\kappa\lambda,kl} = \frac{\delta^2 E_{\text{DFT}}}{\delta D_{\mu\nu,k} \delta D_{\kappa\lambda,l}}. \quad (6.1.14)$$

For hybrid DFT functionals, it reads

$$\mathbf{K}_{\mu\nu\kappa\lambda} = (\mu\nu|\kappa\lambda)\{\boldsymbol{\sigma}_0 \otimes \boldsymbol{\sigma}_0\} - c^x(\mu\lambda|\kappa\nu)\{\boldsymbol{\sigma}_m \otimes \boldsymbol{\sigma}_m\} + \langle \mu\kappa | \hat{\mathbf{g}}^{\text{xc}} | \nu\lambda \rangle \quad (6.1.15)$$

and includes the spin-noncollinear exchange-correlation kernel $\hat{\mathbf{g}}^{\text{xc}}$ in its last term. For GGA functionals, it may be deconstructed as

$$\begin{aligned} \hat{\mathbf{g}}^{\text{xc}} &= \frac{\delta^2 E^{\text{xc}}}{\delta \rho_0(\mathbf{r}) \delta \rho_0(\mathbf{r})} \{\boldsymbol{\sigma}_0 \otimes \boldsymbol{\sigma}_0\} + \frac{\delta^2 E^{\text{xc}}}{\delta \rho_0(\mathbf{r}) \delta s(\mathbf{r}')} \{\boldsymbol{\sigma}_0 \otimes [\boldsymbol{\sigma} \cdot \tilde{\mathbf{s}}(\mathbf{r})]\} \\ &+ \frac{\delta^2 E^{\text{xc}}}{\delta s(\mathbf{r}) \delta \rho_0(\mathbf{r}')} \{[\boldsymbol{\sigma} \cdot \tilde{\mathbf{s}}(\mathbf{r}')] \otimes \boldsymbol{\sigma}_0\} + \sum_{n=1}^3 \frac{1}{s(\mathbf{r})} \frac{\delta E^{\text{xc}}}{\delta s(\mathbf{r})} \delta(\mathbf{r} - \mathbf{r}') \{\boldsymbol{\sigma}_n \otimes \boldsymbol{\sigma}_n\}, \quad (6.1.16) \\ &+ \left[\frac{\delta^2 E^{\text{xc}}}{\delta s(\mathbf{r}) \delta s(\mathbf{r}')} - \frac{1}{s(\mathbf{r})} \frac{\delta E^{\text{xc}}}{\delta s(\mathbf{r})} \delta(\mathbf{r} - \mathbf{r}') \right] \{[\boldsymbol{\sigma} \cdot \tilde{\mathbf{s}}(\mathbf{r})] \otimes [\boldsymbol{\sigma} \cdot \tilde{\mathbf{s}}(\mathbf{r}')]\} \end{aligned}$$

and generally leads to a 4×4 matrix structure of $\mathbf{K}_{\mu\nu\kappa\lambda}$ for spin-noncollinear DFT calculations.^[255–257] For the sake of brevity, eq. (6.1.16) uses the generalized unit spin density $\tilde{\mathbf{s}}(\mathbf{r}) = \mathbf{s}(\mathbf{r})/s(\mathbf{r})$. In cases where the generalized spin density becomes very small in absolute value, the spin-noncollinear xc kernel can become numerically instable, as $\tilde{\mathbf{s}}(\mathbf{r})$ may point in an almost arbitrary direction at any point in space.^[177, 258, 259]

The spin-noncollinear xc kernel may alternatively be deconstructed according to

$$\hat{g}_{kl}^{\text{xc}} = \frac{\delta^2 E^{\text{xc}}}{\delta D_{\mu\nu,k} \delta D_{\kappa\lambda,l}}, \quad (6.1.17)$$

which is equivalent to the form presented in eq. (6.1.16):

$$\begin{aligned} \frac{\delta^2 E_{\text{GGA}}^{\text{xc}}}{\delta D_{\mu\nu,k} \delta D_{\kappa\lambda,l}} &= \iint \left[\left(\frac{\partial^2 f}{\partial \rho_k \partial \rho_l} \right) \left(\frac{\partial \rho_k}{\partial D_{\mu\nu,k}} \frac{\partial \rho_l}{\partial D_{\kappa\lambda,l}} \right) + \left(\frac{\partial^2 f}{\partial \nabla \rho_k \partial \nabla \rho_l} \right) \left(\frac{\partial \nabla \rho_k}{\partial D_{\mu\nu,k}} \frac{\partial \nabla \rho_l}{\partial D_{\kappa\lambda,l}} \right) \right. \\ &+ \left. \left(\frac{\partial^2 f}{\partial \rho_k \partial \nabla \rho_l} \right) \left(\frac{\partial \rho_k}{\partial D_{\mu\nu,k}} \frac{\partial \nabla \rho_l}{\partial D_{\kappa\lambda,l}} \right) + \left(\frac{\partial^2 f}{\partial \nabla \rho_k \partial \rho_l} \right) \left(\frac{\partial \nabla \rho_k}{\partial D_{\mu\nu,k}} \frac{\partial \rho_l}{\partial D_{\kappa\lambda,l}} \right) \right] \delta(\mathbf{r} - \mathbf{r}') d\mathbf{r} d\mathbf{r}'. \quad (6.1.18) \end{aligned}$$

For MGGA functionals incorporating the ground-state current density through the physical kinetic energy density as shown in eq. (5.4.10), the xc kernel can be written

out using the chain rule of derivatives:

$$\begin{aligned}
 \frac{\delta^2 E^{\text{xc}}}{\delta D_{\mu\nu,k} \delta D_{\kappa\lambda,l}} &= \iint \left[\frac{\partial^2 f^{\text{xc}}}{\partial \rho_k \partial \rho_l} \frac{\partial \rho_k}{\partial D_{\mu\nu,k}} \frac{\partial \rho_l}{\partial D_{\kappa\lambda,l}} + \frac{\partial^2 f^{\text{xc}}}{\partial \nabla \rho_k \partial \nabla \rho_l} \frac{\partial \nabla \rho_k}{\partial D_{\mu\nu,k}} \frac{\partial \nabla \rho_l}{\partial D_{\kappa\lambda,l}} \right. \\
 &+ \frac{\partial^2 f^{\text{xc}}}{\partial \tilde{\tau}_k \partial \tilde{\tau}_l} \frac{\partial \tilde{\tau}_k}{\partial D_{\mu\nu,k}} \frac{\partial \tilde{\tau}_l}{\partial D_{\kappa\lambda,l}} + \frac{\partial^2 f^{\text{xc}}}{\partial \rho_k \partial \nabla \rho_l} \frac{\partial \rho_k}{\partial D_{\mu\nu,k}} \frac{\partial \nabla \rho_l}{\partial D_{\kappa\lambda,l}} + \frac{\partial^2 f^{\text{xc}}}{\partial \nabla \rho_k \partial \rho_l} \frac{\partial \nabla \rho_k}{\partial D_{\mu\nu,k}} \frac{\partial \rho_l}{\partial D_{\kappa\lambda,l}} \\
 &+ \frac{\partial^2 f^{\text{xc}}}{\partial \rho_k \partial \tilde{\tau}_l} \frac{\partial \rho_k}{\partial D_{\mu\nu,k}} \frac{\partial \tilde{\tau}_l}{\partial D_{\kappa\lambda,l}} + \frac{\partial^2 f^{\text{xc}}}{\partial \tilde{\tau}_k \partial \rho_l} \frac{\partial \tilde{\tau}_k}{\partial D_{\mu\nu,k}} \frac{\partial \rho_l}{\partial D_{\kappa\lambda,l}} + \frac{\partial^2 f^{\text{xc}}}{\partial \nabla \rho_k \partial \tilde{\tau}_l} \frac{\partial \nabla \rho_k}{\partial D_{\mu\nu,k}} \frac{\partial \tilde{\tau}_l}{\partial D_{\kappa\lambda,l}} \\
 &+ \frac{\partial^2 f^{\text{xc}}}{\partial \tilde{\tau}_k \partial \nabla \rho_l} \frac{\partial \tilde{\tau}_k}{\partial D_{\mu\nu,k}} \frac{\partial \nabla \rho_l}{\partial D_{\kappa\lambda,l}} + \frac{\partial f^{\text{xc}}}{\partial \tilde{\tau}_k} \frac{\partial^2 \tilde{\tau}_k}{\partial \rho_k \partial \mathbf{j}_k^{\text{p}}} \left(\frac{\partial \rho_k}{\partial D_{\mu\nu,k}} \frac{\partial \mathbf{j}_k^{\text{p}}}{\partial D_{\kappa\lambda,k}} + \frac{\partial \mathbf{j}_k^{\text{p}}}{\partial D_{\mu\nu,k}} \frac{\partial \rho_k}{\partial D_{\kappa\lambda,k}} \right) \\
 &\left. + \frac{\partial f^{\text{xc}}}{\partial \tilde{\tau}_k} \frac{\partial^2 \tilde{\tau}_k}{\partial \rho_k^2} \frac{\partial \rho_k}{\partial D_{\mu\nu,k}} \frac{\partial \rho_k}{\partial D_{\kappa\lambda,k}} + \frac{\partial f^{\text{xc}}}{\partial \tilde{\tau}_k} \frac{\partial^2 \tilde{\tau}_k}{\partial (\mathbf{j}_k^{\text{p}})^2} \frac{\partial \mathbf{j}_k^{\text{p}}}{\partial D_{\mu\nu,k}} \frac{\partial \mathbf{j}_k^{\text{p}}}{\partial D_{\kappa\lambda,k}} \right] \delta(\mathbf{r} - \mathbf{r}') \text{d}\mathbf{r} \text{d}\mathbf{r}'.
 \end{aligned} \tag{6.1.19}$$

Finally, by applying additional chain rules of the form presented in eq. (5.4.22) and reordering some terms, we obtain:

$$\begin{aligned}
 \frac{\delta^2 E_{\text{MGGA}}^{\text{xc}}}{\delta D_{\mu\nu,k} \delta D_{\kappa\lambda,l}} &= \frac{\delta^2 E_{\text{GGA}}^{\text{xc}}}{\delta D_{\mu\nu,k} \delta D_{\kappa\lambda,l}} + \iint \left[\left(\frac{\partial^2 f}{\partial \tilde{\tau}_k \partial \tilde{\tau}_l} \right) \left(\frac{\partial \tau_k}{\partial D_{\mu\nu,k}} \frac{\partial \tau_l}{\partial D_{\kappa\lambda,l}} \right) \right. \\
 &- \left(\frac{\delta_{\alpha\beta}}{\rho_k} \frac{\partial f}{\partial \tilde{\tau}_k} \right) \left(\frac{\partial j_{k,\alpha}^{\text{p}}}{\partial D_{\mu\nu,k}} \frac{\partial j_{k,\beta}^{\text{p}}}{\partial D_{\kappa\lambda,k}} \right) + \left(\frac{\partial^2 f}{\partial \tilde{\tau}_k \partial \tilde{\tau}_l} \right) \left(\frac{j_{k,\alpha}^{\text{p}}}{\rho_k} \frac{\partial j_{k,\alpha}^{\text{p}}}{\partial D_{\mu\nu,k}} \right) \left(\frac{j_{l,\beta}^{\text{p}}}{\rho_l} \frac{\partial j_{l,\beta}^{\text{p}}}{\partial D_{\kappa\lambda,l}} \right) \\
 &+ \left(\frac{|\mathbf{j}_k^{\text{p}}|^2 |\mathbf{j}_l^{\text{p}}|^2}{4 \rho_k^2 \rho_l^2} \frac{\partial^2 f}{\partial \tilde{\tau}_k \partial \tilde{\tau}_l} + \frac{|\mathbf{j}_l^{\text{p}}|^2}{2 \rho_l^2} \frac{\partial^2 f}{\partial \rho_k \partial \tilde{\tau}_l} + \frac{|\mathbf{j}_k^{\text{p}}|^2}{2 \rho_k^2} \frac{\partial^2 f}{\partial \tilde{\tau}_k \partial \rho_l} - \delta_{kl} \frac{|\mathbf{j}_k^{\text{p}}|^2}{\rho_k^3} \frac{\partial f}{\partial \tilde{\tau}_k} \right) \left(\frac{\partial \rho_k}{\partial D_{\mu\nu,k}} \frac{\partial \rho_l}{\partial D_{\kappa\lambda,l}} \right) \\
 &+ \left(\frac{|\mathbf{j}_k^{\text{p}}|^2}{2 \rho_k^2} \frac{\partial^2 f}{\partial \tilde{\tau}_k \partial \nabla \rho_l} \right) \left(\frac{\partial \rho_k}{\partial D_{\mu\nu,k}} \frac{\partial \nabla \rho_l}{\partial D_{\kappa\lambda,l}} \right) + \left(\frac{|\mathbf{j}_l^{\text{p}}|^2}{2 \rho_l^2} \frac{\partial^2 f}{\partial \nabla \rho_k \partial \tilde{\tau}_l} \right) \left(\frac{\partial \nabla \rho_k}{\partial D_{\mu\nu,k}} \frac{\partial \rho_l}{\partial D_{\kappa\lambda,l}} \right) \\
 &+ \left(\frac{\partial^2 f}{\partial \rho_k \partial \tilde{\tau}_l} + \frac{|\mathbf{j}_k^{\text{p}}|^2}{2 \rho_k^2} \frac{\partial^2 f}{\partial \tilde{\tau}_k \partial \tilde{\tau}_l} \right) \left(\frac{\partial \rho_k}{\partial D_{\mu\nu,k}} \frac{\partial \tau_l}{\partial D_{\kappa\lambda,l}} \right) + \left(\frac{\partial^2 f}{\partial \tilde{\tau}_k \partial \rho_l} + \frac{|\mathbf{j}_l^{\text{p}}|^2}{2 \rho_l^2} \frac{\partial^2 f}{\partial \tilde{\tau}_k \partial \tilde{\tau}_l} \right) \left(\frac{\partial \tau_k}{\partial D_{\mu\nu,k}} \frac{\partial \rho_l}{\partial D_{\kappa\lambda,l}} \right) \\
 &+ \left(\delta_{kl} \frac{j_{k,\alpha}^{\text{p}}}{\rho_k^2} \frac{\partial f}{\partial \tilde{\tau}_k} - \frac{j_{l,\alpha}^{\text{p}} |\mathbf{j}_k^{\text{p}}|^2}{2 \rho_l \rho_k^2} \frac{\partial^2 f}{\partial \tilde{\tau}_k \partial \tilde{\tau}_l} - \frac{j_{l,\alpha}^{\text{p}}}{\rho_l} \frac{\partial^2 f}{\partial \rho_k \partial \tilde{\tau}_l} \right) \left(\frac{\partial \rho_k}{\partial D_{\mu\nu,k}} \frac{\partial j_{l,\alpha}^{\text{p}}}{\partial D_{\kappa\lambda,l}} \right) \\
 &+ \left(\delta_{kl} \frac{j_{k,\alpha}^{\text{p}}}{\rho_k^2} \frac{\partial f}{\partial \tilde{\tau}_k} - \frac{j_{k,\alpha}^{\text{p}} |\mathbf{j}_l^{\text{p}}|^2}{2 \rho_k \rho_l^2} \frac{\partial^2 f}{\partial \tilde{\tau}_k \partial \tilde{\tau}_l} - \frac{j_{k,\alpha}^{\text{p}}}{\rho_k} \frac{\partial^2 f}{\partial \tilde{\tau}_k \partial \rho_l} \right) \left(\frac{\partial j_{k,\alpha}^{\text{p}}}{\partial D_{\mu\nu,k}} \frac{\partial \rho_l}{\partial D_{\kappa\lambda,l}} \right) \\
 &+ \left(\frac{\partial^2 f}{\partial \nabla \rho_k \partial \tilde{\tau}_l} \right) \left(\frac{\partial \nabla \rho_k}{\partial D_{\mu\nu,k}} \frac{\partial \tau_l}{\partial D_{\kappa\lambda,l}} \right) + \left(\frac{\partial^2 f}{\partial \tilde{\tau}_k \partial \nabla \rho_l} \right) \left(\frac{\partial \tau_k}{\partial D_{\mu\nu,k}} \frac{\partial \nabla \rho_l}{\partial D_{\kappa\lambda,l}} \right) \\
 &- \left(\frac{j_{k,\alpha}^{\text{p}}}{\rho_k} \frac{\partial^2 f}{\partial \tilde{\tau}_k \partial \nabla \rho_l} \right) \left(\frac{\partial j_{k,\alpha}^{\text{p}}}{\partial D_{\mu\nu,k}} \frac{\partial \nabla \rho_l}{\partial D_{\kappa\lambda,l}} \right) + \left(\frac{j_{l,\alpha}^{\text{p}}}{\rho_l} \frac{\partial^2 f}{\partial \nabla \rho_k \partial \tilde{\tau}_l} \right) \left(\frac{\partial \nabla \rho_k}{\partial D_{\mu\nu,k}} \frac{\partial j_{l,\alpha}^{\text{p}}}{\partial D_{\kappa\lambda,l}} \right) \\
 &\left. - \left(\frac{j_{k,\alpha}^{\text{p}}}{\rho_k} \frac{\partial^2 f}{\partial \tilde{\tau}_k \partial \tilde{\tau}_l} \right) \left(\frac{\partial \tau_k}{\partial D_{\mu\nu,k}} \frac{\partial j_{k,\alpha}^{\text{p}}}{\partial D_{\kappa\lambda,k}} \right) + \left(\frac{j_{l,\alpha}^{\text{p}}}{\rho_l} \frac{\partial^2 f}{\partial \tilde{\tau}_k \partial \tilde{\tau}_l} \right) \left(\frac{\partial j_{k,\alpha}^{\text{p}}}{\partial D_{\mu\nu,k}} \frac{\partial \tau_l}{\partial D_{\kappa\lambda,l}} \right) \right] \delta(\mathbf{r} - \mathbf{r}') \text{d}\mathbf{r} \text{d}\mathbf{r}'.
 \end{aligned} \tag{6.1.20}$$

It should be noted that the Einstein summation convention is only used for repeated Greek indices in eq. (6.1.20). It is worthwhile to examine a few of the contributions in the lengthy expression for the full current-dependent xc kernel individually. The first two terms of the xc kernel,

$$\left(\frac{\partial^2 f}{\partial \tilde{\tau}_k \partial \tilde{\tau}_l} \right) \left(\frac{\partial \tau_k}{\partial D_{\mu\nu,k}} \frac{\partial \tau_l}{\partial D_{\kappa\lambda,l}} \right) - \left(\frac{\delta_{\alpha\beta}}{\rho_k} \frac{\partial f}{\partial \tilde{\tau}_k} \right) \left(\frac{\partial j_{k,\alpha}^p}{\partial D_{\mu\nu,k}} \frac{\partial j_{k,\beta}^p}{\partial D_{\kappa\lambda,k}} \right), \quad (6.1.21)$$

are two contributions which also appear in the absence of ground state currents. The inclusion of the second term is needed to ensure gauge origin invariance for the calculation of excited states, which can and do carry currents even if the ground state is current-free.^[189, 260] The third term,

$$\left(\frac{\partial^2 f}{\partial \tilde{\tau}_k \partial \tilde{\tau}_l} \right) \left(\frac{j_{k,\alpha}^p}{\rho_k} \frac{\partial j_{k,\alpha}^p}{\partial D_{\mu\nu,k}} \right) \left(\frac{j_{l,\beta}^p}{\rho_l} \frac{\partial j_{l,\beta}^p}{\partial D_{\kappa\lambda,l}} \right), \quad (6.1.22)$$

ouples all Cartesian components of \mathbf{j}_k^p to all Cartesian components of \mathbf{j}_l^p , as well as the other way around.^[55] The fourth contribution,

$$\left(\frac{|\mathbf{j}_k^p|^2 |\mathbf{j}_l^p|^2}{4\rho_k^2 \rho_l^2} \frac{\partial^2 f}{\partial \tilde{\tau}_k \partial \tilde{\tau}_l} + \frac{|\mathbf{j}_l^p|^2}{2\rho_l^2} \frac{\partial^2 f}{\partial \rho_k \partial \tilde{\tau}_l} + \frac{|\mathbf{j}_k^p|^2}{2\rho_k^2} \frac{\partial^2 f}{\partial \tilde{\tau}_k \partial \rho_l} - \delta_{kl} \frac{|\mathbf{j}_k^p|^2}{\rho_k^3} \frac{\partial f}{\partial \tilde{\tau}_k} \right) \left(\frac{\partial \rho_k}{\partial D_{\mu\nu,k}} \frac{\partial \rho_l}{\partial D_{\kappa\lambda,l}} \right), \quad (6.1.23)$$

is added to the local spin-density contribution also present as the first term of eq. (6.1.18). If $k = l$, this includes a $|\mathbf{j}_k^p|^4 / \rho_k^4$ contribution, which may lead to numerical instabilities, especially if the molecule is moved far away from the center of the Cartesian coordinate system. Terms such as

$$\left(\frac{\partial^2 f}{\partial \rho_k \partial \tilde{\tau}_l} + \frac{|\mathbf{j}_k^p|^2}{2\rho_k^2} \frac{\partial^2 f}{\partial \tilde{\tau}_k \partial \tilde{\tau}_l} \right) \left(\frac{\partial \rho_k}{\partial D_{\mu\nu,k}} \frac{\partial \tau_l}{\partial D_{\kappa\lambda,l}} \right) \quad (6.1.24)$$

contain a contribution which is also present in the absence of magnetic fields. Additionally, they couple the ground state current to the electron density through derivatives of the xc functional with respect to the kinetic energy density.

Finally, contributions such as

$$\left(\delta_{kl} \frac{j_{k,\alpha}^p}{\rho_k^2} \frac{\partial f}{\partial \tilde{\tau}_k} - \frac{j_{l,\alpha}^p |\mathbf{j}_k^p|^2}{2\rho_l \rho_k^2} \frac{\partial^2 f}{\partial \tilde{\tau}_k \partial \tilde{\tau}_l} - \frac{j_{l,\alpha}^p}{\rho_l} \frac{\partial^2 f}{\partial \rho_k \partial \tilde{\tau}_l} \right) \left(\frac{\partial \rho_k}{\partial D_{\mu\nu,k}} \frac{\partial j_{l,\alpha}^p}{\partial D_{\kappa\lambda,l}} \right) \quad (6.1.25)$$

couple the excited state current with the excited state electron density. Similar terms, which couple the excited state current to the gradient of the electron density or the kinetic energy density are also present. None of them exist in the absence of a ground state current. This implies that the excited state current couples to other excited state quantities through the ground state current.

The derivation of the full current-dependent xc kernel was carried out for this work and was presented in Ref. [55] as a central result. Using it is strictly necessary in order to ensure gauge origin invariance for any theory in which currents are induced for electronic ground states. This is not limited to calculations in external magnetic fields and can be equally as important for spin orbit coupling.

6.1.5. Bethe-Salpeter Equation

After having constructed quasiparticle energies using the GW method, the Bethe-Salpeter equation (BSE) can be applied in the framework of LRT in order to calculate excitation energies and excited state properties.^[223, 236, 261–263] While generally more expensive than TD-DFT, the GW /BSE method is capable of handling the description of CT and Rydberg excitations for which TD-DFT performs notoriously poorly.^[190, 264–266] The GW /BSE method for molecules in finite magnetic fields was derived in the frame of this work in collaboration with Holzer and Klopper, see also Ref. [53]. As usual, all integrals are calculated over LAOs.

In contrast to TD-HF and TD-DFT, the orbital rotation matrix \mathbf{A} in the BSE requires quasiparticle energies obtained from a previous GW calculation:

$$A_{ia,jb} = (\varepsilon_i - \varepsilon_a)\delta_{ij}\delta_{ab} + (ia|bj) - W_{ji,ba}; \quad (6.1.26)$$

$$B_{ia,jb} = (ia|jb) - W_{bi,ja}. \quad (6.1.27)$$

The static screened potential^[267]

$$W_{pq,rs} = \sum_{tu} (\epsilon^{-1})_{pq,tu}(ut|rs) \quad (6.1.28)$$

is evaluated using the inverse dielectric function

$$\epsilon_{pq,tu} = \delta_{pt}\delta_{qu} - \sum_{tu} (qp|tu) (\chi_0)_{tu,tu}, \quad (6.1.29)$$

which in turn involves the calculation of the non-interacting response function:

$$(\chi_0)_{tu,tu} = \sum_{kc} \frac{\delta_{tk}\delta_{uc} + \delta_{tc}\delta_{uk}}{\varepsilon_k - \varepsilon_c}. \quad (6.1.30)$$

While the four-center integrals in MO basis are generally complex for LAOs, all quasiparticle energies remain real-valued and thus χ_0 is real-valued and diagonal, even for molecular systems in the presence of an external magnetic field.^[53]

The static screened potential may be calculated with significantly less computational effort by invoking the RI- C approximation:^[268]

$$W_{pq,rs} = B_{pq,P} \chi_{PQ}^{-1} B'_{Q,rs}. \quad (6.1.31)$$

As a consequence, the response function is calculated in the auxiliary subspace,

$$\chi_{PQ} = \delta_{PQ} - 2 \operatorname{Re}\{B'_{P,tu} (\chi_0)_{tu,tu} B_{tu,Q}\}, \quad (6.1.32)$$

which remains both symmetric and real-valued in the presence of external magnetic fields.^[53] For the sake of completeness, it should be noted that a hybrid between TD-DFT and GW /BSE exists, denoted correlation-kernel augmented BSE (cBSE).^[223, 269] For cBSE, the correlation-part of the xc kernel presented in sec. 6.1.4 is included the orbital rotation matrices for the construction of the BSE in eq. (6.1.26) and (6.1.27). The static screened exchange, on the other hand, is evaluated using KS orbital energies instead of quasiparticle energies.^[269] This approach improves considerably upon the otherwise poorly described triplet excitations.^[270–272]

6.2. Calculation of Optical Spectra

6.2.1. Electronic Transition Dipole Moments

Optical spectra can be simulated using any quantum chemical method described in this chapter. For TD-HF, TD-DFT and GW /BSE calculations, this requires solving eq. (6.1.1) for the (de-)excitation vectors \mathbf{X}_j and \mathbf{Y}_j and excitation energies ω_j of all relevant electronic transitions j contributing to the spectrum. Some transitions may not contribute to the spectrum due to molecular symmetry, while other transitions can be neglected because they are energetically too high or low.

For the simulation of optical absorption spectroscopy in the ultraviolet and visi-

ble region (UV/Vis spectroscopy) as well as magnetic circular dichroism (MCD) spectroscopy, it is necessary to compute electronic transition dipole moments:^[250]

$$\langle 0|\hat{\mu}_\alpha|j\rangle = \sum_{ia} \{X_{ia,j} \langle i|\hat{\mu}_\alpha|a\rangle + Y_{ia,j} \langle a|\hat{\mu}_\alpha|i\rangle\}. \quad (6.2.1)$$

The dipole operator can be given in the length gauge ($\hat{\mu}_\alpha = -\hat{r}_\alpha$) or the velocity gauge ($\hat{\mu}_\alpha = -\hat{p}_\alpha$), although both representations are equivalent in a complete basis.^[273] Other properties such as magnetic transition dipole moments or electronic transition quadrupole moments can be relevant for other types of spectroscopy such as electronic circular dichroism or oriented circular dichroism spectroscopy.^[116, 120, 274, 275]

6.2.2. UV/Vis Spectroscopy

UV/Vis spectra are usually measured in SI units of [$\text{L mol}^{-1} \text{cm}^{-1}$]. Using the Beer-Lambert law, a spectrum may be computed according to

$$\varepsilon(\lambda)[\text{L mol}^{-1} \text{cm}^{-1}] = \frac{20\pi^2 N_A}{\ln(10)\varepsilon_0\lambda} \frac{e^2 a_0^4 m_e}{\hbar^2} \alpha''(\omega, \Gamma), \quad (6.2.2)$$

with all quantities given in SI units except for the polarizability α'' which is assumed to be in atomic units instead. The spectrum is calculated as a function of the wavelength λ , which is connected to the frequency (in SI units) according to:

$$\lambda = \frac{2\pi c}{\omega}. \quad (6.2.3)$$

Electronic excitations as calculated using LRT are discrete transitions and generate a line spectrum, whereas vibronic coupling and other effects generally lead to band spectra for molecular systems. For better comparability, the polarizability should thus be calculated in a way which includes line broadening:

$$\alpha''(\omega, \Gamma) = \sum_j g(\omega, \omega_j, \Gamma) D_j; \quad (6.2.4)$$

$$D_j = \frac{1}{3} \text{Re}[\langle 0|\hat{\mu}_\alpha|j\rangle \langle j|\hat{\mu}_\alpha|0\rangle]. \quad (6.2.5)$$

The line-shape function $g(\omega, \omega_j, \Gamma)$ can be a Gaussian or Lorentzian function with Γ being the full width at half maximum (FWHM). In this work, the line-shape function

$$g(\omega, \omega_j, \Gamma) = \frac{1}{\pi} \left[\frac{\frac{1}{2}\Gamma}{(\omega - \omega_j)^2 + (\frac{1}{2}\Gamma)^2} - \frac{\frac{1}{2}\Gamma}{(\omega + \omega_j)^2 + (\frac{1}{2}\Gamma)^2} \right] \quad (6.2.6)$$

is used, which is similar to a Lorentzian function including both excitations and de-excitations. The spectra generated by eq. (6.2.6) in a sum-over-states (SOS) formalism are equivalent to the complex linear polarization propagator approach, which commonly uses a damping factor related to the FWHM by $\gamma_d = \frac{1}{2}\Gamma$.^[276–279]

6.2.3. Magnetic Circular Dichroism Spectroscopy

MCD spectra are experimentally accessible by measuring the difference in absorption between left and right circularly polarized light in the presence of an external magnetic field.^[59, 280] Computationally, MCD spectra can be generated through

$$\Delta\varepsilon(\lambda)[\text{L mol}^{-1} \text{cm}^{-1}] = \frac{20\pi^2 N_A |\mathbf{B}|}{\ln(10)\varepsilon_0 \lambda} \frac{e^3 a_0^6 m_e}{\hbar^3} M(\omega, \Gamma); \quad (6.2.7)$$

$$[\theta]_M(\lambda)[^\circ \text{L mol}^{-1} \text{cm}^{-1} \text{T}^{-1}] = \frac{9 \cdot 10^4 \pi N_A}{\varepsilon_0 \lambda} \frac{e^3 a_0^6 m_e}{\hbar^3} M(\omega, \Gamma), \quad (6.2.8)$$

with $\Delta\varepsilon(\lambda)$ being the molar absorption coefficient and $[\theta]_M$ the closely related specific rotation.^[54, 281–283] All quantities are given in SI units except for the differential absorption M , which is calculated in atomic units. Traditionally, the differential absorption is calculated in the limit of a vanishing magnetic field using perturbation theory.^[284–288]

$$M(\omega, \Gamma) = -\frac{1}{3} \sum_j \left\{ \frac{\partial g(\omega, \omega_j, \Gamma)}{\partial \omega} A_{0j} + g(\omega, \omega_j, \Gamma) \left[B_{0j} + \frac{C_{0j}}{k_B T} \right] \right\}. \quad (6.2.9)$$

Three individual contributions, commonly referred to as A , B and C terms have to be considered, which are calculated using quadratic response theory.^[29, 31, 289–294] Their representations A_{0j} , B_{0j} and C_{0j} in eq. (6.2.9) are defined in eqs. (8.222) – (8.224) of Ref. [288]. The A term results from a Zeeman splitting of degenerate excited states and is given a derivative line-shape.^[287, 295] B term contributions stem from field-induced mixing of excited states.^[287, 296] Temperature-dependent C terms are the consequence of a Zeeman splitting of (nearly) degenerate ground states.^[47, 297] A graphical depiction of the physical processes for all three terms is shown in fig. 6.2.1.

Alternatively, the differential absorption M maybe calculated in the presence of a small external magnetic field using the methods described in this chapter using LRT.^[46, 54] However, since MCD spectra are commonly measured in solution, an isotropic average of the effects induced by an external magnetic field has to be computed. This generally requires three separate calculations with magnetic fields aligned in three arbitrary perpendicular orientations, which can be chosen as the x , y , and z components of the Cartesian coordinate system.^[46, 54] The A and B terms of quadratic response theory resulting from Zeeman splitting may be computed by

$$M(\omega, \Gamma) = \sum_j g(\omega, \omega_j, \Gamma) R_j; \quad (6.2.10)$$

$$R_j = -\frac{1}{3} \varepsilon_{\alpha\beta\gamma} \text{Im} \left[\frac{\langle 0 | \hat{\mu}_\alpha | j \rangle \langle j | \hat{\mu}_\beta | 0 \rangle}{B_\gamma} \right]. \quad (6.2.11)$$

This requires a spin-noncollinear approach for the calculation of A term contributions, as the Zeeman splitting triplet excitations needs to be properly captured. C term contributions are only relevant for systems with (nearly) degenerate ground states and generally require more sophisticated methods capable of calculating static correlation. While the calculation of temperature-dependent C terms has been attempted on the TD-DFT level, especially for systems with spin doublet ground states,^[47, 297] these are not considered in the frame of this work.

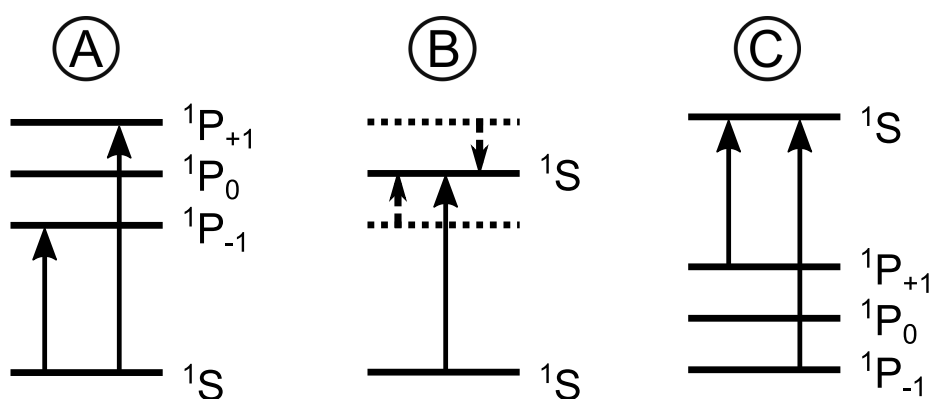


Figure 6.2.1.: Graphical illustration of the excitations leading to A , B and C terms in magnetic circular dichroism spectroscopy. The Zeeman splitting of degenerate excited states leads to A terms, field-induced mixing between states results in B terms and the Zeeman splitting of (nearly) degenerate ground state yields C terms. Reprinted with permission from Ref. [54] and modeled after Ref. [280].

7. Semi-classical Approach for the Nuclear Equation of Motion

The quantum-mechanical description of electronic motion in external magnetic fields has been the topic of the last few chapters of this work. Approximate solutions for both the static and the time-dependent electronic Schrödinger equations were investigated in the framework of the Born-Oppenheimer adiabatic approximation. Various molecular properties including those required for the investigation of optical spectroscopy can be computed using these quantum chemical methods.

For the study of nuclear motion in external magnetic fields, however, the nuclear Schrödinger equation has to be solved. In this chapter, a semi-classical approach for the description of nuclear motion is presented using both Hamiltonian and Lagrangian mechanics. The resulting equations of motion not only include the familiar Born-Oppenheimer force, but also a screened Lorentz force acting on the moving nuclear charges. As a consequence, the equations of motion cannot be solved analytically and require a numerical approach using, for instance, *ab initio* molecular dynamics. The solution to these equations of motion is necessary for the investigation of rotational and vibrational spectra in external magnetic fields.

Of particular interest in this context is the screened Lorentz force acting on the moving nuclei. It involves the Berry curvature, which is intrinsically connected to partial charges of molecular systems, even in the absence of external magnetic fields. Finally, an approximation of the screening force using the Mulliken charge distribution is presented, which is a convenient alternative for *ab initio* molecular dynamics simulations in which the calculation of all involved quantities has to be repeatedly performed.

7.1. Nuclear Equations of Motion

7.1.1. Hamilton's Equations of Motions

The last few chapters were concerned with finding (approximate) solutions to the electronic Schrödinger equation. In the framework of the BO adiabatic approximation, nuclear motion was decoupled from electronic motion, and the total electronic energy E_0^{BO} of the electronic ground state was calculated on any point of the PES.

The Schrödinger equation for nuclear motion along the PES of the electronic ground state can be written as

$$\left[\hat{T}_0^{\text{eff}} + E_0^{\text{BO}} \right] \Psi_0^{\text{nuc}} = i \frac{\partial}{\partial t} \Psi_0^{\text{nuc}}, \quad (7.1.1)$$

if the DBOC is neglected, as previously shown in eq. (3.4.15) for an arbitrary state q . The effects of an external magnetic field are contained both directly in the effective kinetic energy operator in eq. (3.4.13) and indirectly in the total electronic energy.

The nuclear equations of motion can now be solved using classical mechanics by replacing all expectation values with their semi-classical counterparts.^[82, 83] The effective classical Hamiltonian reads

$$\mathcal{H}^{\text{eff}} = \sum_I^{N_{\text{nuc}}} \frac{1}{2M_I} [\mathbf{P}_I - Z_I \mathbf{A}(\mathbf{R}_I) + \boldsymbol{\chi}_I(\mathbf{R})]^2 + E_0^{\text{BO}}(\mathbf{R}) \quad (7.1.2)$$

and requires knowledge of the entire BO PES, or at least the region in which the nuclear motion takes place. The total electronic energy serves as a potential energy contribution in eq. (7.1.2) and is dependent on the reference quantum chemical method. Any region of the BO PES may be simulated on a grid, and a spline interpolation is used to approximate all points in between.^[82]

Hamilton's equations of motion are then constructed as

$$\dot{\mathbf{R}}_I = \frac{\partial \mathcal{H}^{\text{eff}}}{\partial \mathbf{P}_I} = \frac{1}{M_I} [\mathbf{P}_I - Z_I \mathbf{A}(\mathbf{R}_I) + \boldsymbol{\chi}_I(\mathbf{R})], \quad (7.1.3)$$

$$\dot{\mathbf{P}}_I = -\frac{\partial \mathcal{H}^{\text{eff}}}{\partial \mathbf{R}_I}, \quad (7.1.4)$$

and a solution involves the construction and propagation of the gauge-dependent canonical momenta \mathbf{P}_I .^[82, 83] It is therefore preferable to use an alternative method which only involves gauge-invariant quantities.

7.1.2. Lagrangian Equations of Motions

Lagrangian mechanics presents itself as a natural alternative to Hamiltonian mechanics in this case. Closely following Ref. [82], the Lagrangian of eq. (2.3.1) can be constructed similar to eq. (2.3.8) through a Legendre transformation of the Hamiltonian:

$$\mathcal{L} = \sum_I^{N_{\text{nuc}}} \dot{\mathbf{R}}_I \cdot \mathbf{P}_I - \mathcal{H}^{\text{eff}} \quad (7.1.5)$$

An explicit form for the canonical momentum \mathbf{P}_I can be derived from eq. (7.1.3) and written out as:

$$\mathbf{P}_I = M_I \dot{\mathbf{R}}_I + Z_I \mathbf{A}(\mathbf{R}_I) - \boldsymbol{\chi}_I(\mathbf{R}) \quad (7.1.6)$$

Inserting the definitions of the effective Hamiltonian from eq. (7.1.2) and the definitions for velocity and canonical momentum, eq. (7.1.3) and eq. (7.1.6), respectively into eq. (7.1.5) reveals the final expression for the Lagrangian for nuclear motion in an external magnetic field

$$\begin{aligned} \mathcal{L} &= \sum_I^{N_{\text{nuc}}} \left[M_I \dot{\mathbf{R}}_I^2 + Z_I \mathbf{A}(\mathbf{R}_I) \cdot \dot{\mathbf{R}}_I - \boldsymbol{\chi}_I(\mathbf{R}) \cdot \dot{\mathbf{R}}_I \right] - \sum_I^{N_{\text{nuc}}} \frac{1}{2} M_I \dot{\mathbf{R}}_I^2 - E_0^{\text{BO}}(\mathbf{R}) \\ &= \frac{1}{2} \sum_I^{N_{\text{nuc}}} M_I \dot{\mathbf{R}}_I^2 + \sum_I^{N_{\text{nuc}}} [Z_I \mathbf{A}(\mathbf{R}_I) - \boldsymbol{\chi}_I(\mathbf{R})] \cdot \dot{\mathbf{R}}_I - E_0^{\text{BO}}(\mathbf{R}), \end{aligned} \quad (7.1.7)$$

which conveniently separates into contributions corresponding to the kinetic energy and the velocity-dependent potential energy.^[82, 83] The EOM are constructed using the Euler-Lagrange equation (2.3.6):

$$M_I \ddot{\mathbf{R}}_I + Z_I \dot{\mathbf{A}}(\mathbf{R}_I) - \dot{\boldsymbol{\chi}}_I(\mathbf{R}) = Z_I \left[\frac{\partial \mathbf{A}(\mathbf{R}_I)}{\partial \mathbf{R}_I} \right]^\top \dot{\mathbf{R}}_I - \sum_J^{N_{\text{nuc}}} \left[\frac{\partial \boldsymbol{\chi}_J(\mathbf{R})}{\partial \mathbf{R}_I} \right]^\top \dot{\mathbf{R}}_J - \frac{\partial E_0^{\text{BO}}(\mathbf{R})}{\partial \mathbf{R}_I} \quad (7.1.8)$$

The time-derivatives of the lhs can be reframed using the chain rule of derivatives:

$$\dot{\mathbf{A}}(\mathbf{R}_I) = \frac{\partial \mathbf{A}(\mathbf{R}_I)}{\partial \mathbf{R}_I} \frac{\partial \mathbf{R}_I}{\partial t} = \frac{\partial \mathbf{A}(\mathbf{R}_I)}{\partial \mathbf{R}_I} \dot{\mathbf{R}}_I \quad (7.1.9)$$

$$\dot{\boldsymbol{\chi}}_I(\mathbf{R}) = \sum_J^{N_{\text{nuc}}} \frac{\partial \boldsymbol{\chi}_I(\mathbf{R})}{\partial \mathbf{R}_J} \frac{\partial \mathbf{R}_J}{\partial t} = \sum_J^{N_{\text{nuc}}} \frac{\partial \boldsymbol{\chi}_I(\mathbf{R})}{\partial \mathbf{R}_J} \dot{\mathbf{R}}_J \quad (7.1.10)$$

Introducing the definition of the magnetic vector potential in the symmetric gauge from eq. (2.2.16) allows for the identification of its Jacobian. The latter is antisymmetric,

which implies that it can be reframed as:

$$\left[\frac{\partial \mathbf{A}(\mathbf{R}_I)}{\partial \mathbf{R}_I} \right]^\top = -\frac{\partial \mathbf{A}(\mathbf{R}_I)}{\partial \mathbf{R}_I}. \quad (7.1.11)$$

By inserting eq. (7.1.9), (7.1.10) and (7.1.11) into the equation of motion in eq. (7.1.8), it may be rewritten in terms of the forces acting on nucleus I :

$$M_I \ddot{\mathbf{R}}_I = -\frac{\partial E_0^{\text{BO}}(\mathbf{R})}{\partial \mathbf{R}_I} - 2Z_I \frac{\partial \mathbf{A}(\mathbf{R}_I)}{\partial \mathbf{R}_I} \dot{\mathbf{R}}_I + \sum_J^{N_{\text{nuc}}} \left\{ \frac{\partial \chi_I(\mathbf{R})}{\partial \mathbf{R}_J} - \left[\frac{\partial \chi_J(\mathbf{R})}{\partial \mathbf{R}_I} \right]^\top \right\} \dot{\mathbf{R}}_J. \quad (7.1.12)$$

The first term on the rhs corresponds to the geometric gradient of the total energy and can be calculated either directly through *ab initio* quantum chemistry or alternatively through derivation of the splines which interpolate the BO PES. The second term is equivalent to the Lorentz force acting on the bare nucleus I :

$$-2Z_I \frac{\partial \mathbf{A}(\mathbf{R}_I)}{\partial \mathbf{R}_I} \dot{\mathbf{R}}_I = Z_I \dot{\mathbf{R}}_I \times \mathbf{B}. \quad (7.1.13)$$

The last term in eq. (7.1.12) represents a force accounting for the screening of the electrons. It contains the Berry curvature:

$$\Omega_{IJ} = \frac{\partial \chi_I(\mathbf{R})}{\partial \mathbf{R}_J} - \left[\frac{\partial \chi_J(\mathbf{R})}{\partial \mathbf{R}_I} \right]^\top. \quad (7.1.14)$$

Inserting the definition of the Berry connection introduced in eq. (3.4.10) into the Berry curvature, one component can be calculated according to:^[83, 85, 86]

$$\Omega_{IJ,\alpha\beta} = \text{i} \left[\left\langle \frac{\partial \Psi_0}{\partial R_{I\alpha}} \left| \frac{\partial \Psi_0}{\partial R_{J\beta}} \right. \right\rangle - \left\langle \frac{\partial \Psi_0}{\partial R_{J\beta}} \left| \frac{\partial \Psi_0}{\partial R_{I\alpha}} \right. \right\rangle \right] \quad (7.1.15)$$

The final expression for the EOM governing nuclear motion in static, external magnetic fields becomes:^[82]

$$M_I \ddot{\mathbf{R}}_I = -\frac{\partial E_0^{\text{BO}}(\mathbf{R})}{\partial \mathbf{R}_I} + Z_I \dot{\mathbf{R}}_I \times \mathbf{B} + \sum_J^{N_{\text{nuc}}} \Omega_{IJ} \dot{\mathbf{R}}_J. \quad (7.1.16)$$

Several schemes aiming at a numerical solution of eq. (7.1.16) have been presented in the literature.^[57, 82] In this work, a highly efficient algorithm formulated for a similar problem by Tajima^[298] is used, introduced by the author in collaboration with Monzel, Peters, Tellgren, Helgaker, and Klopper in Ref. [57].

7.2. Berry Curvature

7.2.1. General Properties and Connection to Charge Distribution

The screened Lorentz force acting on a moving nucleus I in the presence of a static, external magnetic field can be identified from eq. (7.1.16) as

$$\mathbf{F}_I^{\text{LB}} = -Z_I \mathbf{B} \times \dot{\mathbf{R}}_I + \sum_J^{N_{\text{nuc}}} \boldsymbol{\Omega}_{IJ} \dot{\mathbf{R}}_J. \quad (7.2.1)$$

The Berry curvature $\boldsymbol{\Omega}$ as introduced in eq. (7.1.15) is involved in describing the screening of bare nuclear charges by the electrons. It is a real-valued, antisymmetric $3N_{\text{nuc}} \times 3N_{\text{nuc}}$ matrix:^[83]

$$\boldsymbol{\Omega}_{IJ}^\top = -\boldsymbol{\Omega}_{JI} \quad (7.2.2)$$

It should be noted that the individual tensors of second rank contained in $\boldsymbol{\Omega}$ for each pair of atoms, $\boldsymbol{\Omega}_{IJ}$, are generally non-symmetric, except for the diagonal blocks.^[83] As usual, they may be decomposed according to

$$\boldsymbol{\Omega}_{IJ} = \boldsymbol{\Omega}_{IJ}^{\text{s}} + \boldsymbol{\Omega}_{IJ}^{\text{as}} \quad (7.2.3)$$

into their symmetric and antisymmetric parts. By defining the vector^[83]

$$\boldsymbol{\omega}_{IJ} = \begin{pmatrix} \Omega_{IJ,zy}^{\text{as}} \\ \Omega_{IJ,xz}^{\text{as}} \\ \Omega_{IJ,yx}^{\text{as}} \end{pmatrix}, \quad (7.2.4)$$

the product between the antisymmetric part of the Berry curvature and the velocity may be expressed in terms of a cross product:

$$\mathbf{F}_I^{\text{LB}} = - \sum_J^{N_{\text{nuc}}} \delta_{IJ} Z_I \mathbf{B} \times \dot{\mathbf{R}}_I + \sum_J^{N_{\text{nuc}}} \boldsymbol{\omega}_{IJ} \times \dot{\mathbf{R}}_J + \sum_J^{N_{\text{nuc}}} \boldsymbol{\Omega}_{IJ}^{\text{s}} \dot{\mathbf{R}}_J. \quad (7.2.5)$$

This is only possible for antisymmetric matrices and thus no similar procedure can be performed for the symmetric part of the Berry curvature. Inserting the unit matrix as $|B|^{-2} \mathbf{B}^\top \mathbf{B} = \mathbf{1}$, a charge distribution of the screening charges can be defined using the dyadic product:

$$\boldsymbol{\Theta}_{IJ} = -|B|^{-2} \boldsymbol{\omega}_{IJ} \otimes \mathbf{B}. \quad (7.2.6)$$

The screened Lorentz force may then be rewritten as:

$$\mathbf{F}_I^{\text{LB}} = - \sum_J^{N_{\text{nuc}}} [\delta_{IJ} Z_I + \Theta_{IJ}] \mathbf{B} \times \dot{\mathbf{R}}_J + \sum_{J \neq I}^{N_{\text{nuc}}} \Omega_{IJ}^s \dot{\mathbf{R}}_J. \quad (7.2.7)$$

In cases where the symmetric part of the Berry curvature vanishes due to symmetry reasons, the entire screened Lorentz force may be expressed in terms of the screening charge distribution:

$$Q_{IJ} = \sum_{\alpha, \beta} \Theta_{IJ, \alpha \beta} \quad (7.2.8)$$

Partial charges can then be defined accordingly,^[83]

$$q_I = \sum_J^{N_{\text{nuc}}} Q_{IJ} \quad (7.2.9)$$

for the electronic part and adding them onto the nuclear charges Z_I . The electronic partial charges have to obey the sum rule

$$\sum_I^{N_{\text{nuc}}} q_I = -N_{\text{el}} \quad (7.2.10)$$

and their definition holds even in the limit of a vanishing magnetic field:

$$q_I^{|B| \rightarrow 0} = \lim_{|B| \rightarrow 0} \sum_J^{N_{\text{nuc}}} \sum_{\alpha, \beta} Q_{IJ, \alpha \beta} \neq 0. \quad (7.2.11)$$

This implies that the partial charges obtained through the Berry curvature may be used even in the absence of external fields, provided an external field is considered perturbatively in the calculation of the partial charges.

7.2.2. Approximation through Mulliken Charge Matrix

The Berry curvature as presented in eq. (7.1.15) may be calculated on the HF level using either a numerical differentiation scheme or analytically by solving the coupled perturbed Hartree–Fock equations.^[83, 86] In principle, the Berry curvature could be computed using any wave function-based quantum chemical method, although no implementations using *post* HF methods are currently available. Since the perturbation of the many-electron wave function itself is required for the construction of the Berry

curvature, using DFT could potentially result in inconsistent results, which should be cautiously investigated in future work.

Another option is to calculate the effects of the Berry curvature approximately.^[57] Since the main effect of the Berry curvature is to introduce screening charges, it can be approximated using any charge distribution,

$$\mathbf{F}_I^{\text{LB}} = - \sum_J^{N_{\text{nuc}}} \left[\delta_{IJ} Z_I - \tilde{Q}_{IJ} \right] \mathbf{B} \times \dot{\mathbf{R}}_J, \quad (7.2.12)$$

where the symmetric part of the Berry curvature was neglected, while the charge distribution was obtained in some approximate manner. It should be noted that the approximate charge distribution \tilde{Q} is usually obtained as a $N_{\text{nuc}} \times N_{\text{nuc}}$ matrix, which is equivalent to contracting the Cartesian components charge distribution tensor \mathbf{Q} for every pair of atoms.

One possible approximation for the charge distribution is through the use of Mulliken charges.^[299–301] Using the Mulliken population analysis, the electronic charge distribution may be approximated according to:

$$\tilde{Q}_{IJ} = - \sum_{\mu \in I} \sum_{\nu \in J} \sum_{\sigma \sigma'} \sum_{\tau \tau'} \delta_{\sigma \sigma'} S_{\mu\nu}^{\sigma \sigma'} D_{\mu\nu}^{\tau \tau'}. \quad (7.2.13)$$

The summation $\mu \in I$ runs only over those LAOs $|\mu\rangle$ which are centered at nucleus I . An equivalent procedure is carried out for the summation $\nu \in J$. Thus, atom-centered LAOs are assumed in the construction of \tilde{Q}_{IJ} , with each basis function only counting towards the atom it is centered on. Consequently, the Mulliken population analysis is very dependent on the reference basis set. Mulliken charges are calculated from the charge distribution through summation over one atomic index:

$$\tilde{q}_I = \sum_J^{N_{\text{nuc}}} \tilde{Q}_{IJ}. \quad (7.2.14)$$

It should be noted that the definition given for Mulliken charges differ from the original work of Mulliken^[299] by a minus sign in eq. (7.2.13), with the present work defining the electronic charges obtained from the Mulliken population analysis as negative in order to stay consistent with charges obtained from the Berry curvature tensor. As a consequence, the Mulliken charges obey the sum rule presented in eq. (7.2.10), instead of yielding the positive number of electrons.^[299, 302]

The total partial charge of an atom is then defined as

$$z_I = Z_I + \tilde{q}_I, \quad (7.2.15)$$

or, for charges calculated from the Berry curvature tensor, as:

$$z_I = Z_I + q_I. \quad (7.2.16)$$

The sum over all nuclear and electronic charges yields the total charge of the molecular system. For *ab initio* molecular dynamics simulations, the Mulliken charge distribution presents itself as a convenient alternative to the vastly more complicated calculation of the Berry curvature tensor.

Part III.

Implementation

8. Implementation of Quantum Chemical Methods in Finite Magnetic Fields

The theoretical framework of quantum chemical methods for the calculation of molecular properties in external magnetic fields was presented in chapters 5 and 6 of this work. In this chapter, an efficient implementation of these methods into the TURBOMOLE program suite is presented. Due to previous implementation work carried out in the context of relativistic quantum chemistry, TURBOMOLE is a convenient choice for the implementation of quantum chemical methods in external magnetic fields, as both methods generally require the use of complex algebra. This chapter therefore first introduces TURBOMOLE and its modular structure. Previous implementation work is presented, particularly on the structure of programs capable of quantum chemical calculations using two-component methods.

The general structure and the relevant routines for calculations of electronic ground states using GHF or spin-noncollinear DFT in finite, external magnetic fields is presented. Several methods which improve upon the efficiency of such an implementation are introduced, including Cauchy–Schwarz screening, the direct inversion of the iterative subspace (DIIS) and the difference densities approach. Finally, the calculation of ground-state properties including electromagnetic multipole moments and Mulliken charges is presented. Furthermore, a general outline of the program capable of calculating molecular gradients in external magnetic fields is discussed, including its use for geometry optimizations in external magnetic fields.

The calculation of *post* HF ground-state energies as well as CC2 excitation energies mostly require the evaluation of two-electron integrals with LAOs. By using the RI-*C* approximation, this step can be simplified significantly and thus, only a general outline of the steps necessary to evaluate two-electron integrals with LAOs for GMP2 and CC2 is presented. Finally, the chapter concludes with the presentation of implementations for calculating electronic excitations using TD-HF, TD-DFT, and *GW*/BSE. The computation of excitation energies as well as related properties such as the electronic transition dipole moments is discussed.

8.1. Implementation into TURBOMOLE

The implementation of quantum chemical methods for molecules in finite, external magnetic fields was carried out in the TURBOMOLE^[303–306] program suite. All methods described in chapters 5 and 6 of this work had already been implemented for two-component (2c) calculations in the absence of magnetic fields.^[305] Particularly noteworthy are the implementations of GHF and spin-noncollinear DFT for electronic ground states,^[307–310] electronic excitations^[249, 250, 311] and molecular gradients,^[310, 312] as well as the implementations on two-component CC2,^[154, 313] and *GW*/BSE.^[236, 314, 315] These methods all have in common that they require 2c spinors and are thus capable of explicitly handling complex algebra.

Due to the presence of complex-valued operators in the one-electron Hamiltonian, eq. (5.2.10), and the use of complex-valued LAOs, eq. (4.3.3), for all integrals, calculations on molecules in finite magnetic fields generally require complex algebra.^[32, 36] Thus, the implementation of field-dependent methods into code already capable of handling complex 2c spinors is convenient, as most of the existing architecture can be straightforwardly adapted.

A few major differences between field-free and field-dependent 2c calculations remain. Firstly, new one-electron integrals have to be evaluated for the paramagnetic and diamagnetic terms. Secondly, in addition to the 2c Fock and density matrix, the 2c overlap matrix,

$$\mathbb{S} = \begin{pmatrix} \mathbf{S} & \mathbf{0} \\ \mathbf{0} & \mathbf{S} \end{pmatrix}, \quad (8.1.1)$$

becomes complex-valued. This has to be factored into quite a few steps, including the orthogonalization of spinors and convergence-accelerating methods such as the direct inversion of the iterative subspace (DIIS).^[56] Thirdly, all integrals are evaluated using complex LAOs, which require a few modifications compared to the calculation of their field-free counterparts.^[32, 36, 38] The efficient evaluation of molecular integrals over LAOs is presented in chapter 9 of this work.

Finally, the permutational symmetry of four-center integrals is reduced from eight- to fourfold if they are evaluated using complex LAOs:^[36, 37, 56, 316]

$$(\mu\nu|\kappa\lambda) = (\nu\mu|\lambda\kappa)^* = (\kappa\lambda|\mu\nu) = (\lambda\kappa|\nu\mu)^* \quad (8.1.2)$$

Therefore, any structure making use of an eightfold permutational symmetry of four-center integrals must not be used in the presence of magnetic fields. Fortunately, the

permutational symmetry of two- and three-center integrals is still retained:^[56]

$$\langle \mu | \hat{O} | \nu \rangle = \langle \nu | \hat{O} | \mu \rangle^* ; \quad (8.1.3)$$

$$(\mu\nu | P) = (\nu\mu | P)^* = (P | \mu\nu) = (P | \nu\mu)^* . \quad (8.1.4)$$

Moreover, auxiliary basis functions may be chosen as real-valued GTOs without loss of generality,

$$(P | Q) = (Q | P) , \quad (8.1.5)$$

making the use of the RI approximation in the presence of magnetic fields particularly efficient.^[56, 137] The general structure of code handling the computation of two- and three-center integrals remains similar to the field-free case.

For calculations in the presence of an external magnetic field, the information about the magnetic field vector needs to be available. Two-component TURBOMOLE calculations in finite magnetic fields thus require an additional input, which is presented in fig. 8.1.1. The "\$soghf" keyword is generally required for 2c calculations and the '\$magnetic field' keyword reads in the magnetic field vector, which is needed for the construction of LAOs as well as the para- and diamagnetic operators.

```
$soghf
$magnetic field
  Bx By Bz |B|
```

Figure 8.1.1.: Input required by TURBOMOLE for 2c calculations in finite magnetic fields. The keyword '\$magnetic field' includes the three Cartesian components and the absolute value of the magnetic field vector.

8.2. Electronic Ground States

8.2.1. General Outline of SCF Procedure

In this section, the SCF method as implemented into TURBOMOLE for molecules in magnetic fields is presented. As it is very similar to its field-free counterpart, a detailed discussion is omitted. Instead, the general procedure is shown in form of a flow chart in fig. 8.2.1 and the focus of this chapter shall be on the differences between the field-free and field-dependent cases. Additionally, the methods which can be used to increase the efficiency are highlighted.

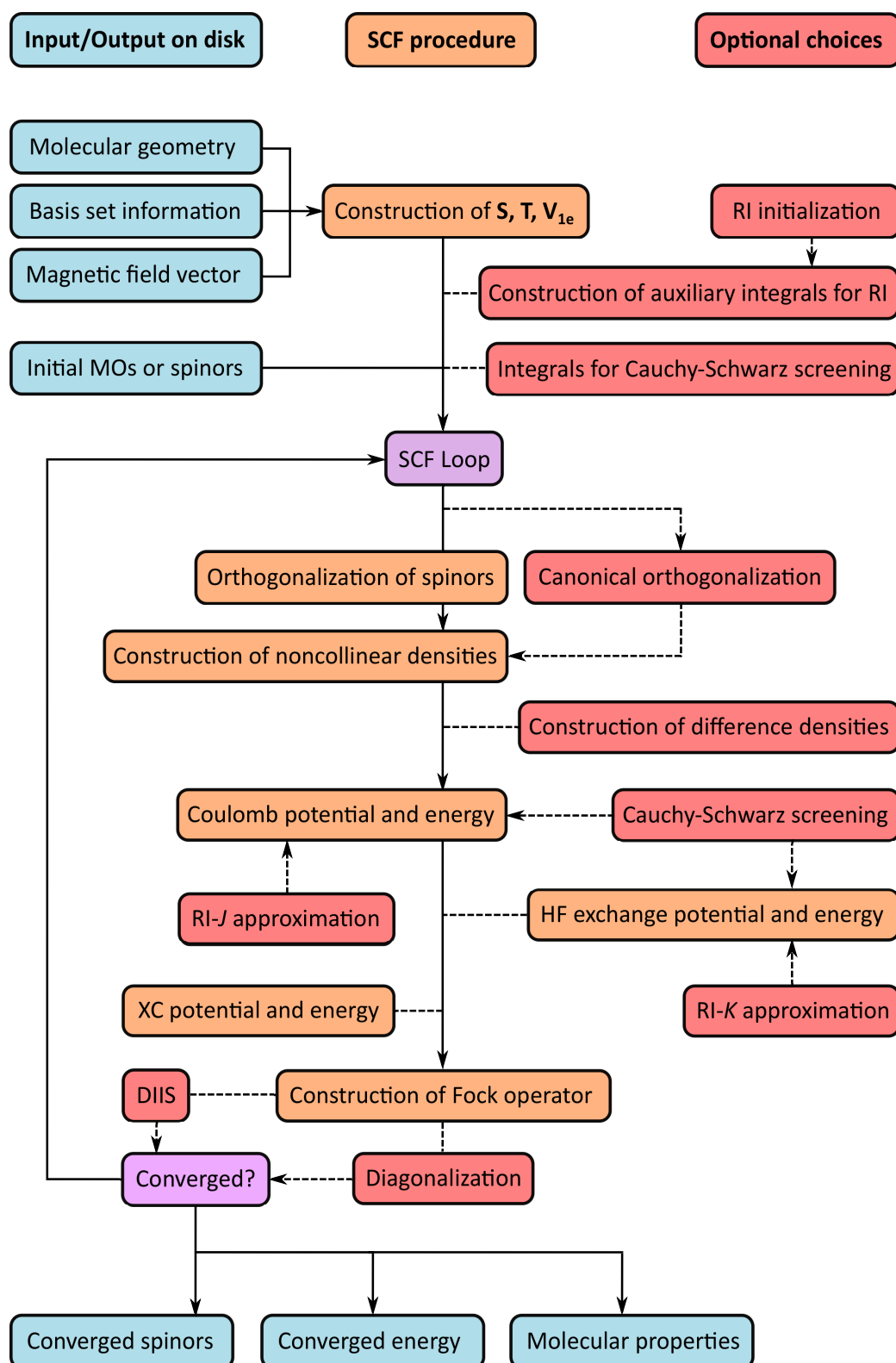


Figure 8.2.1.: Outline of the SCF procedure as implemented in TURBOMOLE for calculations on molecules in finite, external magnetic fields. Optional choices for efficiency increase are highlighted in red. Hartree–Fock and DFT calculations differ only in the calculation of HF exchange and xc potential, with HDFT functionals requiring both.

As input, the molecular geometry, basis set, and magnetic field vector are required. Using this information, the overlap matrix \mathbf{S} as well as matrix representations of the kinetic energy, \mathbf{T} , and nuclear attraction potential, \mathbf{V}_{1e} , are computed. Since they are all hermitian, it is sufficient to store the upper triangle of these matrices. It should be noted that the kinetic energy contains both the para- and diamagnetic terms induced by the presence of the external magnetic field, according to eq. (5.2.10). The spin Zeeman term, however, is treated separately in a two-component approach, as will be discussed in section 8.2.6 of this chapter.

If the RI approximation is used, the integrals containing auxiliary basis functions need to be constructed. For RI- J , this includes the calculation of the auxiliary metric, $(P|Q)^{-1}$, whereas for RI- K , the additional evaluation of the matrix containing all elements of $B_{\mu\nu,Q}$ is required as defined by eq. (5.2.19). While two-index quantities are generally stored in memory, three-index quantities are stored on disk. If Cauchy–Schwarz screening is used, the two-index integrals $(\mu\nu|\nu\mu)$ are calculated and stored in memory. As a direct consequence of the permutational symmetry shown in eq. (8.1.2), they are always real-valued.

As an iterative procedure, the SCF method needs an initial guess for the two-component spinors. Such a guess may be generated using MOs or spinors obtained from extended Hückel theory,^[317] the core Hamiltonian^[318] or even a previous calculation either in the absence or presence of an external magnetic field. These spinors need to be orthogonalized with respect to the two-component metric \mathbb{S} , which can be achieved either using a Cholesky decomposition or alternatively via canonical orthogonalization.^[319] Within the SCF loop, the noncollinear densities are constructed from the spinors according to eq. (5.2.7) and then decomposed such that they parameterize the total electron density and the spin-densities as shown in eq. (5.2.6). Difference densities may be calculated if densities from prior iterations are present. All matrices are separated into their real and imaginary parts.

Both GHF and spin-noncollinear DFT calculations require the evaluation of the Coulomb potential. It can be constructed using either the RI- J approximation or four-center integrals. Cauchy–Schwarz screening may be used in combination with the difference densities approach as described in more detail in sec. 8.2.4 of this chapter. For GHF and HDFT calculations, the exchange potential has to be evaluated. If the RI- K approximation is employed, the three-center integrals previously stored on disk have to be read in every iteration. Alternatively, if the exchange is computed using four-center integrals, it may be evaluated simultaneously to the Coulomb potential and Cauchy–Schwarz screening with difference densities can be applied. For spin-

noncollinear DFT calculations, the xc potential has to be evaluated through numerical integration on a grid.^[320, 321]

Finally, using all contributions including the one-electron Hamiltonian and two-electron potential, the 2c Fock operator is constructed. It is self-consistently optimized either by diagonalizing it or by using the DIIS method. New spinors are evaluated until an energy minimum is found. The solutions obtained through this method are typically analyzed and labeled according to their spin expectation values. In order to assess whether the solution is spin contaminated, the expectation value of the squared spin operator is additionally evaluated.

8.2.2. Coulomb and Exchange Potentials

The evaluation of four-center integrals is typically the most time-consuming part of the SCF procedure.^[322] Optimizing it is thus the most important step in the reduction of computational cost. By properly utilizing the permutational symmetry of four-center integrals over LAOs, the computational cost is reduced by about a factor of four. The general structure of a program which takes advantage of this fourfold permutational symmetry is presented in this section. An outline of this procedure is shown in fig. 8.2.2 in form of a flow chart.

As previously discussed by the author in Ref. [56], the implementation of integral evaluation carried out in this work supports parallelization with open multi-processing (OpenMP). Consequently, the wrapper for the integral evaluation has to be structured in a way which optimally benefits the OpenMP parallelization.

The integrals are evaluated in shell batches, with a shell referring to all degenerate AOs of a single type. Integrals are calculated in the basis of Cartesian atomic orbitals and are thus defined by their angular momentum quantum number $|\mathbf{l}^\mu|$, with

$$\mathbf{l}^\mu = \begin{pmatrix} a_x^\mu \\ a_y^\mu \\ a_z^\mu \end{pmatrix} \quad (8.2.1)$$

as defined in eq. (4.3.4) for GTOs, with $|\mathbf{l}^\mu| = 0$ referring to s -functions, $|\mathbf{l}^\mu| = 1$ to p -functions, $|\mathbf{l}^\mu| = 2$ to d -functions and so forth. Spherical AOs can be obtained at a later point as a linear combination of Cartesian AOs.

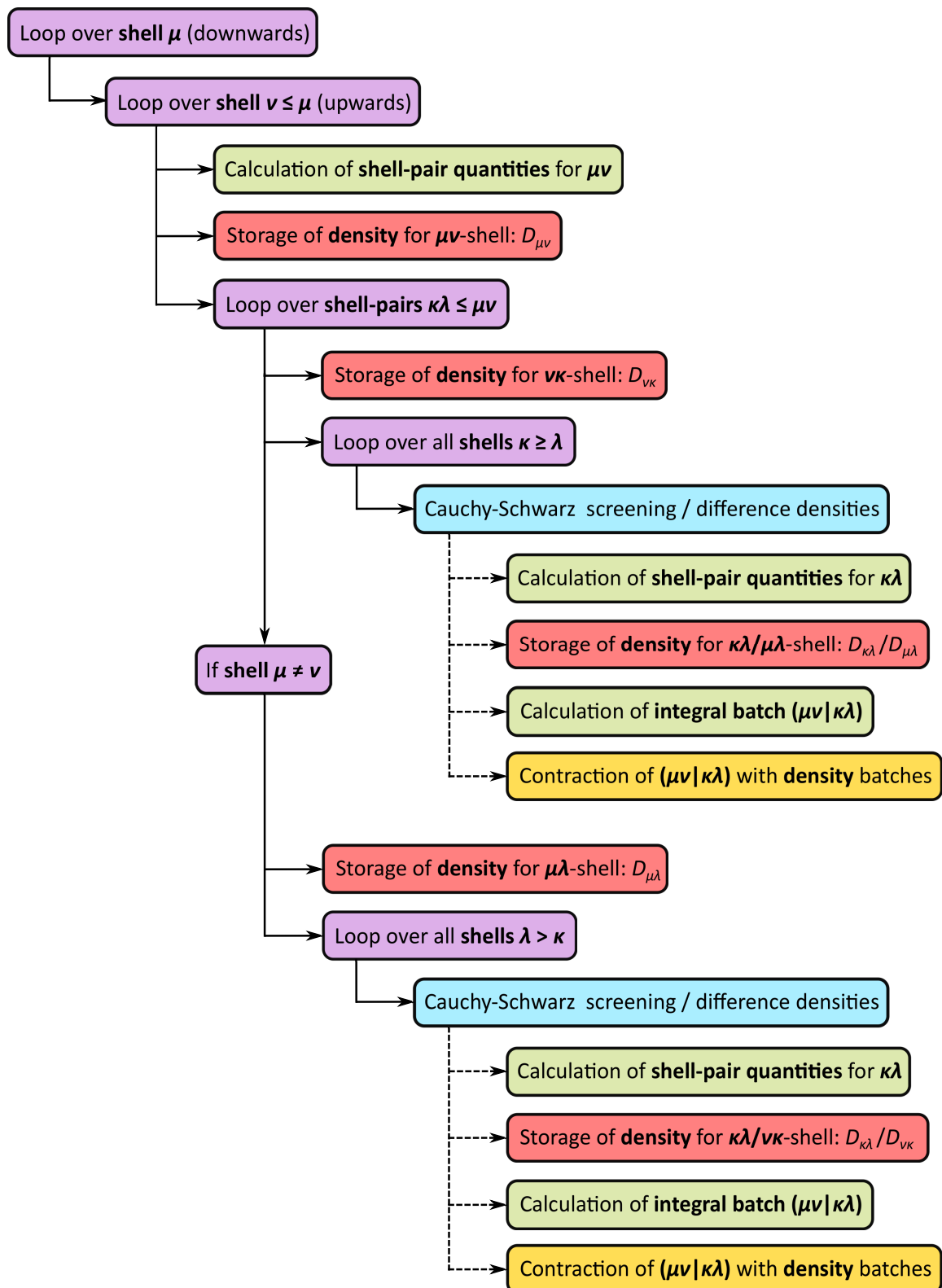


Figure 8.2.2.: Outline of the wrapper for the simultaneous construction of the Coulomb and exchange potentials. The procedure shown here uses the fourfold permutational symmetry of four-center integrals over LAOs, which are calculated in shell batches and directly contracted with their respective noncollinear densities.

The first loop (μ) runs over all shells in descending order of their angular momentum quantum number $|\mathbf{l}^\mu|$. This is important for the OpenMP parallelization, as it prevents the cluttering of different processes. The second loop (ν) runs over all shells smaller or equal to μ in ascending order of their $|\mathbf{l}^\nu|$. Shell-pair quantities for $\mu\nu$ are evaluated here, including LAO phase factors and the overlap integrals for the s -type functions corresponding to μ and ν . Integral screening with respect to these shell-pair quantities can be applied here. The noncollinear densities of shell-pair $\mu\nu$ are stored separately for optimal use of memory.

The third loop runs over all shell-pairs $\kappa\lambda$ less or equal to $\mu\nu$. Two cases are treated separately for shells κ and λ . The first case, $\kappa \geq \lambda$, corresponds to the case also treated for four-center integrals over regular AOs exhibiting an eightfold permutational symmetry. Cauchy–Schwarz screening and the difference densities approach may be applied at this point to avoid the calculation of an integral batch if it is expected to be lower than a certain threshold. For all non-negligible contributions, the additional shell-pair quantities of $\kappa\lambda$ are computed and the relevant batches of noncollinear densities are stored separately. The integral batch ($\mu\nu|\kappa\lambda$) is calculated, corresponding to all possible combinations of $\mathbf{l}^\mu, \mathbf{l}^\nu, \mathbf{l}^\kappa, \mathbf{l}^\lambda$. The efficient integral evaluation of four-center integrals over LAOs is described in chapter 9 of this work. Finally, the integrals are contracted with the noncollinear densities in the prepared batches in order to construct their contribution to the Coulomb and (optionally) exchange potentials. The second case, $\kappa < \lambda$, does not exist for four-center integrals over AOs. Here, it has to be considered in a similar manner to the case $\kappa \geq \lambda$ previously described, but only if $\mu \neq \nu$.

This procedure can be used as described here for GHF and HDFT calculations. For RSH functionals, the evaluation of four-center integrals needs to take the range-separated Coulomb operator as introduced in eq. (5.4.27) into account. This requires an alternative routine capable of handling the error function present in the operator.

8.2.3. Exchange-Correlation Potential

The construction of the exchange-correlation potential works similarly to its field-free counterpart. While any grid typically used for ground-state calculations in the absence of fields can in principle also be used here, larger grids are preferable due to the oscillations described via the LAO phase factors. Instead of AOs, complex LAOs are evaluated on the grid; their real and imaginary parts are stored separately. For MGGA functionals, the noncollinear paramagnetic current densities $\mathbf{j}_m^p(\mathbf{r})$ have to

be additionally evaluated on the grid, which is done in accordance with eq. (5.4.8). The diamagnetic contribution in the first term of eq. (5.4.23) must be added onto the contribution from the local spin-density approximation, but its presence is often omitted in literature.^[38, 193]

8.2.4. Efficiency Increase for SCF Procedure

Calculations in finite magnetic fields are more time-consuming than their field-free counterparts for a multitude of reasons. Firstly, the need for complex algebra generally makes calculations about four times more expensive. Secondly, the reduced permutational symmetry results in an additional factor of two if four-center integrals are used.^[37, 56] Thirdly, the computation of integrals is generally more intricate since the complex LAO phase factor has to be included and translational invariance of integrals can no longer be invoked.^[36, 38] Additional one-electron integrals for the para- and diamagnetic contributions have to be evaluated, which is less relevant as their calculation is not particularly demanding. Finally, as LAOs contain plane-wave contributions, integral screening techniques are generally less advantageous, especially in the presence of very strong magnetic fields.^[316] Several techniques known to accelerate the SCF procedure in the absence of fields were implemented in the context of this work and presented in Ref. [56]. An overview of these methods shall be given here nonetheless.

Cauchy–Schwarz screening^[323–325] can be used in order to estimate whether a batch of integrals is negligible. Using the Schwarz inequality,

$$|(\mu\nu|\kappa\lambda)| \leq \sqrt{|(\mu\nu|\nu\mu)|} \sqrt{|(\kappa\lambda|\lambda\kappa)|}, \quad (8.2.2)$$

the maximum absolute value of an integral batch

$$\tau_{\mu\nu\kappa\lambda} = \max\{|(\mu\nu|\kappa\lambda)|\} \quad (8.2.3)$$

may be evaluated from the two-index quantity $(\mu\nu|\nu\mu)$. As stated prior, these two-index integrals are precomputed and stored in memory. They are real-valued even if evaluated over LAOs.^[56] Additionally, the maximum value of the density contained in a shell-pair, $|D_{\mu\nu}|$, may be stored as a two-index quantity. For $(\mu\nu|\kappa\lambda)$, the maximum value of any density batch it is contracted with is evaluated according to:

$$v_{\mu\nu\kappa\lambda} = \frac{1}{2} \max\{4|D_{\mu\nu}|, 4|D_{\kappa\lambda}|, |D_{\mu\kappa}|, |D_{\mu\lambda}|, |D_{\nu\kappa}|, |D_{\nu\lambda}|\}. \quad (8.2.4)$$

A shell-quartet can thus be skipped entirely if the product of the largest contributions is below a certain threshold denoted by ϵ :

$$\tau_{\mu\nu\kappa\lambda}v_{\mu\nu\kappa\lambda} \geq 10^{-\epsilon}. \quad (8.2.5)$$

It should be mentioned that the screening in eq. (8.2.4) includes density contributions for both the Coulomb and the exchange potential. If they are calculated separately, the screening is more efficient, particularly for large molecules where the majority of atoms are well-separated. On the downside, four-center integrals then have to be evaluated twice. A very similar approach uses difference densities^[323, 326, 327] instead of densities for the screening:

$$\Delta v_{\mu\nu\kappa\lambda} = \frac{1}{2} \max\{4|\Delta D_{\mu\nu}|, 4|\Delta D_{\kappa\lambda}|, |\Delta D_{\mu\kappa}|, |\Delta D_{\mu\lambda}|, |\Delta D_{\nu\kappa}|, |\Delta D_{\nu\lambda}|\}. \quad (8.2.6)$$

The difference density $|\Delta \mathbf{D}|$ is the difference between the density of the current and previous iterations. Thus, if parts of the density are already converged, their contributions can be neglected:

$$\tau_{\mu\nu\kappa\lambda}\Delta v_{\mu\nu\kappa\lambda} \geq 10^{-\epsilon}. \quad (8.2.7)$$

Particularly the last few iterations of the SCF procedure are vastly accelerated by using difference densities.

The direct inversion of the iterative subspace (DIIS)^[328, 329] is an alternative to the (damped) diagonalization of the Fock matrix. Instead, an error vector,

$$\mathbf{e} = \mathbf{FDS} - \mathbf{SDF}, \quad (8.2.8)$$

is evaluated and minimized until a stationary point is reached. If LAOs are used, all quantities including the error vector itself become complex-valued.

8.2.5. Canonical Orthogonalization

While the development of basis sets for molecules in strong magnetic fields has been attempted in the past,^[43, 71, 330, 331] no broadly used basis set has so far emerged. Thus, the use of very large uncontracted basis sets is not uncommon for quantum chemical calculations in such extreme environments.^[19, 35] One problem which may arise if such large uncontracted basis sets are employed, is the appearance of near

linear dependencies in the basis. They correspond to very small eigenvalues λ_i of the overlap matrix,

$$\mathbf{S}\mathbf{v}_i = \lambda_i\mathbf{v}_i, \quad (8.2.9)$$

and may be avoided if canonical orthogonalization^[332, 333] is used for the generation of an orthonormal set of spinors. Eigenvectors of the metric corresponding to eigenvalues lower than a certain threshold η are simply discarded,

$$\mathbf{v}_i = \mathbf{0} \quad \forall \lambda_i < \eta, \quad (8.2.10)$$

and spinors are evaluated accordingly. This functionality was implemented into TURBOMOLE, both for calculations in the absence and presence of external magnetic fields. Since an identical problem may arise for the metric used in the RI approximation, a similar procedure was implemented for the auxiliary metric.

8.2.6. Spin Zeeman Scaling

As previously described in sec. 5.2.1, the 2c SCF method does not impose any spin restrictions onto the electronic wave function or density. Consequently, the solution usually corresponds to the spin state with the lowest total electronic energy. In strong magnetic fields, the spin Zeeman term is incorporated through eq. (5.2.9), which leads to spin states with a very high spin multiplicity ($2|\mathbf{S}| + 1$) in larger fields.

Electronic excited states may also be calculated using the 2c SCF method if they are of a different spin multiplicity. By scaling the spin Zeeman term with a factor z ,

$$h_{\mu\nu,n} = z \left[\frac{1}{2} B_n \langle \mu | \nu \rangle \right], \quad (8.2.11)$$

an additional constraint is imposed, which can lead to a different solution to the SCF method. Values of $z > 1$ can lead to the description of spin states with higher multiplicity, while values of $z < 1$ generally result in lower spin states. For $z = 0$, the spin Zeeman term is neglected entirely.

The resulting scaled spin Zeeman energy is calculated as,

$$E_{\text{BS}} = h_{\mu\nu,n} D_{\nu\mu,n}, \quad (8.2.12)$$

and indirectly includes the spin Zeeman scaling z . Since \mathbf{h}_n only contains the scaled metric of the corresponding generalized eigenvalue problem, any solution which is

variationally stable with z must in principle be stable with $z = 1$. Thus, the spin Zeeman scaling performs the role of a Lagrange multiplier within an SCF calculation. In the last iteration, the scaling is set back to $z = 1$, in order to ensure comparability between differently scaled calculations. If the minimum found is variationally and numerically stable, subsequent calculations with $z = 1$ should yield the same (excited) wave function as a result.

8.2.7. Squared Spin Operator

In order to evaluate the spin contamination, the expectation value of the squared spin operator has to be computed. This was implemented for two-component calculations in the absence and presence of external magnetic fields in the context of this work, and the presentation here closely follows Ref. [334]. The expectation value of the squared spin operator for 2c calculations is given by

$$\begin{aligned} \langle \Psi_0 | \hat{\mathbf{S}}^2 | \Psi_0 \rangle &= \left(\frac{N_\alpha - N_\beta}{2} \right) \left(\frac{N_\alpha - N_\beta}{2} + 1 \right) + \left(N_\beta - \sum_{i,j}^{N_{\text{el}}} \langle \varphi_i^\alpha | \varphi_j^\beta \rangle \langle \varphi_j^\beta | \varphi_i^\alpha \rangle \right) \\ &+ \frac{1}{4} \left(N_{\text{el}} - \sum_{i,j}^{N_{\text{el}}} \left| \langle \varphi_i^\alpha | \varphi_j^\alpha \rangle - \langle \varphi_i^\beta | \varphi_j^\beta \rangle \right|^2 \right) + \left| \sum_i^{N_{\text{el}}} \langle \varphi_i^\beta | \varphi_i^\alpha \rangle \right|^2, \end{aligned} \quad (8.2.13)$$

with N_α being the number of α electrons and N_β the number of β electrons, assuming that $N_\alpha \geq N_\beta$. Consequently, the first term of eq. (8.2.13) is the eigenvalue of a wave function in which the $\hat{\mathbf{S}}^2$ -symmetry is not broken, such as the restricted open-shell Hartree–Fock solution.^[335] The second term is equivalent to the spin contamination of UHF wave functions.^[334, 336] The third term is referred to as z -noncollinearity and it is a direct result of the lifted \hat{S}_z constraint. The last term is called x, y -perpendicularity and is a consequence of the presence of spin density in the x and y direction.^[334]

8.2.8. Ground State Properties and Expectation Values

Molecular properties of the electronic ground state represented by any hermitian operator \hat{O} may be calculated according to

$$\langle \Psi_0 | \hat{O} | \Psi_0 \rangle = \sum_{\mu,\nu} \langle \mu | \hat{O} | \nu \rangle D_{\nu\mu,0}, \quad (8.2.14)$$

using the total electron density matrix \mathbf{D}_0 if the respective property does not reference the electron spin. Electric dipole and quadrupole moments are calculated by default in the current implementation. Their components are represented by the operators \hat{r}_α and $\hat{r}_\alpha\hat{r}_\beta$, respectively. The integrals in eq. (8.2.14) have to be evaluated using LAOs. Mulliken charges may be evaluated as described in eqs. (7.2.13) – (7.2.14). Here, the overlap matrix is calculated using complex LAOs and the noncollinear density is taken from a previous SCF calculation. Additionally, the possibility to print out the Mulliken charge distribution was implemented, which can be used for molecular dynamics simulations in finite magnetic fields.^[57]

While the visualization of complex-valued orbitals has been attempted in the past,^[337] it remains unclear how much can be gained from interpreting the somewhat arbitrary complex phase (see: sec. 4.2). The electron density, however, is an observable quantity and its interpretation is relevant for numerous applications. It may be evaluated on a grid using the tools implemented for Kohn–Sham DFT as previously described in sec. 8.2.3. As usual, LAOs are used to ensure gauge origin invariance.

8.3. Molecular Gradients and Geometry Optimization

8.3.1. General Outline

The evaluation of molecular gradients is a quintessential step in the investigation of molecular structures. Within the BO adiabatic approximation, the electronic wave function can be evaluated for any nuclear configuration \mathbf{R} as detailed in the previous section. For most chemical applications, however, only equilibrium structures satisfying eq. (3.3.23) are relevant. They may be systematically found through a process called geometry optimization, which typically involves the calculation of the molecular gradient in several steps of the procedure. An efficient implementation is therefore desirable for geometry optimizations of larger molecules and other applications such as *ab initio* molecular dynamics simulations.

Molecular gradients may, in principle, be evaluated at any level of theory. For a detailed description of the evaluation of molecular gradients on the RHF as well as UHF and UKS level, the interested reader is referred to the literature.^[34, 38] In this work, molecular gradients were implemented into TURBOMOLE using GHF and spin-noncollinear KS DFT. Their evaluation requires a successfully converged SCF calculation on the same level of theory. An individual element of the gradient on the

HDFT level may be calculated according to:^[338]

$$\begin{aligned}
 \frac{\partial E_0^{\text{BO}}(\mathbf{R})}{\partial R_{I\alpha}} &= \sum_{\mu\nu} \left\{ \left[\left\langle \mu \left| \frac{\partial \hat{V}_{\text{Ne}}}{\partial R_{I\alpha}} \right| \nu \right\rangle + \langle \mu' | \hat{h}_0 | \nu \rangle + \langle \mu | \hat{h}_0 | \nu' \rangle \right] D_{\nu\mu,0} \right. \\
 &+ \frac{1}{2} \sum_{\kappa\lambda} [(\mu'\nu|\kappa\lambda) + (\mu\nu'|\kappa\lambda) + (\mu\nu|\kappa'\lambda) + (\mu\nu|\kappa\lambda')] D_{\lambda\kappa,0} D_{\nu\mu,0} \\
 &- \frac{1}{2} c^x \sum_{\kappa\lambda} [(\mu'\nu|\kappa\lambda) + (\mu\nu'|\kappa\lambda) + (\mu\nu|\kappa'\lambda) + (\mu\nu|\kappa\lambda')] D_{\lambda\mu,m} D_{\kappa\nu,m} \\
 &\left. + [\langle \mu' | \nu \rangle + \langle \mu | \nu' \rangle] \left[\frac{1}{2} B_n D_{\nu\mu,n} - W_{\nu\mu,0} \right] \right\} + \frac{\partial E_{\text{xc}}}{\partial R_{I\alpha}} + \frac{\partial V_{\text{NN}}}{\partial R_{I\alpha}}.
 \end{aligned} \tag{8.3.1}$$

For GHF calculations, the full exchange contribution is taken into account, $c^x = 1$, and no xc energy contribution is present: $E_{\text{xc}} = 0$. For non-hybrid DFT, no exact exchange is calculated: $c^x = 0$. As previously defined in sec. 5.2 of this work, we assume $m \in \{0, 1, 2, 3\}$ and $n \in \{1, 2, 3\}$ for $2c$ calculations. The energy-weighted density matrix \mathbf{W} is defined similarly to the noncollinear density matrix in eq. (5.2.7),

$$W_{\mu\nu}^{\sigma\sigma'} = \varepsilon_j C_{\mu j}^{\sigma} C_{\nu j}^{\sigma'*}, \tag{8.3.2}$$

using spinor energies ε_j for its construction.^[310, 339] It may be decomposed into its individual noncollinear contributions as

$$\mathbf{W} = \mathbf{W}_m \otimes \boldsymbol{\sigma}_m \tag{8.3.3}$$

by using the Pauli matrices. Finally, the abridged notation for the derivative of a LAO may be rewritten as

$$|\mu'\rangle = \frac{\partial \xi_{\mu}(\mathbf{r})}{\partial R_{I\alpha}} = \frac{\partial}{\partial R_{I\alpha}^{\mu}} |\mathbf{l}^{\mu}\rangle, \tag{8.3.4}$$

where we used the atom-centered nature of basis functions in order to discard derivatives with respect to nuclear coordinates which the LAO does not reference. Employing the definition of a LAO in eq. (4.3.3) and its corresponding GTO in eq. (4.3.4), the derivative of any primitive LAO with respect to a nuclear coordinate may be expressed according to:^[34, 38]

$$\begin{aligned}
 \frac{\partial}{\partial R_{I\alpha}^{\mu}} |\mathbf{l}^{\mu}\rangle &= -a_{\alpha}^{\mu} |\mathbf{l}^{\mu} - \mathbf{1}_{\alpha}\rangle + 2\zeta_{\mu} |\mathbf{l}^{\mu} + \mathbf{1}_{\alpha}\rangle + \frac{i}{2} \varepsilon_{\alpha\beta\gamma} B_{\beta} (R_{\gamma}^{\mu} - O_{\gamma}) |\mathbf{l}^{\mu}\rangle \\
 &+ \frac{i}{2} \varepsilon_{\alpha\beta\gamma} B_{\beta} |\mathbf{l}^{\mu} + \mathbf{1}_{\gamma}\rangle.
 \end{aligned} \tag{8.3.5}$$

It should be noted that the derivative with respect to an electron coordinate may similarly be defined as

$$\frac{\partial}{\partial r_\alpha} |\mathbf{l}^\mu\rangle = a_\alpha^\mu |\mathbf{l}^\mu - \mathbf{1}_\alpha\rangle - 2\zeta_\mu |\mathbf{l}^\mu + \mathbf{1}_\alpha\rangle - \frac{i}{2} \varepsilon_{\alpha\beta\gamma} B_\beta (R_\gamma^\mu - O_\gamma) |\mathbf{l}^\mu\rangle \quad (8.3.6)$$

and for the sake of completeness, we note that the derivative with respect to a component of the gauge origin reads

$$\frac{\partial}{\partial O_\alpha} |\mathbf{l}^\mu\rangle = -\frac{i}{2} \varepsilon_{\alpha\beta\gamma} B_\beta |\mathbf{l}^\mu + \mathbf{1}_\gamma\rangle. \quad (8.3.7)$$

Thus, an individual LAO is translationally invariant with respect to the displacement of the nucleus it is centered on, the electron it describes and the gauge origin:

$$\left(\frac{\partial}{\partial R_\alpha^\mu} + \frac{\partial}{\partial r_\alpha} + \frac{\partial}{\partial O_\alpha} \right) |\mathbf{l}^\mu\rangle = 0. \quad (8.3.8)$$

From this notion, a few key differences for the calculation of molecular gradients in the absence and presence of an external magnetic field may be inferred. Firstly, all integrals have to be calculated using complex LAOs. Secondly, the prevalent use of relations invoking translational-invariance of any kind have to be carefully assessed. Thirdly, the lowered permutational symmetry of four-center integrals has to be taken into account similarly to the procedure described in sec. 8.2.2 of this work.

8.3.2. Geometry Optimization in External Magnetic Fields

Molecular geometries in external magnetic fields may be optimized using the quasi-Newton–Raphson method.^[38] The molecular Hessian can be approximated using gradients in the Broyden–Fletcher–Goldfarb–Shanno (BFGS) approach.^[340–343] Geometry optimizations can be carried out in Cartesian coordinates with certain constraints,^[344–346] which may be straightforwardly done for molecules in external magnetic fields. While the optimization in Cartesian coordinates is feasible and has been carried out in the past,^[38, 347] it must be carried out carefully. Due to the presence of the magnetic field, the system is no longer isotropic with respect to rotational degrees of freedom. The additional rotational barrier^[57] with respect to one (linear molecules) or two (non-linear molecules) rotational axis perpendicular to the magnetic field vector has to be taken into account. Particularly in small magnetic fields, in which the barrier is also very small, an optimization may seem to have converged

because compared to the other (vibrational) degrees of freedom, the contribution of the rotational modes to the molecular gradient is extremely small.

The use of internal coordinates^[348, 349] might rectify this problem somewhat. In the absence of magnetic fields, rotational and translational degrees of freedom are generally decoupled from vibrational modes in the internal coordinate Hessian. In the presence of magnetic fields, up to two additional internal coordinates, one for linear molecules and two for non-linear molecules, need to be introduced. As the new degrees of freedom are associated with small gradient contributions, it may be necessary to decouple the Hessian into its field-free form and the additional 2×2 Hessian for field-dependent internal coordinates. The decoupled Hessian for molecules in external magnetic fields is depicted in fig. 8.3.1.

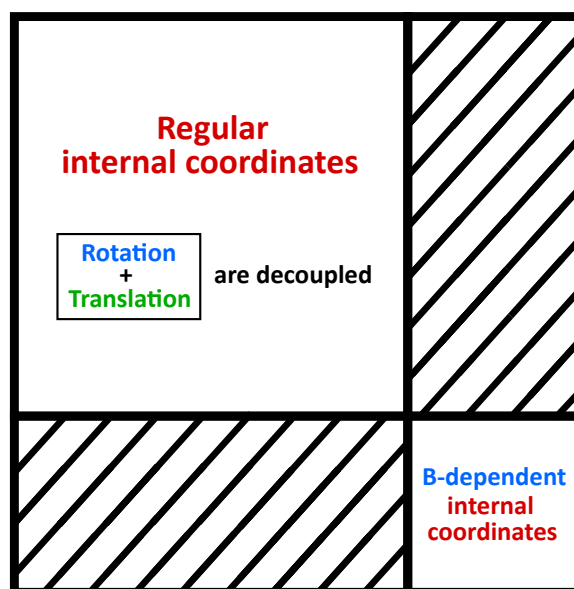


Figure 8.3.1.: Hessian consisting of internal coordinates for molecules in external magnetic fields. Due to rotational anisotropy, one (linear molecules) or two (non-linear molecules) additional field-dependent internal coordinates need to be introduced. If the Hessian is decoupled, the two blocks may be optimized separately in an iterative procedure.

The geometry optimization in internal coordinates may then be carried out using the following procedure: Firstly, the geometry is optimized in regular internal coordinates. Secondly, the two (one for linear molecules) additional field-dependent rotational modes are optimized in a separate step with fixed internal coordinates for vibrational modes. These two separate geometry optimizations are then iteratively carried out, alternating between one and the other until both are converged. This procedure

was developed in collaboration with Kitsaras and is currently not implemented into TURBOMOLE.^[350] For geometry optimizations presented in this work, the second step of this procedure is thus carried out manually.

8.4. **Post Hartree–Fock Methods and Electronic Excitations**

All implementations on *post* Hartree–Fock methods and electronic excitations were carried out in collaboration with Holzer. The implementation of *post* Hartree–Fock methods such as MP2 and CC2 in external magnetic fields is very similar to the implementation of electronic excitations using TD-HF. In both cases, the main part of the program uses quantities in the MO basis, which in the case of two-component calculations is already complex-valued even in the absence of magnetic fields. The information about the magnetic field is implicitly present through the use of spinors generated from a field-dependent HF calculation, which was previously carried out. The only additional ingredient are the two-electron integrals, which have to be calculated using LAOs instead of AOs and then transformed into the MO basis.

For TD-DFT and *post* Kohn–Sham methods which reference the xc part such as cBSE, an additional component has to be evaluated: the xc kernel. Its construction for current-dependent MGGA functionals was described in sec. 6.1.4 of this work. The implementation of this xc kernel is very similar to the field-free MGGA case.^[189, 260] Additional current-dependent terms have to be evaluated and LAOs have to be used for its construction. After a transformation to the MO basis, again, everything works identically to the field-free case.

It should be mentioned that in contrast to the four noncollinear ground state (spin) densities \mathbf{D}_m which are all either hermitian or anti-hermitian, noncollinear (de-)excitation vectors \mathbf{X}_j and \mathbf{Y}_j generally do not possess any symmetry. Thus, they are decomposed into a hermitian and an anti-hermitian part, resulting in eight complex matrices, each yet again decomposable into their real and imaginary parts. Furthermore, it should be noted that the elements of the de-excitation vector \mathbf{Y}_j have to be multiplied with complex conjugated two-electron integrals (see for instance eq. (6.2.1) for reference). In the absence of magnetic fields, this does not make any difference in the AO basis, but it has to be considered for complex-valued LAOs.

Excited state properties may be calculated from converged vectors \mathbf{X}_j and \mathbf{Y}_j , and transition densities may be evaluated similarly to ground state densities.

9. Efficient Integral Evaluation

The previous chapter presented the implementation of quantum chemical calculations in finite magnetic fields into the TURBOMOLE program suite. For two-component calculations, where most quantities are already complex-valued in the MO basis, most of the architecture already present for field-free calculations could be used. One of the major differences was the reduced permutational symmetry of four-center integrals, which required the implementation of an entirely new wrapper for the calculation and processing of these integrals. After having established the main structure of the programs, this chapter introduces the efficient evaluation of integrals over complex-valued LAOs. Excellent reviews of this topic can be found in Ref. [36] and [38], although the formalism used in this work deviates for some key components. Furthermore, the evaluation of integrals relevant for the RI approximation was developed during this work and presented in [56].

This chapter follows the basic structures presented in Ref. [36] and [38]. Initially, the calculation of shell-pair quantities is introduced. This is a relevant step for the evaluation of any integral presented in this chapter, as for instance highlighted in fig. 8.2.2. Thereafter, the calculation of overlap integrals and the implementation of Obara–Saika recurrence relations for overlap integrals over LAOs is presented. It is shown that the computation of kinetic energy integrals can be expressed entirely in terms of overlap integrals.

Nuclear attraction integrals cannot be expressed in terms of overlap integrals. They require the evaluation of the molecular Boys function and a specific set of Obara–Saika recurrence relations. An algorithm capable of efficiently evaluating both is discussed. Finally, the calculation of electron repulsion integrals is presented in terms of four-center integrals as well as three-center integrals. An implementation of the Head-Gordon–Pople algorithm is presented. For all types of integrals except three-center integrals, derivatives with respect to nuclear displacements are discussed as required for molecular gradients.

9.1. Calculation of Shell-Pair Quantities

This section largely follows Ref. [36] and [38]. As illustrated for four-center integrals in fig. 8.2.2, the evaluation of shell-pair quantities is a quintessential step in the calculation of molecular integrals. All molecular integrals require the evaluation of the overlap between two s -type functions for every non-negligible shell-pair $\mu\nu$ according to:^[36, 38]

$$\langle \mu | \nu \rangle = \langle \mathbf{l}^\mu | \mathbf{l}^\nu \rangle = \langle \mathbf{0} | \mathbf{0} \rangle \quad (9.1.1)$$

Using the short-hand notation of the plane wave part of LAO ξ_μ ,

$$\mathbf{k}^\mu = \frac{1}{2} \mathbf{B} \times (\mathbf{R}^\mu - \mathbf{O}), \quad (9.1.2)$$

the overlap between two primitive s -type functions may be written as:

$$\langle \mathbf{0} | \mathbf{0} \rangle = N_\mu N_\nu \int_{-\infty}^{\infty} e^{-\zeta_\mu |\mathbf{r} - \mathbf{R}^\mu|^2 + i \mathbf{k}^\mu \cdot \mathbf{r}} e^{-\zeta_\nu |\mathbf{r} - \mathbf{R}^\nu|^2 - i \mathbf{k}^\nu \cdot \mathbf{r}} \, d\mathbf{r}. \quad (9.1.3)$$

Additional shell-pair quantities are introduced:

$$\zeta = \zeta_\mu + \zeta_\nu, \quad (9.1.4)$$

$$\sigma = \zeta^{-1} \zeta_\mu \zeta_\nu, \quad (9.1.5)$$

$$\mathbf{P} = \zeta^{-1} (\zeta_\mu \mathbf{R}^\mu + \zeta_\nu \mathbf{R}^\nu), \quad (9.1.6)$$

$$\boldsymbol{\chi} = (4\zeta)^{-1} \mathbf{B} \times (\mathbf{R}^\nu - \mathbf{R}^\mu), \quad (9.1.7)$$

$$\tilde{\mathbf{P}} = \mathbf{P} - i\boldsymbol{\chi}, \quad (9.1.8)$$

with ζ being the total exponent, σ the reduced exponent, \mathbf{P} the real part and $\boldsymbol{\chi}$ the imaginary part of the complex center of charge $\tilde{\mathbf{P}}$.^[351] Using these, the overlap of two primitive s -functions may be expressed as:

$$\langle \mathbf{0} | \mathbf{0} \rangle = N_\mu N_\nu e^{-\sigma(\mathbf{R}^\nu - \mathbf{R}^\mu)^2} e^{-\zeta(\chi^2 + 2i\mathbf{P} \cdot \boldsymbol{\chi})} \int_{-\infty}^{\infty} e^{-\zeta(\mathbf{r} - \tilde{\mathbf{P}})^2} \, d\mathbf{r}. \quad (9.1.9)$$

The integral may be decomposed into its three Cartesian components and evaluated as the product of three one-dimensional integrals. Due to the isotropic nature of s -type functions, all three Cartesian components yield identical results. Additionally, the translational invariance of an integral over a Gaussian function with respect to a displacement of its center can be used if the integral is evaluated over all of space. This is valid even for a complex-valued center of the Gaussian, provided the integration

variable is real-valued. The resulting integral reads:

$$\int_{-\infty}^{\infty} e^{-\zeta(\mathbf{r}-\tilde{\mathbf{P}})^2} d\mathbf{r} = \left(\frac{\pi}{\zeta}\right)^{3/2}, \quad (9.1.10)$$

We thus define the overlap of two s -type LAOs as:

$$\langle \mathbf{0} | \mathbf{0} \rangle = N_{\mu} N_{\nu} e^{-\sigma(\mathbf{R}^{\nu} - \mathbf{R}^{\mu})^2} \left(\frac{\pi}{\zeta}\right)^{3/2} e^{-\zeta(\mathbf{x}^2 + 2i\mathbf{P} \cdot \mathbf{x})} = U_{\mathbf{P}} K_{\mathbf{P}} = \tilde{U}_{\mathbf{P}}. \quad (9.1.11)$$

It should be noted that this result differs from the real-valued GTO case ($U_{\mathbf{P}}$) only in the presence of the complex-valued factor $K_{\mathbf{P}} = e^{-\zeta(\mathbf{x}^2 + 2i\mathbf{P} \cdot \mathbf{x})}$. Therefore, an existing code which is able to calculate the overlap between two s -type GTOs only needs to be altered by including this additional factor in order to calculate the overlap between two s -type LAOs. An efficient program may screen integrals via $|\tilde{U}_{\mathbf{P}}|$, as for instance suggested in Ref. [36] and [38]. This might not generally be advisable^[316, 352] and an in-depth analysis of integral screening for LAOs is the subject of future work.

9.2. Overlap Integrals

9.2.1. Horizontal Recurrence Relations

Overlap integrals associated with higher angular momentum quantum numbers can be calculated using recurrence relations. The horizontal recurrence relation (HRR) can be derived using the following relations:^[351]

$$|\mathbf{l}^{\mu} + \mathbf{1}_{\alpha}\rangle = (r_{\alpha} - R_{\alpha}^{\mu}) |\mathbf{l}^{\mu}\rangle, \quad (9.2.1)$$

$$|\mathbf{l}^{\nu} + \mathbf{1}_{\alpha}\rangle = (r_{\alpha} - R_{\alpha}^{\nu}) |\mathbf{l}^{\nu}\rangle. \quad (9.2.2)$$

Projecting onto the respective Bra-vectors and subtracting the two equations yields

$$\langle \mathbf{l}^{\mu} + \mathbf{1}_{\alpha} | \mathbf{l}^{\nu} \rangle - \langle \mathbf{l}^{\mu} | \mathbf{l}^{\nu} + \mathbf{1}_{\alpha} \rangle = \langle \mathbf{l}^{\mu} | (r_{\alpha} - R_{\alpha}^{\mu}) | \mathbf{l}^{\nu} \rangle - \langle \mathbf{l}^{\mu} | (r_{\alpha} - R_{\alpha}^{\nu}) | \mathbf{l}^{\nu} \rangle, \quad (9.2.3)$$

which can be rewritten as the horizontal recurrence relation:^[36]

$$\langle \mathbf{l}^{\mu} + \mathbf{1}_{\alpha} | \mathbf{l}^{\nu} \rangle = \langle \mathbf{l}^{\mu} | \mathbf{l}^{\nu} + \mathbf{1}_{\alpha} \rangle + (R_{\alpha}^{\nu} - R_{\alpha}^{\mu}) \langle \mathbf{l}^{\mu} | \mathbf{l}^{\nu} \rangle. \quad (9.2.4)$$

The HRR for LAOs is identical to its real-valued counterpart in the absence of fields. It is the cheapest recurrence relation from a computational point of view and does not reference any shell-pair quantities.^[353]

9.2.2. Translational Recurrence Relations

Translational recurrence relations (TRR) can be derived by requiring that an integral is translationally invariant with respect to the displacement of both nuclei and the gauge origin:

$$\left(\frac{\partial}{\partial R_\alpha^\mu} + \frac{\partial}{\partial R_\alpha^\nu} + \frac{\partial}{\partial O_\alpha} \right) \langle \mathbf{I}^\mu | \mathbf{I}^\nu \rangle = 0. \quad (9.2.5)$$

As previously described in sec. 8.3, the inclusion of the displacement with respect to the gauge origin is absolutely crucial in the presence of external magnetic fields. Using the product rule for derivatives, the TRR reads:

$$\left\langle \left(\frac{\partial}{\partial R_\alpha^\mu} + \frac{\partial}{\partial O_\alpha} \right) \mathbf{I}^\mu \middle| \mathbf{I}^\nu \right\rangle + \left\langle \mathbf{I}^\mu \middle| \left(\frac{\partial}{\partial R_\alpha^\nu} + \frac{\partial}{\partial O_\alpha} \right) \mathbf{I}^\nu \right\rangle = 0. \quad (9.2.6)$$

Through the definitions introduced in eq. (8.3.5) and (8.3.7), the TRR for overlap integrals may be rewritten as

$$\begin{aligned} 2\zeta_\mu \langle \mathbf{I}^\mu + \mathbf{1}_\alpha | \mathbf{I}^\nu \rangle - a_\alpha^\mu \langle \mathbf{I}^\mu - \mathbf{1}_\alpha | \mathbf{I}^\nu \rangle - \frac{i}{2} \varepsilon_{\alpha\beta\gamma} B_\beta (R_\gamma^\mu - O_\gamma) \langle \mathbf{I}^\mu | \mathbf{I}^\nu \rangle \\ 2\zeta_\nu \langle \mathbf{I}^\mu | \mathbf{I}^\nu + \mathbf{1}_\alpha \rangle - a_\alpha^\nu \langle \mathbf{I}^\mu | \mathbf{I}^\nu - \mathbf{1}_\alpha \rangle + \frac{i}{2} \varepsilon_{\alpha\beta\gamma} B_\beta (R_\gamma^\nu - O_\gamma) \langle \mathbf{I}^\mu | \mathbf{I}^\nu \rangle = 0, \end{aligned} \quad (9.2.7)$$

which may be simplified further by identifying the imaginary part of the complex center of charge introduced in eq. (9.1.7):

$$\begin{aligned} 2\zeta_\mu \langle \mathbf{I}^\mu + \mathbf{1}_\alpha | \mathbf{I}^\nu \rangle + 2\zeta_\nu \langle \mathbf{I}^\mu | \mathbf{I}^\nu + \mathbf{1}_\alpha \rangle + i\chi_\alpha (2\zeta) \langle \mathbf{I}^\mu | \mathbf{I}^\nu \rangle \\ = a_\alpha^\mu \langle \mathbf{I}^\mu - \mathbf{1}_\alpha | \mathbf{I}^\nu \rangle + a_\alpha^\nu \langle \mathbf{I}^\mu | \mathbf{I}^\nu - \mathbf{1}_\alpha \rangle \end{aligned} \quad (9.2.8)$$

In of itself, the TRR are not particularly useful as they relate an increased angular momentum quantum number of μ to one of ν , similarly to the HRR.

9.2.3. Obara–Saika Recurrence Relations

Finally, using both the HRR and TRR, a set of useful recurrence relations can be identified. The Obara–Saika (OS) recurrence relations^[354, 355] are derived by inserting

the HRR into the TRR, which results in the following expression:

$$\begin{aligned} & 2\zeta \langle \mathbf{I}^\mu | \mathbf{I}^\nu + \mathbf{1}_\alpha \rangle + 2\zeta_\mu (R_\alpha^\nu - R_\alpha^\mu) | \langle \mathbf{I}^\mu | \mathbf{I}^\nu \rangle + i\chi_\alpha (2\zeta) \langle \mathbf{I}^\mu | \mathbf{I}^\nu \rangle \\ & = a_\alpha^\mu \langle \mathbf{I}^\mu - \mathbf{1}_\alpha | \mathbf{I}^\nu \rangle + a_\alpha^\nu \langle \mathbf{I}^\mu | \mathbf{I}^\nu - \mathbf{1}_\alpha \rangle . \end{aligned} \quad (9.2.9)$$

Rearranging this relation leads to the OS recurrence relations in external magnetic fields, also referred to as vertical recurrence relations (VRR), which read^[36]

$$\langle \mathbf{I}^\mu | \mathbf{I}^\nu + \mathbf{1}_\alpha \rangle = (\tilde{P}_\alpha - R_\alpha^\nu) \langle \mathbf{I}^\mu | \mathbf{I}^\nu \rangle + \frac{a_\alpha^\mu}{2\zeta} \langle \mathbf{I}^\mu - \mathbf{1}_\alpha | \mathbf{I}^\nu \rangle + \frac{a_\alpha^\nu}{2\zeta} \langle \mathbf{I}^\mu | \mathbf{I}^\nu - \mathbf{1}_\alpha \rangle , \quad (9.2.10)$$

$$\langle \mathbf{I}^\mu + \mathbf{1}_\alpha | \mathbf{I}^\nu \rangle = (\tilde{P}_\alpha - R_\alpha^\mu) \langle \mathbf{I}^\mu | \mathbf{I}^\nu \rangle + \frac{a_\alpha^\mu}{2\zeta} \langle \mathbf{I}^\mu - \mathbf{1}_\alpha | \mathbf{I}^\nu \rangle + \frac{a_\alpha^\nu}{2\zeta} \langle \mathbf{I}^\mu | \mathbf{I}^\nu - \mathbf{1}_\alpha \rangle , \quad (9.2.11)$$

and are almost identical to their real-valued counterparts. The only difference is the use of the complex center of charge, that is, the replacement of

$$\mathbf{P} \rightarrow \mathbf{P} - i\chi \quad (9.2.12)$$

at all points in the procedure and the associated use of complex algebra. Unfortunately, TURBOMOLE does not support the use of OS recurrence relations for overlap integrals over real-valued AOs and instead uses numerical integration techniques.^[320] Thus, an efficient implementation of the OS recurrence for overlap integrals was carried out in the context of this work.

While different algorithms can be constructed using the OS recurrence relations to evaluate the target integral $\langle l_x^\mu | l_x^\nu \rangle$, not all of them are equally efficient. In fig. 9.2.1, three different possible algorithms are depicted. The blue square marks the starting point, $\langle 0|0 \rangle$, while the green square marks the target integral, for instance $\langle 7|4 \rangle$. In this case, the first algorithm (a) uses 29 VRR steps and is the least efficient. The second algorithm (b) only uses 16 VRR steps and is thus already more efficient. The third algorithm (c) is implemented in TURBOMOLE. It uses 11 VRR steps of the form

$$\langle \mathbf{I}^\mu + \mathbf{1}_\alpha | \mathbf{0} \rangle = (\tilde{P}_\alpha - R_\alpha^\mu) \langle \mathbf{I}^\mu | \mathbf{I}^\nu \rangle + \frac{a_\alpha^\mu}{2\zeta} \langle \mathbf{I}^\mu - \mathbf{1}_\alpha | \mathbf{I}^\nu \rangle , \quad (9.2.13)$$

which is more efficient to evaluate than the full VRR in eq. (9.2.11). From the resulting integrals, only $\langle 7|0 \rangle - \langle 11|0 \rangle$ are stored and then used for the subsequent calculation of 10 HRR steps which are computationally less demanding than their VRR counterparts. Algorithms b) and c) were both implemented and carefully benchmarked for several systems. For larger systems in particular, algorithm c) consistently proved to be the

most efficient.

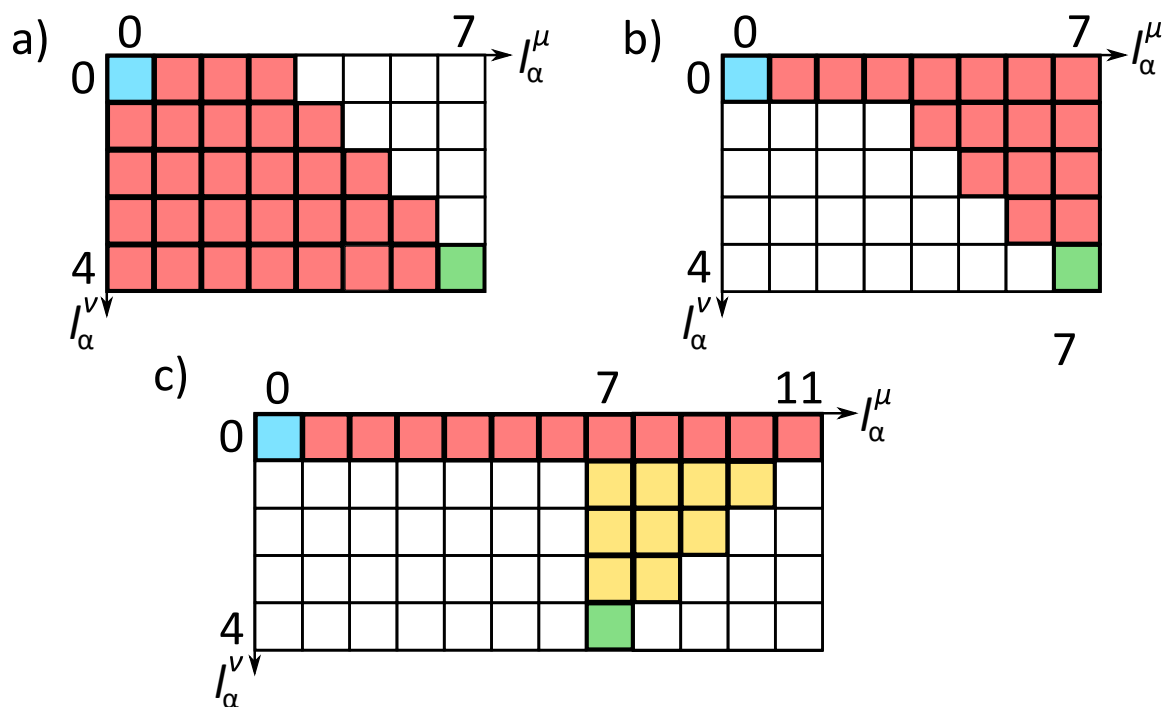


Figure 9.2.1.: Three different possible algorithms for the evaluation of Obara–Saika recurrence relations for overlap integrals. Algorithm a) uses vertical recurrence relations (red) to progress from the starting point (blue) to the target (green) in 29 steps. Algorithm b) only uses 17 vertical recurrence relations. Algorithm c) uses 11 vertical and 10 horizontal recurrence relations (yellow) and is thus the algorithm of choice.

For overlap integrals, the three Cartesian components can be computed separately. Therefore, an overlap integral is evaluated as:

$$\langle \mathbf{I}^\mu | \mathbf{I}^\nu \rangle = \langle l_x^\mu | l_x^\nu \rangle \langle l_y^\mu | l_y^\nu \rangle \langle l_z^\mu | l_z^\nu \rangle \quad (9.2.14)$$

9.2.4. Molecular Gradient

Derivatives of overlap integrals with respect to nuclear displacements have to be calculated for molecular gradients. Using the definition in eq. (8.3.5), the respective integral may be computed as

$$\begin{aligned} \langle \mu | \nu' \rangle = & -a_\alpha^\nu \langle \mathbf{I}^\mu | \mathbf{I}^\nu - \mathbf{1}_\alpha \rangle + ik_\alpha^\nu \langle \mathbf{I}^\mu | \mathbf{I}^\nu \rangle + 2\zeta_\nu \langle \mathbf{I}^\mu | \mathbf{I}^\nu + \mathbf{1}_\alpha \rangle \\ & + \frac{i}{2} \varepsilon_{\alpha\beta\gamma} B_\beta \langle \mathbf{I}^\mu | \mathbf{I}^\nu + \mathbf{1}_\gamma \rangle, \end{aligned} \quad (9.2.15)$$

which is a linear combination of overlap integrals constructed from the following set: $\{\langle \mathbf{l}^\mu | \mathbf{l}^\nu - \mathbf{1}_\alpha \rangle, \langle \mathbf{l}^\mu | \mathbf{l}^\nu \rangle, \langle \mathbf{l}^\mu | \mathbf{l}^\nu + \mathbf{1}_\beta \rangle\}$.^[34] There is a crucial difference between derivative integrals in the absence and presence of magnetic fields. While for field-free calculations, the derivative of a p_x orbital with respect to R_y^ν can be calculated as the linear combination of an s - and a d_{xy} -orbital, the same derivative needs an s -, p_x -, d_{xx} -, d_{xy} - and d_{xz} -orbital for $|\mathbf{B}| > 0$.

At first glance, this might seem like quite a few additional integrals need to be evaluated. However, as the derivative of the overlap integral with respect to all Cartesian components needs to be calculated for molecular gradients, the individual components may be computed simultaneously if for the derivative of a batch of integrals $\langle \mathbf{l}^\mu | \mathbf{l}^\nu \rangle$, additionally all those integrals decreased and increased by one Cartesian component are calculated. From this set, all derivative integrals can be computed. In comparison to the field-free case, only the use of LAOs and the additional evaluation of the batch $\langle \mathbf{l}^\mu | \mathbf{l}^\nu \rangle$ itself is required. Compared to the batch with an increased angular momentum quantum number, this is far less computationally demanding since the latter is both larger and more complicated to evaluate, requiring more recurrence relations.

9.3. Kinetic Energy Integrals

9.3.1. Evaluation of Integrals

The kinetic energy operator in the presence of a magnetic field reads

$$\hat{T} = \frac{\hat{\mathbf{p}}^2}{2} + \frac{1}{2} \mathbf{B} \cdot \hat{\mathbf{l}}^0 + \frac{1}{8} [\mathbf{B}^2 (\hat{\mathbf{r}}^0)^2 - (\mathbf{B} \cdot \hat{\mathbf{r}}^0)^2] , \quad (9.3.1)$$

excluding the spin Zeeman term which only requires the computation of overlap integrals. The individual integrals over the kinetic energy operator can all be calculated as a linear combination of overlap integrals.^[36] In this section, the different contributions are listed, giving an overview of how to evaluate not only the canonical kinetic energy contribution, but also the additional integrals over magnetic field-dependent operators. The spin-independent contribution to the kinetic energy is separated into an integral over the canonical kinetic energy operator,

$$\left\langle \mu \left| \frac{\hat{\mathbf{p}}^2}{2} \right| \nu \right\rangle = -\frac{1}{2} \left\langle \mu \left| \frac{\partial^2}{\partial r_x^2} + \frac{\partial^2}{\partial r_y^2} + \frac{\partial^2}{\partial r_z^2} \right| \nu \right\rangle , \quad (9.3.2)$$

the orbital Zeeman integral,

$$\left\langle \mu \left| \frac{1}{2} \mathbf{B} \cdot \hat{\mathbf{I}}^{\mathbf{O}} \right| \nu \right\rangle = -\frac{1}{2} \varepsilon_{\alpha\beta\gamma} B_{\alpha} \left\langle \mu \left| i \hat{r}_{\beta} \frac{\partial}{\partial r_{\gamma}} \right| \nu \right\rangle, \quad (9.3.3)$$

and the integrals containing the diamagnetic terms:

$$\begin{aligned} & \left\langle \mu \left| \frac{1}{8} [\mathbf{B}^2 (\hat{\mathbf{r}}^{\mathbf{O}})^2 - (\mathbf{B} \cdot \hat{\mathbf{r}}^{\mathbf{O}})^2] \right| \nu \right\rangle \\ &= \frac{1}{8} \left[B_x^2 \langle \mu | \hat{r}_y^2 + \hat{r}_z^2 | \nu \rangle + B_y^2 \langle \mu | \hat{r}_z^2 + \hat{r}_x^2 | \nu \rangle + B_z^2 \langle \mu | \hat{r}_x^2 + \hat{r}_y^2 | \nu \rangle \right] \\ & - \frac{1}{4} \left[B_x B_y \langle \mu | \hat{r}_x \hat{r}_y | \nu \rangle + B_x B_z \langle \mu | \hat{r}_x \hat{r}_z | \nu \rangle + B_y B_z \langle \mu | \hat{r}_y \hat{r}_z | \nu \rangle \right]. \end{aligned} \quad (9.3.4)$$

Thus, all integrals over the kinetic energy operator can be expressed in terms of integrals over multipole operators \hat{r}_{α} , derivative operators and combinations thereof. This is also true for integrals over field-dependent operators. More specifically, the following multipole integrals are required:

$$\langle \mathbf{l}^{\mu} | \hat{r}_{\alpha} | \mathbf{l}^{\nu} \rangle = \langle \mathbf{l}^{\mu} | \mathbf{l}^{\nu} + \mathbf{1}_{\alpha} \rangle + R_{\alpha}^{\nu} \langle \mathbf{l}^{\mu} | \mathbf{l}^{\nu} \rangle \quad (9.3.5)$$

$$\langle \mathbf{l}^{\mu} | \hat{r}_{\alpha}^2 | \mathbf{l}^{\nu} \rangle = \langle \mathbf{l}^{\mu} | \mathbf{l}^{\nu} + \mathbf{2}_{\alpha} \rangle + 2R_{\alpha}^{\nu} \langle \mathbf{l}^{\mu} | \mathbf{l}^{\nu} + \mathbf{1}_{\alpha} \rangle + (R_{\alpha}^{\nu})^2 \langle \mathbf{l}^{\mu} | \mathbf{l}^{\nu} \rangle \quad (9.3.6)$$

Due to the separation of Cartesian components for overlap integrals presented in eq. (9.2.14), contributions of mixed Cartesian components ($\hat{r}_x \hat{r}_y$) are evaluated as

$$\langle \mathbf{l}^{\mu} | \hat{r}_x \hat{r}_y | \mathbf{l}^{\nu} \rangle = \langle l_x^{\mu} | \hat{r}_x | l_x^{\nu} \rangle \langle l_y^{\mu} | \hat{r}_y | l_y^{\nu} \rangle \langle l_z^{\mu} | l_z^{\nu} \rangle, \quad (9.3.7)$$

only requiring electric dipole integrals as presented in eq. (9.3.5). All kinetic energy integrals can be decomposed using this scheme and thus no further implementation for operators with mixed Cartesian components is required.

For the calculation of derivative integrals, the effects of the derivative operator with respect to an electron coordinate, eq. (8.3.6), has to be considered:

$$\left\langle \mathbf{l}^{\mu} \left| \frac{\partial}{\partial r_{\alpha}} \right| \mathbf{l}^{\nu} \right\rangle = a_{\alpha}^{\nu} \langle \mathbf{l}^{\mu} | \mathbf{l}^{\nu} - \mathbf{1}_{\alpha} \rangle - i k_{\alpha}^{\nu} \langle \mathbf{l}^{\mu} | \mathbf{l}^{\nu} \rangle - 2\zeta_{\nu} \langle \mathbf{l}^{\mu} | \mathbf{l}^{\nu} + \mathbf{1}_{\alpha} \rangle, \quad (9.3.8)$$

$$\begin{aligned} \left\langle \mathbf{l}^{\mu} \left| \frac{\partial^2}{\partial r_{\alpha}^2} \right| \mathbf{l}^{\nu} \right\rangle &= a_{\alpha}^{\nu} (a_{\alpha}^{\nu} - 1) \langle \mathbf{l}^{\mu} | \mathbf{l}^{\nu} - \mathbf{2}_{\alpha} \rangle - 2i k_{\alpha}^{\nu} a_{\alpha}^{\nu} \langle \mathbf{l}^{\mu} | \mathbf{l}^{\nu} - \mathbf{1}_{\alpha} \rangle \\ & - [2\zeta_{\nu} (2a_{\alpha}^{\nu} + 1) + (k_{\alpha}^{\nu})^2] \langle \mathbf{l}^{\mu} | \mathbf{l}^{\nu} \rangle \\ & + 4i \zeta_{\nu} k_{\alpha}^{\nu} \langle \mathbf{l}^{\mu} | \mathbf{l}^{\nu} + \mathbf{1}_{\alpha} \rangle + 4\zeta_{\nu}^2 \langle \mathbf{l}^{\mu} | \mathbf{l}^{\nu} + \mathbf{2}_{\alpha} \rangle. \end{aligned} \quad (9.3.9)$$

The Einstein summation convention is not used in eq. (9.3.9). No mixed second derivatives are present in the kinetic energy operator. Finally, the orbital Zeeman integral in eq. (9.3.3) contains mixed multipole and derivative operators. However, due to the presence of the Levi-Civita symbol, only mixed operators with different Cartesian components are obtained. Thus, the resulting integrals are separated similarly to eq. (9.3.7) and require no further implementation.

A general outline of the algorithm responsible for the calculation of kinetic energy integrals is presented in fig. 9.3.1 as implemented into TURBOMOLE. It is capable to handle contracted basis functions and computes an entire shell batch of integrals simultaneously. In contrast to other implementations which use more general recursion schemes,^[32, 36] all individual contributions to the kinetic energy have been implemented manually here, which allows for discarding some negligible terms.

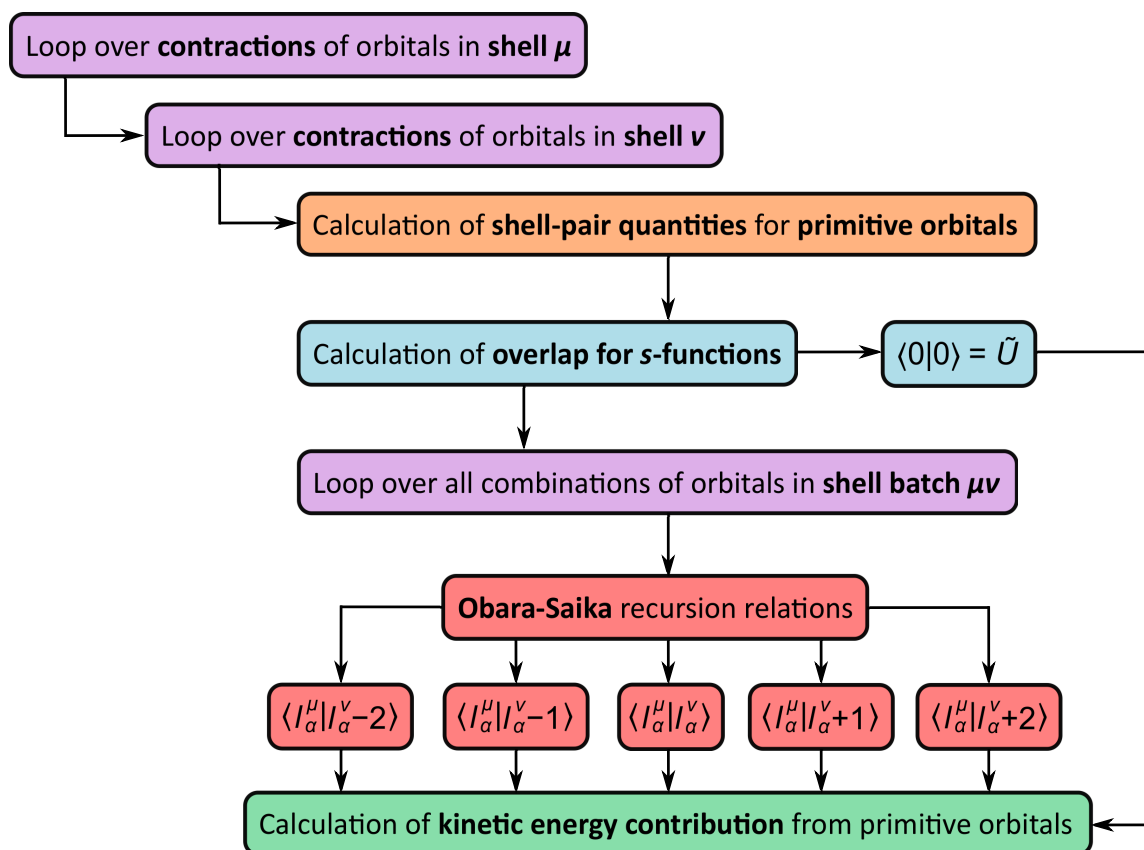


Figure 9.3.1.: Outline of the algorithm capable to calculate kinetic energy integrals in an external magnetic field over LAOs, including the additional orbital Zeeman and diamagnetic contributions. The algorithm can handle contracted basis functions. An entire shell batch of kinetic energy integrals is evaluated simultaneously.

9.3.2. Molecular Gradient

The calculation of molecular gradients requires the evaluation of kinetic energy integrals which include the derivative operator with respect to nuclear displacements:

$$\langle \mu | \hat{T} | \nu' \rangle = \langle \mu | \left(\frac{\hat{\mathbf{P}}^2}{2} + \frac{1}{2} \mathbf{B} \cdot \hat{\mathbf{I}}^{\mathbf{O}} + \frac{1}{8} [\mathbf{B}^2 (\hat{\mathbf{r}}^{\mathbf{O}})^2 - (\mathbf{B} \cdot \hat{\mathbf{r}}^{\mathbf{O}})^2] \right) \frac{\partial}{\partial R_{\alpha}^{\nu}} | \nu \rangle \rangle. \quad (9.3.10)$$

The resulting integrals become very lengthy.^[38] Due to the presence of second derivative operators for the canonical kinetic energy contribution, integrals of the form

$$\left\langle \mathbf{l}^{\mu} \left| \frac{\partial^2}{\partial r_{\alpha}^2} \frac{\partial}{\partial R_{\alpha}^{\nu}} \right| \mathbf{l}^{\nu} \right\rangle = - \left\langle \mathbf{l}^{\mu} \left| \frac{\partial^3}{\partial r_{\alpha}^3} \right| \mathbf{l}^{\nu} \right\rangle - \left\langle \mathbf{l}^{\mu} \left| \frac{\partial^2}{\partial r_{\alpha}^2} \frac{\partial}{\partial O_{\alpha}} \right| \mathbf{l}^{\nu} \right\rangle \quad (9.3.11)$$

have to be evaluated, where the translational invariance as introduced in eq. (8.3.8) has been invoked. The integral containing the third derivative with respect to an electron coordinate reads

$$\begin{aligned} \left\langle \mathbf{l}^{\mu} \left| \frac{\partial^3}{\partial r_{\alpha}^3} \right| \mathbf{l}^{\nu} \right\rangle &= a_{\alpha}^{\nu} (a_{\alpha}^{\nu} - 1) (a_{\alpha}^{\nu} - 2) \langle \mathbf{l}^{\mu} | \mathbf{l}^{\nu} - \mathbf{3}_{\alpha} \rangle \\ &\quad - 3i k_{\alpha}^{\nu} a_{\alpha}^{\nu} (a_{\alpha}^{\nu} - 1) \langle \mathbf{l}^{\mu} | \mathbf{l}^{\nu} - \mathbf{2}_{\alpha} \rangle \\ &\quad - 3a_{\alpha}^{\nu} (2\zeta_{\nu} a_{\alpha}^{\nu} + (k_{\alpha}^{\nu})^2) \langle \mathbf{l}^{\mu} | \mathbf{l}^{\nu} - \mathbf{1}_{\alpha} \rangle \\ &\quad + i k_{\alpha}^{\nu} [6\zeta_{\nu} (2a_{\alpha}^{\nu} + 1) + (k_{\alpha}^{\nu})^2] \langle \mathbf{l}^{\mu} | \mathbf{l}^{\nu} \rangle \\ &\quad + 6\zeta_{\nu} [2(a_{\alpha}^{\nu} + 1) + (k_{\alpha}^{\nu})^2] \langle \mathbf{l}^{\mu} | \mathbf{l}^{\nu} + \mathbf{1}_{\alpha} \rangle \\ &\quad - 12i \zeta_{\nu}^2 k_{\alpha}^{\nu} \langle \mathbf{l}^{\mu} | \mathbf{l}^{\nu} + \mathbf{2}_{\alpha} \rangle \\ &\quad - 8\zeta_{\nu}^3 \langle \mathbf{l}^{\mu} | \mathbf{l}^{\nu} + \mathbf{3}_{\alpha} \rangle, \end{aligned} \quad (9.3.12)$$

and includes all overlap integrals with their angular momentum quantum number decreased and increased up to three times. The algorithm for the calculation of kinetic energy integrals presented in fig. 9.3.1 can to be modified in two steps to calculate kinetic energy integral contributions for the molecular gradient. Firstly, additional overlap integrals of the set $\{ \langle l_{\alpha}^{\mu} | l_{\alpha}^{\nu} - 3 \rangle, \langle l_{\alpha}^{\mu} | l_{\alpha}^{\nu} + 3 \rangle \}$ have to be calculated for every Cartesian component. Secondly, the final integrals are evaluated as linear combinations of the overlap integrals as presented in Ref. [38]. Again, all contributions were implemented manually into TURBOMOLE, discarding all negligible terms.

9.4. Nuclear Attraction Integrals

9.4.1. Basic Integral

Nuclear attraction integrals cannot be calculated as a linear combination of overlap integrals. For the potential energy contribution from the interaction between an electron and nucleus I with coordinate \mathbf{R}_I , the integral over s -type LAOs reads:

$$\left\langle \mathbf{0} \left| \frac{1}{|\mathbf{r} - \mathbf{R}_I|} \right| \mathbf{0} \right\rangle = N_\mu N_\nu e^{-\sigma(\mathbf{R}^\nu - \mathbf{R}^\mu)^2} e^{-\zeta(\boldsymbol{\chi}^2 + 2i\mathbf{P} \cdot \boldsymbol{\chi})} \int_{-\infty}^{\infty} \frac{e^{-\zeta(\mathbf{r} - \tilde{\mathbf{P}})^2}}{|\mathbf{r} - \mathbf{R}_I|} d\mathbf{r}. \quad (9.4.1)$$

The Coulomb operator $|\mathbf{r} - \mathbf{R}_I|^{-1}$ can be rewritten in terms of its Laplace transform^[356]

$$\frac{1}{|\mathbf{r} - \mathbf{R}_I|} = \frac{2}{\sqrt{\pi}} \int_0^\infty e^{-u^2(\mathbf{r} - \mathbf{R}_I)^2} du, \quad (9.4.2)$$

and consequently, the integral in eq. (9.4.1) may be expressed in terms of a double integral. Using the Gaussian product theorem, it may be split into a contribution depending on the electron coordinate and one which does not:^[351]

$$\int_{-\infty}^{\infty} \frac{e^{-\zeta(\mathbf{r} - \tilde{\mathbf{P}})^2}}{|\mathbf{r} - \mathbf{R}_I|} d\mathbf{r} = \frac{2}{\sqrt{\pi}} \int_0^\infty \int_{-\infty}^{\infty} e^{-\zeta(\mathbf{r} - \tilde{\mathbf{P}})^2} e^{-u^2(\mathbf{r} - \mathbf{R}_I)^2} d\mathbf{r} du \quad (9.4.3)$$

$$= \frac{2}{\sqrt{\pi}} \int_0^\infty e^{-\frac{\zeta u^2}{\zeta + u^2}(\tilde{\mathbf{P}} - \mathbf{R}_I)^2} \int_{-\infty}^{\infty} e^{-(\zeta + u^2)(\mathbf{r} - \tilde{\mathbf{S}})^2} d\mathbf{r} du \quad (9.4.4)$$

As usual, the (complex-valued) point $\tilde{\mathbf{S}}$ is defined as a point on the line drawn between $\tilde{\mathbf{P}}$ and \mathbf{R}_I :^[351]

$$\tilde{\mathbf{S}} = \frac{\zeta \tilde{\mathbf{P}} + u^2 \mathbf{R}_I}{\zeta + u^2}. \quad (9.4.5)$$

The integration over \mathbf{r} is carried out as previously shown in eq. (9.1.10) for overlap integrals. The integration variable u may be replaced by

$$t^2 = \frac{u^2}{\zeta + u^2}, \quad (9.4.6)$$

which is evidently only defined in the interval $0 \leq t \leq 1$. After some trivial algebraic manipulations, we arrive at the final form of the nuclear attraction integral for s -type LAOs:^[36]

$$\left\langle \mathbf{0} \left| \frac{1}{|\mathbf{r} - \mathbf{R}_I|} \right| \mathbf{0} \right\rangle = 2\tilde{U}_P \sqrt{\frac{\zeta}{\pi}} \int_0^1 e^{-\zeta(\tilde{\mathbf{P}} - \mathbf{R}_I)^2 t^2} dt \quad (9.4.7)$$

9.4.2. Complex Molecular Boys Function

The integral on the right-hand side in eq. (9.4.7) belongs to a class of functions known as the molecular Boys function in the context of quantum chemistry:^[357]

$$F_m(z) = \int_0^1 t^{2m} e^{-zt^2} dt. \quad (9.4.8)$$

It is related to the error function and equivalent to a scaled version of Kummer's confluent hypergeometric function.^[36, 351] For complex arguments such as in the case of nuclear attraction integrals,

$$z = \zeta(\mathbf{P} - \mathbf{R}_I - i\boldsymbol{\chi})^2, \quad (9.4.9)$$

the Boys function itself becomes complex-valued. A stable algorithm for the evaluation of the Boys function capable of handling arbitrary complex arguments derived from Ref. [358] was implemented in the context of this work and published in collaboration with Klopper in Ref. [56]. It is reexamined here for arguments of $F_m(z)$ appearing the case of nuclear attraction integrals.

The Boys function's argument may be decomposed into a real and imaginary part:

$$\operatorname{Re}(z) = \zeta [(\mathbf{P} - \mathbf{R}_I)^2 - \boldsymbol{\chi}^2]; \quad (9.4.10)$$

$$\operatorname{Im}(z) = -2\zeta(\mathbf{P} - \mathbf{R}_I) \cdot \boldsymbol{\chi}. \quad (9.4.11)$$

It should be noted that since $(\mathbf{P} - \mathbf{R}_I)^2 \geq 0$, the real part of z may become negative if and only if

$$(\mathbf{P} - \mathbf{R}_I)^2 < \boldsymbol{\chi}^2. \quad (9.4.12)$$

Moreover, the imaginary part of z may become larger than the real part if $\mathbf{P} - \mathbf{R}_I \approx \boldsymbol{\chi}$, with purely imaginary arguments being not only possible, but frequent. As pointed out in Ref. [358], the evaluation of the Boys function becomes numerically unstable for cases where $\operatorname{Re}(z) < 0$. In such instances, it is beneficial to evaluate the auxiliary Boys function,^[358]

$$G_m(z) = \int_0^1 t^{2m} e^{-z(1-t^2)} dt, \quad (9.4.13)$$

instead, which guarantees numerical stability for $\operatorname{Re}(z) \leq 0$. It is related to the molecular Boys function through

$$F_m(z) = e^{-z} G_m(-z). \quad (9.4.14)$$

Thus, in cases of $\text{Re}(z) < 0$, the field-dependent part of \tilde{U}_P , denoted K_P in eq. (9.1.11), may be interwoven with the Boys function to generate the expression^[358]

$$e^{-\zeta(\mathbf{x}^2+2i\mathbf{P}\cdot\mathbf{x})} F_m(z) = e^{-\zeta[(\mathbf{P}-\mathbf{R}_I)^2+2i\mathbf{R}_I\cdot\mathbf{x}]} G_m(-z), \quad (9.4.15)$$

which is always numerically stable. Evaluating F_m through G_m is therefore convenient if $\text{Re}(z) < 0$. Furthermore, it should be noted that $F_m(z^*) = F_m^*(z)$, which implies that any algorithm for the computation of F_m can assume $\text{Im}(z) \geq 0$ without loss of generality.^[358]

Four different algorithms are used in the TURBOMOLE implementation for arguments corresponding to different parts of the complex plane, which is illustrated in fig. 9.4.1. For the asymptotic region of $\text{Re}(z) > 0$ in the blue-shaded area ($\text{Re}(z) > 40$ or $\text{Im}(z) > 40$), Ishida's F1 algorithm is used. For the yellow-shaded region ($0 \leq \text{Re}(z) \leq 40$ and $0 \leq \text{Im}(z) \leq 40$), a Taylor expansion is used according to Ishida's F3 algorithm. This requires pre-computed points on a grid, which were generated once using Ishida's F2 algorithm. However, as this algorithm quickly loses numerical accuracy, the grid points were evaluated in quadruple precision, so that double precision accuracy could be guaranteed.

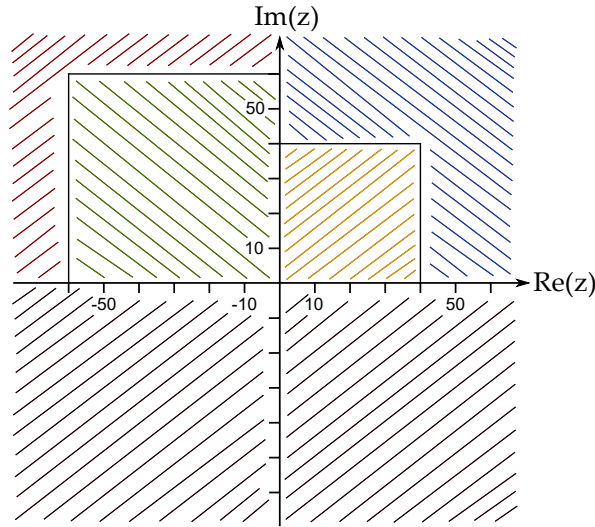


Figure 9.4.1.: Illustration for the different algorithms required to calculate the complex Boys function. The blue- and red-shaded areas use asymptotic approximations (Ishida's F1 and G1 algorithms), while a Taylor series employing a pre-computed grid is used for the yellow- and green-shaded regions (Ishida's F3 and G3 algorithms).^[358] The black-shaded area is evaluated using the function's axial symmetry: $F_m(z^*) = F_m^*(z)$. Reprinted with permission from Ref. [56]

For negative real parts of z , the auxiliary Boys function is evaluated instead. In the red-shaded area ($\text{Re}(z) < -60$ or $\text{Im}(z) > 60$), an asymptotic approximation is chosen, which requires Ishida's G1 algorithm. In the green-shaded area ($0 > \text{Re}(z) \geq -60$ and $0 \leq \text{Im}(z) \leq 60$), Ishida's G3 algorithm is employed, using a Taylor expansion similarly to the previously mentioned F3 algorithm for arguments with positive real part. Again, these points were pre-computed in quadruple precision using Ishida's F2 algorithm and then stored in double precision. The entire program was carefully tested regarding its numerical stability and accuracy, yielding double precision accuracy for all cases.

9.4.3. Obara–Saika Recurrence Relations

Using the definition of the complex Boys function, it is now possible to derive a set of Obara–Saika recurrence relations for nuclear attraction integrals. For the sake of brevity, the short-hand notation for the nuclear attraction operator,

$$\hat{V}_I = \frac{1}{|\mathbf{r} - \mathbf{R}_I|}, \quad (9.4.16)$$

is introduced. The OS recurrence relations require auxiliary integrals over s -type LAOs which can be calculated according to^[36, 358]

$$\langle \mathbf{0} | \hat{V}_I | \mathbf{0} \rangle^{(m)} = 2 U_P \sqrt{\frac{\zeta}{\pi}} e^{-\zeta(\mathbf{x}^2 + 2i\mathbf{P} \cdot \mathbf{x})} F_m(z); \quad (9.4.17)$$

$$= 2 U_P \sqrt{\frac{\zeta}{\pi}} e^{-\zeta[(\mathbf{P} - \mathbf{R}_I)^2 + 2i\mathbf{R}_I \cdot \mathbf{x}]} G_m(-z), \quad (9.4.18)$$

using eq. (9.4.17) if $\text{Re}(z) \geq 0$ and eq. (9.4.18) otherwise. Horizontal recurrence relations can be derived equivalently to overlap integrals and they read:

$$\langle \mathbf{I}^\mu + \mathbf{1}_\alpha | \hat{V}_I | \mathbf{I}^\mu \rangle^{(m)} = \langle \mathbf{I}^\mu | \hat{V}_I | \mathbf{I}^\nu + \mathbf{1}_\alpha \rangle^{(m)} + (R_\alpha^\nu - R_\alpha^\mu) \langle \mathbf{I}^\mu | \hat{V}_I | \mathbf{I}^\nu \rangle^{(m)}. \quad (9.4.19)$$

Translational recurrence relations require not only the displacement of both nuclei the LAOs are centered on and the gauge origin, but also the center of charge in the operator:

$$\left(\frac{\partial}{\partial R_\alpha^\mu} + \frac{\partial}{\partial R_\alpha^\nu} + \frac{\partial}{\partial O_\alpha} + \frac{\partial}{\partial R_{I\alpha}} \right) \langle \mathbf{I}^\mu | \hat{V}_I | \mathbf{I}^\nu \rangle^{(m)} = 0. \quad (9.4.20)$$

Using the derivative of the Boys function with respect to its argument,^[36, 358]

$$\frac{\partial F_m(z)}{\partial z} = -F_{m+1}(z), \quad (9.4.21)$$

as well as the chain rule of derivatives, the OS recurrence relations may then be derived similarly to those obtained for overlap integrals:^[36]

$$\begin{aligned} \langle \mathbf{l}^\mu | \hat{V}_I | \mathbf{l}^\nu + \mathbf{1}_\alpha \rangle^{(m)} &= (\tilde{P}_\alpha - R_\alpha^\nu) \langle \mathbf{l}^\mu | \hat{V}_I | \mathbf{l}^\nu \rangle^{(m)} - (\tilde{P}_\alpha - R_{I\alpha}) \langle \mathbf{l}^\mu | \hat{V}_I | \mathbf{l}^\nu \rangle^{(m+1)} \\ &+ \frac{a_\alpha^\mu}{2\zeta} \left[\langle \mathbf{l}^\mu - \mathbf{1}_\alpha | \hat{V}_I | \mathbf{l}^\nu \rangle^{(m)} - \langle \mathbf{l}^\mu - \mathbf{1}_\alpha | \hat{V}_I | \mathbf{l}^\nu \rangle^{(m+1)} \right] \\ &+ \frac{a_\alpha^\nu}{2\zeta} \left[\langle \mathbf{l}^\mu | \hat{V}_I | \mathbf{l}^\nu - \mathbf{1}_\alpha \rangle^{(m)} - \langle \mathbf{l}^\mu | \hat{V}_I | \mathbf{l}^\nu - \mathbf{1}_\alpha \rangle^{(m+1)} \right] \end{aligned} \quad (9.4.22)$$

$$\begin{aligned} \langle \mathbf{l}^\mu + \mathbf{1}_\alpha | \hat{V}_I | \mathbf{l}^\mu \rangle^{(m)} &= (\tilde{P}_\alpha - R_\alpha^\mu) \langle \mathbf{l}^\mu | \hat{V}_I | \mathbf{l}^\nu \rangle^{(m)} - (\tilde{P}_\alpha - R_{I\alpha}) \langle \mathbf{l}^\mu | \hat{V}_I | \mathbf{l}^\nu \rangle^{(m+1)} \\ &+ \frac{a_\alpha^\mu}{2\zeta} \left[\langle \mathbf{l}^\mu - \mathbf{1}_\alpha | \hat{V}_I | \mathbf{l}^\nu \rangle^{(m)} - \langle \mathbf{l}^\mu - \mathbf{1}_\alpha | \hat{V}_I | \mathbf{l}^\nu \rangle^{(m+1)} \right] \\ &+ \frac{a_\alpha^\nu}{2\zeta} \left[\langle \mathbf{l}^\mu | \hat{V}_I | \mathbf{l}^\nu - \mathbf{1}_\alpha \rangle^{(m)} - \langle \mathbf{l}^\mu | \hat{V}_I | \mathbf{l}^\nu - \mathbf{1}_\alpha \rangle^{(m+1)} \right] \end{aligned} \quad (9.4.23)$$

In contrast to overlap integrals, nuclear attraction integrals cannot be decomposed according to their Cartesian components.^[38] Consequently, the OS recurrence relations as well as the HRR have to be applied subsequently. A total number of $m = |\mathbf{l}^\mu| + |\mathbf{l}^\nu| + 1$ auxiliary integrals over s -type LAOs have to be evaluated.

For field-free cases, nuclear attraction integrals are implemented into TURBOMOLE using numerical integration schemes. The algorithm implemented in the context of this work uses OS recurrence relations. The integral wrapper is similar to that used for overlap and kinetic energy integrals as presented in fig. 9.3.1. It is capable of handling contracted basis functions and evaluates an entire shell batch $\mu\nu$. Auxiliary integrals over s -type LAOs are calculated using the complex molecular Boys function, which requires access to the pre-computed values on a grid as described in sec. 9.4.2.

The subsequent application of OS recurrence relations and HRR is illustrated in fig. 9.4.2 for the example of a nuclear attraction integral over orbitals with angular momentum quantum numbers $\mathbf{l}^\mu = (2, 3, 1)^\top$ and $\mathbf{l}^\nu = (1, 3, 1)^\top$. The $|\mathbf{l}^\mu| + |\mathbf{l}^\nu| + 1 = 12$ auxiliary integrals (blue) are calculated using either eq. (9.4.17) or (9.4.18). A total number of $l_x^\mu + l_x^\nu = 3$ VRR steps (red) are applied for the x direction, thereby reducing

the required number of auxiliary integrals (m) by one per VRR step. The simplified OS recurrence relation for $\mathbf{I}^\nu = 0$ is used:

$$\begin{aligned} \langle \mathbf{1}^\mu + \mathbf{1}_\alpha | \hat{V}_I | \mathbf{0} \rangle^{(m)} &= (\tilde{P}_\alpha - R_\alpha^\mu) \langle \mathbf{1}^\mu | \hat{V}_I | \mathbf{0} \rangle - (\tilde{P}_\alpha - R_{I\alpha}) \langle \mathbf{1}^\mu | \hat{V}_I | \mathbf{0} \rangle^{(m+1)} \\ &+ \frac{a_\alpha^\mu}{2\zeta} \left[\langle \mathbf{1}^\mu - \mathbf{1}_\alpha | \hat{V}_I | \mathbf{0} \rangle^{(m)} - \langle \mathbf{1}^\mu - \mathbf{1}_\alpha | \hat{V}_I | \mathbf{0} \rangle^{(m+1)} \right]. \end{aligned} \quad (9.4.24)$$

In a following step, the HRR (yellow) is used on all resulting nine auxiliary integrals. The resulting integrals (purple) are used in the same procedure for the y -component of the angular momentum quantum number and, finally, the z -component.

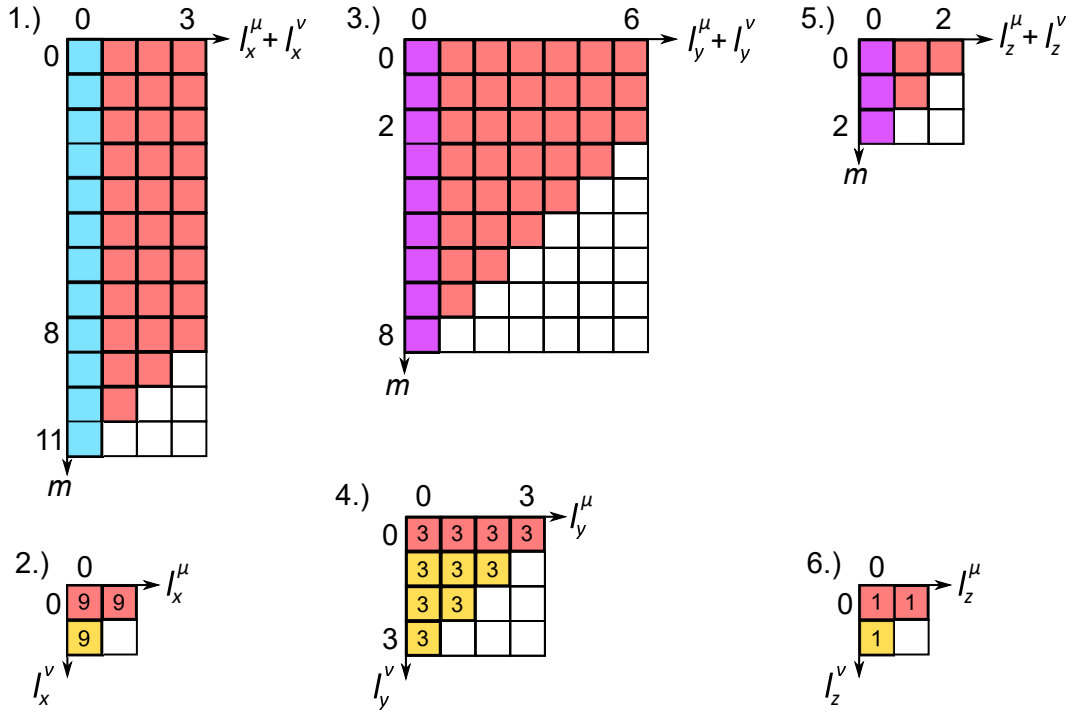


Figure 9.4.2.: Overview of algorithm using Obara–Saika and horizontal recurrence relations to evaluate nuclear attraction integrals. The procedure is shown for the example of angular momentum quantum numbers $\mathbf{I}^\mu = (2, 3, 1)^\top$ and $\mathbf{I}^\nu = (1, 3, 1)^\top$. VRR (red) and HRR (yellow) steps are subsequently applied, first for the x -component (step 1 and 2), then for the y -component (step 3 and 4) and finally for the z -component (step 5 and 6). Blue squares symbolize the starting integrals over s -type LAOs. Purple squares symbolize the starting integrals as taken from a previous step of the procedure.

It should be mentioned, that the relevant arrays which store all auxiliary quantities are allocated at the very beginning of the integral evaluation process, that is, outside of the very first shell loop as shown, for instance, in fig. 8.2.2. During the procedure, all integrals are stored without gaps in memory and are referenced through an indexing technique, allowing for an efficient usage of computational resources.

9.4.4. Molecular Gradient

For the calculation of molecular gradients, both the Pulay contributions of nuclear attraction integrals, as well as the Hellman–Feynman contributions, have to be computed.^[359–363] While the calculation of the former is relatively straightforward

$$\begin{aligned} \langle \mu | \hat{V}_I | \nu' \rangle &= -a_\alpha^\nu \langle \mathbf{1}^\mu | \hat{V}_I | \mathbf{1}^\nu - \mathbf{1}_\alpha \rangle + ik_\alpha^\nu \langle \mathbf{1}^\mu | \hat{V}_I | \mathbf{1}^\nu \rangle \\ &+ 2\zeta_\nu \langle \mathbf{1}^\mu | \hat{V}_I | \mathbf{1}^\nu + \mathbf{1}_\alpha \rangle + \frac{i}{2} \varepsilon_{\alpha\beta\gamma} B_\beta \langle \mathbf{1}^\mu | \hat{V}_I | \mathbf{1}^\nu + \mathbf{1}_\gamma \rangle, \end{aligned} \quad (9.4.25)$$

and requires the same contributions already discussed for overlap integrals in sec. 9.2.4, the latter are typically calculated by invoking translational invariance.^[364, 365] This is no longer possible for integrals over LAOs as they are also dependent on the gauge origin and thus the contribution has to be evaluated directly. The evaluation of the Hellmann–Feynman contribution was recently presented in Ref. [38] for an integral evaluation scheme using London Hermite Gaussian functions. In this work, the Obara–Saika recurrence relations presented for real-valued AOs in Ref. [354] is used instead. The modifications for complex-valued LAOs have been derived and implemented in the context of this work and have not yet been published.

The auxiliary integrals over s -type LAOs may be calculated according to:

$$\langle \mathbf{0} | \hat{V}'_I | \mathbf{0} \rangle^{(m)} = 2(\tilde{P}_\alpha - R_{I\alpha}) \langle \mathbf{0} | \hat{V}_I | \mathbf{0} \rangle^{(m+1)}; \quad (9.4.26)$$

a result which can be easily obtained through application of the chain rule of derivatives into the definition of the original nuclear attraction integral in eq. (9.4.17),

$$\langle \mathbf{0} | \hat{V}'_I | \mathbf{0} \rangle^{(m)} = 2\tilde{U}_P \sqrt{\frac{\zeta}{\pi}} \frac{\partial F_m(z)}{\partial z} \frac{\partial z}{\partial R_{I\alpha}}, \quad (9.4.27)$$

and by additionally using eq. (9.4.9) as well as (9.4.21), respectively. The resulting VRR can be derived as usual by invoking translational invariance regarding the

displacement of all nuclei involved, as well as the gauge origin:

$$\left(\frac{\partial}{\partial R_\alpha^\mu} + \frac{\partial}{\partial R_\alpha^\nu} + \frac{\partial}{\partial O_\alpha} + \frac{\partial}{\partial R_{I\alpha}} \right) \langle \mathbf{I}^\mu | \hat{V}'_I | \mathbf{I}^\nu \rangle^{(m)} = 0. \quad (9.4.28)$$

HRR may be applied similarly to regular nuclear attraction integrals. They are presented here for the sake of completeness:

$$\langle \mathbf{I}^\mu + \mathbf{1}_\alpha | \hat{V}'_I | \mathbf{I}^\mu \rangle^{(m)} = \langle \mathbf{I}^\mu | \hat{V}'_I | \mathbf{I}^\nu + \mathbf{1}_\alpha \rangle^{(m)} + (R_\alpha^\nu - R_\alpha^\mu) \langle \mathbf{I}^\mu | \hat{V}'_I | \mathbf{I}^\nu \rangle^{(m)}. \quad (9.4.29)$$

The OS recurrence relations for Hellmann–Feynman integrals over complex-valued LAOs read:

$$\begin{aligned} \langle \mathbf{I}^\mu | \hat{V}'_I | \mathbf{I}^\nu + \mathbf{1}_\alpha \rangle^{(m)} &= (\tilde{P}_\alpha - R_\alpha^\nu) \langle \mathbf{I}^\mu | \hat{V}'_I | \mathbf{I}^\nu \rangle^{(m)} - (\tilde{P}_\alpha - R_{I\alpha}) \langle \mathbf{I}^\mu | \hat{V}'_I | \mathbf{I}^\nu \rangle^{(m+1)} \\ &\quad + \frac{a_\alpha^\mu}{2\zeta} \left[\langle \mathbf{I}^\mu - \mathbf{1}_\alpha | \hat{V}'_I | \mathbf{I}^\nu \rangle^{(m)} - \langle \mathbf{I}^\mu - \mathbf{1}_\alpha | \hat{V}'_I | \mathbf{I}^\nu \rangle^{(m+1)} \right] \\ &\quad + \frac{a_\alpha^\nu}{2\zeta} \left[\langle \mathbf{I}^\mu | \hat{V}'_I | \mathbf{I}^\nu - \mathbf{1}_\alpha \rangle^{(m)} - \langle \mathbf{I}^\mu | \hat{V}'_I | \mathbf{I}^\nu - \mathbf{1}_\alpha \rangle^{(m+1)} \right] \\ &\quad + \langle \mathbf{I}^\mu | \hat{V}'_I | \mathbf{I}^\nu \rangle^{(m+1)} \end{aligned} \quad (9.4.30)$$

$$\begin{aligned} \langle \mathbf{I}^\mu + \mathbf{1}_\alpha | \hat{V}'_I | \mathbf{I}^\mu \rangle^{(m)} &= (\tilde{P}_\alpha - R_\alpha^\mu) \langle \mathbf{I}^\mu | \hat{V}'_I | \mathbf{I}^\nu \rangle^{(m)} - (\tilde{P}_\alpha - R_{I\alpha}) \langle \mathbf{I}^\mu | \hat{V}'_I | \mathbf{I}^\nu \rangle^{(m+1)} \\ &\quad + \frac{a_\alpha^\mu}{2\zeta} \left[\langle \mathbf{I}^\mu - \mathbf{1}_\alpha | \hat{V}'_I | \mathbf{I}^\nu \rangle^{(m)} - \langle \mathbf{I}^\mu - \mathbf{1}_\alpha | \hat{V}'_I | \mathbf{I}^\nu \rangle^{(m+1)} \right] \\ &\quad + \frac{a_\alpha^\nu}{2\zeta} \left[\langle \mathbf{I}^\mu | \hat{V}'_I | \mathbf{I}^\nu - \mathbf{1}_\alpha \rangle^{(m)} - \langle \mathbf{I}^\mu | \hat{V}'_I | \mathbf{I}^\nu - \mathbf{1}_\alpha \rangle^{(m+1)} \right] \\ &\quad + \langle \mathbf{I}^\mu | \hat{V}'_I | \mathbf{I}^\nu \rangle^{(m+1)} \end{aligned} \quad (9.4.31)$$

Thus, during the evaluation of Hellmann–Feynman integrals, the original nuclear attraction integrals need to be considered as well. The algorithm capable of evaluating the OS for Hellmann–Feynman integrals over LAOs works very similarly to the one presented in fig. 9.4.2, but requires auxiliary integrals of both types presented in eq. (9.4.17) and (9.4.27). Furthermore, the algorithm illustrated in fig. 9.4.2 has to be altered to evaluate Hellmann–Feynman integrals and nuclear potential integrals simultaneously, as the former require the latter in every step of the procedure.

9.5. Electron Repulsion Integrals

9.5.1. Four-Center Integrals

As previously discussed, the evaluation of four-center integrals is the most time-consuming step of the SCF procedure. Considerable effort has been put into finding efficient techniques for the computation of these integrals, and the resulting algorithms by McMurchie and Davidson^[366], Head-Gordon and Pople,^[353] as well as the Rys polynomial approach^[367] are considered standard approaches in modern quantum chemistry.^[351] All of these algorithms are discussed in the context of four-center integrals over complex LAOs in Ref. [36], which the interested reader is referred to. In this work, only the Head-Gordon–Pople algorithm was implemented for complex LAOs. In TURBOMOLE, this algorithm was already implemented for real-valued AOs and thus only needed to be altered in order to work for complex LAOs. The necessary modifications are described in this section.

Following the general structure of the wrapper preparing the integral evaluation over LAOs presented in fig. 8.2.2, the additional computation of shell-pair quantities for shell $\kappa\lambda$ is required. They are defined analogously to eq. (9.1.4) – (9.1.8) as:

$$\eta = \zeta_\kappa + \zeta_\lambda, \quad (9.5.1)$$

$$\tau = \eta^{-1} \zeta_\kappa \zeta_\lambda, \quad (9.5.2)$$

$$\mathbf{Q} = \eta^{-1} (\zeta_\kappa \mathbf{R}^\kappa + \zeta_\lambda \mathbf{R}^\lambda), \quad (9.5.3)$$

$$\mathbf{\Xi} = (4\eta)^{-1} \mathbf{B} \times (\mathbf{R}^\lambda - \mathbf{R}^\kappa), \quad (9.5.4)$$

$$\tilde{\mathbf{Q}} = \mathbf{Q} - i \mathbf{\Xi}. \quad (9.5.5)$$

The complex overlap of s -type LAOs is then defined equivalently to eq. (9.1.11) as:

$$\tilde{U}_Q = U_Q K_Q = N_\kappa N_\lambda e^{-\tau(\mathbf{R}^\lambda - \mathbf{R}^\kappa)^2} \left(\frac{\pi}{\eta} \right)^{3/2} e^{-\eta(\mathbf{\Xi}^2 + 2i \mathbf{Q} \cdot \mathbf{\Xi})}. \quad (9.5.6)$$

It should be noted that at this point, the batch of integrals can be screened by neglecting it if $|\tilde{U}_Q|$ is below a certain threshold,^[36] but preliminary studies have suggested that caution should be advised for complex LAOs.^[316, 352]

In addition to shell-pair quantities, a few shell-quartet quantities have to be calculated. The complex overlap of a shell-quartet of s -type LAOs is given by

$$\tilde{U}_{PQ} = \tilde{U}_P \tilde{U}_Q, \quad (9.5.7)$$

and the reduced exponent of both shell-pairs is defined as:

$$\vartheta = \frac{\zeta\eta}{\zeta + \eta}. \quad (9.5.8)$$

Following Ref. [36] and [354], the Coulomb operator may be expressed using the complex molecular Boys function, incorporating it into the integral similarly to its introduction for nuclear attraction integrals in sec. 9.4. The auxiliary integrals over s -type LAOs may then be calculated according to

$$(\mathbf{00}|\mathbf{00})^{(m)} = 2U_P U_Q \sqrt{\frac{\vartheta}{\pi}} e^{-\zeta(\mathbf{x}^2 + 2i\mathbf{P}\cdot\mathbf{x}) - \eta(\mathbf{\Xi}^2 + 2i\mathbf{Q}\cdot\mathbf{\Xi})} F_m(z), \quad (9.5.9)$$

$$= 2U_P U_Q \sqrt{\frac{\vartheta}{\pi}} e^{-\zeta(\mathbf{x}^2 + 2i\mathbf{P}\cdot\mathbf{x}) - \eta(\mathbf{\Xi}^2 + 2i\mathbf{Q}\cdot\mathbf{\Xi}) - \vartheta(\tilde{\mathbf{P}} - \tilde{\mathbf{Q}})^2} G_m(-z), \quad (9.5.10)$$

with the argument of the Boys function being

$$z = \vartheta(\tilde{\mathbf{P}} - \tilde{\mathbf{Q}})^2. \quad (9.5.11)$$

Again, eq. (9.5.9) is used for arguments of the Boys function with a positive real part ($\text{Re}(z) \geq 0$), while eq. (9.5.10) is used otherwise. This guarantees numerical stability for arbitrary arguments of the Boys function.

The Head-Gordon–Pople algorithm subsequently performs VRR steps, first for index μ with all other indices being held at zero. It counts up to $|\mathbf{I}^\mu + \mathbf{I}^\nu|$.

$$\begin{aligned} (\mathbf{I}^\mu + \mathbf{1}_\alpha \mathbf{0}|\mathbf{00})^{(m)} &= (\tilde{P}_\alpha - R_\alpha^\mu)(\mathbf{I}^\mu \mathbf{0}|\mathbf{00})^{(m)} - \frac{\vartheta}{\zeta}(\tilde{P}_\alpha - \tilde{Q}_\alpha)(\mathbf{I}^\mu \mathbf{0}|\mathbf{00})^{(m+1)} \\ &+ \frac{a_\alpha^\mu}{2\zeta} \left[(\mathbf{I}^\mu - \mathbf{1}_\alpha \mathbf{0}|\mathbf{00})^{(m)} - \frac{\vartheta}{\zeta}(\mathbf{I}^\mu - \mathbf{1}_\alpha \mathbf{0}|\mathbf{00})^{(m+1)} \right] \end{aligned} \quad (9.5.12)$$

Second, index κ is being raised using the respective OS recurrence relations, counting up to $|\mathbf{I}^\kappa + \mathbf{I}^\lambda|$:

$$\begin{aligned} (\mathbf{I}^\mu \mathbf{0}|\mathbf{I}^\kappa + \mathbf{1}_\alpha \mathbf{0})^{(m)} &= (\tilde{Q}_\alpha - R_\alpha^\kappa)(\mathbf{I}^\mu \mathbf{0}|\mathbf{I}^\kappa \mathbf{0})^{(m)} + \frac{\vartheta}{\eta}(\tilde{P}_\alpha - \tilde{Q}_\alpha)(\mathbf{I}^\mu \mathbf{0}|\mathbf{I}^\kappa \mathbf{0})^{(m+1)} \\ &+ \frac{a_\alpha^\kappa}{2\eta} \left[(\mathbf{I}^\mu \mathbf{0}|\mathbf{I}^\kappa - \mathbf{1}_\alpha \mathbf{0})^{(m)} - \frac{\vartheta}{\eta}(\mathbf{I}^\mu \mathbf{0}|\mathbf{I}^\kappa - \mathbf{1}_\alpha \mathbf{0})^{(m+1)} \right] \\ &+ \frac{a_\alpha^\mu}{2(\zeta + \eta)}(\mathbf{I}^\mu - \mathbf{1}_\alpha \mathbf{0}|\mathbf{I}^\kappa \mathbf{0})^{(m+1)} \end{aligned} \quad (9.5.13)$$

Finally, HRR steps are applied, first for ν , then for λ :

$$(\mathbf{1}^\mu \mathbf{1}^\nu + \mathbf{1}_\alpha | \mathbf{1}^\kappa \mathbf{0})^{(m)} = (\mathbf{1}^\mu + \mathbf{1}_\alpha \mathbf{1}^\nu | \mathbf{1}^\kappa \mathbf{0})^{(m)} + (R_\alpha^\mu - R_\alpha^\nu) (\mathbf{1}^\mu \mathbf{1}^\nu | \mathbf{1}^\kappa \mathbf{0})^{(m)} \quad (9.5.14)$$

$$(\mathbf{1}^\mu \mathbf{1}^\nu | \mathbf{1}^\kappa \mathbf{1}^\lambda + \mathbf{1}_\alpha)^{(m)} = (\mathbf{1}^\mu \mathbf{1}^\nu | \mathbf{1}^\kappa + \mathbf{1}_\alpha \mathbf{1}^\lambda)^{(m)} + (R_\alpha^\kappa - R_\alpha^\lambda) (\mathbf{1}^\mu \mathbf{1}^\nu | \mathbf{1}^\kappa \mathbf{1}^\lambda)^{(m)} \quad (9.5.15)$$

These HRR steps do not reference the exponents of either shell-pair or the shell-quartet. Therefore, they can be applied outside of the loops taking care of basis set contractions. This makes the use of contracted basis sets particularly efficient if the Head-Gordon–Pople algorithm is employed.

This procedure is almost identical for integrals over AOs and LAOs. To summarize, the three necessary changes, which have to be introduced into code capable of computing four-center integrals over real-valued AOs, are highlighted here again. Firstly, two additional shell-pair quantities have to be calculated, $\boldsymbol{\chi}$ and $\boldsymbol{\Xi}$, corresponding to the imaginary parts of the respective center of charges \mathbf{P} and \mathbf{Q} . Their definitions are given in eqs. (9.1.7) and (9.5.4). Secondly, the program needs to calculate auxiliary integrals using the complex molecular Boys function $F_m(z) \in \mathbb{C}$. To ensure numerical stability, the two cases $\text{Re}(z) \geq 0$ and $\text{Re}(z) < 0$ have to be distinguished, with the latter requiring the evaluation of the auxiliary Boys function $G_m(-z)$ instead. Thirdly, during the OS recurrence relations, only the following two replacements have to be introduced:

$$\mathbf{P} \rightarrow \mathbf{P} - i \boldsymbol{\chi} \quad (9.5.16)$$

$$\mathbf{Q} \rightarrow \mathbf{Q} - i \boldsymbol{\Xi} \quad (9.5.17)$$

Most variables in the code have to be set to complex variables instead of real-valued ones, with the notable exception of the three exponents ζ, η, ϑ .

9.5.2. Molecular Gradient

The analytical calculation of molecular gradients requires the evaluation of four-center integrals which include the derivatives of LAOs with respect to nuclear displacements. Analogously to the derivative of overlap integrals (see eq. (9.2.15) for reference), such a derivative may be defined for four-center integrals as:

$$\begin{aligned} (\mu\nu | \kappa \lambda') &= -a_\alpha^\lambda (\mathbf{1}^\mu \mathbf{1}^\nu | \mathbf{1}^\kappa \mathbf{1}^\lambda - \mathbf{1}_\alpha) + ik_\alpha^\lambda (\mathbf{1}^\mu \mathbf{1}^\nu | \mathbf{1}^\kappa \mathbf{1}^\lambda) \\ &\quad + 2\zeta_\lambda (\mathbf{1}^\mu \mathbf{1}^\nu | \mathbf{1}^\kappa \mathbf{1}^\lambda + \mathbf{1}_\alpha) + \frac{i}{2} \varepsilon_{\alpha\beta\gamma} B_\beta (\mathbf{1}^\mu \mathbf{1}^\nu | \mathbf{1}^\kappa \mathbf{1}^\lambda + \mathbf{1}_\gamma), \end{aligned} \quad (9.5.18)$$

and equivalently for the derivatives of the other three basis functions. In contrast to four-center integrals over real-valued AOs, translational invariance with respect to the displacement of all four nuclei cannot be invoked:

$$(\mu'\nu|\kappa\lambda) + (\mu\nu'|\kappa\lambda) + (\mu\nu|\kappa'\lambda) + (\mu\nu|\kappa\lambda') \neq 0. \quad (9.5.19)$$

Rather, the displacement of all functions with respect to the gauge origin also has to be taken into account, leading to the following relation for translational invariance:

$$\left(\frac{\partial}{\partial R_\alpha^\mu} + \frac{\partial}{\partial R_\alpha^\nu} + \frac{\partial}{\partial R_\alpha^\kappa} + \frac{\partial}{\partial R_\alpha^\lambda} + \frac{\partial}{\partial O_\alpha} \right) (\mu\nu|\kappa\lambda) = 0. \quad (9.5.20)$$

The general workflow for the calculation of derivatives of four-center integrals is different for real-valued AOs and complex-valued LAOs. Both cases are illustrated in fig. 9.5.1, emphasizing on what kind of integrals have to be evaluated for the derivatives. In the case of LAOs, roughly 4/3 more integrals have to be evaluated. Due to an additional factor of two from the lowered permutational symmetry and a factor of four from the use of complex algebra, the calculation of these integrals is at least about eleven times more expensive for LAOs. Since this integral evaluation is the most time-consuming step for the computation of molecular gradients with HF and DFT, this implies that the evaluation of the gradient itself is at least about eleven times more computationally demanding compared to the field-free case.

On the left-hand side of fig. 9.5.1, the workflow of an algorithm calculating derivatives of four-center integrals for AOs is presented. Using translational invariance, the calculation of certain integrals can be avoided.^[368] Derivatives with respect to a certain Cartesian component α only require those integrals where the identical component is raised or lowered. Since the molecular gradient requires derivatives with respect to all Cartesian components, this does not mean that any integrals can be neglected, but the entire algorithm is generally more streamlined.

The workflow of an algorithm which calculates the derivatives of four-center integrals for LAOs is presented on the right-hand side of fig. 9.5.1. Derivatives of four-center integrals over LAOs require the additional calculation of four-center integrals where no component was increased or decreased. No translational invariance can be invoked, and thus also the derivatives with respect to orbital λ have to be explicitly calculated. Due to the presence of the last term in eq. (9.5.18), the derivative with respect to the nuclear displacement in any Cartesian component requires the integrals with all increased Cartesian components. Thus, the algorithm first evaluates all integrals with

decreased, unaltered, and increased angular momentum numbers, which are stored in memory in batches. In the next step, the final integrals are computed through the use of a specially constructed sorting algorithm.

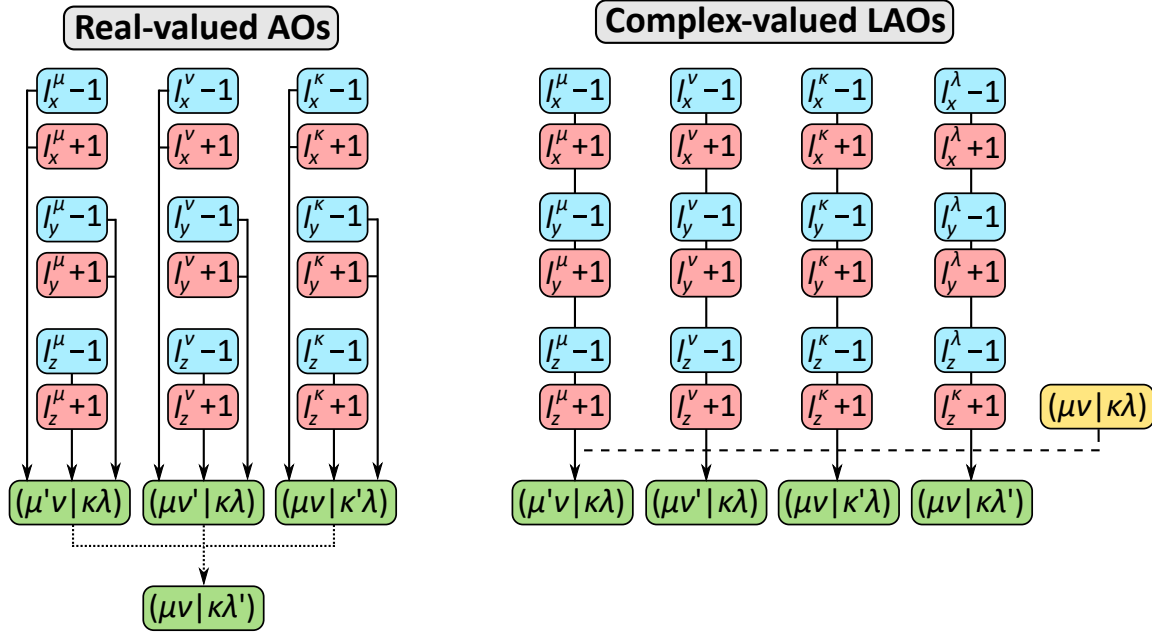


Figure 9.5.1.: General workflow for the calculation of derivatives of four-center integrals, both for real-valued AOs (left) and complex-valued LAOs. The integrals with one angular momentum quantum number decreased (blue) and increased (red) are required in both cases. For LAOs, the unaltered (yellow) four-center integrals are additionally needed. Further, the derivative with respect to orbital λ can be obtained by invoking translational invariance (dotted line) for AOs, but not for LAOs.

9.5.3. Three-Center Integrals

Three-center integrals are required if the RI approximation is used. Their efficient evaluation was described for real-valued AOs in Ref. [322]. The necessary modifications for LAOs were derived during this work and published in collaboration with Klopper in Ref. [56]. Without loss of generality, it is possible to utilize real-valued GTOs denoted as

$$|P\rangle = \chi_P(\mathbf{r}) := |\mathbf{L}\rangle \quad (9.5.21)$$

for auxiliary basis functions.^[137] They ought not to be confused with the center of charge of shell-pair $\mu\nu$, which was previously defined by its position vector \mathbf{P} . The exponent of auxiliary basis functions shall be written as ρ , while it is centered at a point with position vector \mathbf{Q} . Finally, the overlap of an auxiliary function with itself, or more precisely its norm, may be defined as:

$$V_{\mathbf{Q}} = N_P \left(\frac{\pi}{\theta} \right)^{3/2}, \quad (9.5.22)$$

with N_P being the prefactor of $|P\rangle$, which is particularly relevant for contracted auxiliary basis sets. The reduced exponent for the shell-triplet can be expressed as:

$$\theta = \frac{\zeta\rho}{\zeta + \rho} \quad (9.5.23)$$

Auxiliary integrals may then be straightforwardly inferred from eq. (9.5.9) and (9.5.10) by replacing shell-pair $\kappa\lambda$ with the auxiliary basis function:

$$(\mathbf{00}|\mathbf{0})^{(m)} = 2 U_P V_{\mathbf{Q}} \sqrt{\frac{\theta}{\pi}} e^{-\zeta(\chi^2 + 2i\mathbf{P}\cdot\boldsymbol{\chi})} F_m(z), \quad (9.5.24)$$

$$= 2 U_P V_{\mathbf{Q}} \sqrt{\frac{\theta}{\pi}} e^{-\zeta(\chi^2 + 2i\mathbf{P}\cdot\boldsymbol{\chi}) - \theta(\tilde{\mathbf{P}} - \mathbf{R})^2} G_m(-z), \quad (9.5.25)$$

with the argument of the Boys function being

$$z = \theta(\tilde{\mathbf{P}} - \mathbf{Q})^2. \quad (9.5.26)$$

The resulting OS recurrence relations may be constructed similarly to their counterparts for four-center integrals as given in eqs. (9.5.12) – (9.5.14).^[56, 322] The VRR for the first index μ and the auxiliary index are defined as:

$$\begin{aligned} (\mathbf{I}^\mu + \mathbf{1}_\alpha \mathbf{0}|\mathbf{0})^{(m)} &= (\tilde{P}_\alpha - R_\alpha^\mu)(\mathbf{I}^\mu \mathbf{0}|\mathbf{0})^{(m)} - \frac{\theta}{\zeta}(\tilde{P}_\alpha - Q_\alpha)(\mathbf{I}^\mu \mathbf{0}|\mathbf{0})^{(m+1)} \\ &+ \frac{a_\alpha^\mu}{2\zeta} \left[(\mathbf{I}^\mu - \mathbf{1}_\alpha \mathbf{0}|\mathbf{0})^{(m)} - \frac{\theta}{\zeta}(\mathbf{I}^\mu - \mathbf{1}_\alpha \mathbf{0}|\mathbf{0})^{(m+1)} \right]; \end{aligned} \quad (9.5.27)$$

$$\begin{aligned} (\mathbf{I}^\mu \mathbf{0}|\mathbf{L} + \mathbf{1}_\alpha)^{(m)} &= (Q_\alpha - R_\alpha^P)(\mathbf{I}^\mu \mathbf{0}|\mathbf{L})^{(m)} + \frac{\theta}{\rho}(\tilde{P}_\alpha - Q_\alpha)(\mathbf{I}^\mu \mathbf{0}|\mathbf{L})^{(m+1)} \\ &+ \frac{a_\alpha^P}{2\rho} \left[(\mathbf{I}^\mu \mathbf{0}|\mathbf{L} - \mathbf{1}_\alpha)^{(m)} - \frac{\theta}{\rho}(\mathbf{I}^\mu \mathbf{0}|\mathbf{L} - \mathbf{1}_\alpha)^{(m+1)} \right] \\ &+ \frac{a_\alpha^\mu \theta}{2\zeta\rho} (\mathbf{I}^\mu - \mathbf{1}_\alpha \mathbf{0}|\mathbf{L})^{(m+1)}. \end{aligned} \quad (9.5.28)$$

The second VRR can be significantly simplified in two steps. First, by realizing that $Q_\alpha = R_\alpha^P$, which follows directly from the definition of \mathbf{Q} given above. Therefore, the first term vanishes. Second, if the components of $|\mathbf{L}\rangle$ are transformed to spherical harmonics, the third and fourth term must eliminate one another, which is discussed in great detail in Ref. [322]. Thus, the second VRR may be conveniently simplified to:

$$(\mathbf{1}^\mu \mathbf{0} | \mathbf{L} + \mathbf{1}_\alpha)^{(m)} = \frac{\theta}{\rho} (\tilde{P}_\alpha - Q_\alpha) (\mathbf{1}^\mu \mathbf{0} | \mathbf{L})^{(m+1)} + \frac{a_\alpha^\mu \theta}{2\zeta\rho} (\mathbf{1}^\mu - \mathbf{1}_\alpha \mathbf{0} | \mathbf{L})^{(m+1)}. \quad (9.5.29)$$

Finally, the HRR are defined as usual and can be applied after shell contractions have been applied, making this procedure particularly efficient for highly contracted (auxiliary) basis sets:

$$(\mathbf{1}^\mu \mathbf{1}^\nu + \mathbf{1}_\alpha | \mathbf{L})^{(m)} = (\mathbf{1}^\mu + \mathbf{1}_\alpha \mathbf{1}^\nu | \mathbf{L})^{(m)} + (R_\alpha^\mu - R_\alpha^\nu) (\mathbf{1}^\mu \mathbf{1}^\nu | \mathbf{L})^{(m)} \quad (9.5.30)$$

It should be stressed that an existing code capable of handling the RI approximation for real-valued AOs only has to be modified in three steps:

1. The construction of the auxiliary integrals requires the inclusion of the complex phase factor K_P .
2. The argument of the Boys function becomes complex-valued and thus the Boys function has to be evaluated using the algorithm introduced in sec. 9.4.2.
3. The OS recursion remains identical if the center of charge is replaced through its complex-valued counterpart as shown in eq. (9.5.16), resulting in most quantities having to be labeled as complex.

10. Assessment of Accuracy and Efficiency

In the previous two chapters, the implementation of quantum chemical methods in finite magnetic fields was presented. Several schemes for the acceleration of calculations were introduced, and the efficient evaluation of molecular integrals was discussed. In particular, two approaches for the evaluation of two-electron integrals were presented. Firstly, the calculation of four-center integrals, which was found to be more intricate for LAOs due to a decreased permutational symmetry. Secondly, the use of the RI approximation, in which only three- and two-center integrals had to be evaluated. In this chapter, the accuracy and efficiency of the implemented quantum chemical methods is examined, with a focus on how well the RI approximation performs in strong magnetic fields.

Using a test set of 36 small to medium-sized molecules, the accuracy for the RI approximation is evaluated. For electronic ground states, the accuracy of RI is assessed in increasingly strong magnetic fields up to $|\mathbf{B}| = 1B_0$. An estimate on the approximate threshold, up to which RI can safely be used, is discussed. It should be noted that this discussion assumes the use of auxiliary basis sets parameterized for the field-free case. Furthermore, a similar assessment is presented for the use of RI in linear response methods, where magnetic fields of up to 10,000 T are used within this work.

After a brief discussion on the accuracy of linear response methods, the efficiency of the present implementation is assessed. Due to the previously mentioned problems with integral screening, no detailed benchmark study was carried out in the context of this thesis. However, exemplary calculations carried out on aromatic molecules are presented, in order to give a more general estimate on how much more computational cost is to be expected for calculations in finite magnetic fields, compared to the field free-case. The chapter concludes with a short presentation of the OpenMP parallelization, which was implemented for every integral evaluation routine presented in this work. Part of the results presented in this section were previously discussed by the author in Refs. [53], [54], and [56].

10.1. Molecules Used for Benchmark Calculations

A test set of 36 small to medium-sized molecules was used for benchmark calculations carried out in this chapter. The structural formulas of these molecules are depicted in fig. 10.2.1. This test set was introduced in Ref. [369], and also used for benchmark calculations in Refs. [53] and [54]. It consists of the following molecules: acetaldehyde (1), acetylene (2), CCl_2 (3), CClF (4), CF_2 (5), cyanoacetylene (6), cyanoformaldehyde (7), cyanogen (8), diacetylene (9), difluorodiazirine (10), formaldehyde (11), formic acid (12), formyl chloride (13), formyl fluoride (14), glyoxal (15), H_2C_3 (16), HCN (17), HCP (18), HNO (19), HPO (20), HPS (21), HSiF (22), isocyanogen (23), nitrosamine (24), nitrosylcyanide (25), phosgene (26), propynal (27), pyrazine (28), selenoformaldehyde (29), SiCl_2 (30), silylidene (31), tetrazine (32), thioformaldehyde (33), thioformylchloride (34), thionylcarbonylfluoride (35), and thiophosgene (36). Their respective numbers are used as abbreviations in later chapters.

10.2. Accuracy of the RI Approximation

10.2.1. Computational Methods

In this section, the accuracy of the RI approximation is assessed for electronic ground states and electronic excitations. Calculations were performed using the 36 molecules presented in fig. 10.2.1. For electronic ground states, these molecules were placed in a magnetic field of up to $|\mathbf{B}| = 1B_0$, which was always applied in the Cartesian z -direction. All calculations were carried out on the $\text{GHF}/\text{def2-TZVP}^{[370]}$ level of theory. For calculations employing the $\text{RI-}J$ and $\text{RI-}K$ approximation, the corresponding auxiliary def2-TZVP basis^[371, 372] was used. Calculations were always converged up to at least $10^{-9}E_h$. Only the lowest singlet state was considered, which becomes an excited state in stronger fields. For these cases, it was converged using a spin Zeeman scaling of $z = 0$.

For electronic excitations, the corresponding ground states were computed without use of the RI approximation. Two subsequent sets of linear response calculations were performed, one in which the RI approximation was used and one where it was not used. All calculations were carried out on the $\text{PBE0}^{[373]}/\text{def2-TZVP}$ level of theory with a corresponding def2-TZVP auxiliary basis^[157] parameterized for the use in correlated methods if the RI approximation was used. A large grid (grid 4)^[320] was used for the evaluation of the density functional part.

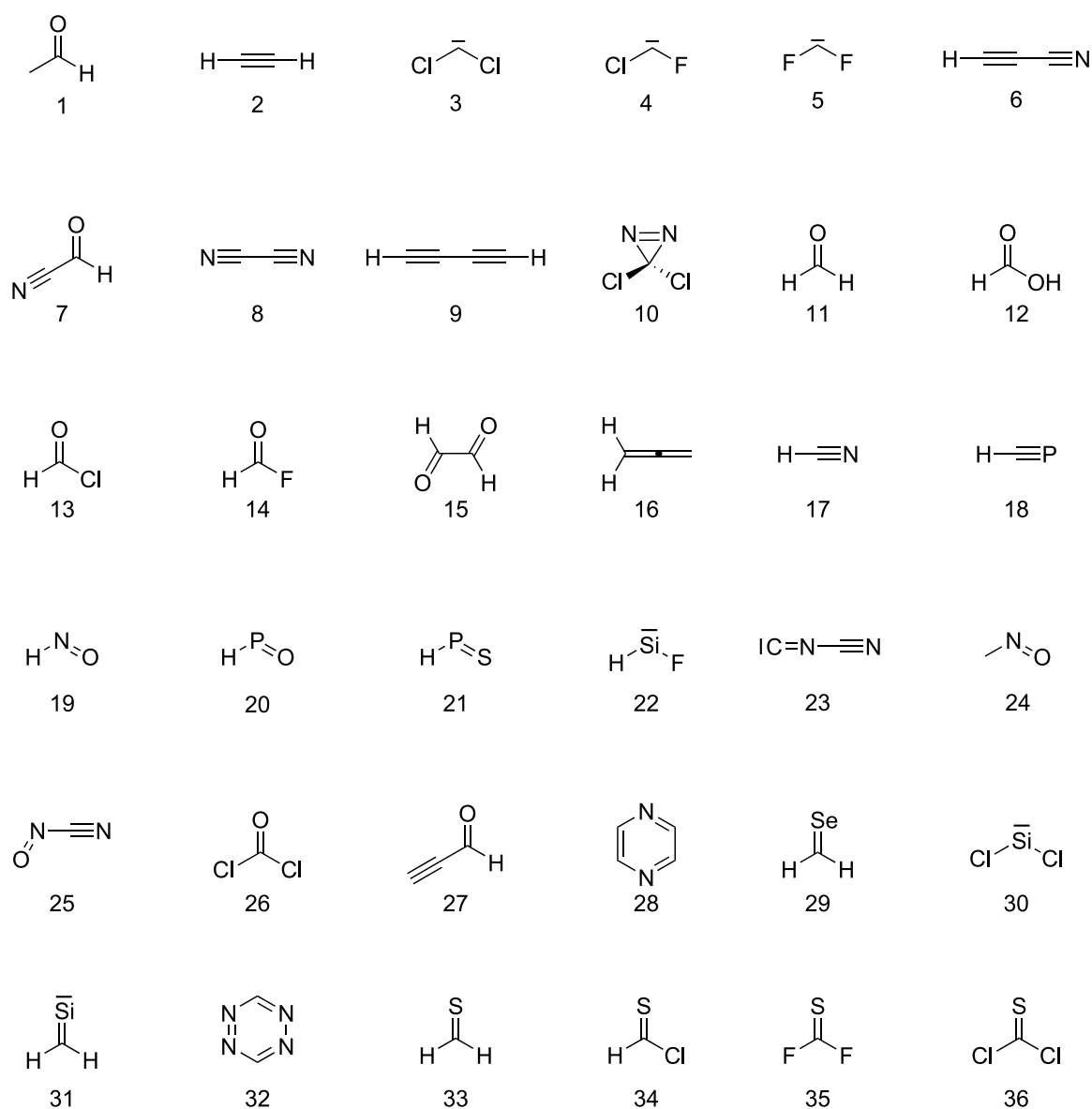


Figure 10.2.1.: Test set of 36 small molecules: acetaldehyde (1), acetylene (2), CCl_2 (3), CClF (4), CF_2 (5), cyanoacetylene (6), cyanoformaldehyde (7), cyanogen (8), diacetylene (9), difluorodiazirine (10), formaldehyde (11), formic acid (12), formyl chloride (13), formyl fluoride (14), glyoxal (15), H_2C_3 (16), HCN (17), HCP (18), HNO (19), HPO (20), HPS (21), HSiF (22), isocyanogen (23), nitrosamine (24), nitrosylcyanide (25), phosgene (26), propynal (27), pyrazine (28), selenoformaldehyde (29), SiCl_2 (30), silylidene (31), tetrazine (32), thioformaldehyde (33), thioformylchloride (34), thionylcarbonylfluoride (35), and thiophosgene (36). This test set was introduced in Ref. [369].

10.2.2. Electronic Ground States

First, the accuracy of the RI approximation for electronic ground states is assessed. This is relevant, because the auxiliary basis sets were optimized for the use in the absence of fields. Preliminary investigations on the lowest singlet state of methane and benzene were carried out by the author in Ref. [56], showing that the RI error increases non-linearly with the magnetic field strength. Here, a more detailed examination shall be given. Using both the RI- J and RI- K approximations for the 36 molecules within the test set yields errors which are depicted in fig. 10.2.2 for different magnetic field strengths of up to $|\mathbf{B}| = 1B_0$.

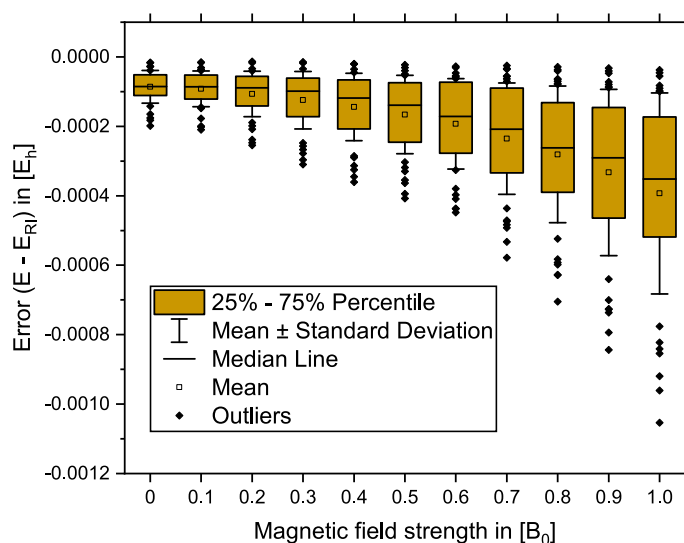


Figure 10.2.2.: Box plot presenting the error of the RI- JK approximation for a test set of 36 small to medium-sized molecules.^[369] All calculations were performed on the GHF/def2-TZVP level of theory. The straight line indicates the median, while the square represents the mean of the RI error. The orange colored box marks the 25–75th percentile, whiskers denote the mean \pm the standard deviation, and outliers are represented by diamonds.

Evidently, the RI error increases significantly in the presence of external magnetic fields. In the absence of a field, the mean error is $0.086 \text{ m}E_h$, while it increases to a mean of $0.393 \text{ m}E_h$ in a field of $|\mathbf{B}| = 1B_0$, which is almost five times larger. More significantly, the standard deviation also increases by a factor of more than six, from $0.046 \text{ m}E_h$ in the zero-field to $0.286 \text{ m}E_h$ in a field of $|\mathbf{B}| = 1B_0$. Maximum errors behave even more egregiously, with errors of over $1 \text{ m}E_h$ in the strongest investigated magnetic field.

The individual errors of RI- J and RI- K behave even more poorly, which is depicted in fig. 10.2.3. Thus, the combined use of RI- JK contains some error cancellation, even in the absence of a field.

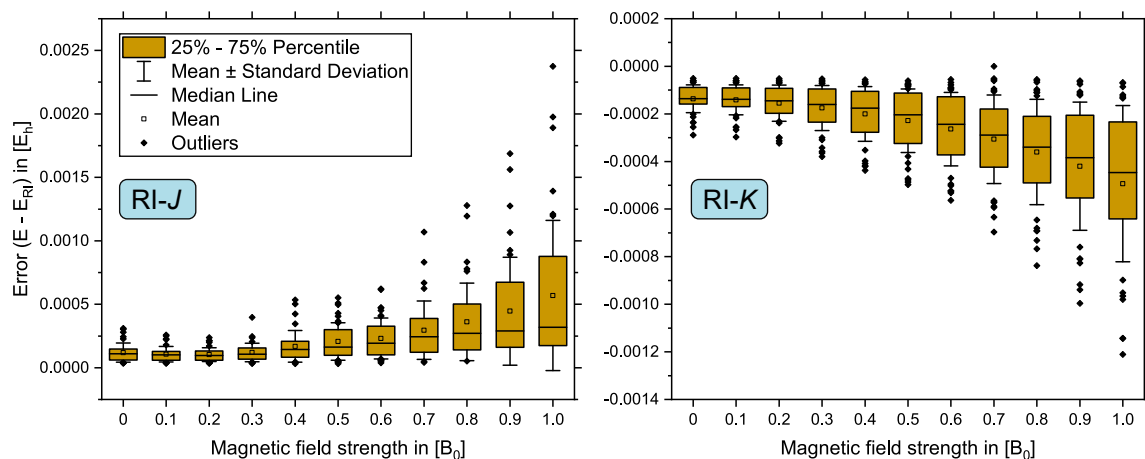


Figure 10.2.3.: Box plots presenting the error of the RI- J (left) and RI- K (right) approximations for a test set of 36 small to medium-sized molecules.^[369] All calculations were performed on the GHF/def2-TZVP level of theory. The straight line indicates the median, while the square represents the mean of the RI error. The orange colored box marks the 25–75th percentile, whiskers denote the mean \pm the standard deviation, and outliers are represented by diamonds.

The preliminary investigations carried out in Ref. [56] suggested that the use of uncontracted basis sets can reduce the RI error, which was not further investigated in this work. However, it is worth noting a few key points for the use of the RI approximation in an external magnetic field:

1. Up to magnetic field strengths of about $|\mathbf{B}| = 0.2 - 0.3B_0$, the RI error does not seem to increase too much compared to its zero-field counterpart. These are field strengths of up to about 70,000 T, below which the RI approximation can be safely used.
2. For magnetic field strengths above this threshold, the RI approximation should currently only be used with extreme caution, if at all. While maximum errors of about $1mE_h$ at a field strength of $|\mathbf{B}| = 1B_0$ might not seem much compared to errors expected from the use of HF or DFT, the associated errors for molecular properties can be expected to be much larger.^[56]

- The development of a new auxiliary basis set, optimized for the use in strong magnetic fields, is absolutely crucial. Such a development remains the subject of future work.

10.2.3. Electronic Excitations

For the closed-shell molecules of the test set shown in fig. 10.2.1, the lowest 10 excitations were examined, both with and without the use of RI. The resulting RI errors are shown in fig. 10.2.4 for magnetic field strengths of up to 10,000 T. Beyond this limit, spin-phase transitions were confirmed for some of the molecules, resulting in instabilities which prevent the investigation of electronic excitations using linear response theory.^[54] As these ‘moderately strong’ magnetic fields of up to 10,000 T are well below the critical threshold determined in sec. 10.2.2, the RI approximation can safely be used under these conditions. This is emphasized through fig. 10.2.4, where RI errors are similar for all presented magnetic field strengths. Maximum errors are approximately 1 meV, well below the expected error of the quantum chemical method.

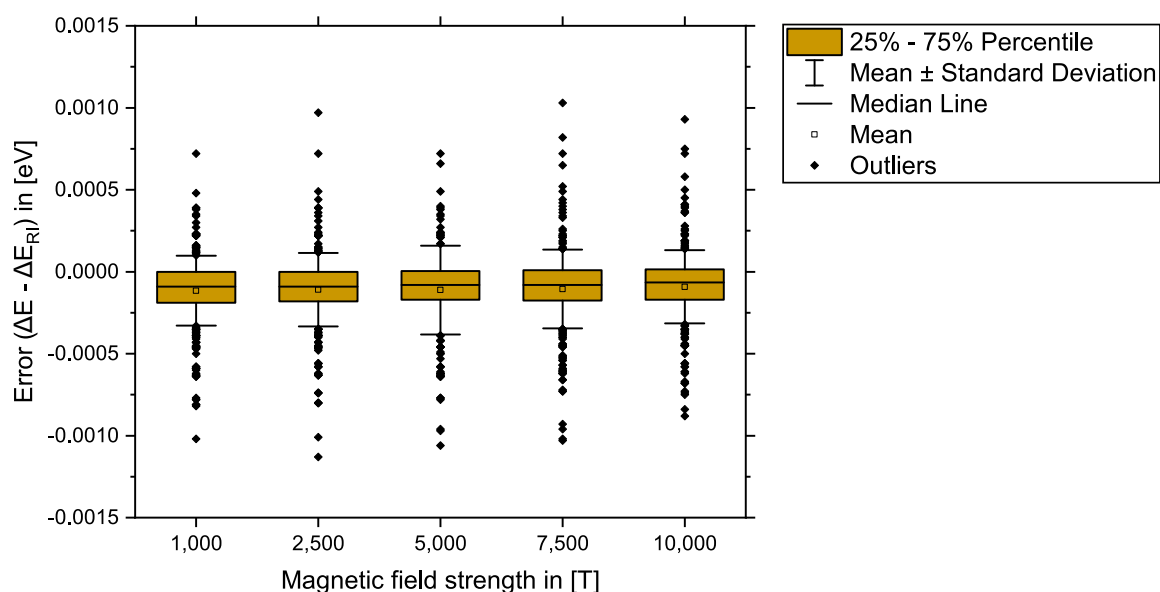


Figure 10.2.4.: Box plots presenting the RI error of electronic excitations for a test set of 36 small to medium-sized molecules.^[369] All calculations were performed on the PBE0/def2-TZVP level of theory. The straight line indicates the median, while the square represents the mean of the RI error. The orange colored box marks the 25–75th percentile, whiskers denote the mean \pm the standard deviation, and outliers are represented by diamonds. Adapted with permission from Ref. [54].

10.3. Accuracy of Linear Response Methods

The accuracy of the TD-DFT and GW /BSE methods in the presence of magnetic fields were tested by the author in collaboration with Holzer and Klopper in Refs. [53] and [54]. A detailed review is omitted here, and the interested reader is referred to these publications. A short outline of the main results presented therein shall be given here nonetheless for the sake of completeness.

In Ref. [53], triplet excitations calculated using the $evGW$ /BSE method were benchmarked against TD-CC2 excitation energies for the test set of molecules shown in fig. 10.2.1. Generally, the methods show good agreement, with $evGW$ /BSE systematically (but slightly) red-shifted compared to TD-CC2. This is not unexpected, since TD-CC2 is known to overestimate excitation energies, while $evGW$ /BSE has a tendency to underestimate triplet states.^[266, 369] The errors show a dependence on the reference functional, denoted @DFT. The two choices @BHLYP and @CAM-B3LYP performed reasonably well, with mean average errors of 0.53 and 0.59 eV, as well as maximum errors of 1.05 and 1.19 eV, respectively.

In Ref. [54], singlet excitations calculated using TD-DFT were benchmarked against TD-CC2 excitation energies for the same test set of molecules. The performance of TD-DFT was excellent for all investigated field strengths, up to 10,000 T. The errors did not change with an increasing field, with a mean absolute error of 0.10 eV at 1,000 T and 0.09 at 10,000 T. The conclusion is that TD-DFT can be used in ‘moderately strong’ magnetic fields with the same amount of accuracy expected in the absence of fields.

In conclusion, both the GW /BSE and TD-DFT methods may be used in moderately strong magnetic fields. Their accuracy can be expected to be similar to the zero-field case for this region. However, the TD-CC2 reference may have a bias in that regard, yielding similar errors induced by the presence of a magnetic field, which result in error cancellation.

10.4. Efficiency of the Implementation

10.4.1. Assessment of Efficiency

In this section, the efficiency of the present implementation is briefly assessed. Due to the aforementioned problems with integral screening, which have yet to be properly investigated, a detailed benchmark study remains the subject of future work. Instead,

the focus of this section shall lie on two aspects concerning computational efficiency. Firstly, a short comparison between field-free and field-dependent calculations is presented. Secondly, the scaling of the OpenMP parallelization is examined. These investigations are carried out for electronic ground states, as they are expected to be the ‘worst case scenario’, with the expensive integral evaluation generally being the most time-consuming step.^[56, 322]

10.4.2. Computational Methods

For the benchmark calculations presented in this section, the benzene, naphthalene, and anthracene molecules were examined. Calculations were performed using the GHF method with either the def2-TZVP or def2-QZVP basis set.^[370] If the RI approximation was used, the corresponding auxiliary def2-TZVP or def2-QZVP basis sets were employed.^[371, 372] Calculations were converged up to $10^{-8}E_h$. Difference densities and Cauchy-Schwarz screening were used. Since these approaches do not represent approximations, their use is henceforth assumed for all calculations within this work, even if not specified.

10.4.3. Comparison to Field-Free Calculations

To assess how well the current implementation performs, benchmark calculations were carried out on benzene, naphthalene, and anthracene. All calculations were done with TURBOMOLE^[306] in the two-component framework, once with the use of regular AOs and once with LAOs, using a magnetic field strength of $|\mathbf{B}| = 0.01B_0$. An identical number of iterations was obtained for both cases. Similar calculations were carried out using the RI-*JK* approximation. All timings are listed in table 10.4.1.

As previously discussed in chapters 8 and 9, the computational effort for four-center integrals over LAOs results in at least an additional factor of eight for calculations in finite magnetic fields. In actual calculations, this factor will be even higher, since, for instance, additional shell-pair quantities have to be evaluated. For benzene, an additional factor of roughly 16 is obtained, while the calculations on larger systems are only slower by a factor of about 12 compared to the field-free case. This is already very close to the theoretical limit of an additional factor of eight. However, it should be mentioned that a modified screening will likely negatively affect the efficiency for these calculations.

Table 10.4.1.: Timings in seconds for benchmark calculations carried out on aromatic molecules. The GHF method was used in combination with def2-TZVP (four-center integrals) and def2-QZVP (RI-*JK* approximation). All calculations were done on CPUs of type Intel[®] Xeon[®] E5-2687W v4 @ 3.00GHz. Adapted with permission from Ref. [56].

	Benzene	Naphthalene	Anthracene
Exact GHF (AOs)	617	3670	11870
Exact GHF (LAOs)	9781	45430	144418
Slower by factor	15.85	12.38	12.17
RI- <i>JK</i> (AOs)	328	1694	7065
RI- <i>JK</i> (LAOs)	1717	7252	21098
Slower by factor	5.23	4.28	2.99

For the RI approximation, the comparison to the field-free (AO) case is even more favorable, with an additional factor of roughly five for benzene, and less than three for anthracene. The computational cost for the evaluation of three-center integrals over LAOs increases by a factor of four compared to the AO case. However, for the present implementation of RI-*JK*, the computation of three-center integrals over LAOs is not the most time-consuming step, since they are precomputed only once and then stored on disk (see sec. 8.2.1). For calculations on larger systems, the most time-consuming step eventually becomes the transformation from the AO to MO basis in eq. (5.2.21). This transformation is formally only slower by a factor of two in the LAO case compared to a field-free two-component calculation.^[56]

In combination with the results obtained in sec. 10.2, the conclusion is that RI presents an excellent compromise between accuracy and efficiency for calculations in finite magnetic fields, at least for fields in the ‘moderately strong’ regime. This is a strong incentive for the development of auxiliary basis sets parameterized for the use in strong magnetic fields.

10.4.4. OpenMP Parallelization

To test the efficiency of the OpenMP parallelization, calculations were run on one, two, four, six, eight, ten, and twelve OpenMP threads. The resulting timings are plotted against the inverse number of cores in fig. 10.4.1. A linear regression is presented, which can be used to evaluate how well parallelized the implementation is. Furthermore,

the computational overhead may be calculated, which is discussed in more detail in Ref. [56]. For the present discussion, the most important feature of fig. 10.4.1 is how well the data is represented through the linear regression. This implies that a (sufficiently large) calculation run on twelve cores will be approximately twelve times cheaper compared to a calculation run on only one core. This gives access to the computation of larger systems like the ones presented in this thesis.

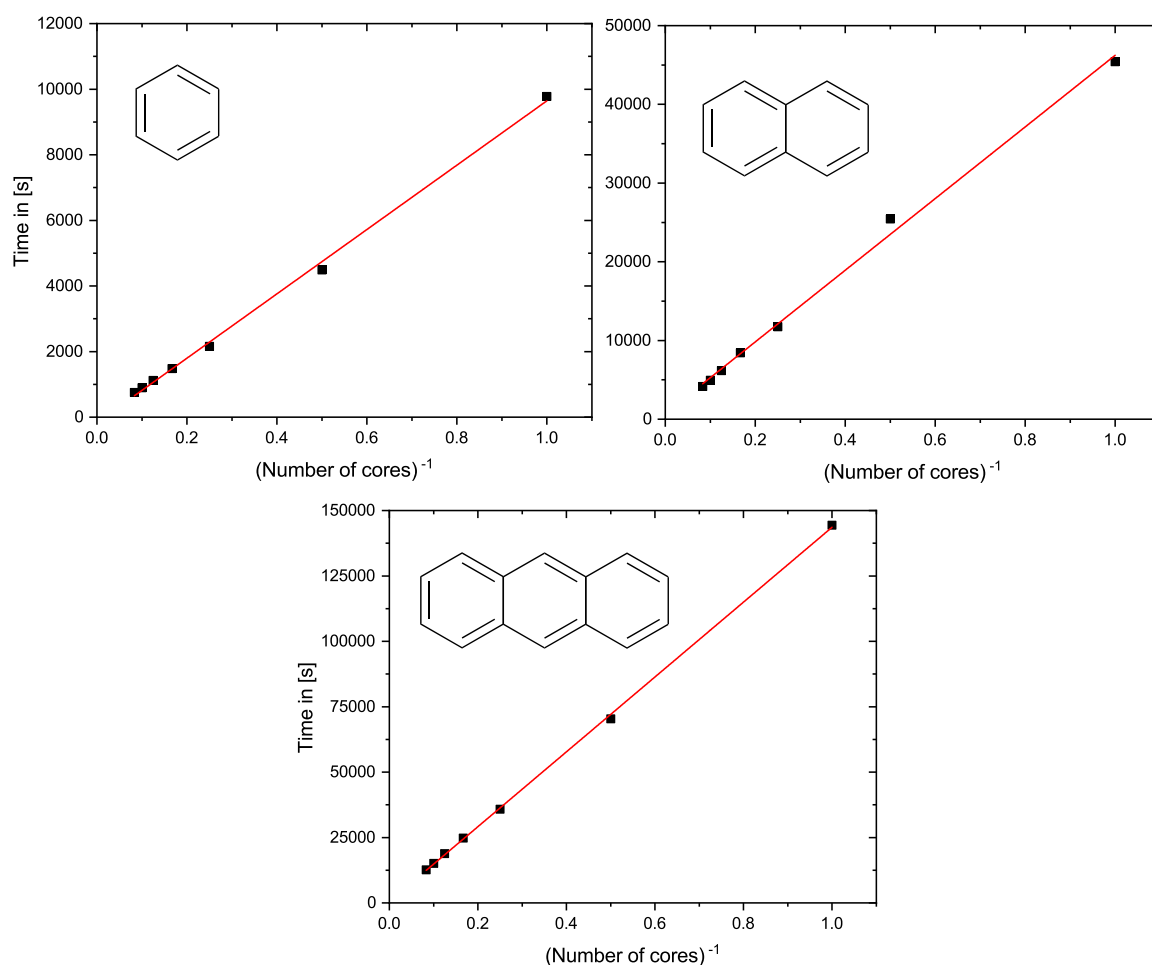


Figure 10.4.1.: Assessment of the efficiency for the OpenMP parallelization. The electronic ground state was computed at the GHF/def2-TZVP level of theory, using the difference density approach and Cauchy-Schwarz screening. For benzene, naphthalene, and anthracene, the computation time is plotted against the reciprocal number of cores. All calculations were done on CPUs of type Intel[®] Xeon[®] E5-2687W v4 @ 3.00GHz. Adapted with permission from Ref. [56].

11. Berry Curvature: Implementation and Connection to Partial Charges

The Berry curvature tensor plays a crucial role for molecular dynamics in finite magnetic fields. It is responsible for screening the Lorentz forces acting on nuclear charges by taking the electronic charge distribution into consideration. It was derived in sec. 7 of this work, similarly to the very recently published approach of Ref. [82] and [83]. In the latter publication, a numerical approach for the calculation of the Berry curvature tensor is proposed for complex RHF wave functions, while the former is concerned with its application.

In this chapter, the approach is adapted to complex GHF wave function consisting of two-component spinors. The numerical derivation of wave functions with respect to nuclear displacements is presented. Since coefficient vectors need to be directly subtracted, their arbitrary global phase factors already discussed in sec. 4.2.1 need to be eliminated. This is done by correcting them using the phase factor of the unperturbed wave function as a common gauge. The general outline of an algorithm capable of numerically evaluating the Berry curvature tensor is shown and all relevant steps are discussed, highlighting which quantities need to be computed with an external quantum-chemical program like TURBOMOLE.

The Berry curvature tensor itself is later used in sec. 14 for the computation of rotational-vibrational spectra of small molecules in strong, external magnetic fields. The validity of the presented implementation for molecules in strong magnetic fields is thus verified later. In the remaining part of this chapter, charge distributions and corresponding partial charges are calculated from the Berry curvature tensor in the limit of vanishing magnetic fields. Surprisingly, they do not vanish even though the Berry curvature itself does. A general scheme for the calculation of these 'Berry charges' is introduced. Their basis set dependence is investigated and compared to that of Mulliken charges for the lithium hydride and lithium fluoride molecules.

11.1. Implementation of Numerical Evaluation

The Berry curvature tensor was introduced in sec. 7 of this work. It is used to screen the Lorenz force acting on moving nuclear charges in the presence of an external magnetic field. One element of the tensor is defined as^[83, 86]

$$\Omega_{IJ,\alpha\beta} = i \left[\left\langle \frac{\partial \Psi_0}{\partial R_{I\alpha}} \left| \frac{\partial \Psi_0}{\partial R_{J\beta}} \right\rangle - \left\langle \frac{\partial \Psi_0}{\partial R_{J\beta}} \left| \frac{\partial \Psi_0}{\partial R_{I\alpha}} \right\rangle \right], \quad (11.1.1)$$

with Ψ_0 being the ground state electronic wave function. The Berry curvature tensor shown in eq. 11.1.1 can be evaluated using numerical derivatives, which was presented in Ref. [83] for RHF and UHF. In this work, a similar algorithm is introduced for the GHF case, closely following Ref. [83].

The numerical derivative of the electronic wave function as evaluated at a certain point of the BO PES (\mathbf{R}) may be written as

$$\frac{\partial \Psi_0(\mathbf{R})}{\partial R_{I\alpha}} \approx \frac{\Psi_0(\mathbf{R} + \delta \mathbf{e}_{I\alpha}) - \Psi_0(\mathbf{R} - \delta \mathbf{e}_{I\alpha})}{2\delta}, \quad (11.1.2)$$

with δ being a small number and $\mathbf{e}_{I\alpha}$ a unit vector in $I\alpha$ direction of the $(3N_{\text{muc}})$ -dimensional space of the BO PES. For all calculations presented in this work, we assume $\delta = 10^{-4}$. Unfortunately, eq. (11.1.2) cannot be calculated directly, as the two disturbed wave functions require two separate SCF calculations. As previously mentioned in sec. 4.2.1, the wave function is attributed with an arbitrary phase factor. More precisely, each spinor ψ_j contained in the Slater determinant carries an arbitrary complex phase which, in contrast to the phase ± 1 for real-valued MOs, is not trivial to eliminate. Culpitt et al.^[83] have proposed a solution to this problem, here written in terms of two-component spinors.

The algorithm presented here requires a few definitions. Firstly, the coefficients of the unperturbed spinor j are written as \mathbf{C}_j^σ , while the coefficients of the perturbed spinors are denoted as $\mathbf{C}_j^\sigma(\pm I\alpha)$. Secondly, the overlap matrix may be perturbed either in the Bra or Ket. The Bra-perturbed overlap matrix is written as $\mathbf{S}(\pm I\alpha; 0)$, while the Ket-perturbed overlap matrix is given by $\mathbf{S}(0; \pm I\alpha)$. Finally, the Bra- and Ket-perturbed overlap matrix reads $\mathbf{S}(\pm I\alpha; \pm J\beta)$. The overlap between an unperturbed and a perturbed spinor yields:

$$\begin{pmatrix} \mathbf{C}_j^\alpha \\ \mathbf{C}_j^\beta \end{pmatrix}^\dagger \begin{pmatrix} \mathbf{S}(0; \pm I\alpha) & \mathbf{0} \\ \mathbf{0} & \mathbf{S}(\pm I\alpha; 0) \end{pmatrix} \begin{pmatrix} \mathbf{C}_j^\alpha(\pm I\alpha) \\ \mathbf{C}_j^\beta(\pm I\alpha) \end{pmatrix} \approx e^{i\phi_j(\pm I\alpha)} \quad (11.1.3)$$

Thus, the perturbed spinor may be corrected for its global phase relative to the unperturbed spinor by multiplication with $e^{-i\phi_j(\pm I\alpha)}$. Calculating the auxiliary overlap,

$$S_{I\alpha J\beta}^{\pm\pm} = \sum_j^{N_{\text{occ}}} \begin{pmatrix} \mathbf{C}_j^\alpha(\pm I\alpha) \\ \mathbf{C}_j^\beta(\pm I\alpha) \end{pmatrix}^\dagger \begin{pmatrix} \mathbf{S}(\pm I\alpha; \pm J\beta) & \mathbf{0} \\ \mathbf{0} & \mathbf{S}(\pm I\alpha; \pm J\beta) \end{pmatrix} \begin{pmatrix} \mathbf{C}_j^\alpha(\pm J\beta) \\ \mathbf{C}_j^\beta(\pm J\beta) \end{pmatrix} e^{i\phi_j(\pm I\alpha)} e^{-i\phi_j(\pm J\beta)}, \quad (11.1.4)$$

the final integral may be evaluated as:^[83]

$$\left\langle \frac{\partial \Psi_0}{\partial R_{I\alpha}} \middle| \frac{\partial \Psi_0}{\partial R_{J\beta}} \right\rangle = \frac{S_{I\alpha J\beta}^{++} - S_{I\alpha J\beta}^{+-} - S_{I\alpha J\beta}^{-+} + S_{I\alpha J\beta}^{--}}{4\delta^2}. \quad (11.1.5)$$

Evidently, the other integral in the definition of the Berry curvature tensor is simply the complex conjugate of eq. (11.1.5) and does not require further calculations. The algorithm evaluating the Berry curvature tensor is constructed in a fairly simple manner, requiring five basic steps as illustrated in fig. 11.1.1.

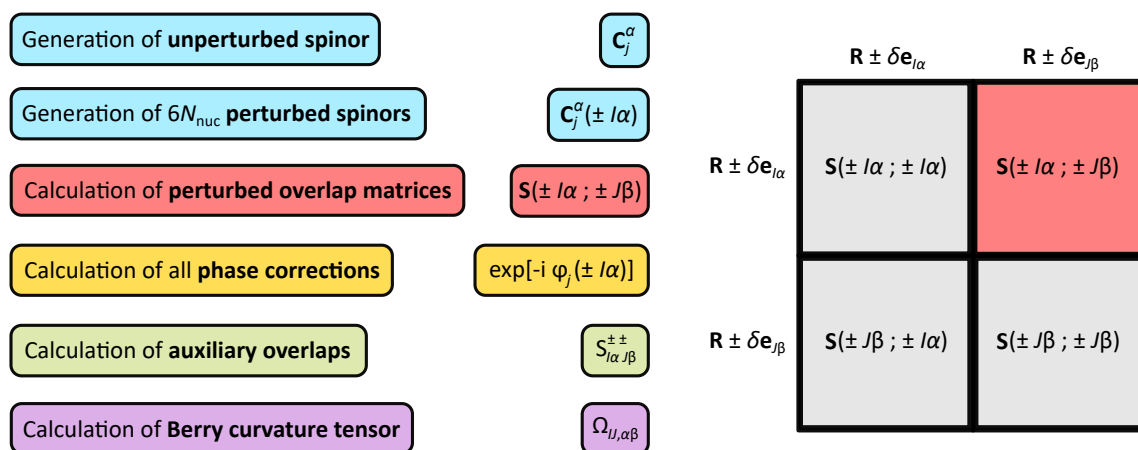


Figure 11.1.1.: Illustration of algorithm for the calculation of the Berry curvature tensor. In the first step (blue), the unperturbed spinor and all perturbed spinors are generated using TURBOMOLE. In the second step (red), the perturbed overlap matrices are calculated from the off-diagonal blocks of perturbed molecular superstructures. In the third (yellow), fourth (green) and fifth (purple) steps, the perturbed spinors and overlap matrices are processed to generate phase corrections, auxiliary overlaps and, finally, the Berry curvature tensor.

Firstly, the unperturbed spinors and all $6N_{\text{nuc}}$ perturbed spinors are generated using TURBOMOLE. Secondly, the perturbed overlap matrices are computed with TURBOMOLE. This does not require any additional implementations and can be achieved by

printing out the overlap matrix for a hypothetical system consisting of two blocks, one for the Bra-perturbation and one for the Ket-perturbation. The off-diagonal block is identical to the perturbed overlap matrix, which is generally non-hermitian. Thirdly, the phase corrections $e^{-i\phi_j(\pm I\alpha)}$ are computed for all occupied spinors j in all $6N_{\text{nuc}}$ perturbations using eq. (11.1.3). Fourthly, the auxiliary overlaps are calculated with eq. (11.1.4). Finally, the integrals constituting the Berry curvature are computed using eq. (11.1.5), from which the Berry curvature tensor is then constructed.

It should be noted that in the current implementation, only diatomic molecules can be handled, which is sufficient for all cases presented in this work. While the adaption of the algorithm to larger systems is, in principle, relatively straightforward, an analytical approach for the calculation of the Berry curvature tensor was recently introduced in Ref. [86]. It requires the solution of the coupled perturbed Hartree-Fock equations with the perturbation being the displacement of a nuclear coordinate. This is also required for second analytical derivatives of the electronic energy with respect to nuclear displacements, which is needed for the calculation of vibrational spectra in the absence of magnetic fields.^[338, 339] Implementing the analytical calculation of the Berry curvature tensor into TURBOMOLE is the subject of future work.

11.2. Partial Charges in the Limit of a Vanishing Field

11.2.1. Computational Details

In this section, charge distributions and partial charges for lithium hydride (LiH) and lithium fluoride (LiF) are calculated from the Berry curvature tensor as shown in eq. (7.2.6), with an additional contraction of the Cartesian components according to eq. (7.2.8). First, the charge distribution of LiH is evaluated in sec. 11.2.2. The geometry was optimized at the RHF/def2-SVP level in the absence of fields, yielding a bond length of $3.0351 a_0$, which was held fix for all calculations. All subsequent calculations were performed in magnetic fields at the GHF/def2-SVP level of theory. Tight convergence criteria were chosen, with the energy being converged to $10^{-15} E_h$ and the norm of the density matrix up to 10^{-13} . This is strictly needed, as finite differences of spinor coefficients are computed for the Berry curvature tensor.

In the following section, 11.2.3, partial charges of the LiH and LiF molecule were calculated using the GHF method. A variety of basis sets were used to test the basis set dependence of results: def2-SV(P), def2-SVP, def2-TZVP, def2-TZVPP, def2-QZVP,

cc-pVDZ, cc-pVTZ, cc-pVQZ, aug-cc-pVDZ, aug-cc-pVTZ, aug-cc-pVQZ.^[370, 374–376] It should be noted, that the def2-QZVPP basis is not listed, as it is identical to def2-QZVP for LiH and LiF. The aforementioned tight convergence criteria were used for every calculation. Mulliken charges were calculated for comparison at the same levels of theory. The magnetic field was applied in the z -direction in each calculation.

11.2.2. Charge Distribution and Sum Rule

The aim of this section is to test the validity of using the Berry curvature tensor for the calculation of charge distributions and partial charges in the limit of a vanishing field. This is done for the exemplary case of the LiH molecule in equilibrium geometry. The asymptotic limit $|B| \rightarrow 0$ was evaluated by applying magnetic fields of different sizes from $0.1B_0 \approx 23,505$ T to $10^{-6}B_0 \approx 0.235$ T perpendicular to the bond axis. For all cases, charge distributions were calculated from the Berry curvature tensor. Additionally, the sum rule was evaluated. The results are listed in table 11.2.1. It should be noted that a numerical evaluation scheme was used for the calculation of the Berry curvature tensor, with nuclear displacements of $10^{-4} a_0$. Thus, the resulting values are also only expected to be accurate up to the same order of magnitude.

Table 11.2.1.: Charge distributions of LiH in different magnetic field strengths from $0.1B_0 \approx 23,505$ T to $10^{-6}B_0 \approx 0.235$ T. In all cases, the magnetic field was applied perpendicular to the bond. All calculations were carried out at the GHF/def2-SVP level. The asymptotic behaviour ($|B| \rightarrow 0$) of the charge distribution is clearly visible, with field strengths below about 500 T showing no discernible differences. Sum rules are fulfilled, yielding $-N_{\text{el}}$ for all field strengths. All charge distributions Q and sum rules are given in units of $[e]$.

Magnetic field strength	$Q(\text{Li-Li})$	$Q(\text{Li-H})$	$Q(\text{H-H})$	Sum rule
$ B = 0.1B_0$	-2.0044	-0.4573	-1.0810	-4.0000
$ B = 0.01B_0$	-2.0067	-0.4850	-1.0232	-3.9997
$ B = 0.001B_0$	-2.0069	-0.4853	-1.0226	-4.0001
$ B = 0.0001B_0$	-2.0069	-0.4853	-1.0226	-4.0001
$ B = 0.00001B_0$	-2.0069	-0.4853	-1.0226	-4.0001
$ B = 0.000001B_0$	-2.0069	-0.4853	-1.0226	-4.0001

The charge distribution corresponding to the Li–Li block yields $-2.0069 e$ for all field strengths below about 500 T. The H–H block converges similarly to $-1.0226 e$ and the Li–H block to $-0.4853 e$. Sum rules yield $\sum_{IJ} Q_{IJ} = -4 = -N_{\text{el}}$ for all field strengths up to the expected limit of numerical precision. For the evaluation of the sum rules, the off-diagonal block $Q(\text{Li–H})$ has to be considered twice.

Next, the magnetic field was applied in a parallel orientation to the lithium hydride bond. This was done identically to the perpendicular orientation and the results are listed in table 11.2.2. Again, the asymptotic limit is reached for all field strengths below about 500 T. Sum rules are satisfied for all field strengths up to the expected numerical accuracy.

Table 11.2.2.: Charge distributions of LiH in different magnetic field strengths from $0.1B_0 \approx 23,505 \text{ T}$ to $10^{-6}B_0 \approx 0.235 \text{ T}$. In all cases, the magnetic field was applied parallel to the bond. All calculations were carried out at the GHF/def2-SVP level. The results are similar to the perpendicular case, with charge distributions converging up to the expected numerical precision and sum rules being fulfilled for all cases. However, the results themselves are different from the perpendicular case. All charge distributions Q and sum rules are given in units of $[e]$.

Magnetic field strength	Q(Li–Li)	Q(Li–H)	Q(H–H)	Sum rule
$ B = 0.1B_0$	-2.3073	0.0607	-1.8141	-4.0000
$ B = 0.01B_0$	-2.3046	0.0079	-1.7112	-4.0000
$ B = 0.001B_0$	-2.3046	0.0073	-1.7102	-4.0002
$ B = 0.0001B_0$	-2.3047	0.0074	-1.7103	-4.0002
$ B = 0.00001B_0$	-2.3047	0.0074	-1.7102	-4.0001
$ B = 0.000001B_0$	-2.3047	0.0075	-1.7103	-4.0000

In the asymptotic limit of a vanishing field, the charge distribution for the Li–Li block converges to $-2.3047 e$, while the H–H block yields $-1.7103 e$ and the Li–H block amounts to $0.0075 e$. These values are drastically different than those obtained from the perpendicular orientation. This dependence on the angle between the bond and the external magnetic field needs to be further investigated.

In order to examine this angular dependence, the angle between bond and magnetic field was rotated in steps of 10° , computing the charge distribution at each step. The parallel orientation was taken as the starting point (0°) and the molecule was rotated about the Cartesian x - and y -axis, respectively. Evidently, the perpendicular orienta-

tion already evaluated above corresponds to the 90° case. The angular dependence of all three contributions of the charge distribution is plotted in fig. 11.2.1 for the rotation about both the x - and y -axis. While the sum rules are satisfied for each orientation, the charge distribution itself is not rotationally invariant. The general patterns exhibited for the rotations about the x - and y -axis are similar, but the total values are shifted about a phase of 45° .

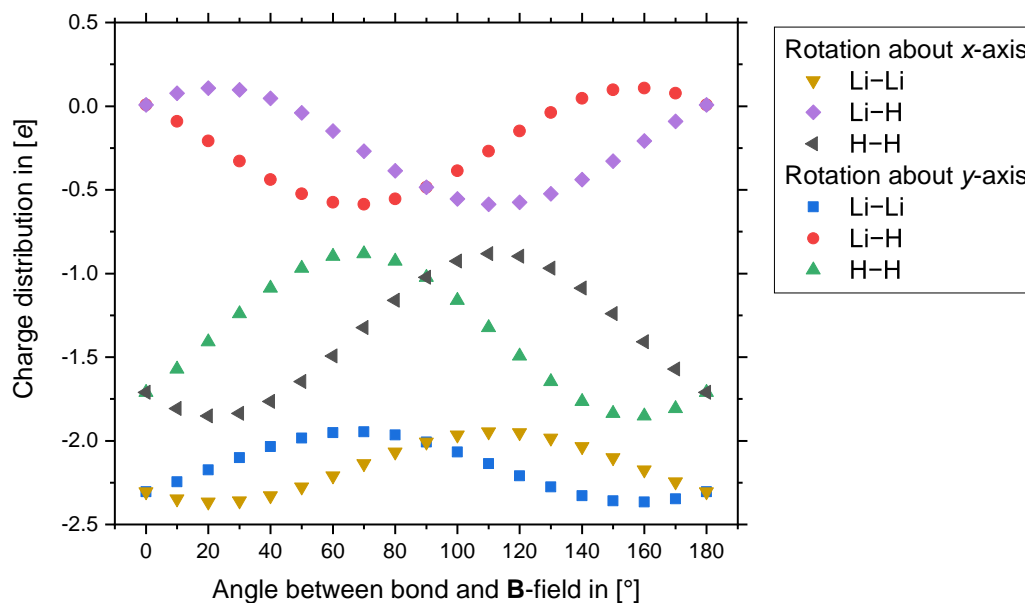


Figure 11.2.1.: Angular dependence of Berry charge distribution in the limit of a vanishing magnetic field (\mathbf{B}). Starting from a parallel orientation (0°), the molecule is rotated about the Cartesian x -axis (yellow, purple and black) and y -axis (blue, red and green). The charge distributions are evaluated in steps of 10° , showing that the results are not rotationally invariant. Sum rules are fulfilled for every orientation.

Partial charges obtained from the Berry curvature are, similarly to the charge distributions discussed so far, also not rotationally invariant.

The rotational invariance of both the charge distribution and, consequently, the partial charges may be restored if the isotropic average is considered. This was carefully investigated for a number of different orientations and proven to be true for all examples. Following the orientations represented by the rotation about the y -axis (the blue, red and green points in fig. 11.2.1), this is shown in table 11.2.3, where the isotropic averages for all orientations from 0° to 50° are listed. This list is not exhaustive and is presented as such in order to showcase that, indeed, the isotropic average of the charge distribution as calculated from the Berry curvature is rotationally invariant.

Combining all of these results, it is shown that the charge distribution calculated from the Berry curvature tensor does not vanish in the asymptotic limit $|B| \rightarrow 0$. Instead, its isotropic average yields reliable results which obey the relevant sum rules and which are not dependent on the choice of magnetic field. This leads to the conclusion, that the Berry curvature tensor may be used to generate charge distributions and partial charges even if the magnetic field is only treated perturbatively. This is somewhat surprising, as the Berry curvature tensor itself does vanish in the absence of a magnetic field.

Table 11.2.3.: Isotropic average of the charge distribution as calculated from the Berry curvature tensor at a field strength of $10^{-6}B_0 \approx 0.235$ T. The angle between molecule and magnetic field is varied in steps of 10° , but the isotropic average is not affected. The sum rule is thus also satisfied for all orientations. The calculations were carried out at the GHF/def2-SVP level. All charge distributions Q and sum rules are given in units of $[e]$.

Angle	Q(Li–Li)	Q(Li–H)	Q(H–H)	Sum rule
0°	-2.1061	-0.3211	-1.2519	-4.0002
10°	-2.1061	-0.3210	-1.2518	-4.0000
20°	-2.1061	-0.3210	-1.2518	-4.0000
30°	-2.1061	-0.3211	-1.2519	-4.0001
40°	-2.1061	-0.3211	-1.2518	-4.0001
50°	-2.1062	-0.3211	-1.2519	-4.0002

11.2.3. Partial Charges and Basis Set Dependence

Having established that the isotropic average of the charge distribution calculated from the Berry curvature tensor can be used in the limit of a vanishing field, this section aims at evaluating the corresponding partial charges. They are denoted as ‘Berry charges’ in the following section. This term is introduced in the spirit of Mulliken charges, which denote partial charges computed from a Mulliken population analysis. The basis set dependence of Berry charges was investigated using a variety of basis sets. They were compared to Mulliken charges which were calculated in the absence of a field at the same level of theory. This procedure was carried out for the two molecules lithium hydride and lithium fluoride. The results are listed in table 11.2.4, including the mean and standard deviation (SD).

For the computation of Berry charges, the Berry curvature tensor was evaluated in an external magnetic field of $10^{-4}B_0 \approx 23.5$ T. This was done three separate times, aligning the linear molecules with the Cartesian x -, y - and z -axis to calculate the isotropic average of the charge distribution. For the sake of better comparability, the charge distributions of each molecular orientation were normalized to fulfill the sum rule exactly. Berry charges for lithium were calculated by summation over the Li–Li and one respective non-diagonal block of the charge distribution matrix.

Table 11.2.4.: Basis set dependence of Berry and Mulliken charges for the lithium atom in lithium hydride and lithium fluoride. Berry charges were obtained from the isotropic average of charge distributions calculated from the Berry curvature tensor and normalized to satisfy the sum rule exactly. Mulliken charges were obtained at the same level of theory. Mean and standard deviation (SD) are shown to highlight the contrast between the basis set dependence of both approaches. All values are given in units of [e].

Basis set	Lithium hydride (LiH)		Lithium fluoride (LiF)	
	Berry charge	Mulliken charge	Berry charge	Mulliken charge
def2-SV(P)	0.5792	0.3760	0.8845 ^(a)	0.7398 ^(a)
def2-SVP	0.5728	0.3968	0.8845	0.7398
def2-TZVP	0.6036	0.4225	0.8875	0.8379
def2-TZVPP	0.6305	0.4707	0.8579	0.7782
def2-QZVP	0.6779	0.3044	0.8847	0.6562
cc-pVDZ	0.6030	0.1186	0.8039	0.6223
cc-pVTZ	0.6658	0.2608	0.8216	0.5722
cc-pVQZ	0.6748	0.3243	0.8581	0.6131
aug-cc-pVDZ	0.6723	0.1407	0.8688	0.7095
aug-cc-pVTZ	0.6736	0.3086	0.8824	0.7637
aug-cc-pVQZ	0.6834	0.2148	0.9008	0.8163
Mean	0.6397	0.3035	0.8650	0.7109
SD	0.0387	0.1040	0.0293	0.0866

(a) def2-SV(P) and def2-SVP are identical for LiF.

For LiH, Berry and Mulliken charges show drastically different results. While both are always positive for the lithium atom, Berry charges generally predict a much more positively polarized lithium atom compared to equivalent calculations with the Mulliken charge. For the investigated basis sets, Berry charges are within the range of $0.5728 e - 0.6834 e$ with a mean of $0.6397 e$. Mulliken charges of the lithium atom lie between $0.1186 e - 0.4707 e$, with a mean of 0.3035 , less than half of what was predicted for Berry charges. Furthermore, Berry charges tend to get larger with an increasing basis, while there is no equivalent trend for Mulliken charges. The inconsistent behaviour with respect to basis set dependence is a well-known problem of the Mulliken population analysis.^[377] Berry charges, on the other hand, do not appear to suffer from this problem. The standard deviation for Mulliken charges ($0.1040 e$) is more than twice as large as that of Berry charges ($0.0387 e$) for the small sample of basis sets investigated here.

The LiF molecule shows similar trends to those discussed for LiH. Berry charges deviate even less from the mean ($0.8650 e$), falling in between $0.8039 e$ and $0.9008 e$. The systematic increase with larger basis sets can in principle be found again, particularly for the Dunning basis sets (pVXZ). For the Karlsruhe basis sets (def2), this trend is somewhat broken, with def2-TZVPP producing a slightly lower value than def2-TZVP. Mulliken charges, on the other hand, show very inconsistent behaviour for both Dunning and Karlsruhe basis sets with values between $0.5722 e$ and $0.8379 e$ and a mean of $0.7109 e$. The standard deviation ($0.0866 e$) is almost three times larger than for Berry charges ($0.0293 e$), indicating how unreliable the Mulliken approach is compared to the calculation of Berry charges.

As a final remark, it should be noted that the numerical stability of the calculation of Berry charges for LiF becomes somewhat problematic, particularly for larger basis sets. The sum rules exhibit errors of about 1% in extreme cases. As mentioned above, the Berry charges given in table 11.2.4 are all normalized to fulfill the sum rule exactly for the sake of consistency. It should be stressed, that these errors are a problem of the numerical evaluation scheme and not the method itself. Also, in most cases sum rules were still satisfied up to six digits, which is the expected accuracy given the nature of the method. Likely, this problem would not exist for an analytical approach in the limit of vanishing fields. The implementation of an analytical evaluation for the Berry curvature and investigation of Berry charges using a proper test set of molecules is the subject of future work.

Part IV.

Selected Applications

12. Magnetic Circular Dichroism Spectroscopy

Magnetic circular dichroism (MCD) spectra are experimentally obtained as the difference in absorption between left and right circularly polarized light for a compound in the presence of a small magnetic field. It is mainly used for highly symmetric molecules, as the presence of an external field breaks the symmetry and allows for the investigation of otherwise 'dark' transitions. The computation of MCD spectra is the first application for the methods developed in the context of this work.

MCD spectroscopy is a convenient starting point for the application of the methods developed in this work for two reasons. Firstly, since fully perturbative treatments of MCD spectroscopy are available, the validity of the current implementation may be verified by comparing the results. This is done for the two compounds *p*-benzoquinone and tetrachloro-*p*-benzoquinone, which were previously investigated in Ref. [286] using TD-DFT. Calculations were carried out in the context of this work with the finite field approach at the same level of theory, producing practically identical results.

Secondly, the corresponding experiments are carried out in the presence of magnetic fields, and therefore in conditions which can be explicitly treated by finite field calculations. Thus, to further test the validity of the implementation carried out in this work, calculations are compared to experimental data. As an exemplary case, the Zn(DiNTAP) molecule, a zinc tetraazaporphyrin with two fused naphthalene units, is investigated. Using a variety of density functionals, the experimental spectrum taken from Ref. [280] can be reproduced. The efficiency of the implementation is highlighted by the calculations on the Zn(DiNTAP) molecule, which has 57 atoms. At the DFT/def2-TZVP level of theory, the system is represented by 1384 contracted basis functions, which corresponds to more than 2000 primitive basis functions. Using the present implementation, systems of such a size can be routinely calculated, making the methods accessible for a wide variety of chemical applications.

The results presented here were published by the author in Ref. [54] and this chapter follows the general structure and line of reasoning introduced therein.

12.1. Comparison to Perturbative Approach

12.1.1. Computational Details

In this section, MCD spectra obtained from the linear response approach in finite magnetic fields are compared to spectra generated using a fully perturbative approach. In Ref. [286], the quantum-chemical calculation of *p*-benzoquinone (*p*BQ) and tetrachloro-*p*-benzoquinone (TC*p*BQ) is presented using the complex polarization propagator method,^[276, 277] itself an approximation to quadratic response theory. The two molecular structures are depicted in fig. 12.1.1.



Figure 12.1.1.: Molecular structures of the two molecules *p*-benzoquinone (*p*BQ) on the left and tetrachloro-*p*-benzoquinone (TC*p*BQ) on the right.

To compare the two approaches, the MCD spectra of *p*BQ and TC*p*BQ were calculated at the same level of theory also presented in Ref. [286]. All calculations were performed using TURBOMOLE and a large gridsizes (grid 5)^[320] for the evaluation of density functionals. Molecular geometries were optimized at the B3LYP^[212, 378, 379]/cc-pVTZ^[374–376] level of theory, using RKS in the absence of a magnetic field. Subsequent calculations for the electronic ground state were carried out at the DFT/aug-cc-pVDZ^[374–376] level with the three density functionals B3LYP, CAM-B3LYP,^[380] and BHLYP,^[212] using a spin-noncollinear approach in the absence of a magnetic field. After having converged, a magnetic field of $|\mathbf{B}| = 4 \text{ T}$ was applied in the Cartesian *x*-, *y*- and *z*-directions. Only a handful of iterations are then required to converge the system in the presence of the magnetic field, choosing relatively tight convergence criteria of $10^{-10} E_h$ for the electronic energy and 10^{-8} for the norm of the density matrix (denoted denconv 8 in the context of this work). Finally, TD-DFT calculations were performed at the same level of theory, using the RI approximation for both the exchange and Coulomb parts (RI-*JK*) with the auxiliary cc-pVTZ basis.^[161] For both molecules and all three orientations, the 500 lowest electronic excitations were calculated. The final results were broadened with with a FWHM of $4,000 \text{ cm}^{-1}$, corresponding to the damping factor of $2,000 \text{ cm}^{-1}$ employed in Ref. [286].

12.1.2. *p*-Benzoquinone

The MCD spectrum of *p*BQ as generated using the three functionals B3LYP, CAM-B3LYP and BHLYP is shown in fig. 12.1.2. The differential absorption $M(\omega, \Gamma)$ in atomic units of $[e^3 a_0^6 m_e \hbar^{-3}]$ as defined in eq. (6.2.10) is plotted versus the wavelength in the region between 200 nm and 400 nm. The result is almost indistinguishable from the corresponding plot presented in Ref. [286], which was calculated using the complex polarization propagator method.

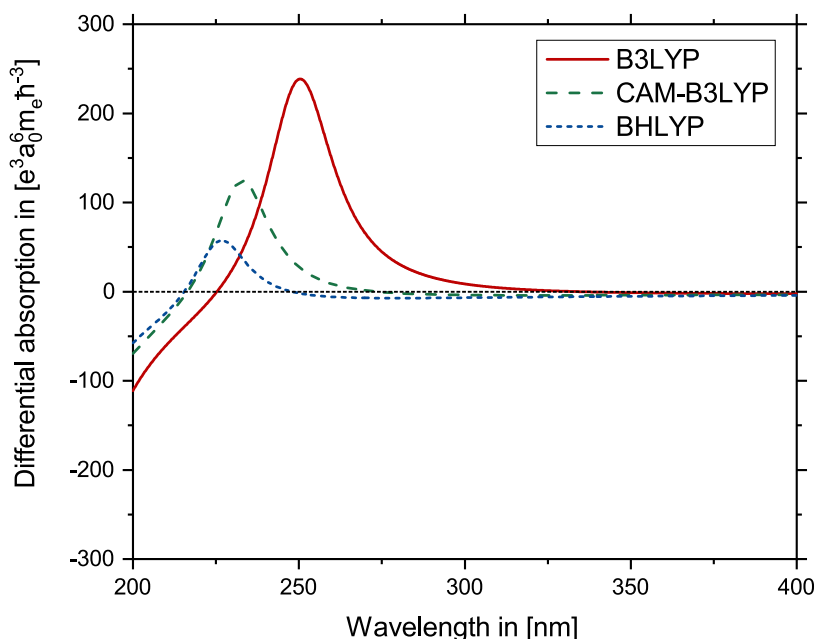


Figure 12.1.2.: Magnetic circular dichroism spectrum of *p*-benzoquinone as calculated using linear response theory in a finite magnetic field of $|\mathbf{B}| = 4$ T. Calculations were carried out at the DFT/aug-cc-pVDZ level of theory using B3LYP (red, solid), CAM-B3LYP (green, dashed) and BHLYP (blue, dotted). Adapted with permission from Ref. [54].

In the long-wavelength region depicted here, the spectrum is dominated by one positive band. This is similar to the experimental spectrum measured in *n*-hexane, where one dipole-allowed singlet-transition of character ${}^1A_g \rightarrow {}^1B_{1u}$ was identified with a maximum of 241 nm.^[381] The B3LYP calculation predicts the maximum of this band at 250 nm, while CAM-B3LYP puts it at 233 nm, and BHLYP at 226 nm. The purely perturbative approach puts them at 250 nm, 232 nm, and 227 nm, respectively.^[286] Several other, dipole-forbidden transitions are weakly visible in the experimental spectrum, but are not obtained in the calculations as spin-orbit coupling was neglected.^[381]

12.1.3. Tetrachloro-*p*-Benzoquinone

The MCD spectrum of TC*p*BQ was computed using the functionals B3LYP, CAM-B3LYP and BHLYP in a finite magnetic field of $|\mathbf{B}| = 4$ T. The results are presented in fig. 12.1.3, where the differential absorption $M(\omega, \Gamma)$ in atomic units is plotted against the wave length in the interval between 150 nm and 400 nm. As expected, the spectra are almost identical to those generated from the complex polarization propagator method in Ref. [286].

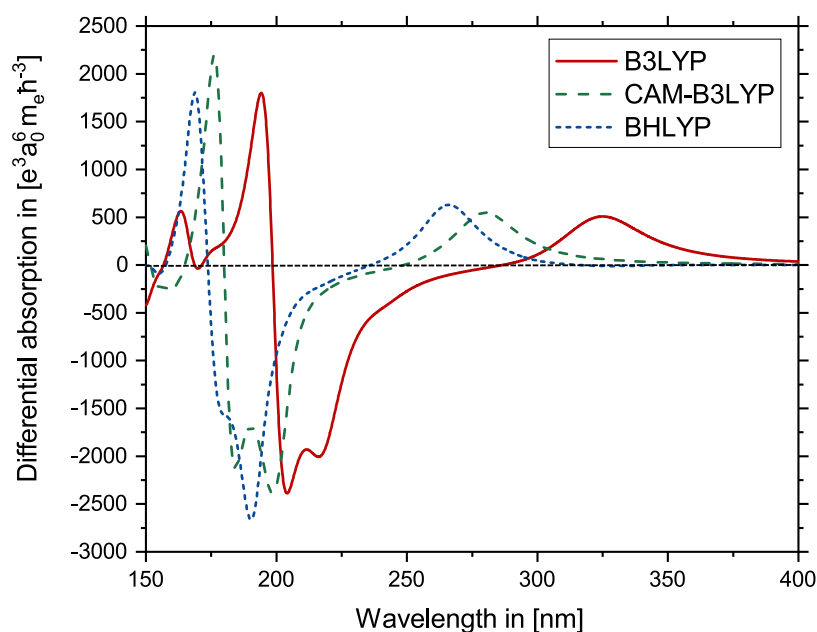


Figure 12.1.3.: Magnetic circular dichroism spectrum of tetrachloro-*p*-benzoquinone as calculated using linear response theory in a finite magnetic field of $|\mathbf{B}| = 4$ T. Calculations were carried out at the DFT/aug-cc-pVDZ level of theory using B3LYP (red, solid), CAM-B3LYP (green, dashed) and BHLYP (blue, dotted). Adapted with permission from Ref. [54].

The general structure of the spectrum is very similar to the one obtained for *p*BQ, with all bands being red-shifted. The positive dipole-allowed ${}^1A_g \rightarrow {}^1B_{1u}$ transition is shifted to 285 nm in the experimental spectrum.^[381] Calculations yield a maximum at 324 nm for B3LYP, 280 nm for CAM-B3LYP and 266 nm for BHLYP. The purely perturbative approach only differs in the value for B3LYP, predicting it at 325 nm instead.^[286] The strong negative split-band at about 210 – 230 nm is equally well reproduced with the finite field approach, as is the rest of the spectrum.

12.2. Comparison to Experiment: The ZnDiNTAP Molecule

12.2.1. Computational Details

In order to become a standard tool in quantum chemistry, finite field calculations need to be able to routinely compute sizeable molecules and their spectroscopic properties. This is put to the test in this section for the calculation of MCD spectra for the ZnDiNTAP molecule, a zinc tetraazaporphyrin with two fused naphthalene units,^[280] depicted in fig. 12.2.1.

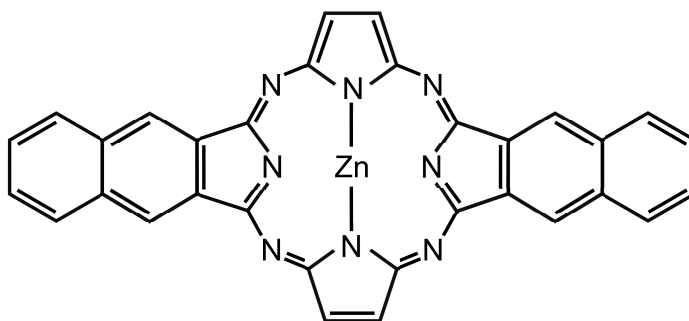


Figure 12.2.1.: Molecular structure of the ZnDiNTAP molecule, a zinc tetraazaporphyrin with two fused naphthalene units. Reprinted with permission from Ref. [54].

The geometry of ZnDiNTAP was optimized at the B3LYP/def2-TZVP^[370] level of theory using RKS in the absence of a magnetic field. All subsequent calculations of MCD spectra in this section follow the same general procedure. First, the electronic ground state is evaluated at any level of theory using RKS. Second, the converged result is taken as an input for a spin-noncollinear calculation in the absence of magnetic fields at the same level of theory. Third, a magnetic field of $|\mathbf{B}| = 5$ T is applied in the x -, y - and z -direction in three separate calculations, using the previously converged spin-noncollinear calculation as input, thereby requiring only a few iterations to converge. A convergence criterium of $10^{-9} E_h$ is used. The 200 lowest excitations are calculated using RI- JK with a matching auxiliary basis developed for correlation methods.^[157] Finally, the MCD spectrum is obtained through broadening with a lorentzian function using a FWHM of 0.3 eV.

In sec. 12.2.2, the choice of basis set is discussed. Calculations are carried out at the B3LYP/def2-TZVP level, as well as using a mixed basis of def2-TZVP for Zn and def2-SVP^[370] for all other atoms. In sec. 12.2.3, the choice of density functional is discussed. Calculations are carried out in the mixed basis using the functionals BP86,^[209, 382, 383] PBE,^[384] PBE0,^[373] B3LYP,^[212] and CAM-B3LYP.^[380]

12.2.2. Choice of Basis Set

In order to properly assess the MCD of ZnDiNTAP and compare with an experimental spectrum, an appropriate basis set must be chosen. As the corresponding quantum-chemical method is TD-DFT, a basis of triple-zeta quality is sufficiently accurate. Using the def2-TZVP basis for all atoms results in 1384 contracted or 2063 primitive basis functions. If, however, the def2-TZVP basis is only used for the Zn atom and the def2-SVP basis is used for all other atoms, a significantly reduced basis of 688 contracted or 1167 primitive basis functions is obtained. The magnetic circular dichroism of ZnDiNTAP in both basis sets was calculated using the B3LYP functional. The resulting spectrum is shown in fig. 12.2.2.

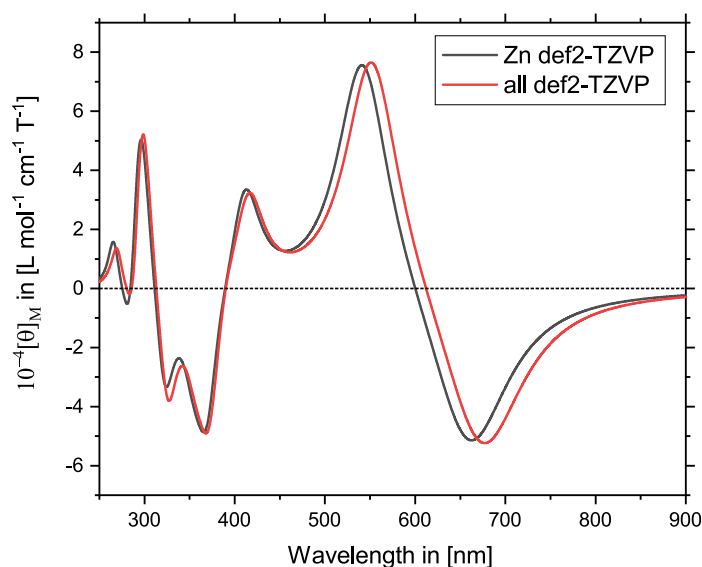


Figure 12.2.2.: MCD spectrum of ZnDiNTAP calculated using two different basis sets. First (red), the def2-TZVP basis was chosen for all atoms. Second (black), only Zn is equipped with def2-TZVP, while def2-SVP was chosen for all other atoms. Due to the similarity of both spectra, the smaller basis may be chosen. Reprinted with permission from Ref. [54].

Evidently, the mixed basis set produces very similar results when compared to the large basis set. The lowest energy band is negative in sign and peaks at 677 nm for the large and 662 nm for the mixed basis. For the second lowest band, positive in sign, the error is even less pronounced with peaks at 553 nm for the large and 543 nm for the mixed basis. Finally, the smaller bands between 250 nm and 500 nm are almost indistinguishable for the two calculations. To reduce the computational effort, the smaller basis is chosen for all further calculations in this section.

12.2.3. Choice of Density Functional

Having chosen a basis, the next step is to assess the influence of the choice of density functional on the MCD spectrum of ZnDiNTAP. A variety of different choices are presented, including the two GGA functionals PBE and BP86, as well as the hybrid functionals PBE0 and BHLYP, and the range-separated hybrid CAM-B3LYP. The resulting spectra for these functionals are presented in fig. 12.2.3. The B3LYP results, which were already shown in fig. 12.2.2, are omitted here as they are almost identical to those obtained using PBE0. MGGA functionals were not considered here, as the xc kernel for this case in eq. (6.1.20) was not yet derived, nor implemented, at the time this study was made.^[55] In any case, the influence of the current density in an external magnetic field of $|B| = 5$ T is likely negligible.

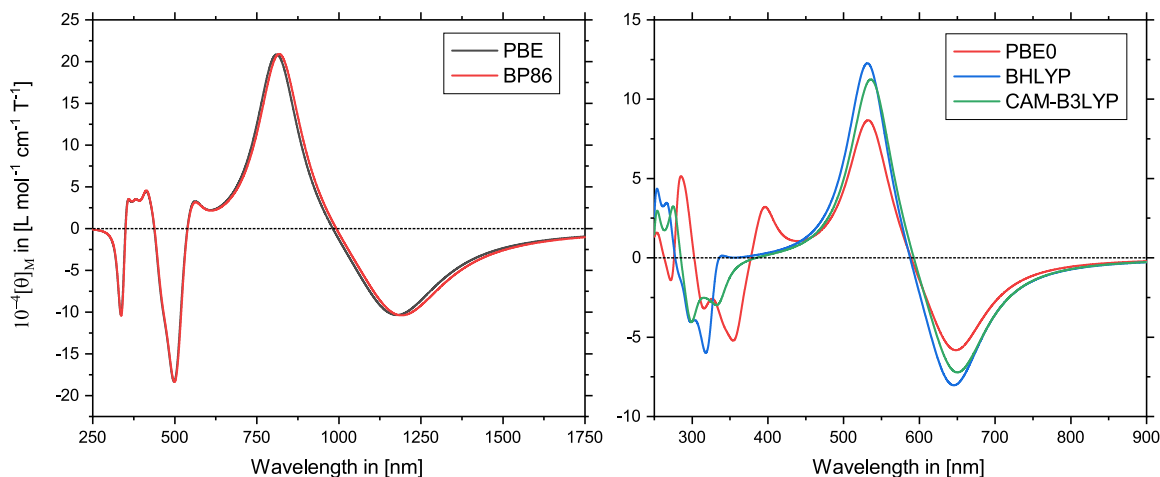


Figure 12.2.3.: MCD spectrum of ZnDiNTAP obtained from different functionals. On the left, the spectra computed from the two GGA functionals PBE (black) and BP86 (red). On the right, the spectra generated from the two hybrid functionals PBE0 (red), BHLYP (blue), and the range-separated hybrid CAM-B3LYP (green). Reprinted with permission from Ref. [54].

The two GGA functionals PBE and BP86 produce extremely similar spectra with a negative B term responsible for a band peaking at 1181 and 1196 nm, respectively. The next band corresponds to a positive B term with a maximum at 815 and 823 nm, respectively. Additional bands with relatively high intensity are visible in the region between 250 – 750 nm. The (range-separated) hybrid functionals PBE0, BHLYP, and CAM-B3LYP produce spectra which are quite similar in their general structure compared to the GGA calculations. However, the entire spectrum is blue-shifted for all

cases, with the lowest energy band having a peak at 648, 645, and 649 nm, respectively. The positive B term shows its maximum at 534, 533, and 538 nm, respectively. This corresponds to a blue-shift of more than 500 nm for the negative B term and roughly half the deviation for the positive B term compared to GGA functionals.

The main difference between the spectra calculated by the different (range-separated) hybrid functionals is the location, intensity and sign of the low-intensity bands between 250 – 450 nm. They are caused by a complex interplay of several close-lying B terms. Probably the most prominent effect is how the positive band, clearly visible for PBE0 at about 400 nm, is blue-shifted and almost diminished for BHLYP, only weakly visible at about 330 nm. For CAM-B3LYP, it completely vanishes. The main difference between these three functionals is how they treat long-range interactions through the incorporation of exact exchange. PBE0 uses 25% exact exchange, BHLYP uses 50%, and CAM-B3LYP takes a more dynamic approach by separating the long- and short-range interactions in the two-electron operator itself. The long-range interaction is thus generally described better in the order CAM-B3LYP > BHLYP > PBE0. For a more detailed comparison of these approaches, see also sec. 5.4.4 of this work.

12.2.4. Comparison to Experimental Spectrum

Finally, having discussed the influence of both the basis set and the density functional, the calculated spectra may be compared to the experimental spectrum in Ref. [280]. First, the low-energy region of the spectrum (above 550 nm) is analyzed. Three high-intensity Q bands are clearly visible, corresponding to B terms of the MCD. The first two peaks (806 and 749 nm) correspond to a split band of the spectrum, likely the result of a coupling to vibrational modes.^[54] The positive Q band peaks at 652 nm, also corresponding to a B term.

All calculations qualitatively reproduce the shape of these bands, although the split band is not visible in any of them as molecular vibrations were not taken into account. However, the two GGA functionals fail to correctly predict the location of these two bands, exhibiting a massive red-shift compared to the experimental spectrum. The (range-separated) hybrid functionals, on the other hand, exhibit a blue-shift of about 100 nm. Both the use of a larger basis set (see sec. 12.2.2) and the incorporation of solvation effects would likely stabilize the excited states, thereby red-shifting these excitations. As a general conclusion, the (range-separated) hybrid functionals reproduce the experimental spectrum much more reliably than GGA functionals for the most prominent part of the spectrum: the Q bands.

Having examined the low-energy region of the spectrum, the second step is to investigate the low-intensity bands in the region between 300 and 550 nm. The experimental spectrum shows only bands with negative specific rotations between 340 and 550 nm, and finally two weak positive bands between 300 and 340 nm. This general structure is only reproduced by the CAM-B3LYP calculation, which suggests that a good description of long-range interactions is required for the low-intensity bands. The CAM-B3LYP spectrum and the experimental spectrum taken from Ref. [280] are compared in fig. 12.2.4. Apart from the aforementioned blue-shift of the computed spectrum and the lack of coupling to vibrational modes, there seems to be an excellent agreement between theory and experiment for the MCD spectrum of ZnDiNTAP.

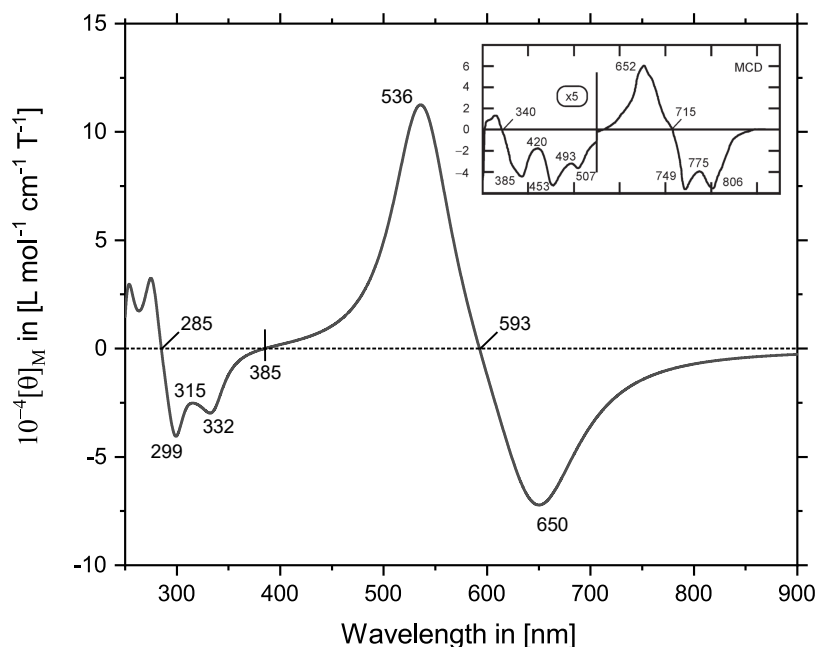


Figure 12.2.4.: MCD spectrum of ZnDiNTAP as calculated using CAM-B3LYP as well as def2-TZVP for Zn and def2-SVP for all other molecules. The two Q bands are located at 650 and 536 nm. Additional low-intensity peaks are highlighted between 250 and 400 nm. The experimental spectrum taken from Ref. [280] is presented for comparison. Both spectra are given in the same units. Printed with permission from Ref. [54].

This example emphasizes that the implementation carried out in this work can be used for real-world chemical applications. The calculation of MCD spectra in finite magnetic fields presents itself as a feasible alternative to approaches using second order perturbation theory, giving access to a tool which can be routinely used for sizeable molecules with dozens of atoms and more than a thousand basis functions.

13. Absorption Spectroscopy in Moderately Strong Magnetic Fields

In the previous chapter, the influence of weak magnetic fields on optical spectroscopy was discussed. The resulting magnetic circular dichroism spectroscopy was a consequence of two effects induced by the external magnetic field. Firstly, the reduced symmetry of electronic wave functions due to the presence of a magnetic field and secondly, the Zeeman splitting of degenerate excited states and, potentially, a degenerate ground state. In this chapter, moderately strong magnetic fields of up to 10,000 T are applied to molecular systems and the resulting absorption spectra are investigated. The term ‘moderately strong’ magnetic fields is somewhat ambiguous, as the largest non-destructive magnetic fields currently produced on earth exhibit field strengths of about 150 T.^[13] It is used here nonetheless in order to signify a certain regime of field strengths, where non-linear effects already affect molecular spectroscopy, but electronic ground states have not yet undergone spin-phase transitions.

As experimental data is not available for molecular spectroscopy under these conditions, the effects described from this chapter forward can currently only be investigated through quantum-chemical calculations. Consequently, great care should be taken in the study of molecular and spectroscopic properties in such conditions. For quantitative results, only high-level methods can be used and qualitative results should be carefully assessed using a variety of different methods.

In this chapter, the influence of moderately strong magnetic fields on electronic excitations is assessed. This is investigated for a variety of small and medium-sized molecules to evaluate which excitations are strongly affected by the presence of an external magnetic field. Such a more general study makes it possible to determine specific compounds which should have a strong field-dependence of their absorption spectrum in the ultraviolet/visible (UV/Vis) region. As an illustrative example of this behaviour, the influence of a magnetic field on the UV/Vis spectrum of tetracene is investigated, which constitutes a spectacular change of color. The results presented here have been published by the author in Refs. [53], [54] and [55].

13.1. Influence of Magnetic Field on Electronic Excitations

13.1.1. Computational Details

In this section, the influence of moderately strong magnetic fields on electronic excitations of small and medium-sized molecules is investigated. This constitutes a more general, qualitative study meant to highlight the cases in which molecules exhibit a strong field-dependence. As such, the TD-DFT method was used for most of the investigation carried out in this section. The molecules computed here belong to the set of 36 molecules introduced in sec. 10.1.^[53, 369] Molecular geometries were optimized using GMP2/def2-TZVP and numerical gradients, with the magnetic field aligned with either the Cartesian x -, y -, or z -axis.

In the first part of this section, sec. 13.1.2, electronic excitations for all 36 molecules were calculated at the PBE0^[373]/def2-TZVP^[370] level of theory. First, the electronic ground states were converged up to a threshold of $10^{-10} E_h$ for the electronic energy and 10^{-9} for the norm of the density matrix (denconv 9). All calculations were carried out using grid 4^[320] in TURBOMOLE. Using a spin Zeeman scaling of 0, the electronic ground state was kept as closed shell for each calculation, which was confirmed to be the electronic ground state for almost all examples using a stability analysis on the PBE0/def2-TZVP and CC2/def2-TZVP level. For more details on this stability analysis, see the supporting information in Ref. [54]. Finally, electronic excitations were calculated on the PBE0/def2-TZVP level using the RI- JK approximation with the corresponding def2-TZVP auxiliary basis set.^[371, 372]

A more detailed study of four electronic excitations of pyrazine, also part of the set of 36 molecules, is carried out in sec. 13.1.3. Electronic ground states were calculated at the DFT/def2-TZVPP^[370] level of theory using the functionals PBE,^[384] TPSS,^[385] TPSSh,^[385] and ω B97M,^[386] using grid 4 as implemented in TURBOMOLE. Corresponding excited states were calculated on the same level of theory using the RI- JK approximation with the def2-TZVPP auxiliary basis set.^[371]

13.1.2. Small and Medium-Sized Molecules

The aim of this section is to gain a more general understanding on the influence a moderately strong magnetic field has on electronic excitations. A selection of 36 small and medium-sized molecules was investigated, their structures were shown in fig. 10.2.1. Linear molecules were aligned with the Cartesian z -direction. For these

13. Absorption Spectroscopy in Moderately Strong Magnetic Fields

molecules, applying a magnetic field in the B_x or B_y direction is identical due to symmetry reasons. Non-linear molecules were aligned following the conventions of their respective point groups in the absence of magnetic fields. For pyrazine and tetrazine, the z -axis is aligned perpendicular to the molecular plane, with the x -axis and y -axis chosen such that the molecular point group is C_{2h} within the external field for all cases. Magnetic fields were applied at 1,000, 2,500, 5,000, 7,500, and 10,000 T.^[54] The resulting excitation energies are presented in fig. 13.1.1 for all molecules with electronic excitations below 4 eV in the absence of fields.

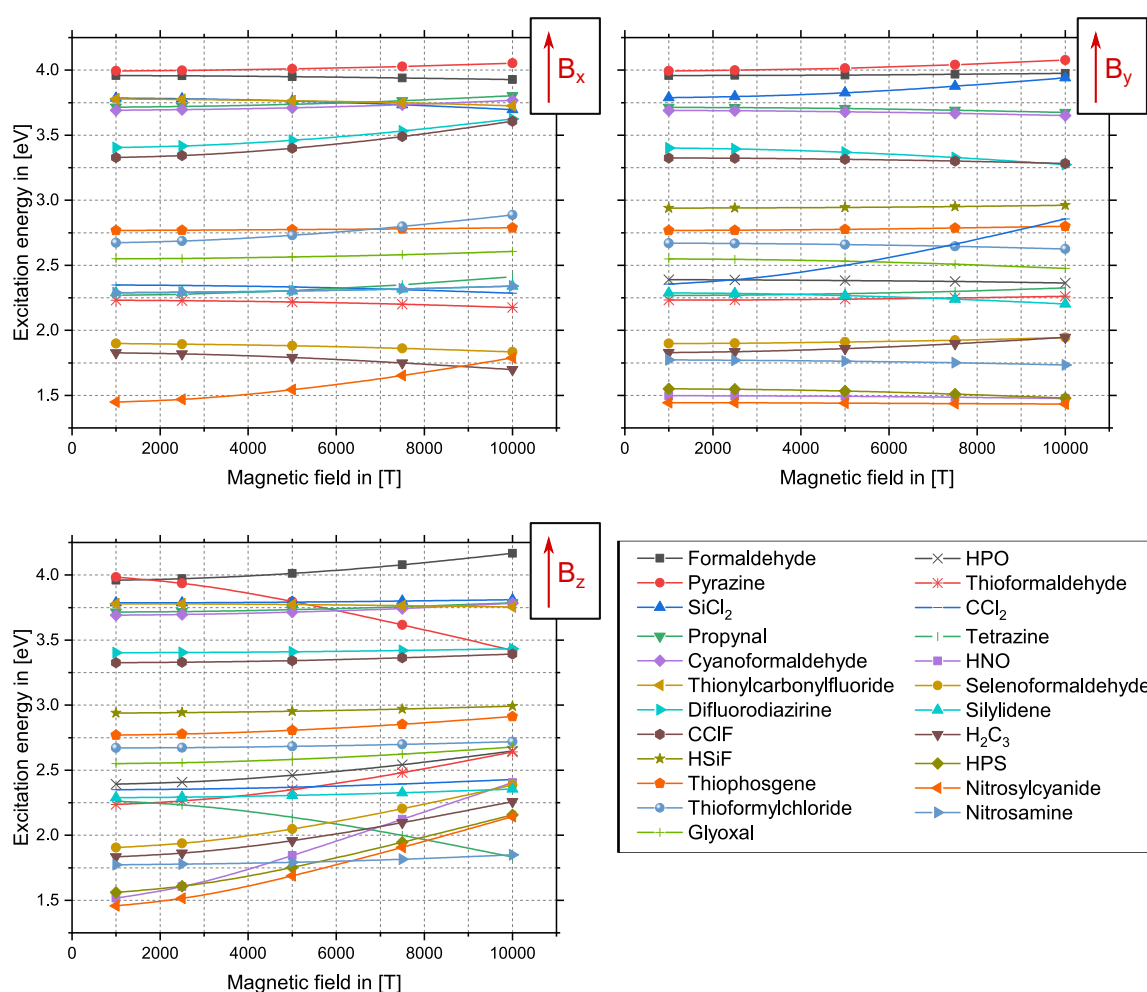


Figure 13.1.1.: Influence of an external magnetic field on the electronic excitations of several small to medium sized molecules. The magnetic field is aligned with the Cartesian components x (upper left), y (upper right) and z (lower left). Linear molecules are omitted in the B_x diagram due to symmetry. Geometries were optimized in the respective external field on the GMP2/def2-TZVP level. Electronic excitations are calculated using PBE0/def2-TZVP. Adapted with permission from Ref. [54].

Upon closer examination of fig. 13.1.1, a few more general patterns may be extracted. First and foremost, only a few molecules exhibit a strong field-dependence of their lowest singlet excited state. The direction of the external field appears to play a crucial role as well, and thus the three different cases should be discussed separately. Which molecules have excited states that strongly depend on the external field?

For a field only the B_x direction, four noteworthy examples are nitrosylcyanide (25), thioformylchloride (34), CCIF (4), and H_2C_3 (16). Nitrosylcyanide is a planar molecule with C_s symmetry ($\rightarrow C_1$ in the external magnetic field), which lies in the xz -plane. The magnetic field is partly aligned with the π -system, and the lowest excitation energy rises with an increasing external magnetic field. Thioformylchloride is similar to nitrosylcyanide in almost every regard. CCIF is an electrophilic carbene with C_s ($\rightarrow C_1$) symmetry. While not exhibiting a traditional π -system, singlet carbenes are generally considered similarly, with traditional descriptions suggesting an sp^2 hybridization of the carbon atom.^[387] The excitation energy of CCIF is significantly increased if larger fields are applied. The H_2C_3 molecule, on the other hand, is C_{2v} ($\rightarrow C_s$) symmetric, and lies in the yz -plane. The magnetic field is aligned in a perpendicular orientation to the molecule's π -system and the excitation energy is reduced with an increasing field.

If the external magnetic field is applied in the B_y direction, a different picture emerges. The two most prominent examples with a strong field-dependence are CCl_2 (3) and $SiCl_2$ (30), both with C_{2v} ($\rightarrow C_s$) symmetry. They are derivatives of methylene and silylene, respectively, and behave similarly to the previously discussed CCIF molecule. The magnetic field is applied perpendicular to the C_2 axis, which constitutes a symmetry axis only present in the absence of a field. As a result, the lowest excitation energy is considerably increased.

Finally, applying the magnetic field in the B_z direction, quite a few molecules are strongly affected. Noteworthy examples are HNO (19), HPO (20), HPS (21), selenoformaldehyde (29), thioformaldehyde (33), and thiophosgene (36). All of these molecules have their lowest excited state increased by the presence of an external magnetic field. They all have in common that the field is applied in parallel orientation to their respective π bonds. For HNO, HPO, and HPS the symmetry is C_s ($\rightarrow C_1$), while 29, 33, and 36 constitute a set of molecules with C_{2v} ($\rightarrow C_2$) symmetry. There are two examples of molecules for which the lowest excitation energy is considerably lowered due to the presence of an external magnetic field: pyrazine (28) and tetrazine (32). Both are highly symmetric D_{2h} ($\rightarrow C_{2h}$) molecules with aromatic systems and π -systems aligned perpendicular to the external magnetic field.

To conclude, excitation energies of π -systems are most affected by the presence of external magnetic fields. Two general tendencies can be observed. First, the lowest excitation energies for π -systems are blue-shifted if a field is aligned parallel to the respective π -bonds, particularly apparent for systems with low excitation energies. Second, π -systems in general and aromatic π -systems in particular exhibit significant red-shifts if the external field is applied perpendicular to their π -bonds.

13.1.3. Electronic Excitations of Pyrazine

Pyrazine is an aromatic compound, which, in the previous section, was shown to exhibit a significant dependence of its lowest excitation energy with an increasing, perpendicularly applied magnetic field. It is worth examining the absorption spectra of this compound in more detail. The four excitations lowest excitations of symmetry $B_{1u} (\rightarrow B_u)$, $A_u (\rightarrow A_u)$, $B_{3u} (\rightarrow B_u)$, and $B_{2u} (\rightarrow B_u)$ are investigated here, with their field-dependence being depicted in fig. 13.1.2.

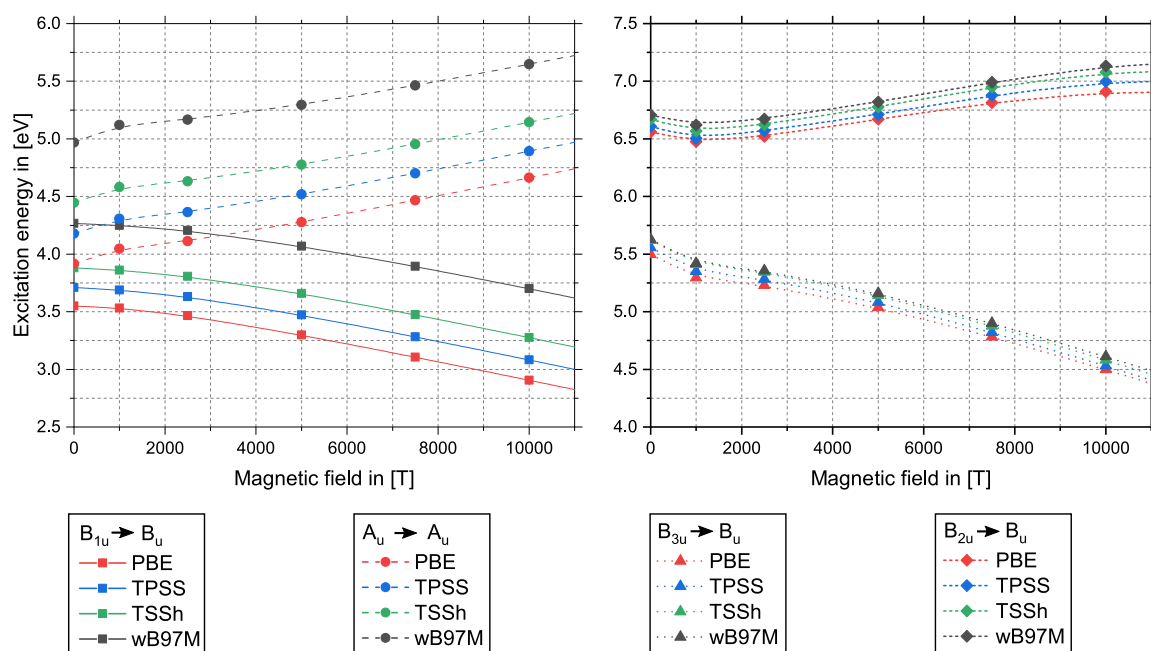


Figure 13.1.2.: Field-dependence of excitation energies for pyrazine. Magnetic fields of up to 10,000 T are applied perpendicular to the π -system. Depicted here are the lowest excitations of symmetry $B_{1u} (\rightarrow B_u)$ and $A_u (\rightarrow A_u)$ on the left, as well as $B_{3u} (\rightarrow B_u)$ and $B_{2u} (\rightarrow B_u)$ on the right. All calculations were carried out on the DFT/def2-TZVPP level using PBE (red), TPSS (blue), TPSSh (green), and ω B97M (black). Adapted with permission from Ref. [55].

The results from calculations employing different types of density functionals are in very good agreement qualitatively for the B_{1u} ($\rightarrow B_u$) and A_u ($\rightarrow A_u$) excitations, as well as quantitatively for B_{3u} ($\rightarrow B_u$) and B_{2u} ($\rightarrow B_u$). The GGA functional PBE generally predicts the lowest excitation energies for every excitation, followed by the MGGA functional TPSS, the hybrid MGGA functional TPSSh and, finally, the range-separated hybrid MGGA functional ω B97M. All excitations exhibit a strong field-dependence, with B_{1u} ($\rightarrow B_u$) and B_{3u} ($\rightarrow B_u$) having their respective excitation energies lowered in an increasing field, while excitation energies of A_u ($\rightarrow A_u$) and B_{2u} ($\rightarrow B_u$) are raised.

In passing, it should be noted that the field-dependence of all excitations in fig. 13.1.2 is practically linear. However, they show non-linear behaviour close to zero-field case, with smooth transitions into the linear part at about 1,000T. Presumably, this is a consequence of the external field lowering the system's molecular symmetry, but a careful investigation of this behaviour remains the subject of future work.

In conclusion, the field-dependence of excitation energies was examined for a variety of small to medium-sized molecules and for the pyrazine molecule in more detail. This study now enables us to predict molecules with strong field-dependence in the visible part of the absorption spectrum. For instance, for a significant red-shift, an aromatic compound with a relatively low $\pi \rightarrow \pi^*$ excitation should be aligned perpendicular to an external magnetic field.

13.2. UV/Vis Spectroscopy and Color Change of Tetracene

13.2.1. Computational Details

One example for a molecule expected to exhibit a significant red-shift of its absorption spectrum in the visible region is tetracene. It is an aromatic compound with a sizeable π -system and its orange-red color indicates a relatively low-lying absorption band for the $\pi \rightarrow \pi^*$ transition. Its molecular structure (D_{2h}) is depicted in fig. 13.2.1.

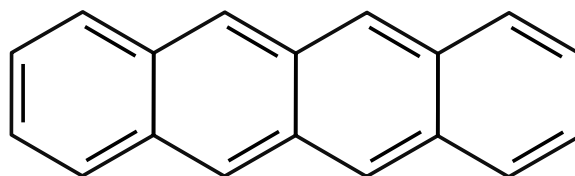


Figure 13.2.1.: Molecular structure of the tetracene molecule.

In order to obtain more quantitative results, the GW/BSE method is used for investigations carried out in this section. First, the molecular geometry was optimized at the DFT/def2-TZVP^[370] level of theory in the absence of magnetic fields using the hybrid and range-separated hybrid functionals PBE0,^[373] B3LYP,^[212, 378, 379] BHLYP,^[212] and CAM-B3LYP,^[380] respectively. These functionals predict somewhat different molecular sizes of tetracene. While all functionals result in a very similar short axis, the long axis of the molecule has a size-dependence of the order PBE0 > B3LYP > CAM-B3LYP > BHLYP. Subsequent calculations are carried out using the optimized geometries for every functional, as well as using the CAM-B3LYP geometry for every functional in order to estimate the indirect influence of the density functional through the molecular geometry.

Finally, GW/BSE calculations were carried out using all four reference functionals, here denoted as @DFT. All calculations were performed using TURBOMOLE and grid 5.^[320] Convergence criteria of $10^{-10}E_h$ for the electronic energy and $10^{-8}a_0^{-3}$ for the norm of the density matrix (denconv 8). First, the electronic ground state was computed on the DFT/def2-TZVP level. Second, the $evGW$ method was used in combination with the contour-deformation (CD) technique. Here, the ten highest occupied and ten lowest unoccupied spinors are corrected using $evGW$, while the remaining spinor energies are shifted accordingly.^[53] This is written as CD- $evGW(10)$. Subsequently, the BSE was evaluated for the lowest 75 eigenvalues. The abbreviation for the entire approach is CD- $evGW(10)/BSE@DFT$. UV/Vis spectra are obtained by broadening with Lorentzian functions and a FWHM of 0.3 eV.

13.2.2. UV/Vis Spectrum in Absence of Magnetic Field

The absorption spectrum of tetracene in the ultraviolet and visible region has been extensively studied in the literature, both experimentally and theoretically.^[388–392] In the absence of magnetic fields, it is dominated by three electronic excitations. The transition from the highest occupied molecular orbital (HOMO) to the lowest unoccupied molecular orbital (LUMO) is referred to as p -excitation and shows a band which peaks between 455–477 nm depending on external factors. This transition is of B_{2u} symmetry and polarized along the short axis of the molecule.^[388] It is responsible for the vibrant, orange color of tetracene.

The α -excitation denotes the HOMO \rightarrow LUMO+1 transition, peaking between 373–393 nm. Its oscillator strength is comparatively small. The β -excitation corresponds to the HOMO–1 \rightarrow LUMO transition and shows a peak at 272–275 nm. Its oscillator

strength is the largest of the three excitations, and as a result, it is the most intense band in the UV/Vis spectrum of tetracene. Both the α - and β -excitations are of B_{3u} symmetry and polarized along the long axis of the molecule.^[388] Transition densities for all three transitions were calculated using the CD-ev $GW(10)/BSE@CAM-B3LYP$ method and def2-TZVP basis set. They are presented in fig. 13.2.4 and discussed in more detail later.

In the theoretical study carried out in this work, the geometries were first optimized using the four density functionals PBE0, B3LYP, BHLYP, and CAM-B3LYP. Subsequently, excitation energies of the lowest three excitations were evaluated at the CD-ev $GW(10)/BSE@DFT$ level of theory. The results are listed in table 13.2.1.

Table 13.2.1.: Excitation energies for the three lowest transitions of tetracene in the absence of a magnetic field. Geometries were optimized using the four indicated functionals and vertical transitions were obtained using the CD-ev $GW(10)/BSE@DFT$ method and def2-TZVP basis set. Experimental values^[388–392] are listed for comparison. All values in [nm]. Adapted with permission from Ref. [53]

Excitation	@PBE0	@B3LYP	@BHLYP	@CAM-B3LYP	Exp. ^[388–392]
p -Excitation	614	505	465	470	455–477
α -Excitation	370	369	349	354	373–393
β -Excitation	270	269	260	265	272–275

The excitation energies obtained from these calculations show good agreement with the experiment for the α - and β -excitation. However, the p -excitation is described very poorly with @PBE0 and @B3LYP, while @BHLYP and @CAM-B3LYP show very similar to results with one another and generally agree well with the experiment. However, as a *post* Kohn-Sham method, GW/BSE should not yield results which are this strongly dependent on the reference functional.

But maybe the reference functional is not the root cause of this problematic behaviour? Another option could be the molecular geometries which were optimized using different functionals. In order to test this, the geometry as optimized using CAM-B3LYP was taken, which yielded good results for the excitation energy using CD-ev $GW(10)/BSE@CAM-B3LYP$. Subsequent calculations with the CD-ev $GW(10)/BSE@DFT$ method were performed, using this fixed geometry. The resulting excitation energies are listed in fig. 13.2.2.

Table 13.2.2.: Excitation energies for the three lowest transitions of tetracene in the absence of a magnetic field. Geometries were optimized at the CAM-B3LYP/def2-TZVP level for all calculations. Experimental values^[388–392] are listed for comparison. All values in [nm]. Adapted with permission from Ref. [53]

Excitation	@PBE0	@B3LYP	@BHLYP	@CAM-B3LYP	Exp. ^[388–392]
p -Excitation	484	487	468	470	455–477
α -Excitation	359	360	351	354	373–393
β -Excitation	264	264	261	265	272–275

The dependence of electronic excitations on the reference functional is almost completely eliminated if all calculations are carried out using the same molecular geometry, indicating that the inconsistent results were a consequence of poor molecular geometries. The @PBE0 and @B3LYP results for the p -excitations are still slightly red-shifted compared to the experimental values, but both the @BHLYP and @CAM-B3LYP show excellent agreement with the experiment. It should be noted that the α - and β -excitations are still slightly blue-shifted compared to the experimental spectrum. The UV/Vis spectra as calculated with the CD-*evGW*(10)/BSE@BHLYP and @CAM-B3LYP methods are presented in table. 13.2.2.

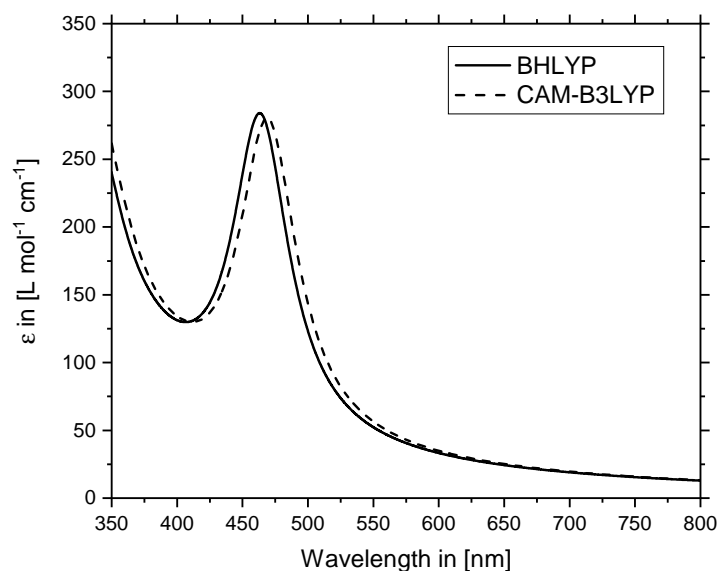


Figure 13.2.2.: UV/Vis spectrum of tetracene as calculated using the CD-*evGW*(10)/BSE@BHLYP (solid line) and @CAM-B3LYP (dashed line) methods and def2-TZVP basis set. Excitation energies were broadened using Lorentzians and a FWHM of 0.3 eV.

13.2.3. Influence of External Magnetic Field

The electronic excitations of tetracene in the absence of a field were assessed using the *GW*/*BSE* method, finding good results particularly with the @BHLYP and @CAM-B3LYP reference functionals. Using these two methods and the molecular geometry optimized on the CAM-B3LYP/def2-TZVP level, the influence of an external magnetic field on the UV/Vis spectrum is now examined. As discussed in detail in sec. 13.1 of this work, the magnetic field should be applied in perpendicular orientation to the π -system to induce a significant red-shift of the spectrum.

Calculations were carried out in steps of 1,000 T up to a field strength of 9,000 T, above which the ground state becomes unstable. Within the perpendicularly applied field, the molecular symmetry is lowered to C_{2h} . All excitations were carefully tracked, including γ and δ which were included to assess whether lower lying states play a role in the visible part of the spectrum at higher field strengths. All five excitations (p , α – δ) are of B_u symmetry in the field. The results are presented in fig. 13.2.3.

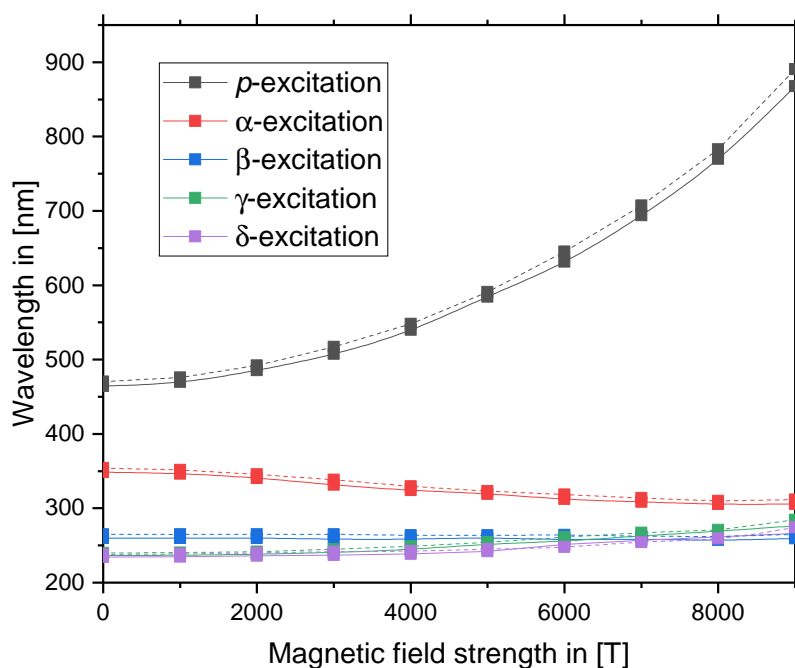


Figure 13.2.3.: Influence of an external magnetic field on the electronic excitations of tetracene. The field is applied in perpendicular orientation to the molecule's π -system. All calculations were carried out using the CD-*evGW*(10)/*BSE*@BHLYP (solid line) and @CAM-B3LYP (dashed line) methods and def2-TZVP basis set. Reprinted with permission from Ref. [53].

As expected, the p -excitation is strongly red-shifted by the presence of the external field, while higher excitations are less strongly affected. The entire structure of these excitation changes due to the presence of the external field, which can be investigated by examining the transition densities. They are presented in fig. 13.2.4 in the absence of fields and in the presence of a magnetic field with a strength of 8,000 T. Particularly the p - and β -excitations appear to be more delocalized within an external magnetic field, while the transition density for the α -excitation seems the least affected.

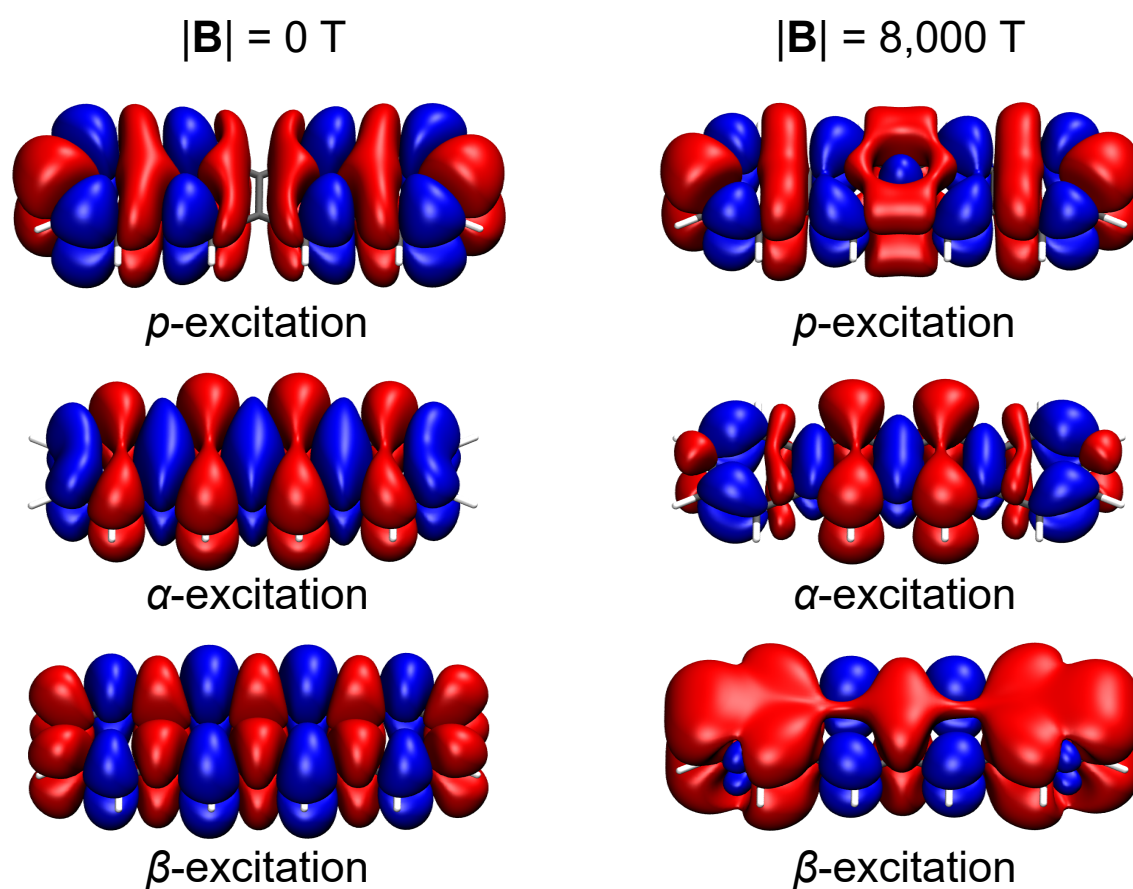


Figure 13.2.4.: Transition densities of the p -, α - and β -excitations of tetracene in the absence of a magnetic field (left) and in a field of 8,000 T. The color blue indicates the loss of electron density, while the color red indicates a gain thereof. Calculated using CD-evGW(10)/BSE@CAM-B3LYP and the def2-TZVP basis set. Plots were generated using VMD with an isovalue of $0.0001a_0^{-3}$ for the p -excitation and $0.0002a_0^{-3}$ for α and β . Partly reprinted with permission from Ref. [53].

Using all of these results, the UV/Vis spectra in the presence of increasingly large magnetic fields may be computed in an identical manner to the zero-field case. The resulting spectra are shown in fig. 13.2.5, where not only the five aforementioned

excitations were used to generate the spectra, but the lowest 75 excitations. While some excitations do exhibit very small oscillator strengths in the visible region within stronger fields, the UV/Vis spectrum is still dominated by the five excitations which were previously mentioned (p , α - γ).

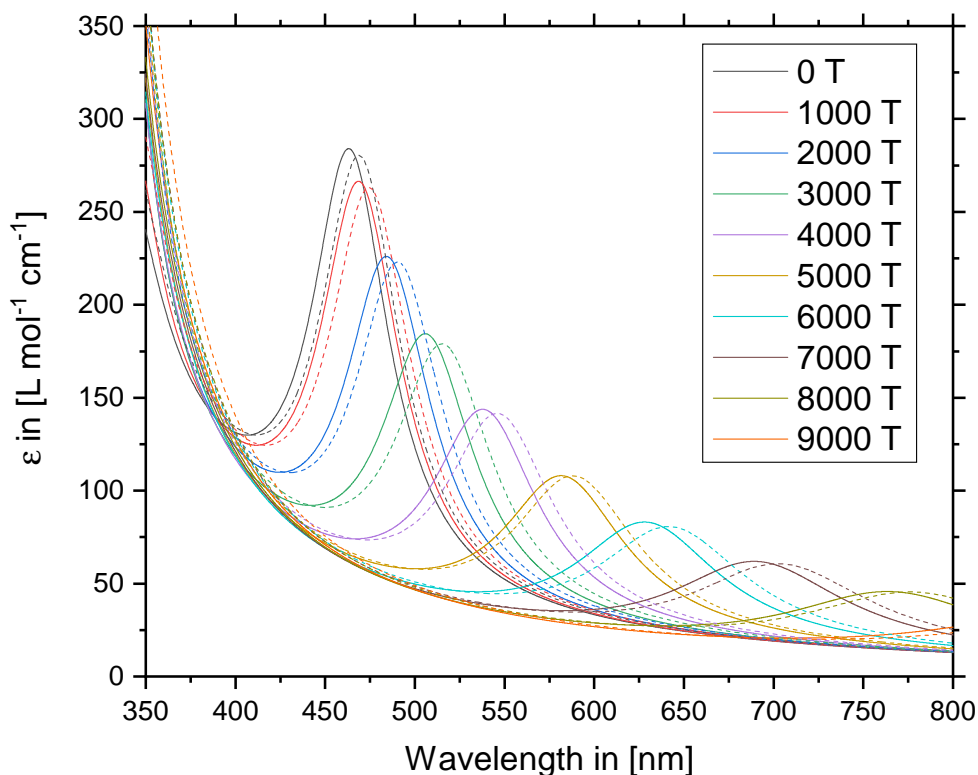


Figure 13.2.5.: Influence of an external magnetic field on the UV/Vis spectrum of tetracene. Calculations were carried out with CD-evGW(10)/BSE@B3LYP (solid lines) and @CAM-B3LYP (dashed lines) and the def2-TZVP basis set. Excitation energies were broadened using Lorentzians and a FWHM of 0.3 eV. Reprinted with permission from Ref. [53].

13.2.4. Prediction of Color Change

As mentioned before, the UV/Vis spectrum is the optical absorption spectrum in the ultraviolet and visible region of electromagnetic radiation. Thus, the color of a compound is intrinsically linked to this form of spectroscopy. The RGB color code can be obtained through numerical integration over the red (R), green (G), and blue (B) parts of the spectrum. Relative intensities may additionally obtained by integration over the entire visible part of the spectrum.

For tetracene, the color was evaluated using the UV/Vis spectra shown in fig. 13.2.5. The resulting colors are presented in fig. 13.2.6. Starting from the vibrant orange color tetracene is known to exhibit in the absence of fields, the color starts changing with an increasing magnetic field. As the p -excitation is red-shifted through the entire visible part of the spectrum, the molecule shifts from orange-red to pink and purple, until reaching a vibrant blue and finally a light cyan color. In a field of 9,000 T, the p -band hardly absorbs any more light in the visible region of the spectrum and the resulting color is almost exclusively a consequence of its absorption at the very edge of the infrared region.

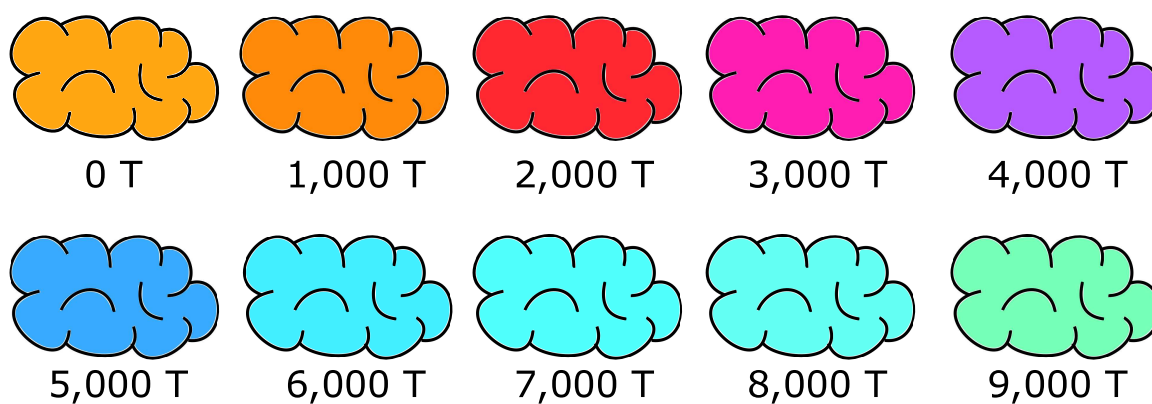


Figure 13.2.6.: Color change of tetracene induced by the presence of increasingly strong magnetic fields up to 9,000 T. Calculations were carried out with the CD-evGW(10)/BSE@CAM-B3LYP method and def2-TZVP basis set. All excitation energies were broadened using Lorentzians and a FWHM of 0.3 eV. The resulting UV/Vis spectra were used to obtain the RGB codes of the color through a numerical integration over the red, green and blue sections of the spectrum. The intensity was scaled relatively to the zero-field case. Reprinted with permission from Ref. [53].

14. Rotational-Vibrational Spectroscopy in Strong Magnetic Fields

The previous two applications discussed in this work were concerned with molecular spectroscopy in the ultraviolet and visible region of the electromagnetic spectrum. Both MCD and UV/Vis spectroscopy need (polarized) light in this region, as it is capable of inducing electronic excitations. Consequently, the theoretical description of this phenomenon required the time-dependent propagation of the electronic wave function and/or electron density. The influence of an external magnetic field on the resulting absorption spectra was investigated through an explicitly quantum-mechanical treatment of the field. In this chapter, molecular spectroscopy in the infrared and microwave region of the electromagnetic spectrum is examined. Absorption spectroscopy in this region is used to investigate molecular vibrations and rotations. For molecules in the gas phase, both forms of nuclear motion are typically coupled. The theoretical description of molecular motion is typically carried out using a semi-classical approach. For molecules in strong magnetic fields, it was introduced in sec. 7 of this work. Compared to the field-free case, the solution to the resulting equations of motion is vastly more complicated due to the presence of (screened) Lorentz forces acting on the moving nuclear charges. Therefore, *ab initio* molecular dynamics is used in this work for the simulation of rovibrational spectra in strong magnetic fields.

Two small systems are investigated in this chapter: molecular hydrogen (H_2) and lithium hydride (LiH). The outline for the investigation of rovibrational spectra of these two molecules is identical. First, general effects induced by the presence of an external magnetic field are discussed. Second, selected nuclear trajectories for the nuclear motion are presented. Third, an exemplary rovibrational spectrum for one magnetic field strength is introduced and discussed. Finally, Boltzmann-averaged spectra generated from a canonical ensemble of trajectories are shown and the influence of a strong magnetic field is considered. The results discussed here were obtained in collaboration with Monzel, Peters, Tellgren, Helgaker, and Klopper and presented in Ref. [57]. This chapter follows the general outline introduced therein.

14.1. Computational Details

All trajectories and corresponding rovibrational spectra presented in this chapter have been computed using the Tajima^[298] algorithm as presented in Ref. [57]. For more information on this algorithm, the interested reader is referred to this publication. In order to function, it requires the following quantities for the relevant region, where the nuclear motion takes place:

- Total electronic energies,
- Corresponding molecular gradients,
- The Berry curvature tensor.

All of these quantities may be pre-computed on a grid using *ab initio* quantum chemistry and approximated through splines for all points in between. The *ab initio* computation of molecular gradients can be circumvented, using gradients of the corresponding total electronic energy spline instead. The total electronic energies were obtained on the GMP2/def2-TZVP^[370] level for all calculations discussed in this chapter. They were computed using TURBOMOLE, requiring a prior calculation done with GHF/def2-TZVP. For GMP2, the RI-*C* approximation was used with an auxiliary def2-TZVP^[371, 372] basis. The Berry curvature tensor was computed using the implementation presented in chapter 11. It was calculated on the GHF/def2-TZVP level and normalized to fulfill the relevant sum rules exactly. This step is relevant, as otherwise a small portion of Lorentz forces are not properly screened, leading to inconsistent results. The magnetic field is applied in the *z*-direction for all cases.

14.2. Rovibrational Spectrum of Molecular Hydrogen

14.2.1. Potential Energy Surface

Before investigating molecular rotations and vibrations for H₂ in a strong magnetic field, the BO potential energy surface should be examined. This will help in estimating the general effects which should be expected as a result of the external field. First, the electronic states of H₂ should be discussed. In the absence of a magnetic field, H₂ has a singlet ground state of ¹Σ_g⁺ symmetry and a non-binding excited state characterized by the term symbol ³Σ_u⁺.^[393] Within an external magnetic field, the point group of H₂ is either C_{∞h} if the field is applied parallel to the bond, C_{2h} for a perpendicular orientation and C_i otherwise.^[133] The ground state (S₀) thus becomes ¹Σ_g in the

parallel case, and 1A_g in all other cases, while the excited state (T_1) becomes $^3\Sigma_u$ for the parallel case, and 3A_u otherwise.

While the HF method properly describes the spin symmetry of the electronic wave function close to the equilibrium distance, this is not generally true when considering the dissociation limit. Beyond the Coulson–Fischer point, the RHF method retains the proper spin symmetry, $\langle S^2 \rangle = 0$, of the electronic wave function while dissociating to an egregiously wrong limit. The UHF method dissociates to the proper limit, but exhibits a strongly spin-contaminated electronic wave function.^[394, 395] To illustrate the effects of an external magnetic field, MP2 calculations were performed at exemplary field strengths of $|\mathbf{B}| = 0.01B_0$ and $|\mathbf{B}| = 0.5B_0$, both for the parallel and perpendicular orientation. The resulting PES are shown in fig. 14.2.1. All calculations use a GHF reference, but the RHF limit was carefully converged as well, ensuring that $\langle S^2 \rangle = 0$ for every single calculation. Excited states were obtained through spin Zeeman scaling.

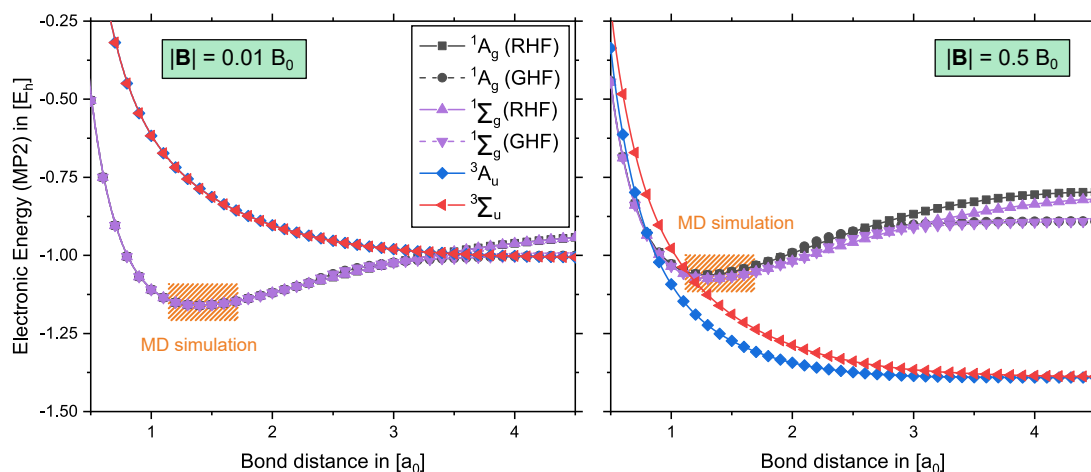


Figure 14.2.1.: Potential energy surface of H_2 in two magnetic fields, $|\mathbf{B}| = 0.01B_0$ (left) and $|\mathbf{B}| = 0.5B_0$ (right), calculated on the GMP2/def2-TZVP level. The perpendicular (black, blue) and parallel (purple, red) orientations of the external field with respect to the bond are considered. The relevant regions for the MD simulations are indicated, lying well before the Coulson–Fischer point.

For field strengths beyond about $|\mathbf{B}| = 0.4B_0$, T_1 becomes the electronic ground state at equilibrium distance. As T_1 is non-binding, no molecular vibrations or rotations can be observed, as the molecule would simply dissociate. Therefore, all observations described in this section reference the S_0 state. It should be emphasized that such an investigation is relevant for several reasons, even if S_0 is not the electronic ground state. First and foremost, the observations for rovibrational spectra of H_2 in strong magnetic

fields can be used for a more general understanding of how nuclear motion is affected in external fields. Additionally, excited states may be populated, especially under conditions where such strong magnetic fields are present, such as in the atmosphere of magnetic white dwarfs.

The relevant regions in which MD simulations are run are indicated in fig. 14.2.1. They all lie well before the Coulson–Fischer point, which was carefully checked for all cases. Therefore, GHF may be used as a reference for the MP2 calculations, exhibiting the correct spin symmetry. Finally, it should be noted that a rotational barrier is induced by the presence of the magnetic field. The parallel orientation between the hydrogen-hydrogen bond and the external field appears to be more stable for both the S_0 and T_1 states. The rotational barrier was calculated for different field strengths and is illustrated in fig. 14.2.2

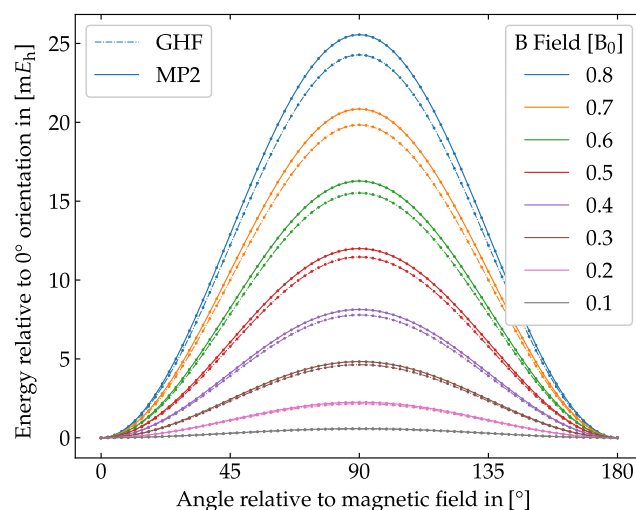


Figure 14.2.2.: Potential energy barrier for the rotation of the H_2 molecule relative to the 0° (parallel) orientation. Calculated on the GHF/def2-TZVP (dashed line) and GMP2/def2-TZVP (solid line) levels of theory, respectively. All calculations are carried out for the equilibrium bond length in the parallel orientation, assuming a rigid rotator. Reprinted with permission from Ref. [57].

The rotational barrier can be well described through a cosine-like potential with a maximum at the perpendicular orientation. Rotational barriers are generally larger if correlation effects are taken into account. This is expected to have a large impact for molecular rotations, as any rotation must overcome this barrier. Even in weak fields, rotational movement will therefore be slower close to a perpendicular orientation. If the field strength is large enough, the H_2 molecule may not overcome this barrier at all, leading to librational motion.

14.2.2. Molecular Rotations and Vibrations

Having discussed the general features of the underlying BO PES, two exemplary trajectories representing molecular rotation shall now be examined. Both were obtained in a magnetic field of $|\mathbf{B}| = 0.2B_0$, one with a slightly higher initial kinetic energy of $3.5 mE_h$ and the other one with a slightly lower initial kinetic energy of $2.8 mE_h$. Both trajectories were obtained through a simulation of 435 fs. They are depicted in fig. 14.2.3, with darker colors indicating slower motion and brighter colors representing faster motion.

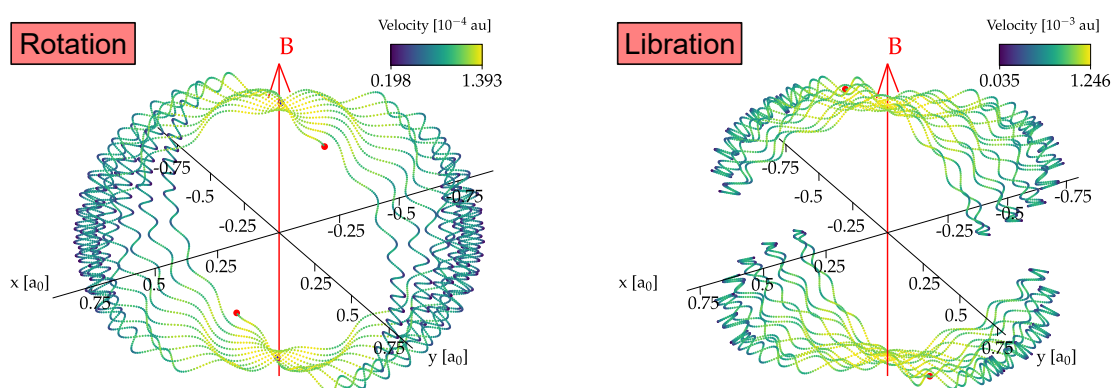


Figure 14.2.3.: Trajectories as calculated for a rotational (left) and librational motion of H_2 in an external magnetic field of $|\mathbf{B}| = 0.2B_0$. The rotation was initiated with a kinetic energy of $3.5 mE_h$ and the libration with $2.8 mE_h$. Darker colors indicate slower motion and brighter colors indicate faster motion. Both rotational and vibrational motion is coupled to stretching vibrations, since the rotational barrier is dependent on the bond length. Intramolecular cyclotron rotation is responsible for a rotation of 90° about the z -axis in 435 fs of simulation time. Adapted with permission from Ref. [57].

Three main effects induced by the presence of a strong, external magnetic field can be observed from these two trajectories:

1. Rotational motion gets considerably slower close to the maximum of the rotational barrier at the perpendicular orientation. On the one hand, an initial kinetic energy of $3.5 mE_h$ is enough to cross this barrier, resulting in rotational motion. On the other hand, the lower initial kinetic energy of $2.8 mE_h$ is not enough, resulting in a libration.
2. The equilibrium bond length depends on the angle between molecule and magnetic field. As a consequence, rotational (and librational) motion is generally

coupled to stretching vibrations of the molecule. An example for such a coupled motion can be seen in fig. 14.2.3.

3. An additional motion corresponding to a very slow intramolecular rotation can be seen for both vibrations and librations. This is induced by Lorentz forces acting on the moving nuclei and directly corresponds to a cyclotron rotation as introduced in sec. 2.3.2 of this work. This intramolecular cyclotron rotation also couples to rotational and librational motion.

Molecular vibrations should be expected to behave similarly to their zero-field counterparts, with only stretching vibrations existing for linear molecules. Due to the interdependence between bond length and rotation barrier, vibronic motion is generally coupled to rotations and intramolecular cyclotron rotations. Furthermore, vibrational and rotational overtones should be more pronounced in an external magnetic field due to the increased anharmonicity of the PES.

14.2.3. Rotational-Vibrational Spectra in Strong Magnetic Fields

The resulting rovibrational spectra are highly complicated, even for the simple case of molecular hydrogen. A power spectrum may be obtained from a trajectory through a Fourier transformation of the velocity, requiring simulation times of a few picoseconds. For the two initial conditions chosen for the trajectories in fig. 14.2.3, the resulting rovibrational spectra are presented in fig. 14.2.4. The spectra depicted therein were simulated using a BO PES generated from the GHF and MP2 methods, respectively, to highlight the effects of electron correlation.

First, the rotational part of the spectrum should be examined. As the rotational isotropy is broken due to the presence of an external field, the corresponding rotations must be decomposed into their (z)-, as well as (x,y)-components. The fundamental frequency for the rotational movement can be found at about 200 cm^{-1} , with the signal being split into a triplet overall. Upon further examination, the triplet turns out to be a combination of singlet corresponding to the (z)-component, and a doublet of peaks corresponding to the (x,y)-components. The coupling constant is exactly twice the intramolecular cyclotron frequency, indicating that this motion only couples to the (x,y)-components of rotational motion. Due to molecular symmetry, rotational overtones only appear at every odd multiple of the fundamental frequency.

For librations, a slightly different picture presents itself. While the (x,y)-component of librational motion behaves similarly to its rotational counterpart, the (z)-component only appears at every even multiple of the fundamental frequency. This may be under-

stood by imagining only the Cartesian z -component of such a librational movement and comparing it to the rotational one. Since the nuclei cannot pass the rotational barrier, they arrive at their initial positions in the same interval, in which only half a 'proper' rotation is carried out. As such, the (z)-component of a libration should be expected at twice the frequency of its rotational counterpart. Further, peaks for librational motion are slightly blue-shifted compared to their rotational counterparts, due to them not having to pass the rotational barrier itself and thus the region in which the motion is slowed down the furthest (see the dark blue parts in fig. 14.2.3).

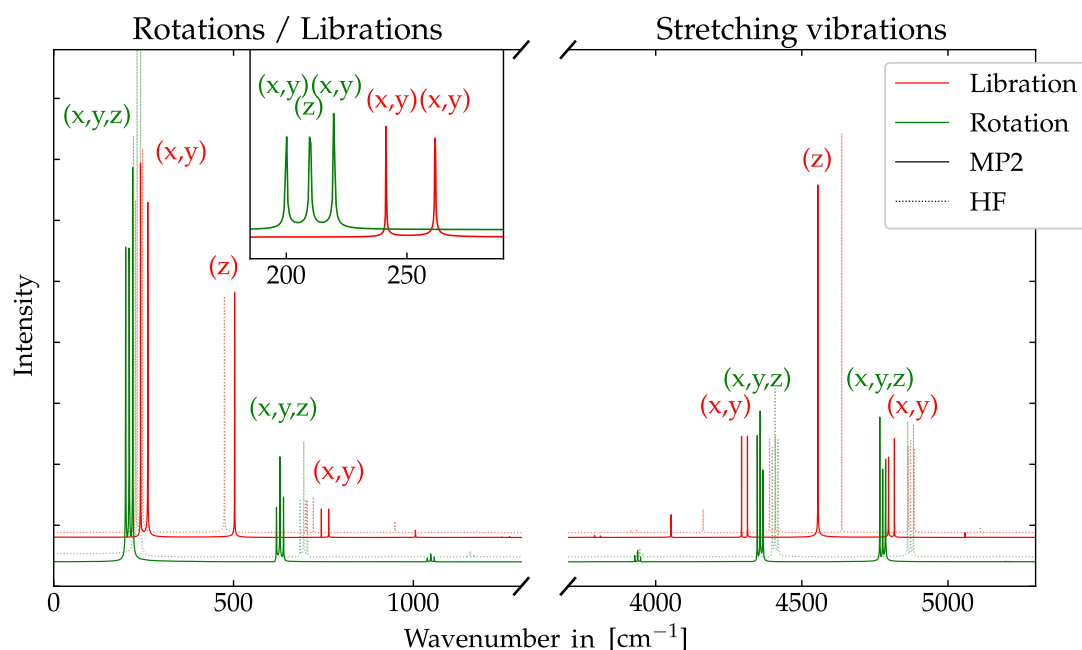


Figure 14.2.4.: Rovibrational spectrum of H_2 simulated from identical initial conditions used for the trajectories depicted in fig. 14.2.3. Power spectra are obtained through a Fourier transformation of the corresponding MD simulations. Depicted here are the spectra for initial conditions leading to librations (red) and rotations (green) using the MP2 (bold) and GHF (pale) methods. Reprinted with permission from Ref. [57].

Investigating the vibrational part of the spectrum, the stretching vibration appears at about 4600 cm^{-1} , blue-shifted compared to the zero-field case. This shift to higher frequencies follows directly from the steeper potential energy minimum, visible for instance in fig. 14.2.1. As previously discussed, vibronic motion will always be coupled to rotational motion due to the anharmonicity of the potential energy surface, an effect which is even more pronounced in the presence magnetic fields. The resulting vibronic spectrum for a coupling to rotational motion exhibits a P - and R -branch,

in which a hyperfine structure can be observed. It corresponds to the coupling of rotations to the intramolecular cyclotron rotation. Consequently, the structure of this spectrum may be described as a triplet of a doublet.

For the coupling to a librational motion, a slightly different pattern emerges. In addition to the P - and R -branches, a Q -branch becomes visible, corresponding to the decoupled (z)-component of librational motion. Consequently, the P - and R -branches are both doublets due to coupling with the intramolecular cyclotron rotation, while the Q -branch only contains a high-intensity singlet. The existence of a Q -branch in a rovibrational spectrum of H_2 is thus an indication for librational movement.

Finally, a canonical ensemble of spectra should be calculated, as initial conditions have a high impact on the resulting rovibrational spectra. This was done for field strengths up to $|\mathbf{B}| = 1.8 B_0$, using Boltzmann-distributed initial conditions and a target temperature of 1500 K. The resulting canonical ensemble of spectra is presented in fig. 14.2.5.

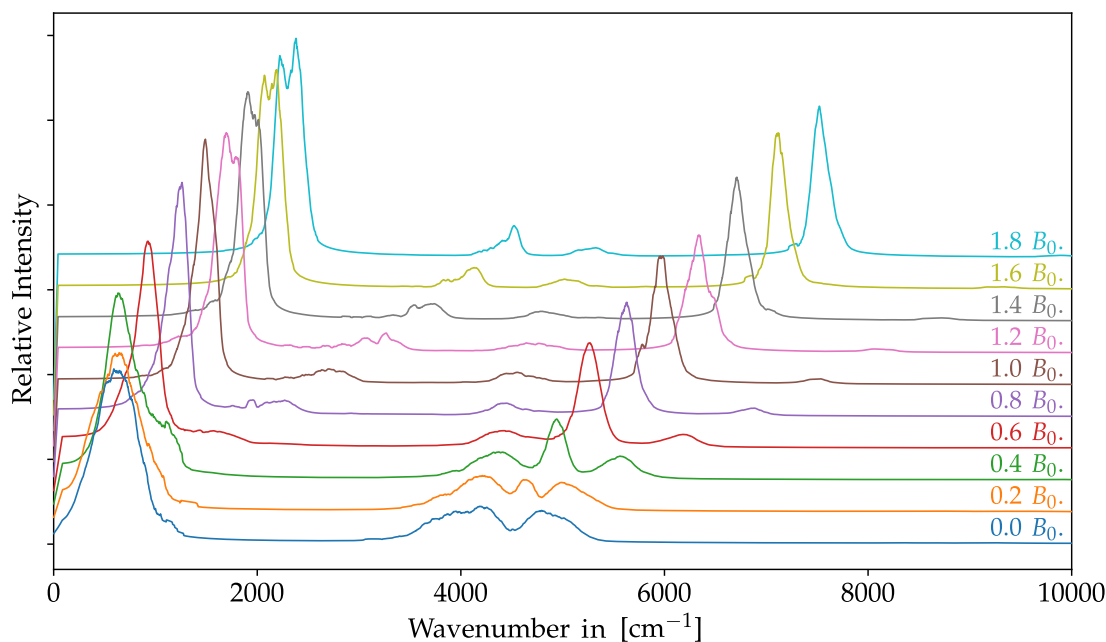


Figure 14.2.5.: Canonical ensemble of rovibrational spectra for H_2 in strong magnetic fields. Initial conditions were obtained from a Boltzmann-distributed set of velocities. The simulation time for each spectrum is 1 ps, and the averaged spectrum is obtained by smoothing over an interval of $\omega = \pm 20 \text{ cm}^{-1}$. Adapted with permission from Ref. [57].

It reveals the averaged influence of strong external magnetic fields on the rovibrational spectrum of molecular hydrogen. The entire spectrum is generally blue-shifted.

Overtone become clearly visible and more pronounced in an external field. For the zero-field, only the *P*- and *R*-branch are visible, while an increasingly large *Q*-branch emerges in stronger fields. This indicates how important librational motion becomes compared to rotational motion, dominating the spectra in increasingly large fields. However, it should be stressed that the results presented here should only be understood as an illustrative example of effects, which can be induced in such extreme environments. The comparison between spectra generated on the GHF and GMP2 level in fig. 14.2.4 reveals the importance of electron correlation in the underlying BO PES. As such, a more detailed study using the full configuration interaction method as a reference should be carried out in future work. Furthermore, the semi-classical nature of the MD simulations is not able to properly describe a few important phenomena, such as nuclear tunneling, which would circumvent librational motion. The resulting motion is likely a combination of libration and rotation, and requires a purely quantum-mechanical treatment to be properly described.

14.3. Rovibrational Spectrum of Lithium Hydride

14.3.1. Infrared Spectroscopy in Strong Magnetic Fields

While hydrogen is an abundant material in the vicinity of magnetic white dwarfs, other light elements such as helium and several second-row elements have been observed in their atmospheres.^[396, 397] Could rovibrational spectroscopy be used in order to verify the existence of small molecules in the vicinity of magnetic white dwarfs? Molecules without a permanent dipole moment only possess a Raman active stretching vibration, the excitation of which requires the use of a monochromatic light source. As such an experiment is currently not feasible, molecular hydrogen will not be detected through rovibrational spectroscopy in the near future.

Linear molecules with a permanent dipole moment, however, possess an infrared active stretching vibration. In principle, such molecules could be detected using infrared spectroscopy. In order to evaluate these results, highly accurate quantum-chemical methods are required.^[14] For a qualitative description of the expected effects of strong magnetic fields on molecules with a permanent dipole moment, the methods presented in this work are sufficient. As an exemplary case, the lithium hydride molecule shall be investigated in this section.

14.3.2. Potential Energy Surface

First, the potential energy surface of LiH should be investigated. In the absence of a magnetic field, the molecular point group of LiH is $C_{\infty v}$. The electronic ground state has $^1\Sigma^+$ symmetry and there exist several excited states, one of which has the character $^3\Pi$.^[398] In the presence of a weak external magnetic field, the molecule has C_{∞} symmetry in a parallel orientation, with the corresponding electronic ground state becoming $^1\Sigma$, and with the excited state $^3\Pi$ retaining its character. For a perpendicular orientation, the molecular symmetry is C_s , the electronic ground state has $^1A'$ character, and the excited state is $^3A'$. In all other cases, the system has C_1 symmetry and the two states become 1A and 3A , respectively.

In weak fields, the singlet state (S_0) is the electronic ground state, while beyond a magnetic field of about $0.1 B_0$, the triplet state (T_1) becomes the ground state of the system.^[35] Two exemplary potential energy surfaces are presented in fig. 14.3.1, one for a field strength of $|\mathbf{B}| = 0.02 B_0$ and one for $|\mathbf{B}| = 0.2 B_0$. The region, in which the MD simulation takes place, is indicated. Since T_1 is non-binding, all MD simulations are carried out for S_0 .

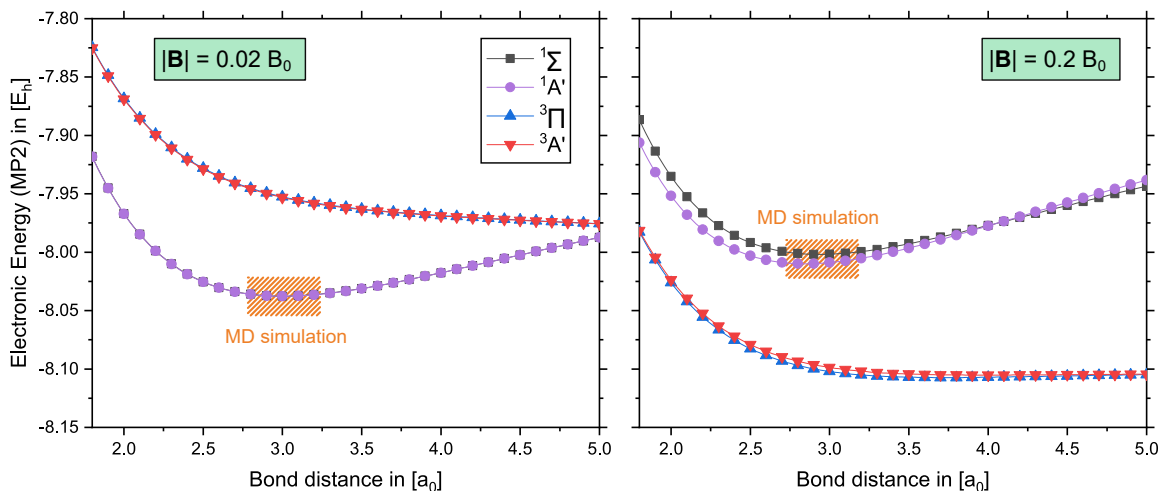


Figure 14.3.1.: Potential energy surface of LiH in two magnetic fields, $|\mathbf{B}| = 0.02 B_0$ (left) and $|\mathbf{B}| = 0.2 B_0$ (right), calculated on the GMP2/def2-TZVP level. The parallel (black, blue) and perpendicular (purple, red) orientations of the external field with respect to the bond are considered. The relevant regions for the MD simulations are indicated. Adapted with permission from Ref. [57].

As illustrated in fig. 14.3.1, the perpendicular orientation is energetically more stable than the parallel orientation, at least in the relevant region for the MD simulation. As such, the LiH should be expected to behave somewhat differently than H_2 for

molecular rotations. For the equilibrium distance in the perpendicular orientation, the rotation barrier is depicted in fig. 14.3.2.

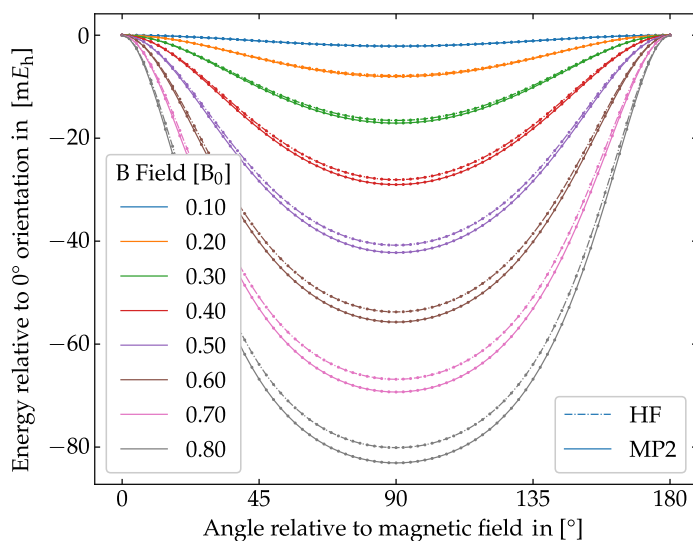


Figure 14.3.2.: Potential energy barrier for the rotation of LiH relative to the 0° (parallel) orientation. Calculated on the GHF/def2-TZVP (dashed line) and GMP2/def2-TZVP (solid line) levels of theory, respectively. All calculations are carried out for the equilibrium bond length in the perpendicular orientation, assuming a rigid rotator. Reprinted with permission from Ref. [57].

While the parallel orientation of the molecule with respect to the external field is somewhat unique, there exist infinitely many degenerate perpendicular orientations. As a consequence, there is no necessity for LiH to cross the potential energy maximum during any form of motion. This is in clear contrast to molecular hydrogen, which had to cross one of the infinitely many points corresponding to the maximum potential energy for a rotational movement.

14.3.3. Molecular Rotations and Vibrations

Having examined the potential energy surface of LiH and particularly the rotational barrier, the impact of an external magnetic field on molecular rotations and vibrations may now be assessed. First, rotational motion is examined. Since the molecule does not have to cross the potential energy barrier, the clear distinction between rotations and librations is eliminated. Instead, motion should be expected to behave more like a precession. In weak fields, this precession is more rotation-like and in stronger fields it becomes more libration-like. However, this change is continuous, even disregarding

quantum effects such as tunneling of the nuclei. Two exemplary trajectories for a more rotation-like and more libration-like motion are depicted in fig. 14.3.3.

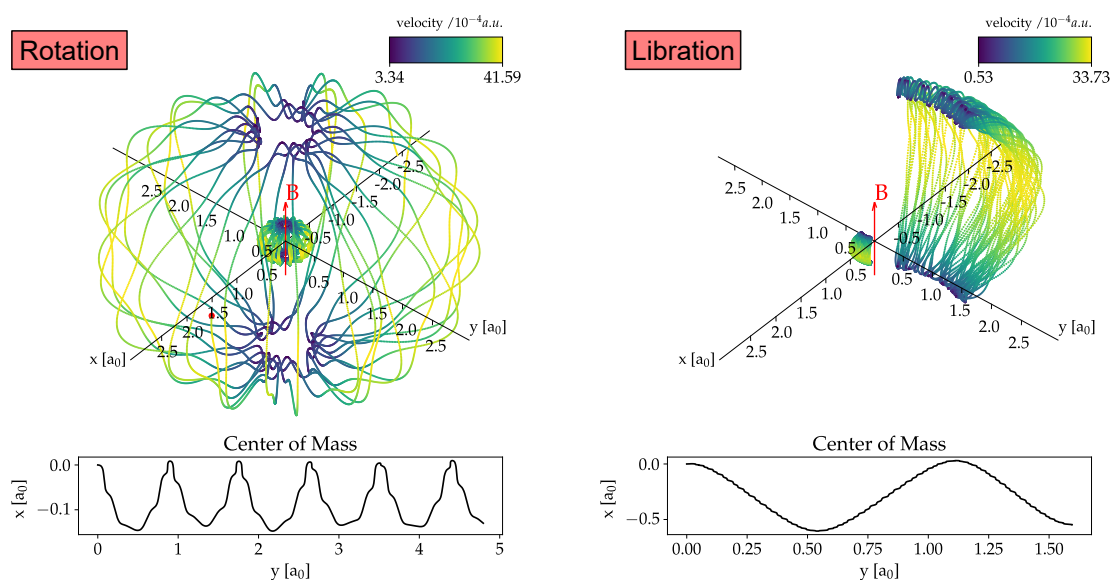


Figure 14.3.3.: Trajectories as calculated for a more rotation-like (left) and more libration-like motion of LiH in an external magnetic field of $|\mathbf{B}| = 0.2B_0$. Darker colors indicate slower motion and brighter colors indicate faster motion. Intramolecular cyclotron rotations are visible for both cases. The center-of-mass motion in the xy -plane is highlighted below, while it was decoupled for the depicted trajectories. Adapted with permission from Ref. [57].

Both cases were initiated with the molecule aligned with the Cartesian x -axis. The initial velocities only had components for the rotation about the y -axis and the stretching vibration. In both cases, a center-of-mass motion can be seen, resembling an oscillating motion within the xy -plane. Due to net neutrality of LiH, no cyclotron rotation of the center-of-mass motion is observed. Overall, the oscillating propagation moves forward in the y -component. If the screening of the Lorentz forces are not taken into account through either the Berry curvature tensor or the Mulliken charge distribution, an unphysical center-of-charge cyclotron rotation is induced. This highlights the importance of including these screening terms in the simulations. Intramolecular cyclotron rotations on the other hand, are observed similarly to H_2 .

14.3.4. Rotational-Vibrational Spectra in Strong Magnetic Fields

Finally, the rovibrational spectrum of LiH in strong external magnetic fields may be examined. For the initial conditions used for the trajectories in fig. 14.3.3, two rovibrational spectra may be computed through a Fourier transformation of the velocity (power spectrum) or dipole moments (infrared spectrum). The corresponding spectra are presented in fig. 14.3.4.

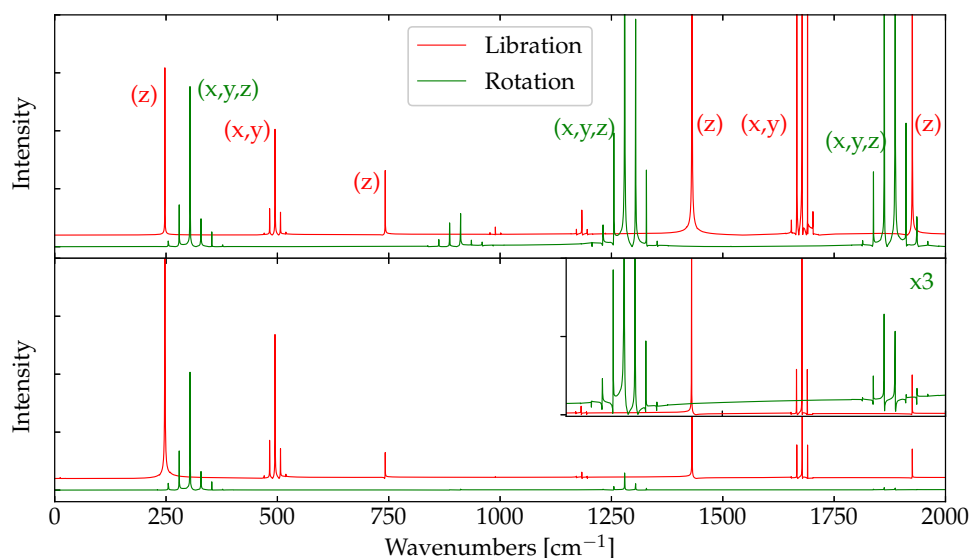


Figure 14.3.4.: Rovibrational spectrum of LiH simulated from identical initial conditions used for the trajectories depicted in fig. 14.3.3. Power spectrum (top) and IR spectrum (bottom) are obtained through a Fourier transformation of the corresponding MD simulations. Depicted here are the spectra for initial conditions leading to more libration-like (red) and more rotation-like (green) motion on the MP2/def2-TZVP level of theory. Reprinted with permission from Ref. [57].

For a more rotation-like motion, the rotational spectrum looks similar to H_2 , with the fundamental frequency coupling to intramolecular cyclotron rotation and being split into a multiplet. For a more libration-like motion, a different pattern is found. LiH molecule is not inhibited in the motion of its (z)-component, which appears at the fundamental frequency of about 250 cm^{-1} . Overtones of this peak can be found at every odd multiple of the fundamental frequency due to symmetry reasons. The multiplet corresponding to the (x,y)-component appears at every even multiple due to similar reasons discussed for the (z)-component of H_2 . In the infrared spectrum of LiH, the intramolecular cyclotron rotation appears for libration-like motion.

Molecular vibrations behave very similarly to H_2 , with P - and R -branches being present for a coupling to a more rotation-like motion and an additional Q -branch appearing for a coupling to more libration-like motion. A hyperfine structure corresponding to the additional coupling of rotations and librations to an intramolecular cyclotron rotation can likewise be observed. A canonical ensemble of spectra may be obtained similarly to H_2 , with Boltzmann-distributed initial conditions and a target temperature of 1500 K. 2000 individual spectra were calculated for each canonical ensemble, with a simulation time of 1 ps per spectrum. The final result was averaged over an interval of $\omega = \pm 20 \text{ cm}^{-1}$. It is depicted in fig. 14.3.5.

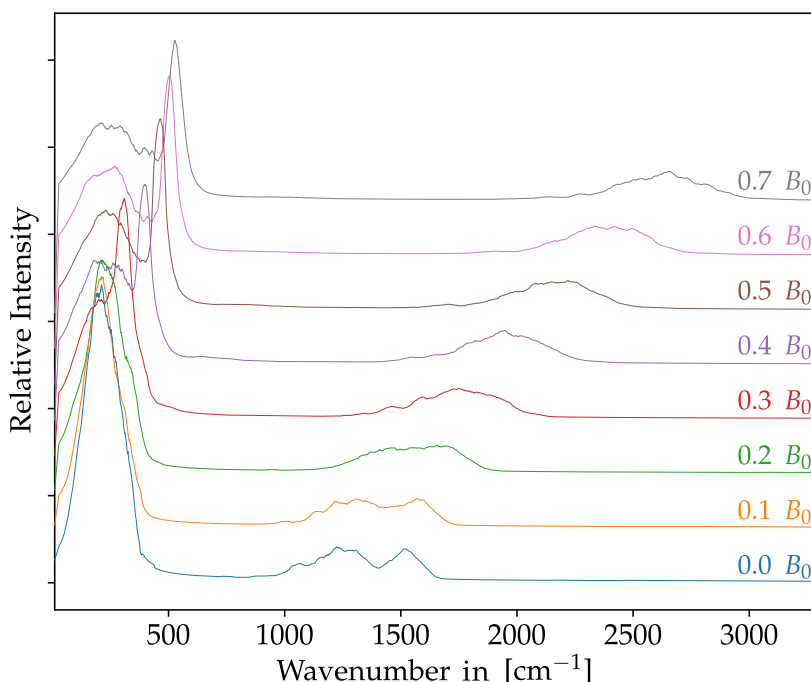


Figure 14.3.5.: Canonical ensemble of infrared spectra for LiH in strong magnetic fields. Initial conditions were obtained from a Boltzmann-distributed set of velocities. The simulation time for each spectrum is 1 ps, and the averaged spectrum is obtained by smoothing over an interval of $\omega = \pm 20 \text{ cm}^{-1}$. Reprinted with permission from Ref. [57].

Again, the appearance of the Q -branch in increasing external magnetic fields can clearly be observed. Furthermore, libration- and rotation-like motion happen simultaneously in stronger magnetic fields. This leads to a broad band corresponding to the (x,y,z) -components of rotation-like motion and the (z) -component of libration-like motion as well as a relatively sharp ‘overtone’ corresponding to the (x,y) -components of libration-like motion.

The investigation of such spectra using more high-level methods such as full configuration interaction remains the subject of future work. While the signals may be shifted, a qualitative agreement between the resulting spectra and the ones generated here using an MP2 reference can be expected. The missing description of quantum effects such as tunneling is likely less important for LiH for the aforementioned reasons, but in general, a smoother transition between more rotation-like and more libration-like motion should be expected.

14.3.5. Mulliken Charge Approximation

The main purpose of the Berry curvature tensor is screening the Lorentz force acting on nuclear charges. If not properly screened, unphysical behaviour such as center-of-mass cyclotron rotations may be the result. The Mulliken charge distribution may be used to approximate the Berry curvature tensor, resulting in very similar rovibrational spectra. Both approaches are compared in fig. 14.3.6 for the rovibrational spectrum of LiH in an external magnetic field of $0.2 B_0$. The presented spectra differ mainly in the higher multiplet visible for rotation-like motion if the Berry curvature tensor is used. The further investigation of these differences is the subject of future work.

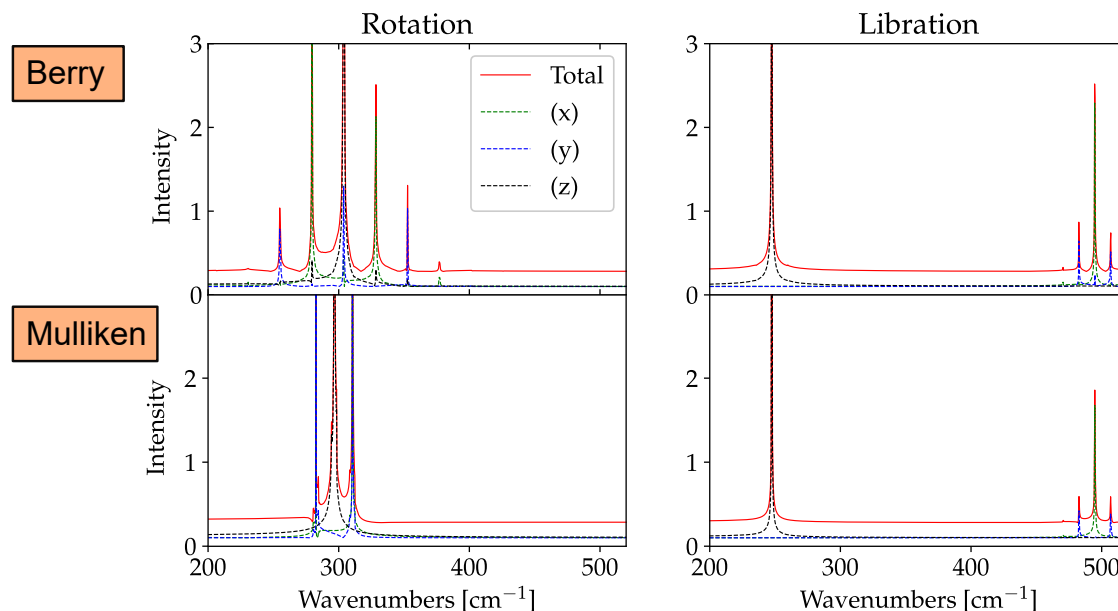


Figure 14.3.6.: Comparison between rovibrational spectrum of LiH, calculated using the Berry curvature tensor (top) and Mulliken charge distribution (bottom). The spectrum was computed using identical conditions to those discussed for fig. 14.3.4. Kindly provided by Monzel.

15. Geometry Optimization of Helium Clusters in Strong Magnetic Fields

The effects of a strong magnetic field on the Born-Oppenheimer equilibrium geometry of a molecule can be substantial. While this can be mostly neglected for molecules with singlet electronic ground states in weak to moderately strong magnetic fields, it may become pivotal for the accurate description of molecular spectroscopy in stronger fields. Generally, investigations on the geometry of molecules require the evaluation of the molecular gradient as described in sec. 8.3, including an approach to optimize the additional degrees of freedom for internal coordinates discussed therein. In passing, it should be noted that this step was avoided for the computation of rovibrational spectra in chapter 14, as the relevant part of the BO PES was approximated through splines, and the gradient was calculated as an analytical derivative thereof.

In this chapter, the effects of a strong, external magnetic field on the equilibrium geometry of helium clusters is assessed. This serves the purpose to showcase that geometry optimizations can routinely be performed using the methods implemented in the context of this thesis. Helium clusters provide an interesting test case for these geometry optimizations. They are among the only systems, for which reference data exists in the literature.^[34, 399] They are particularly appealing for such an application, as they are bound through a type of chemical bond which does not exist in the absence of magnetic fields. This ‘perpendicular paramagnetic bond’ was first described in Ref. [19], where the helium dimer in its singlet state was used as an example.

Very recently, geometry optimizations in finite magnetic fields on the CDFT level were published in Ref. [38]. Therefore, this chapter is particularly concerned with the assessment of both GHF and spin-noncollinear CDFT for the geometry optimization of helium clusters. First, the potential energy surface of the helium dimer is discussed, comparing the results obtained from GHF and different (C)DFT functionals to the full configuration interaction (FCI) results presented in the literature.^[19] Finally, the geometries of helium clusters of up to 19 atoms are optimized, both in their electronic ground states and the excited singlet state.

15.1. Helium Dimer and Perpendicular Paramagnetic Bonding

15.1.1. Computational Details

In this section, the potential energy surfaces of the helium dimer are examined. Only the perpendicular orientation of the molecular bond with respect to an external magnetic field is considered. All calculations are carried out using an uncontracted version of the aug-cc-pVTZ basis set,^[374–376] here denoted un-aug-cc-pVTZ, similar to the investigations in Ref. [19]. To assess how well different quantum-chemical methods perform, calculations were performed using GHF, GMP2 and spin-noncollinear versions of the following functionals: PBE,^[384] B3LYP,^[212, 378, 379] TPSS,^[385] and TPSSh.^[385] For all DFT calculations, a large gridsize (grid 5)^[320] was employed. Tight convergence criteria were used, with $10^{-12}E_h$ for the electronic energy and 10^{-12} for the norm of the density matrix (denconv 12). For GMP2, the RI-*C* approximation was used in combination with an auxiliary aug-cc-pVTZ basis.^[161] This auxiliary basis is not contracted in its standard form.^[400] Calculations in sec. 15.1.2 are performed in a magnetic field of $|\mathbf{B}| = 2.5 B_0$, in accordance with Ref. [19], while calculations in sec. 15.1.3 use a magnetic field of $|\mathbf{B}| = 2.0 B_0$, similarly to Ref. [34]. Geometry optimizations were carried out using the method described in sec. 8.3 of this work, using analytical gradients for every method except for GMP2, for which numerical gradients were used.

15.1.2. Perpendicular Paramagnetic Bonding

In the presence of strong magnetic fields, a new type of chemical bond can be induced.^[19] This perpendicular paramagnetic bond has a variety of unique features, including its capability to create strongly bound molecules with a bond order of zero. This was investigated in Ref. [19] for the Helium dimer in a magnetic field of $|\mathbf{B}| = 2.5 B_0$ using the HF and FCI methods. HF yields a qualitatively correct description, but correlation effects need to be taken into account for quantitative results. FCI represents the exact solution to the electronic Schrödinger equation within the limits of the chosen basis, and may therefore be used as a benchmark for quantum chemical methods.

The singlet ground state of He₂ ($^1\Sigma_g^+$) is only weakly bound in the absence of magnetic fields. A chemical bond does exist due to dispersion effects, with an equilibrium bond length of 297 pm and an associated dissociation energy of 0.092 kJ/mol.^[19, 401] In a

perpendicular magnetic field, the singlet ground state has 1A_g character. Due to the presence of the spin Zeeman term in the electronic Hamiltonian, it eventually becomes an excited state in larger fields. The potential energy surface in a field of $|\mathbf{B}| = 2.5 B_0$ is presented in fig. 15.1.1 for the lowest singlet state.

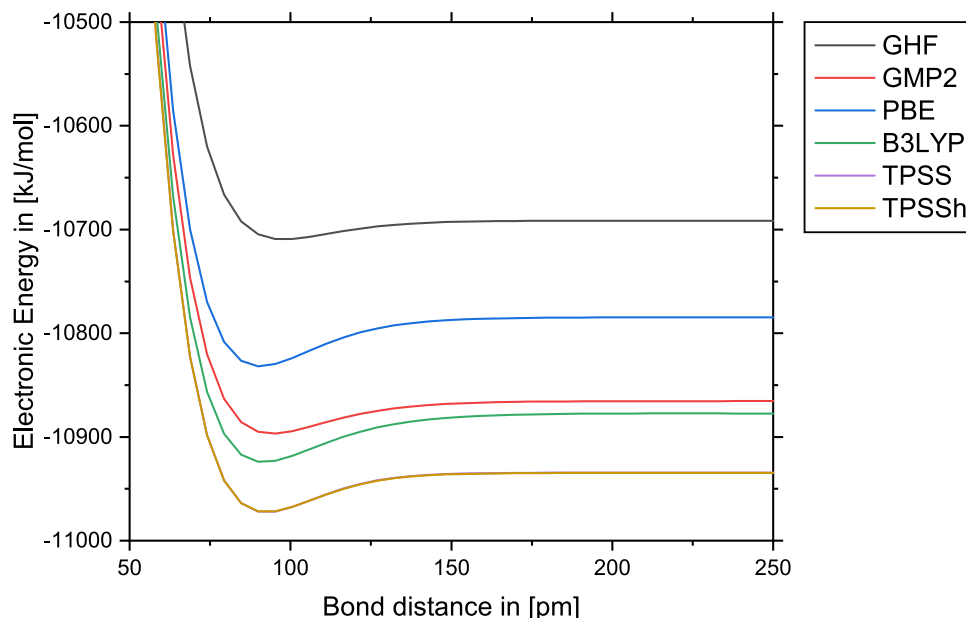


Figure 15.1.1.: Potential energy surface for the lowest 1A_g state of He_2 in an external magnetic field of $|\mathbf{B}| = 2.5 B_0$, applied in perpendicular orientation to the bond axis. All calculations use the un-aug-cc-pVTZ basis and the indicated method: GHF (black), GMP2 (red), spin-noncollinear DFT with PBE (blue), B3LYP (green), TPSS (purple) and TPSSh (yellow). TPSS and TPSSh yield almost identical results.

All methods yield qualitatively similar results, predicting a bond with a corresponding equilibrium bond length of below 100 pm. Geometry optimizations were carried out on all levels of theory indicated in fig. 15.1.1. The resulting bond lengths and dissociation energies are shown in table 15.1.1. Dissociation energies were calculated in comparison to the results of a calculation with a bond length of $4.9 a_0 \approx 259$ pm. The basis set superposition error (BSSE) was not taken into account, but was shown to be very small in Ref. [19], with a counterpoise correction of 2 kJ/mol.

The values obtained for the equilibrium bond length obtained from the geometry optimizations are in perfect agreement with those generated using the PES. For GHF, the bond length (97.9 pm) and dissociation energy (17.8 kJ/mol) are in accordance with those generated using RHF in Ref. [19]. GMP2 yields practically identical results to FCI, apparently capturing most correlation effects for this system. All DFT methods overestimate the strength of this bond, with PBE and B3LYP in particular

yielding dissociation energies which are approximately 50% too large. The two CDFT functionals TPSS and TPSSh yield almost identical results, both much closer to the FCI dissociation energy and bond length than PBE and B3LYP. Whether this is an effect of MGGA functionals in general, or their dependence on the current density in particular is impossible to say, as those effects cannot be separated from one another. However, investigations carried out on the He₂ molecule within a magnetic field of $|\mathbf{B}| = 1 B_0$ in Ref. [193] reveal similar trends, with GGA functionals overbinding the system and MGGA functionals yielding good agreement with benchmark values generated on the FCI level.

Table 15.1.1.: Bond length and dissociation energy of the lowest singlet state of He₂ in a perpendicular magnetic field of $|\mathbf{B}| = 2.5 B_0$. The un-aug-cc-pVTZ basis was used for all calculations. BSSE was not taken into account.

Method	Bond length in [pm]	Dissociation energy in [kJ/mol]
GHF	97.9	17.8
GMP2	94.3	31.3
PBE	90.6	47.1
B3LYP	91.7	46.7
TPSS	92.4	38.4
TPSSh	90.9	37.7
FCI ^[19]	94	31

15.1.3. Geometry Optimization of Different Electronic States

In the previous section, only the lowest singlet electronic state (¹A_g) of He₂ was considered. In strong magnetic fields, this is not the ground state of the system due to the presence of the spin Zeeman term. The triplet state ³A_u was examined in Ref. [19], itself also not the ground state in strong fields. In this section, the lowest quintet state (⁵A_g) is considered and compared to the singlet state in a magnetic field of $|\mathbf{B}| = 2 B_0$. Subsequent investigations on helium clusters in sec. 15.2 will also be carried out using this field strength. It was chosen for comparison with the study presented in Ref. [34], which was done using identical conditions. The potential energy surfaces for the lowest ¹A_g and ⁵A_g states are depicted in fig. 15.1.2.

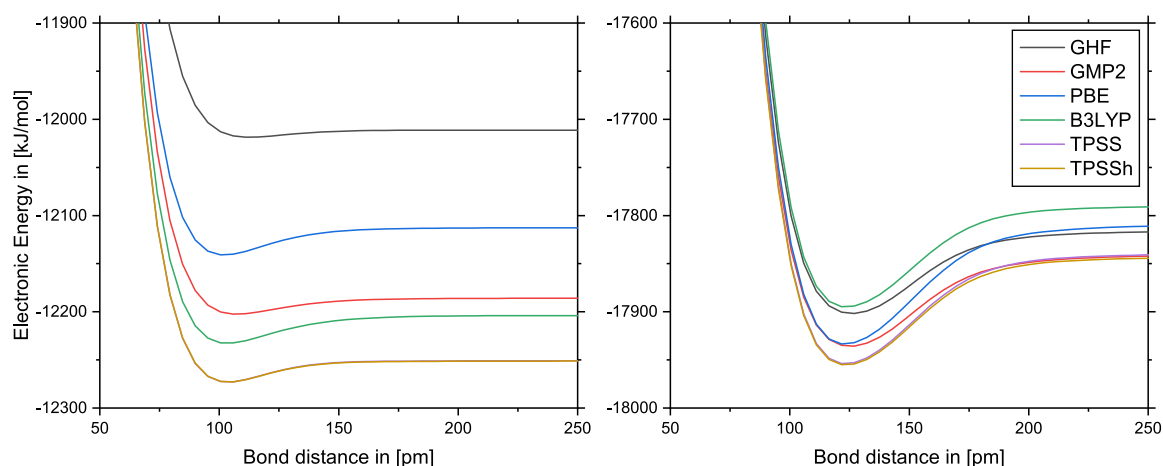


Figure 15.1.2.: Potential energy surface for the lowest 1A_g (left) and 5A_g (right) states of He_2 in an external magnetic field of $|\mathbf{B}| = 2B_0$, applied in perpendicular orientation to the bond axis. All calculations use the un-aug-cc-pVTZ basis and the indicated method: GHF (black), GMP2 (red), spin-noncollinear DFT with PBE (blue), B3LYP (green), TPSS (purple) and TPSSh (yellow). TPSS and TPSSh yield similar results.

For the singlet state, results are qualitatively similar to those obtained in a field of $|\mathbf{B}| = 2.5B_0$, with slightly larger bond lengths and smaller dissociation energies. The quintet state shows an even stronger bond with dissociation energies between 85 (GHF) and 123 kJ/mol (PBE). Bond lengths are generally longer than for the singlet state, with predicted values between 120 pm (TPSSh) and 126 pm (GHF). The results are listed in table 15.1.2.

Table 15.1.2.: Bond length and dissociation energy of the lowest singlet and quintet states for He_2 in a perpendicular magnetic field of $|\mathbf{B}| = 2B_0$. The un-aug-cc-pVTZ basis was used for all calculations.

Method	Bond length in [pm]		Dissociation energy in [kJ/mol]	
	Singlet	Quintet	Singlet	Quintet
GHF	112.4	125.9	7.3	84.8
GMP2	105.7	125.1	16.6	94.0
PBE	102.0	123.0	28.3	123.0
B3LYP	103.3	123.7	28.8	104.1
TPSS	103.5	123.3	22.3	113.6
TPSSh	101.4	119.9	21.5	110.1

15.2. Helium Clusters: Structure and Symmetry

15.2.1. Computational Details

Geometry optimizations for Helium clusters were presented in Ref. [34], where a magnetic field of $|\mathbf{B}| = 2 B_0$ was applied perpendicular to the plane in which all atoms are located. Very recently, additional investigations on the structure of helium clusters were presented in Ref. [399]. In this section, helium clusters are examined in identical conditions to Ref. [34], for comparison with the results obtained for the lowest singlet state on the RHF/un-aug-cc-pVTZ level. Furthermore, calculations are performed on the electronic ground state in these conditions, which is the state with highest possible spin multiplicity ($S = 2N_{\text{nuc}}$). All calculations are performed using the un-aug-cc-pVTZ basis set in combination with GHF, as well as spin-noncollinear DFT with the two functionals PBE and TPSS. Spin Zeeman scaling was used to obtain the molecules in singlet states. Electronic energies are converged up to at least $10^{-8} E_h$, norm of density matrices up to 10^{-6} . For calculations on He_{19} , DIIS was used.

15.2.2. Geometry Optimization of Helium Clusters

The equilibrium geometries for small helium clusters were examined on the RHF/un-aug-cc-pVTZ level in Ref. [34]. Therein, a magnetic field of $|\mathbf{B}| = 2 B_0$ was applied perpendicular to the molecular plane. Using GHF/un-aug-cc-pVTZ with a spin Zeeman scaling of $z = 0$, the singlet state was obtained for all structures. Four helium clusters were examined, He_3 , He_4 , He_7 , and He_{19} . The resulting structures are presented in fig. 15.2.1. As previously observed in Ref. [34], helium atoms in strong magnetic fields are prone to cluster in equilateral triangular shape. The He_3 cluster has C_{3h} symmetry, He_4 forms a rhombus with C_{2h} symmetry, and both the He_7 and He_{19} clusters form hexagonal shapes with C_{6h} symmetry.

For the electronic ground states of these clusters, which contains only unpaired electrons, similar structures are formed. They generally exhibit bond lengths which are about 30 pm longer than for the clusters formed for the singlet state. For calculations on the TPSS/un-aug-cc-pVTZ level, the resulting bond lengths are shown in fig. 15.2.1 for both the electronic ground state and lowest singlet state. In table 15.2.1, the bond lengths are additionally given for GHF and PBE. Particularly for He_{19} , the reduced symmetry due to the presence of the magnetic field ($D_{6h} \rightarrow C_{6h}$) can clearly be observed.

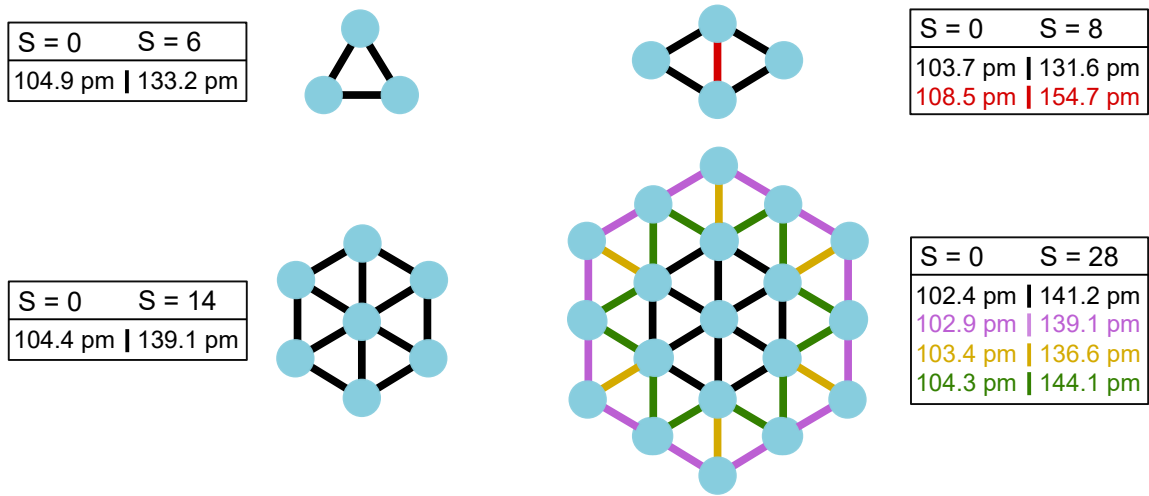


Figure 15.2.1.: Equilibrium geometries of helium clusters with up to 19 atoms in a magnetic field of $|\mathbf{B}| = 2B_0$, applied perpendicular to the plane in which all atoms are located. All calculations were carried out on the TPSS/un-aug-cc-pVTZ level of theory. Bond lengths are given for the lowest singlet state ($S = 0$) and the ground state ($S = 2N_{\text{nuc}}$).

The geometries obtained for the electronic ground state from PBE and TPSS are extremely similar. This is not an error, and was carefully confirmed to be true for He_3 , He_7 , and He_{19} , but could not be further investigated in the frame of this work.

Table 15.2.1.: Bond lengths for equilibrium geometries of helium clusters in a perpendicular magnetic field of $|\mathbf{B}| = 2B_0$. All bond lengths are given in [pm]. The calculations were carried out using the un-aug-cc-pVTZ basis and the indicated methods. Indicated bond colors reference fig. 15.2.1.

Cluster	Indicated bond	Electronic ground state			Lowest singlet state		
		GHF	PBE	TPSS	GHF	PBE	TPSS
He_3	black	132.5	133.2	133.2	110.5	103.8	104.9
He_4	black	131.0	131.5	131.6	109.2	102.4	103.7
	red	157.0	155.4	154.7	110.4	108.5	108.5
He_7	black	138.9	139.1	139.1	107.4	103.5	104.4
He_{19}	black	141.0	141.2	141.2	103.4	101.8	102.4
	purple	138.8	139.1	139.1	105.0	102.0	102.9
	yellow	136.1	136.6	136.6	105.2	102.2	103.4
	green	144.6	144.1	144.1	106.6	103.9	104.3

Part V.

Conclusion and Outlook

16. Conclusion and Outlook

The aim of this thesis was the development and application of efficient computational methods for molecular spectroscopy in finite magnetic fields. This required three separate steps:

1. The derivation of theoretical methods for the description of molecular properties in finite magnetic fields.
2. The efficient and parallel implementation of these methods.
3. The application to different types of molecular spectroscopy in magnetic fields.

Regarding the first of the three steps, chapters 2–7 introduced the theoretical description required for the calculation of molecular spectroscopy in finite magnetic fields. The relevant theoretical background of classical electromagnetism was discussed in chapter 2. In particular, the gauge origin problem was introduced – as well as the principle of minimal coupling, which can be used to derive a gauge origin invariant formalism for the motion of charged particles in external magnetic fields. Moving on, the quantum mechanical framework for this work was introduced in chapter 3. In particular, the Born–Oppenheimer approximation was used to separate electronic and nuclear motion within a molecule, and both resulting equations of motion were discussed. In chapter 4, the construction and symmetry of the electronic wave function were presented. In particular, the use of London atomic orbitals (LAOs) was introduced, which are needed for a gauge origin invariant formalism. Further, the spatial symmetry of the wave function was examined, yielding an easily accessible scheme for the identification of the molecular point group in a magnetic field.

Chapters 5 and 6 introduced quantum chemical methods for electronic ground states and excitations in finite magnetic fields. In particular, approximate coupled cluster theory (CC2), current density functional theory (CDFT), and *GW* in combination with the Bethe–Salpeter equation (BSE) were adapted for the use in finite magnetic fields for this thesis. Finally, chapter 7 presented a review of a recently introduced approach for the semi-numerical solution to the Schrödinger equation for nuclear motion. The Berry curvature tensor was established as a fundamental quantity for

such a description. In summation, these chapters introduced the theoretical framework required for the calculation of spectroscopic properties in finite magnetic fields.

Having established the theoretical background, an implementation of these methods was carried out and assessed in chapters 8–11. A convenient choice for such an implementation was the TURBOMOLE program suite, in which all of the aforementioned quantum chemical methods had already been implemented in the absence of magnetic fields. In chapter 8, the general structure of the implementation into TURBOMOLE was presented. The most important change for finite field calculations was the use of LAOs in all integral evaluation steps. Therefore, chapter 9 introduced the efficient evaluation of integrals over LAOs and the implementation of related algorithms.

In chapter 10, the accuracy and efficiency of the implementations carried out in this work was assessed. A particular focus was the implementation of the resolution of the identity (RI) approximation. This method has long been established for calculations in the absence of fields and is known to substantially improve the efficiency of quantum chemical calculations with only very limited loss of accuracy. Here, it could be shown that RI performs even more favorably for finite field calculations. As such, it enables the calculation of spectroscopic properties for sizeable molecules.

Finally, chapter 11 concluded the presentation of implementations carried out in this work, focusing on the Berry curvature tensor. A numerical scheme for the quantum chemical calculation of this property was introduced. Partial charges derived from the Berry curvature tensor were assessed, even in the limit of a vanishing magnetic field. These ‘Berry charges’ were compared to Mulliken charges, emphasizing their consistent behaviour with respect to the choice of basis.

With the theoretical framework derived and an efficient implementation at hand, several applications were examined in chapters 12–15. The first application was magnetic circular dichroism (MCD) spectroscopy in weak magnetic fields like those typically used for such experiments. Results obtained using time-dependent density functional theory (TD-DFT) were compared to perturbative approaches found in the literature, yielding identical results. Furthermore, MCD spectra were computed using TD-DFT in the finite field approach for an organometallic compound, a zinc tetraazaporphyrin with two fused naphthalene units. The results were compared to experimental data, showing excellent agreement between theory and experiment.

Having confirmed that the finite field approach implemented in this work yields correct results for earth-like conditions, the next step was its application to ‘moderately strong’ magnetic fields of up to 10,000 T in chapter 13. The influence on electronic excitations was investigated for a set of 36 small to medium-sized molecules. Some more general

trends could be extracted, showing in particular that aromatic $\pi \rightarrow \pi^*$ excitations are strongly affected by perpendicularly applied magnetic fields. Using the *GW/BSE* method, the effects of increasingly strong magnetic fields on the tetracene molecule were examined. By calculating the absorption spectrum in the ultraviolet and visible (UV/Vis) region of the electromagnetic spectrum, the color change expected for this molecule could be determined.

For strong magnetic fields, the calculation of rotational-vibrational spectra of two diatomic molecules, H_2 and LiH was presented in chapter 14. The effects induced by such strong magnetic fields were discussed, including the complex coupling patterns obtained under such extreme conditions. Responsible for the complexity of the resulting spectra is, among other things, an intramolecular cyclotron rotation. Moreover, rotational barriers induced by the magnetic field lead to librational motion, which may be used as an indicator for the presence of a magnetic field in infrared spectra obtained from magnetic white dwarfs. The final application, presented in chapter 15, was concerned with the geometry optimization of helium clusters of up to 19 atoms. As shown in this section, strong magnetic fields may have a large impact on the molecular structure of compounds, which should not be neglected for applications in molecular spectroscopy.

To summarize the results of this thesis, established quantum chemical methods were adapted for the use in finite magnetic fields. They were efficiently implemented into quantum chemical software. Applications for molecular spectroscopy were presented for a variety of magnetic field strengths, from earth-like conditions to those with astrochemical relevancy.

There exist a number of possibilities for the next steps of the research presented in this thesis. First, its use for molecular spectroscopy and magnetic properties in earth-like conditions could be further explored. The option to calculate numerical derivatives with respect to the external magnetic fields opens up an entire new realm of possibilities, giving immediate access to a number of properties such as magnetizabilities which are otherwise complicated to obtain. The use of ‘Berry charges’ was briefly explored in this work, and could turn out to be a real alternative if one is interested in partial charges for some application. Furthermore, it could be investigated, whether the Berry curvature tensor might be used to derive a new form of population analysis. For astrochemical applications, the methods presented in this work could be further developed and might be used to detect small molecules in the vicinity of magnetic white dwarfs. In particular, infrared and MCD spectroscopy could be used for such investigations.

Lastly, the incorporation of relativistic effects seems to be a natural continuation for this work. The two-component framework used throughout this thesis can be straightforwardly adapted to include relativistic effects, for instance through the use of the exact two-component theory in combination with the magnetic balance condition. Such an implementation would make the calculation of heavy elements in finite magnetic fields possible. In particular, the investigation of non-linear effects induced by magnetic fields on spin orbit coupling could be revealed, a phenomenon which is likely observable even in earth-like conditions.

A. Appendix

A.1. Abbreviations and Acronyms

A.1.1. Abbreviations in Mathematics

FWHM: Full Width at Half Maximum

lhs: left hand side

rhs: right hand side

SD: Standard Deviation

A.1.2. Abbreviations in Chemistry

EPR: Electron Pair Resonance

MCD: Magnetic Circular Dichroism

NMR: Nuclear Magnetic Resonance

***p*BQ:** *p*-benzoquinone

TC*p*BQ: Tetrachloro-*p*-benzoquinone

UV/Vis: Ultraviolet and Visible

A.1.3. Abbreviations in Quantum Chemistry

BFGS: Broyden–Fletcher–Goldfarb–Shanno

BO: Born–Oppenheimer

BSSE: Basis Set Superposition Error

CC2: Approximate Coupled Cluster singles and doubles

CD: Contour-Deformation

CT: Charge-Transfer

DBOC: Diagonal Born–Oppenheimer Correction

DIIS: Direct Inversion of the Iterative Subspace
EOM: Equation Of Motion
HRR: Horizontal Recurrence Relation
LRT: Linear Response Theory
OS: Obara–Saika
PES: Potential Energy Surface
RI: Resolution of the Identity
RI-C: Resolution of the Identity for Correlated methods
RI-J: Resolution of the Identity for the Coulomb part
RI-K: Resolution of the Identity for the exchange part
SCF: Self-Consistent Field
SOS: Sum-over-states
TD: Time-Dependent
VRR: Vertical Recurrence Relation
xc: Exchange-correlation

A.1.4. Orbital-Related Acronyms

AO: Atomic Orbital
GIAO: Gauge-Including Atomic Orbital
GTO: Gaussian-Type Orbital
HOMO: Highest Occupied Molecular Orbital
LAO: London Atomic Orbital
LCAO: Linear Combination of Atomic Orbitals
LUMO: Lowest Unoccupied Molecular Orbital
MO: Molecular Orbital

A.1.5. Quantum Chemical Methods

AC: Analytical Continuation
BSE: Bethe–Salpeter Equation
cBSE: Correlation-kernel augmented Bethe–Salpeter Equation
CDFT: Current Density Functional Theory
DFT: Density Functional Theory
dRPA: Direct Random Phase Approximation

evGW: Eigenvalue-only self-consistent *GW*
FCI: Full Configuration Interaction
GGA: Generalized Gradient Approximation
GHF: Generalized Hartree–Fock
GMP n : Generalized Møller–Plesset perturbation theory up to n -th order
HDFT: Hybrid Density Functional Theory
HF: Hartree–Fock
KS: Kohn–Sham
MGGA: *Meta*-Generalized Gradient Approximation
MP n : Møller–Plesset perturbation theory up to n -th order
RHF: Restricted Hartree–Fock
RKS: Restricted Kohn–Sham
RPA: Random Phase Approximation
RSH: Range-Separated Hybrid
UHF: Unrestricted Hartree–Fock
UKS: Unrestricted Kohn–Sham

A.1.6. Abbreviations for Basis Sets

def2: Karlsruhe basis set
SVP: Split Valence Polarization
TZVP: Triple-Zeta Valence Polarization
TZVPP: Triple-Zeta Valence with two sets of polarization functions
QZVP: Quadruple-Zeta Valence Polarization
QZVPP: Quadruple-Zeta Valence with two sets of polarization functions
cc-pVDZ: Correlation-consistent polarized Valence Double-Zeta
cc-pVTZ: Correlation-consistent polarized Valence Triple-Zeta
aug-cc-pVDZ: Augmented correlation-consistent polarized Valence Double-Zeta
aug-cc-pVTZ: Augmented correlation-consistent polarized Valence Triple-Zeta
un: Uncontracted

Bibliography

- [1] S. E. Whittaker, *A History of the Theories of Aether and Electricity - Vol. I: The Classical Theories; Vol. II: The Modern Theories, 1900-1926*, Courier Dover Publications, Mineola, NY, USA, **1989**.
- [2] J. B. Carlson, *Science* **1975**, *189*, 753–760.
- [3] I. Charvátová, J. Klokočník, J. Kolmaš, J. Kostelecký, *Stud. Geophys. Geod.* **2011**, *55*, 159–174.
- [4] V. H. Malmstrom, *Nature* **1976**, *259*, 390–391.
- [5] R. Lanza, A. Meloni, *The Earth's Magnetism - An Introduction for Geologists*, 1st ed., Springer Science & Business Media, Berlin, Heidelberg, Germany, **2006**.
- [6] A. Parson, A Magneton Theory of the Structure of the Atom, *Smithsonian Publication*, *2371*, **1915**.
- [7] E. Schrödinger, *Ann. Phys.* **1926**, *384*, 361–376.
- [8] E. Schrödinger, *Ann. Phys.* **1926**, *385*, 437–490.
- [9] C. C. Finlay, S. Maus, C. D. Beggan, T. N. Bondar, A. Chambodut, T. A. Chernova, A. Chulliat, V. P. Golovkov, B. Hamilton, M. Hamoudi, R. Holme, G. Hulot, W. Kuang, B. Langlais, V. Lesur, F. J. Lowes, H. Lühr, S. Macmillan, M. Manda, S. McLean, C. Manoj, M. Menvielle, I. Michaelis, N. Olsen, J. Rauberg, M. Rother, T. J. Sabaka, A. Tangborn, L. Tøffner-Clausen, E. Thébault, A. W. P. Thomson, I. Wardinski, Z. Wei, T. I. Zvereva, *Geophys. J. Int.* **2010**, *183*, 1216–1230.
- [10] P. D. Dauce, G. B. de Castro, M. M. F. Lima, R. M. F. Lima, *J. Mater. Res. Technol.* **2019**, *8*, 1052–1059.
- [11] H. Maeda, Y. Yanagisawa, *J. Magn. Reson.* **2019**, *306*, 80–85.

-
- [12] K. Hashi, S. Ohki, S. Matsumoto, G. Nishijima, A. Goto, K. Deguchi, K. Yamada, T. Noguchi, S. Sakai, M. Takahashi, Y. Yanagisawa, S. Iguchi, T. Yamazaki, H. Maeda, R. Tanaka, T. Nemoto, H. Suematsu, T. Miki, K. Saito, T. Shimizu, *J. Magn. Reson.* **2015**, *256*, 30–33.
- [13] M. Jaime, C. Corvalán Moya, F. Weickert, V. Zapf, F. Balakirev, M. Wartenbe, P. Rosa, J. Betts, G. Rodriguez, S. Crooker, R. Daou, *Sensors (Basel)* **2017**, *17*, 2572.
- [14] S. Stopkowicz, *Int. J. Quantum Chem.* **2017**, *118*, e25391.
- [15] L. Ferrario, D. de Martino, B. T. Gänsicke, *Space Sci. Rev.* **2015**, *191*, 111–169.
- [16] L. Ferrario, D. Wickramasinghe, A. Kawka, *Adv. Space Res.* **2020**, *66*, 1025–1056.
- [17] S. Mereghetti, J. A. Pons, A. Melatos, *Space Sci. Rev.* **2015**, *191*, 315–338.
- [18] J. Liebert, L. Ferrario, D. T. Wickramasinghe, P. S. Smith, *Astrophys. J.* **2015**, *804*, 93.
- [19] K. K. Lange, E. I. Tellgren, M. Hoffmann, T. Helgaker, *Science* **2012**, *337*, 327–331.
- [20] F. London, *J. Phys. Radium* **1937**, *8*, 397–409.
- [21] R. Ditchfield, *J. Chem. Phys.* **1972**, *56*, 5688–5691.
- [22] J. Gauss, J. F. Stanton, *J. Chem. Phys.* **1995**, *103*, 3561–3577.
- [23] T. Helgaker, M. Jaszuński, K. Ruud, *Chem. Rev.* **1999**, *99*, 293–352.
- [24] J. Vaara, *Phys. Chem. Chem. Phys.* **2007**, *9*, 5399–5418.
- [25] S. Gillhuber, Y. J. Franzke, F. Weigend, *J. Phys. Chem. A* **2021**, *125*, 9707–9723.
- [26] F. Neese in *EPR Spectroscopy - Fundamentals and Methods*, (Eds.: D. Goldfarb, S. Stoll), John Wiley & Sons, New York, NY, USA, **2018**, pp. 115–142.
- [27] Y. J. Franzke, J. M. Yu, *J. Chem. Theory Comput.* **2022**, *18*, 323–343.
- [28] Y. J. Franzke, J. M. Yu, *J. Chem. Theory Comput.* **2022**, *18*, 2246–2266.
- [29] S. Coriani, P. Jørgensen, A. Rizzo, K. Ruud, J. Olsen, *Chem. Phys. Lett.* **1999**, *300*, 61–68.
- [30] T. Kjærgaard, S. Coriani, K. Ruud, *Wiley Interdiscip. Rev. Comput. Mol. Sci.* **2012**, *2*, 443–455.

- [31] R. Faber, S. Ghidinelli, C. Hättig, S. Coriani, *J. Chem. Phys.* **2020**, *153*, 114105.
- [32] E. I. Tellgren, A. Soncini, T. Helgaker, *J. Chem. Phys.* **2008**, *129*, 154114.
- [33] E. I. Tellgren, T. Helgaker, A. Soncini, *Phys. Chem. Chem. Phys.* **2009**, *11*, 5489–5498.
- [34] E. I. Tellgren, S. S. Reine, T. Helgaker, *Phys. Chem. Chem. Phys.* **2012**, *14*, 9492–9499.
- [35] S. Stopkowicz, J. Gauss, K. K. Lange, E. I. Tellgren, T. Helgaker, *J. Chem. Phys.* **2015**, *143*, 074110.
- [36] T. J. P. Irons, J. Zemen, A. M. Teale, *J. Chem. Theory Comput.* **2017**, *13*, 3636–3649.
- [37] S. Sun, D. B. Williams-Young, T. F. Stetina, X. Li, *J. Chem. Theory Comput.* **2019**, *15*, 348–356.
- [38] T. J. P. Irons, G. David, A. M. Teale, *J. Chem. Theory Comput.* **2021**, *17*, 2166–2185.
- [39] S. Sen, E. I. Tellgren, *J. Chem. Phys.* **2018**, *148*, 184112.
- [40] R. H. Garstang, *Rep. Prog. Phys.* **1977**, *40*, 105–154.
- [41] D. T. Wickramasinghe, L. Ferrario, *Publ. Astron. Soc. Pac.* **2000**, *112*, 873–924.
- [42] L. B. Zhao, *Astrophys. J.* **2018**, *856*, 157.
- [43] W. Becken, P. Schmelcher, *Phys. Rev. A* **2001**, *63*, 053412.
- [44] T. F. Stetina, S. Sun, D. B. Williams-Young, X. Li, *ChemPhotoChem* **2019**, *3*, 739–746.
- [45] S. Sen, K. K. Lange, E. I. Tellgren, *J. Chem. Theory Comput.* **2019**, *15*, 3974–3990.
- [46] S. Sun, R. A. Beck, D. Williams-Young, X. Li, *J. Chem. Theory Comput.* **2019**, *15*, 6824–6831.
- [47] S. Sun, X. Li, *J. Chem. Theory Comput.* **2020**, *16*, 4533–4542.
- [48] G. David, T. J. P. Irons, A. E. A. Fouda, J. W. Furness, A. M. Teale, *J. Chem. Theory Comput.* **2021**, *17*, 5492–5508.
- [49] M. Wibowo, T. J. P. Irons, A. M. Teale, *J. Chem. Theory Comput.* **2021**, *17*, 2137–2165.

-
- [50] S. V. Berdyugina, A. V. Berdyugin, V. Piirola, *Phys. Rev. Lett.* **2007**, *99*, 091101.
- [51] T. Vornanen, S. V. Berdyugina, A. V. Berdyugin, V. Piirola, *Astrophys. J.* **2010**, *720*, L52–L55.
- [52] A. Pausch, M. Gebele, W. Klopper, *J. Chem. Phys.* **2021**, *155*, 201101.
- [53] C. Holzer, A. Pausch, W. Klopper, *Front. Chem.* **2021**, *9*, 746162.
- [54] A. Pausch, C. Holzer, W. Klopper, *J. Chem. Theory Comput.* **2022**, *18*, 3747–3758.
- [55] A. Pausch, C. Holzer, *J. Phys. Chem. Lett.* **2022**, *13*, 4335–4341.
- [56] A. Pausch, W. Klopper, *Mol. Phys.* **2020**, *118*, e1736675.
- [57] L. Monzel, A. Pausch, L. D. M. Peters, E. I. Tellgren, T. Helgaker, W. Klopper, *J. Chem. Phys.* **2022**, *157*, 054106.
- [58] D. R. Hartree, *Math. Proc. Camb. Philos. Soc.* **1928**, *24*, 89–110.
- [59] L. D. Barron, *Molecular Light Scattering and Optical Activity*, Cambridge University Press, Cambridge, UK, **2009**.
- [60] A. Einstein, *Ann. Phys.* **1916**, *354*, 769–822.
- [61] R. P. Feynman, R. B. Leighton, M. Sands, *The Feynman Lectures on Physics Vol. II: Mainly Electromagnetism and Matter*, Basics books, New York, NY, USA, **2011**.
- [62] J. D. Jackson, *Classical Electrodynamics*, 3rd ed., John Wiley & Sons, New York, NY, USA, **1998**.
- [63] A. M. Stewart, *Eur. J. Phys.* **2003**, *24*, 519–524.
- [64] C. Kittel, *Introduction to Solid State Physics*, 8th ed., John Wiley & Sons, Hoboken, NJ, USA, **2005**.
- [65] C. Ballhausen, A. E. Hansen, *Annu. Rev. Phys. Chem.* **1972**, *23*, 15–38.
- [66] M. Born, R. Oppenheimer, *Ann. Phys.* **1927**, *389*, 457–484.
- [67] W. Kutzelnigg, *Mol. Phys.* **1997**, *90*, 909–916.
- [68] J. Avron, I. Herbst, B. Simon, *Ann. Phys.* **1978**, *114*, 431–451.
- [69] H. Herold, H. Ruder, G. Wunner, *J. Phys. B* **1981**, *14*, 751–764.
- [70] B. R. Johnson, J. O. Hirschfelder, K.-H. Yang, *Rev. Mod. Phys.* **1983**, *55*, 109–153.

- [71] P. Schmelcher, L. S. Cederbaum, *Phys. Rev. A* **1988**, *37*, 672–681.
- [72] P. Schmelcher, L. S. Cederbaum, H. D. Meyer, *J. Phys. B* **1988**, *21*, L445–L450.
- [73] M. Born, K. Huang, *Dynamical Theory of Crystal Lattices*, Clarendon Press, Oxford, UK, **1988**.
- [74] N. C. Handy, A. M. Lee, *Chem. Phys. Lett.* **1996**, *252*, 425–430.
- [75] H. C. Longuet-Higgins, *Adv. Spectrosc.* **1961**, *2*, 429–472.
- [76] A. Tachibana, T. Iwai, *Phys. Rev. A* **1986**, *33*, 2262–2269.
- [77] J. Gauss, A. Tajti, M. Kállay, J. F. Stanton, P. G. Szalay, *J. Chem. Phys.* **2006**, *125*, 144111.
- [78] E. F. Valeev, C. D. Sherrill, *J. Chem. Phys.* **2003**, *118*, 3921–3927.
- [79] P. A. M. Dirac, R. H. Fowler, *Proc. Roy. Soc. Lond. A* **1928**, *117*, 610–624.
- [80] T. Saue, *ChemPhysChem* **2011**, *12*, 3077–3094.
- [81] M. Gell-Mann, *Nuovo Cimento* **1956**, *4*, 848–866.
- [82] L. D. M. Peters, T. Culpitt, L. Monzel, E. I. Tellgren, T. Helgaker, *J. Chem. Phys.* **2021**, *155*, 024105.
- [83] T. Culpitt, L. D. M. Peters, E. I. Tellgren, T. Helgaker, *J. Chem. Phys.* **2021**, *155*, 024104.
- [84] M. V. Berry, *Proc. Roy. Soc. Lond. A* **1984**, *392*, 45–57.
- [85] D. Ceresoli, R. Marchetti, E. Tosatti, *Phys. Rev. B* **2007**, *75*.
- [86] T. Culpitt, L. D. M. Peters, E. I. Tellgren, T. Helgaker, *J. Chem. Phys.* **2022**, *156*, 044121.
- [87] D. Ceresoli, E. Tosatti, *Phys. Rev. Lett.* **2002**, *89*, 116402.
- [88] S. Matsika, P. Krause, *Annu. Rev. Phys. Chem.* **2011**, *62*, 621–643.
- [89] M. H. Farag, A. Mandal, P. Huo, *Phys. Chem. Chem. Phys.* **2021**, *23*, 16868–16879.
- [90] F. Hampe, *Accurate treatment of the electronic structure of atoms and molecules in strong magnetic fields*, Dissertation, Johannes Gutenberg-Universität Mainz, Mainz, Germany, **2019**.
- [91] L. D. Landau, E. M. Lifshitz, *Lehrbuch der Theoretischen Physik III: Quantenmechanik*, Akademie-Verlag, Berlin, Germany, **1979**.
- [92] J. E. Lennard-Jones, *J. Chem. Soc. Faraday Trans.* **1929**, *25*, 668–686.

-
- [93] R. S. Mulliken, *Science* **1967**, *157*, 13–24.
- [94] W. Kutzelnigg, *Angew. Chem. Int. Ed.* **1996**, *35*, 572–586.
- [95] F. Jensen, *Introduction to Computational Chemistry*, 3rd ed., John Wiley & Sons, New York, NY, USA, **2016**.
- [96] P. Dahle, K. Ruud, T. Helgaker, P. R. Taylor in *Pauling's Legacy*, (Eds.: Z. Maksić, W. Orville-Thomas), Theoretical and Computational Chemistry, Elsevier, Amsterdam, The Netherlands, **1999**, pp. 147–188.
- [97] K. Wolinski, J. F. Hinton, P. Pulay, *J. Am. Chem. Soc.* **1990**, *112*, 8251–8260.
- [98] A. Schäfer, H. Horn, R. Ahlrichs, *J. Chem. Phys.* **1992**, *97*, 2571–2577.
- [99] A. Schäfer, C. Huber, R. Ahlrichs, *J. Chem. Phys.* **1994**, *100*, 5829–5835.
- [100] K. Eichkorn, F. Weigend, O. Treutler, R. Ahlrichs, *Theor. Chem. Acc.* **1997**, *97*, 119–124.
- [101] K. L. Bak, A. E. Hansen, K. Ruud, T. Helgaker, J. Olsen, P. Jørgensen, *Theoret. Chim. Acta* **1995**, *90*, 441–458.
- [102] T. B. Pedersen, H. Koch, L. Boman, A. M. Sánchez de Merás, *Chem. Phys. Lett.* **2004**, *393*, 319–326.
- [103] W. Kutzelnigg, *J. Mol. Struct. (Theochem)* **1989**, *202*, 11–61.
- [104] W. Kutzelnigg, *Isr. J. Chem.* **1980**, *19*, 193–200.
- [105] M. Schindler, W. Kutzelnigg, *J. Chem. Phys.* **1982**, *76*, 1919–1933.
- [106] A. E. Hansen, T. D. Bouman, *J. Chem. Phys.* **1985**, *82*, 5035–5047.
- [107] T. D. Bouman, A. E. Hansen, *Chem. Phys. Lett.* **1990**, *175*, 292–299.
- [108] T. Keith, R. Bader, *Chem. Phys. Lett.* **1992**, *194*, 1–8.
- [109] T. A. Keith, R. F. Bader, *Chem. Phys. Lett.* **1993**, *210*, 223–231.
- [110] P. Lazzeretti, M. Malagoli, R. Zanasi, *Chem. Phys. Lett.* **1994**, *220*, 299–304.
- [111] R. Zanasi, P. Lazzeretti, M. Malagoli, F. Piccinini, *J. Chem. Phys.* **1995**, *102*, 7150–7157.
- [112] F. Hampe, S. Stopkowicz, *J. Chem. Phys.* **2017**, *146*, 154105.
- [113] J. Gauss, *Chem. Phys. Lett.* **1992**, *191*, 614–620.
- [114] G. Schreckenbach, T. Ziegler, *J. Phys. Chem.* **1995**, *99*, 606–611.
- [115] S. Coriani, C. Hättig, P. Jørgensen, T. Helgaker, *J. Chem. Phys.* **2000**, *113*, 3561–3572.

- [116] J. Autschbach, *ChemPhysChem* **2011**, *12*, 3224–3235.
- [117] S. Loibl, M. Schütz, *J. Chem. Phys.* **2014**, *141*, 024108.
- [118] K. Reiter, M. Kühn, F. Weigend, *J. Chem. Phys.* **2017**, *146*, 054102.
- [119] Y. J. Franzke, F. Weigend, *J. Chem. Theory Comput.* **2019**, *15*, 1028–1043.
- [120] I. Fernandez-Corbaton, D. Beutel, C. Rockstuhl, A. Pausch, W. Klopper, *ChemPhysChem* **2020**, *21*, 878–887.
- [121] S. Burger, F. Lipparini, J. Gauss, S. Stopkowicz, *J. Chem. Phys.* **2021**, *155*, 074105.
- [122] P.-O. Löwdin, P. Lykos, G. W. Pratt, *Rev. Mod. Phys.* **1963**, *35*, 496–501.
- [123] H. Fukutome, *Int. J. Quantum Chem.* **1981**, *20*, 955–1065.
- [124] C. A. Jiménez-Hoyos, T. M. Henderson, G. E. Scuseria, *J. Chem. Theory Comput.* **2011**, *7*, 2667–2674.
- [125] J. M. Kasper, A. J. Jenkins, S. Sun, X. Li, *J. Chem. Phys.* **2020**, *153*, 090903.
- [126] H. A. Kramers, *Proc. Acad. Amst* **1930**, *33*.
- [127] J. J. Goings, F. Egidi, X. Li, *Int. J. Quantum Chem.* **2018**, *118*, e25398.
- [128] M. Gebele, *Symmetrieeigenschaften von Molekülen in Magnetfeldern*, Master's Thesis, Karlsruher Institut für Technologie (KIT), Karlsruhe, Germany, **2021**.
- [129] P. R. Bunker, *Molecular Symmetry and Spectroscopy*, Academic Press, San Diego, CA, USA, **1979**.
- [130] S. L. Altmann, P. Herzig, *Point-Group Theory Tables*, Vienna, Austria, **2011**.
- [131] D. M. Bishop, *Group Theory and Chemistry*, Dover Publications, Mineola, NY, **1993**.
- [132] A. J. Ceulemans, *Group Theory Applied to Chemistry*, Springer, Dordrecht, Heidelberg, New York, London, **2013**.
- [133] P. Schmelcher, L. S. Cederbaum, *Phys. Rev. A* **1990**, *41*, 4936–4943.
- [134] J. Goss, Character Table of $C_{\infty h}$, <https://www.staff.ncl.ac.uk/j.p.goss/symmetry/Cinfh.html>, Accessed: 2022-03-24.
- [135] E. Baerends, D. Ellis, P. Ros, *Chem. Phys.* **1973**, *2*, 41–51.
- [136] K. Eichkorn, O. Treutler, H. Öhm, M. Häser, R. Ahlrichs, *Chem. Phys. Lett.* **1995**, *240*, 283–290.
- [137] R. D. Reynolds, T. Shiozaki, *Phys. Chem. Chem. Phys.* **2015**, *17*, 14280–14283.

-
- [138] J. C. Slater, *Phys. Rev.* **1928**, *32*, 339–348.
- [139] V. Fock, *Z. Phys.* **1930**, *61*, 126–148.
- [140] J. C. Slater, *Phys. Rev.* **1930**, *35*, 210–211.
- [141] J. C. Slater, *Phys. Rev.* **1951**, *81*, 385–390.
- [142] P.-O. Löwdin, I. Mayer in (Ed.: P.-O. Löwdin), *Advances in Quantum Chemistry*, Academic Press, **1992**, pp. 79–114.
- [143] J. Stuber, J. Paldus in *Fundamental World of Quantum Chemistry, A Tribute Volume to the Memory of Per-Olov Lowdin, Vol. 1*, (Eds.: E. Brandas, E. Kryachko), Kluwer Academic Publishers, Dordrecht, The Netherlands, **2003**, pp. 67–139.
- [144] S. F. Boys, I. Shavitt, *A Fundamental Calculation of the Energy Surface for the System of Three Hydrogen Atoms*, University of Wisconsin Technical Report WIS-AF-13, **1959**.
- [145] J. L. Whitten, *J. Chem. Phys.* **1973**, *58*, 4496–4501.
- [146] B. I. Dunlap, J. Connolly, J. Sabin, *J. Chem. Phys.* **1979**, *71*, 3396–3402.
- [147] O. Vahtras, J. Almlöf, M. Feyereisen, *Chem. Phys. Lett.* **1993**, *213*, 514–518.
- [148] S. Reine, E. Tellgren, A. Krapp, T. Kjærgaard, T. Helgaker, B. Jansik, S. Høst, P. Salek, *J. Chem. Phys.* **2008**, *129*, 104101.
- [149] F. Weigend, *Phys. Chem. Chem. Phys.* **2002**, *4*, 4285–4291.
- [150] Y. S. Kim, S. Y. Lee, W. S. Oh, B. H. Park, Y. K. Han, S. J. Park, Y. S. Lee, *Int. J. Quantum Chem.* **1998**, *66*, 91–98.
- [151] M. Nakano, J. Seino, H. Nakai, *Chem. Phys. Lett.* **2017**, *675*, 137–144.
- [152] B. Helmich-Paris, M. Repisky, L. Visscher, *J. Chem. Phys.* **2016**, *145*, 014107.
- [153] F. A. Bischoff, W. Klopper, *J. Chem. Phys.* **2010**, *132*, 094108.
- [154] K. Krause, W. Klopper, *J. Chem. Phys.* **2015**, *142*, 104109.
- [155] M. Feyereisen, G. Fitzgerald, A. Komornicki, *Chem. Phys. Lett.* **1993**, *208*, 359–363.
- [156] F. Weigend, M. Häser, *Theor. Chem. Acc.* **1997**, *97*, 331–340.
- [157] F. Weigend, M. Häser, H. Patzelt, R. Ahlrichs, *Chem. Phys. Lett.* **1998**, *294*, 143–152.
- [158] O. Christiansen, H. Koch, P. Jørgensen, *Chem. Phys. Lett.* **1995**, *243*, 409–418.

- [159] C. Hättig, A. Köhn, K. Hald, *J. Chem. Phys.* **2002**, *116*, 5401–5410.
- [160] C. Hättig, F. Weigend, *J. Chem. Phys.* **2000**, *113*, 5154–5161.
- [161] F. Weigend, A. Köhn, C. Hättig, *J. Chem. Phys.* **2002**, *116*, 3175–3183.
- [162] C. Hättig, A. Köhn, *J. Chem. Phys.* **2002**, *117*, 6939–6951.
- [163] K. Sneskov, O. Christiansen, *Wiley Interdiscip. Rev. Comput. Mol. Sci.* **2012**, *2*, 566–584.
- [164] P. Hohenberg, W. Kohn, *Phys. Rev.* **1964**, *136*, B864–B871.
- [165] W. Kohn, L. J. Sham, *Phys. Rev.* **1965**, *140*, A1133–A1138.
- [166] H. S. Yu, S. L. Li, D. G. Truhlar, *J. Chem. Phys.* **2016**, *145*, 130901.
- [167] A. Görling, *Phys. Rev. A* **1996**, *54*, 3912–3915.
- [168] M. Weimer, W. Hieringer, F. D. Sala, A. Görling, *Chem. Phys.* **2005**, *309*, 77–87.
- [169] J. F. Janak, *Phys. Rev. B* **1978**, *18*, 7165–7168.
- [170] A. M. Teale, S. Coriani, T. Helgaker, *J. Chem. Phys.* **2010**, *132*, 164115.
- [171] J. Harris, R. O. Jones, *J. Phys. F: Met. Phys.* **1974**, *4*, 1170–1186.
- [172] D. Langreth, J. Perdew, *Solid State Commun.* **1975**, *17*, 1425–1429.
- [173] D. C. Langreth, J. P. Perdew, *Phys. Rev. B* **1977**, *15*, 2884–2901.
- [174] O. Gunnarsson, B. I. Lundqvist, *Phys. Rev. B* **1976**, *13*, 4274–4298.
- [175] O. Gunnarsson, B. I. Lundqvist, *Phys. Rev. B* **1977**, *15*, 6006–6006.
- [176] G. Scalmani, M. J. Frisch, *J. Chem. Theory Comput.* **2012**, *8*, 2193–2196.
- [177] F. Egidi, S. Sun, J. J. Goings, G. Scalmani, M. J. Frisch, X. Li, *J. Chem. Theory Comput.* **2017**, *13*, 2591–2603.
- [178] L. J. Sham, W. Kohn, *Phys. Rev.* **1966**, *145*, 561–567.
- [179] U. von Barth, L. Hedin, *J. Phys. C: Solid State Phys.* **1972**, *5*, 1629–1642.
- [180] K. Boguslawski, C. R. Jacob, M. Reiher, *J. Chem. Phys.* **2013**, *138*, 044111.
- [181] G. Vignale, M. Rasolt, *Phys. Rev. Lett.* **1987**, *59*, 2360–2363.
- [182] G. Vignale, M. Rasolt, *Phys. Rev. B* **1988**, *37*, 10685–10696.
- [183] G. Vignale, M. Rasolt, D. J. W. Geldart, *Phys. Rev. B* **1988**, *37*, 2502–2507.
- [184] E. I. Tellgren, S. Kvaal, E. Sagvolden, U. Ekström, A. M. Teale, T. Helgaker, *Phys. Rev. A* **2012**, *86*, 062506.

-
- [185] E. I. Tellgren, A. M. Teale, J. W. Furness, K. K. Lange, U. Ekström, T. Helgaker, *J. Chem. Phys.* **2014**, *140*, 034101.
- [186] C. J. Grayce, R. A. Harris, *Phys. Rev. A* **1994**, *50*, 3089–3095.
- [187] S. Reimann, A. Borgoo, E. I. Tellgren, A. M. Teale, T. Helgaker, *J. Chem. Theory Comput.* **2017**, *13*, 4089–4100.
- [188] S. Reimann, A. Borgoo, J. Austad, E. I. Tellgren, A. M. Teale, T. Helgaker, S. Stopkowicz, *Mol. Phys.* **2019**, *117*, 97–109.
- [189] J. E. Bates, F. Furche, *J. Chem. Phys.* **2012**, *137*, 164105.
- [190] M. Kehry, Y. J. Franzke, C. Holzer, W. Klopper, *Mol. Phys.* **2020**, *118*, e1755064.
- [191] Y. J. Franzke, F. Mack, F. Weigend, *J. Chem. Theory Comput.* **2021**, *17*, 3974–3994.
- [192] J. Tao, *Phys. Rev. B* **2005**, *71*, 205107.
- [193] J. W. Furness, J. Verbeke, E. I. Tellgren, S. Stopkowicz, U. Ekström, T. Helgaker, A. M. Teale, *J. Chem. Theory Comput.* **2015**, *11*, 4169–4181.
- [194] C. Holzer, Y. J. Franzke, M. Kehry, *J. Chem. Theory Comput.* **2021**, *17*, 2928–2947.
- [195] J. F. Dobson, *J. Chem. Phys.* **1993**, *98*, 8870–8872.
- [196] A. D. Becke, *J. Chem. Phys.* **2002**, *117*, 6935–6938.
- [197] A. D. Becke, *J. Chem. Phys.* **1998**, *109*, 2092–2098.
- [198] J. P. Perdew, S. Kurth, A. Zupan, P. Blaha, *Phys. Rev. Lett.* **1999**, *82*, 2544–2547.
- [199] M. Hoffmann-Ostenhof, T. Hoffmann-Ostenhof, *Phys. Rev. A* **1977**, *16*, 1782–1785.
- [200] C. F. von Weizsäcker, *Z. Phys.* **1935**, *96*, 431–458.
- [201] P. Skudlarski, G. Vignale, *Phys. Rev. B* **1993**, *48*, 8547–8559.
- [202] A. M. Lee, N. C. Handy, S. M. Colwell, *J. Chem. Phys.* **1995**, *103*, 10095–10109.
- [203] J. Tao, J. P. Perdew, *Phys. Rev. Lett.* **2005**, *95*, 196403.
- [204] J. Tao, G. Vignale, *Phys. Rev. B* **2006**, *74*, 193108.
- [205] K. Higuchi, M. Higuchi, *Phys. Rev. B* **2006**, *74*, 195122.

- [206] K. Higuchi, M. Miyasita, M. Kodera, M. Higuchi, *J. Magn. Magn. Mater.* **2007**, *310*, 1065–1066.
- [207] S. Sen, E. I. Tellgren, *J. Chem. Phys.* **2018**, *149*, 144109.
- [208] W. Zhu, L. Zhang, S. B. Trickey, *Phys. Rev. A* **2014**, *90*, 022504.
- [209] A. D. Becke, *Phys. Rev. A* **1988**, *38*, 3098–3100.
- [210] A. D. Becke, *J. Chem. Phys.* **1992**, *96*, 2155–2160.
- [211] A. D. Becke, *J. Chem. Phys.* **1992**, *97*, 9173–9177.
- [212] A. D. Becke, *J. Chem. Phys.* **1993**, *98*, 5648–5652.
- [213] R. Baer, E. Livshits, U. Salzner, *Annu. Rev. Phys. Chem.* **2010**, *61*, 85–109.
- [214] P. M. W. Gill, R. D. Adamson, J. A. Pople, *Mol. Phys.* **1996**, *88*, 1005–1009.
- [215] T. Leininger, H. Stoll, H.-J. Werner, A. Savin, *Chem. Phys. Letters.* **1997**, *275*, 151–160.
- [216] H. Iikura, T. Tsuneda, T. Yanai, K. Hirao, *J. Chem. Phys.* **2001**, *115*, 3540–3544.
- [217] J. P. Perdew, K. Schmidt, *AIP Conf. Proc.* **2001**, *577*, 1–20.
- [218] J. P. Perdew, *MRS Bull.* **2013**, *38*, 743–750.
- [219] L. Goerigk, A. Hansen, C. Bauer, S. Ehrlich, A. Najibi, S. Grimme, *Phys. Chem. Chem. Phys.* **2017**, *19*, 32184–32215.
- [220] M. G. Medvedev, I. S. Bushmarinov, J. Sun, J. P. Perdew, K. A. Lyssenko, *Science* **2017**, *355*, 49–52.
- [221] M. Korth, *Angew. Chem. Int. Ed.* **2017**, *56*, 5396–5398.
- [222] N. Mardirossian, M. Head-Gordon, *Mol. Phys.* **2017**, *115*, 2315–2372.
- [223] C. Holzer, *Die GW-Methode und Bethe-Salpeter-Gleichung in der Quantenchemie: Theorie und Anwendung*, Dissertation, Karlsruher Institut für Technologie (KIT), Karlsruhe, Germany, **2019**.
- [224] L. Hedin, *Phys. Rev.* **1965**, *139*, A796–A823.
- [225] L. Hedin, *Nucl. Instr. Methods Phys. Res. Section A* **1991**, *308*, 169–177.
- [226] M. J. van Setten, F. Weigend, F. Evers, *J. Chem. Theory Comput.* **2013**, *9*, 232–246.
- [227] F. Kaplan, M. E. Harding, C. Seiler, F. Weigend, F. Evers, M. J. van Setten, *J. Chem. Theory Comput.* **2016**, *12*, 2528–2541.

-
- [228] C. Holzer, A. M. Teale, F. Hampe, S. Stopkowicz, T. Helgaker, W. Klopper, *J. Chem. Phys.* **2019**, *150*, 214112.
- [229] C. Holzer, A. M. Teale, F. Hampe, S. Stopkowicz, T. Helgaker, W. Klopper, *J. Chem. Phys.* **2019**, *151*, 069902.
- [230] X. Blase, C. Attaccalite, V. Olevano, *Phys. Rev. B* **2011**, *83*, 115103.
- [231] H. Eshuis, J. E. Bates, F. Furche, *Theor. Chem. Acc.* **2012**, *131*, 1084.
- [232] M. Kühn, *J. Chem. Theory Comput.* **2014**, *10*, 623–633.
- [233] J. Toulouse, W. Zhu, A. Savin, G. Jansen, J. G. Ángyán, *J. Chem. Phys.* **2011**, *135*, 084119.
- [234] X. Ren, P. Rinke, V. Blum, J. Wieferink, A. Tkatchenko, A. Sanfilippo, K. Reuter, M. Scheffler, *New J. Phys.* **2012**, *14*, 053020.
- [235] J. Wilhelm, M. Del Ben, J. Hutter, *J. Chem. Theory Comput.* **2016**, *12*, 3623–3635.
- [236] C. Holzer, W. Klopper, *J. Chem. Phys.* **2019**, *150*, 204116.
- [237] R. W. Godby, M. Schlüter, L. J. Sham, *Phys. Rev. B* **1988**, *37*, 10159–10175.
- [238] D. Golze, J. Wilhelm, M. J. van Setten, P. Rinke, *J. Chem. Theory Comput.* **2018**, *14*, 4856–4869.
- [239] J. J. Goings, P. J. LeStrange, X. Li, *Wiley Interdiscip. Rev. Comput. Mol. Sci.* **2018**, *8*, e1341.
- [240] X. Li, N. Govind, C. Isborn, A. E. DePrince, K. Lopata, *Chem. Rev.* **2020**, *120*, 9951–9993.
- [241] M. E. Casida in *Recent Advances in Density Functional Methods, Vol. 1*, (Ed.: D. P. Chong), World Scientific, Singapore, **1995**, pp. 155–192.
- [242] A. Dreuw, M. Head-Gordon, *Chem. Rev.* **2005**, *105*, 4009–4037.
- [243] M. E. Casida, *J. Mol. Struct. (Theochem)* **2009**, *914*, 3–18.
- [244] R. Bauernschmitt, R. Ahlrichs, *Chem. Phys. Lett.* **1996**, *256*, 454–464.
- [245] F. Hampe, S. Stopkowicz, *J. Chem. Theory Comput.* **2019**, *15*, 4036–4043.
- [246] D. Kats, T. Korona, M. Schütz, *J. Chem. Phys.* **2006**, *125*, 104106.
- [247] F. Wang, T. Ziegler, E. van Lenthe, S. van Gisbergen, E. J. Baerends, *J. Chem. Phys.* **2005**, *122*, 204103.
- [248] F. Wang, T. Ziegler, *J. Chem. Phys.* **2005**, *123*, 154102.

- [249] M. Kühn, F. Weigend, *J. Chem. Theory Comput.* **2013**, *9*, 5341–5348.
- [250] M. Kühn, *Zweikomponentige Methoden im Rahmen der zeitabhängigen Dichtefunktionaltheorie - Theorie, Implementierung und Anwendung*, Dissertation, Karlsruher Institut für Technologie (KIT), Karlsruhe, Germany, **2015**.
- [251] F. Furche, *J. Chem. Phys.* **2001**, *114*, 5982–5992.
- [252] H. J. Xiang, M.-H. Whangbo, *Phys. Rev. Lett.* **2007**, *99*, 257203.
- [253] M. J. Han, H.-S. Kim, D. G. Kim, J. Yu, *Phys. Rev. B* **2013**, *87*, 184432.
- [254] C. Becker, J. Hafner, R. Lorenz, *J. Magn. Magn. Mater.* **1996**, *157-158*, 619–621.
- [255] D. Peng, W. Zou, W. Liu, *J. Chem. Phys.* **2005**, *123*, 144101.
- [256] J. Gao, W. Zou, W. Liu, Y. Xiao, D. Peng, B. Song, C. Liu, *J. Chem. Phys.* **2005**, *123*, 054102.
- [257] F. Wang, T. Ziegler, *J. Chem. Phys.* **2004**, *121*, 12191–12196.
- [258] J. Gao, W. Zou, W. Liu, Y. Xiao, D. Peng, B. Song, C. Liu, *J. Chem. Phys.* **2005**, *123*, 054102.
- [259] S. Komorovsky, P. J. Cherry, M. Repisky, *J. Chem. Phys.* **2019**, *151*, 184111.
- [260] J. E. Bates, M. C. Heiche, J. Liang, F. Furche, *J. Chem. Phys.* **2022**, *156*, 159902.
- [261] G. Onida, L. Reining, A. Rubio, *Rev. Mod. Phys.* **2002**, *74*, 601–659.
- [262] S. Sagmeister, C. Ambrosch-Draxl, *Phys. Chem. Chem. Phys.* **2009**, *11*, 4451–4457.
- [263] F. Bruneval, S. M. Hamed, J. B. Neaton, *J. Chem. Phys.* **2015**, *142*, 244101.
- [264] F. Neese, *Coord. Chem. Rev.* **2009**, *253*, 526–563.
- [265] X. Blase, C. Attaccalite, *Appl. Phys. Lett.* **2011**, *99*, 171909.
- [266] X. Gui, C. Holzer, W. Klopper, *J. Chem. Theory Comput.* **2018**, *14*, 2127–2136.
- [267] L. Reining, V. Olevano, A. Rubio, G. Onida, *Phys. Rev. Lett.* **2002**, *88*, 066404.
- [268] K. Krause, W. Klopper, *J. Comput. Chem.* **2017**, *38*, 383–388.
- [269] C. Holzer, W. Klopper, *J. Chem. Phys.* **2018**, *149*, 101101.
- [270] J. M. Busch, D. M. Zink, P. Di Martino-Fumo, F. R. Rehak, P. Boden, S. Steiger, O. Fuhr, M. Nieger, W. Klopper, M. Gerhards, S. Bräse, *Dalton Trans.* **2019**, *48*, 15687–15698.

-
- [271] P. Boden, P. Di Martino-Fumo, J. M. Busch, F. R. Rehak, S. Steiger, O. Fuhr, M. Nieger, D. Volz, W. Klopper, S. Bräse, M. Gerhards, *Chem. Eur. J.* **2021**, *27*, 5439–5452.
- [272] Y. J. Franzke, C. Holzer, F. Mack, *J. Chem. Theory Comput.* **2022**, *18*, 1030–1045.
- [273] L. A. Nafie, *J. Chem. Phys.* **1992**, *96*, 5687–5702.
- [274] S. Grimme, *Chem. Phys. Lett.* **2001**, *339*, 380–388.
- [275] S. Grimme, F. Furche, R. Ahlrichs, *Chem. Phys. Lett.* **2002**, *361*, 321–328.
- [276] P. Norman, D. M. Bishop, J. Jensen, Hans Jørgen Aa. and Oddershede, *J. Chem. Phys.* **2001**, *115*, 10323–10334.
- [277] P. Norman, D. M. Bishop, J. Jensen, Hans Jørgen Aa. and Oddershede, *J. Chem. Phys.* **2005**, *123*, 194103.
- [278] A. Jiemchooraj, P. Norman, *J. Chem. Phys.* **2007**, *126*, 134102.
- [279] M. N. Pedersen, E. D. Hedegård, J. M. H. Olsen, J. Kauczor, P. Norman, J. Kongsted, *J. Chem. Theory Comput.* **2014**, *10*, 1164–1171.
- [280] N. Kobayashi, K. Nakai, *Chem. Commun.* **2007**, 4077–4092.
- [281] S. B. Piepho, P. N. Schatz, *Group Theory in Spectroscopy: with Applications to Magnetic Circular Dichroism*, John Wiley & Sons, New York, NY, USA, **1983**.
- [282] W. R. Mason, *A Practical Guide to Magnetic Circular Dichroism Spectroscopy*, John Wiley & Sons, New York, NY, USA, **2007**.
- [283] T. Kjærgaard, B. Jansík, P. Jørgensen, S. Coriani, J. Michl, *J. Phys. Chem. A* **2007**, *111*, 11278–11286.
- [284] A. Buckingham, P. Stephens, *Annu. Rev. Phys. Chem.* **1966**, *17*, 399–432.
- [285] P. J. Stephens, *J. Chem. Phys.* **1970**, *52*, 3489–3516.
- [286] H. Solheim, K. Ruud, S. Coriani, P. Norman, *J. Chem. Phys.* **2008**, *128*, 094103.
- [287] H. Solheim, K. Ruud, S. Coriani, P. Norman, *J. Phys. Chem. A* **2008**, *112*, 9615–9618.
- [288] P. Norman, K. Ruud, T. Saue, *Principles and Practices of Molecular Properties*, Wiley-Blackwell, Hoboken, NJ, USA, **2018**.
- [289] Y. Honda, M. Hada, M. Ehara, H. Nakatsuji, J. Downing, J. Michl, *Chem. Phys. Lett.* **2002**, *355*, 219–225.

- [290] M. Krykunov, M. Seth, T. Ziegler, J. Autschbach, *J. Chem. Phys.* **2007**, *127*, 244102.
- [291] M. Seth, T. Ziegler, *J. Chem. Phys.* **2007**, *127*, 134108.
- [292] D. Ganyushin, F. Neese, *J. Chem. Phys.* **2008**, *128*, 114117.
- [293] S. K. Khani, R. Faber, F. Santoro, C. Hättig, S. Coriani, *J. Chem. Theory Comput.* **2019**, *15*, 1242–1254.
- [294] Y. N. Heit, D.-C. Sergentu, J. Autschbach, *Phys. Chem. Chem. Phys.* **2019**, *21*, 5586–5597.
- [295] M. Seth, M. Krykunov, T. Ziegler, J. Autschbach, *J. Chem. Phys.* **2008**, *128*, 234102.
- [296] M. Seth, M. Krykunov, T. Ziegler, J. Autschbach, A. Banerjee, *J. Chem. Phys.* **2008**, *128*, 144105.
- [297] M. Seth, T. Ziegler, J. Autschbach, *J. Chem. Phys.* **2008**, *129*, 104105.
- [298] T. Tajima, *Computational plasma physics: with applications to fusion and astrophysics*, CRC press, Boca Raton, FL, USA, **2018**.
- [299] R. S. Mulliken, *J. Chem. Phys.* **1955**, *23*, 1833.
- [300] R. S. Mulliken, *J. Chem. Phys.* **1955**, *23*, 1841.
- [301] R. S. Mulliken, *J. Chem. Phys.* **1955**, *23*, 2343.
- [302] X. Qian, J. Li, L. Qi, C.-Z. Wang, T.-L. Chan, Y.-X. Yao, K.-M. Ho, S. Yip, *Phys. Rev. B*, *78*, 245112.
- [303] R. Ahlrichs, M. Bär, M. Häser, H. Horn, C. Kölmel, *Chem. Phys. Lett.* **1989**, *162*, 165–169.
- [304] F. Furche, R. Ahlrichs, C. Hättig, W. Klopper, M. Sierka, F. Weigend, *Wiley Interdiscip. Rev. Comput. Mol. Sci.* **2014**, *4*, 91–100.
- [305] S. G. Balasubramani, G. P. Chen, S. Coriani, M. Diedenhofen, M. S. Frank, Y. J. Franzke, F. Furche, R. Grotjahn, M. E. Harding, C. Hättig, A. Hellweg, B. Helmich-Paris, C. Holzer, U. Huniar, M. Kaupp, A. Marefat Khah, S. Karbalaei Khani, T. Müller, F. Mack, B. D. Nguyen, S. M. Parker, E. Perlt, D. Rappoport, K. Reiter, S. Roy, M. Rückert, G. Schmitz, M. Sierka, E. Tapavicza, D. P. Tew, C. van Wüllen, V. K. Voora, F. Weigend, A. Wodyński, J. M. Yu, *J. Chem. Phys.* **2020**, *152*, 184107.

-
- [306] TURBOMOLE Version 7.6 (2022), a development of University of Karlsruhe (TH) and Forschungszentrum Karlsruhe GmbH, 1989-2007, TURBOMOLE GmbH, since 2007, available from <http://www.turbomole.org>.
- [307] M. K. Armbruster, W. Klopper, F. Weigend, *Phys. Chem. Chem. Phys.* **2006**, *8*, 4862–4865.
- [308] M. K. Armbruster, F. Weigend, C. van Wüllen, W. Klopper, *Phys. Chem. Chem. Phys.* **2008**, *10*, 1748–1756.
- [309] P. Plessow, F. Weigend, *J. Comput. Chem.* **2012**, *33*, 810–816.
- [310] A. Baldes, F. Weigend, *Mol. Phys.* **2013**, *111*, 2617–2624.
- [311] M. Kühn, F. Weigend, *J. Chem. Phys.* **2015**, *142*, 034116.
- [312] Y. J. Franzke, N. Middendorf, F. Weigend, *J. Chem. Phys.* **2018**, *148*, 104110.
- [313] K. Krause, M. Bauer, W. Klopper, *J. Chem. Theory Comput.* **2016**, *12*, 2853–2860.
- [314] M. Kühn, F. Weigend, *J. Chem. Theory Comput.* **2015**, *11*, 969–979.
- [315] C. Holzer, X. Gui, M. E. Harding, G. Kresse, T. Helgaker, W. Klopper, *J. Chem. Phys.* **2018**, *149*, 144106.
- [316] S. Blaschke, S. Stopkowicz, *J. Chem. Phys.* **2022**, *156*, 044115.
- [317] R. Hoffmann, *J. Chem. Phys.* **1963**, *39*, 1397–1412.
- [318] S. Lehtola, *J. Chem. Theory Comput.* **2019**, *15*, 1593–1604.
- [319] J. G. Aiken, J. A. Erdos, J. A. Goldstein, *Int. J. Quantum Chem.* **1980**, *18*, 1101–1108.
- [320] O. Treutler, R. Ahlrichs, *J. Chem. Phys.* **1995**, *102*, 346–354.
- [321] Y. J. Franzke, R. Treß, T. M. Pazdera, F. Weigend, *Phys. Chem. Chem. Phys.* **2019**, *21*, 16658–16664.
- [322] R. Ahlrichs, *Phys. Chem. Chem. Phys.* **2004**, *6*, 5119–5121.
- [323] M. Häser, R. Ahlrichs, *J. Comput. Chem.* **1989**, *10*, 104–111.
- [324] C. Ochsenfeld, C. A. White, M. Head-Gordon, *J. Chem. Phys.* **1998**, *109*, 1663–1669.
- [325] T. H. Thompson, C. Ochsenfeld, T.-C. Jagau, *J. Chem. Phys.* **2019**, *151*, 184104.
- [326] J. Almlöf, K. Faegri Jr., K. Korsell, *J. Comput. Chem.* **1982**, *3*, 385–399.

- [327] D. Cremer, J. Gauss, *J. Comput. Chem.* **1986**, *7*, 274–282.
- [328] P. Pulay, *Chem. Phys. Lett.* **1980**, *73*, 393–398.
- [329] P. Pulay, *J. Comput. Chem.* **1982**, *3*, 556–560.
- [330] U. Kappes, P. Schmelcher, *J. Chem. Phys.* **1994**, *100*, 2878–2887.
- [331] S. Lehtola, M. Dimitrova, D. Sundholm, *Mol. Phys.* **2020**, *118*, e1597989.
- [332] P.-O. Löwdin, *J. Chem. Phys.* **1950**, *18*, 365–375.
- [333] P.-O. Löwdin in (Ed.: P.-O. Löwdin), *Adv. Quantum Chem.* Academic Press, Amsterdam, The Netherlands, **1970**, pp. 185–199.
- [334] P. Cassam-Chenaï, *Theor. Chem. Acc.* **2015**, *134*, 1–6.
- [335] P. Cassam-Chenaï, *J. Math. Chem.* **1994**, *15*, 303–321.
- [336] A. T. Amos, G. G. Hall, H. Jones, *Proc. Roy. Soc. Lond. A* **1961**, *263*, 483–493.
- [337] R. Al-Saadon, T. Shiozaki, G. Knizia, *J. Phys. Chem. A* **2019**, *123*, 3223–3228.
- [338] J. A. Pople, R. Krishnan, H. B. Schlegel, J. S. Binkley, *Int. J. Quantum Chem.* **1979**, *16*, 225–241.
- [339] P. Deglmann, F. Furche, R. Ahlrichs, *Chem. Phys. Lett.* **2002**, *362*, 511–518.
- [340] C. G. Broyden, *IMA J. Appl. Math.* **1970**, *6*, 76–90.
- [341] R. Fletcher, *Comput. J.* **1970**, *13*, 317–322.
- [342] D. Goldfarb, *Math. Comput.* **1970**, *24*, 23–26.
- [343] D. F. Shanno, *Math. Comput.* **1970**, *24*, 647–656.
- [344] J. Baker, *J. Comput. Chem.* **1992**, *13*, 240–253.
- [345] J. Baker, *J. Comput. Chem.* **1993**, *14*, 1085–1100.
- [346] J. Baker, D. Bergeron, *J. Comput. Chem.* **1993**, *14*, 1339–1346.
- [347] A. Appenzeller, *Strukturoptimierung von Molekülen in starken Magnetfeldern*, Bachelor’s Thesis, Karlsruher Institut für Technologie (KIT), Karlsruhe, Germany, **2020**.
- [348] P. Pulay, G. Fogarasi, F. Pang, J. E. Boggs, *J. Am. Chem. Soc.* **1979**, *101*, 2550–2560.
- [349] M. von Arnim, R. Ahlrichs, *J. Chem. Phys.* **1999**, *111*, 9183–9190.
- [350] M.-P. Kitsaras, personal communication, **2022**.

-
- [351] T. Helgaker, P. Jorgensen, J. Olsen, *Molecular Electronic-Structure Theory*, John Wiley & Sons, Nashville, TN, USA, **2013**.
- [352] S. Blaschke, personal communication, **2021**.
- [353] M. Head-Gordon, J. A. Pople, *J. Chem. Phys.* **1988**, *89*, 5777–5786.
- [354] S. Obara, A. Saika, *J. Chem. Phys.* **1986**, *84*, 3963–3974.
- [355] S. Obara, A. Saika, *J. Chem. Phys.* **1988**, *89*, 1540–1559.
- [356] I. Shavitt in *Methods Comput. Phys. Vol. 3*, (Eds.: B. Alder, S. Fernbach, M. Rotenberg), Academic Press Inc., New York, NY, USA, **1963**, pp. 1–45.
- [357] S. F. Boys, A. C. Egerton, *Proc. Roy. Soc. Lond. A* **1950**, *200*, 542–554.
- [358] K. Ishida, *J. Comput. Chem.* **2004**, *25*, 739–748.
- [359] H. Hellmann, *Eur. Phys. J. A* **1933**, *85*, 180–190.
- [360] R. P. Feynman, *Phys. Rev.* **1939**, *56*, 340–343.
- [361] P. Pulay, *Mol. Phys.* **1969**, *17*, 197–204.
- [362] C. Coulson, *Mol. Phys.* **1971**, *20*, 687–694.
- [363] P. Pulay, *Wiley Interdiscip. Rev. Comput. Mol. Sci.* **2014**, *4*, 169–181.
- [364] A. Komornicki, K. Ishida, K. Morokuma, R. Ditchfield, M. Conrad, *Chem. Phys. Lett.* **1977**, *45*, 595–602.
- [365] M. Bürkle, J. K. Viljas, T. J. Hellmuth, E. Scheer, F. Weigend, G. Schön, F. Pauly, *Phys. Status Solidi B* **2013**, *250*, 2468–2480.
- [366] L. E. McMurchie, E. R. Davidson, *J. Comput. Phys.* **1978**, *26*, 218–231.
- [367] H. F. King, M. Dupuis, *J. Comput. Phys.* **1976**, *21*, 144–165.
- [368] A. Banerjee, J. O. Jensen, J. Simons, *J. Chem. Phys.* **1985**, *82*, 4566–4576.
- [369] C. Suellen, R. G. Freitas, P.-F. Loos, D. Jacquemin, *J. Chem. Theory Comput.* **2019**, *15*, 4581–4590.
- [370] F. Weigend, R. Ahlrichs, *Phys. Chem. Chem. Phys.* **2005**, *7*, 3297–3305.
- [371] F. Weigend, *Phys. Chem. Chem. Phys.* **2006**, *8*, 1057–1065.
- [372] F. Weigend, *J. Comput. Chem.* **2008**, *29*, 167–175.
- [373] J. P. Perdew, M. Ernzerhof, K. Burke, *J. Chem. Phys.* **1996**, *105*, 9982–9985.
- [374] R. A. Kendall, T. H. Dunning, R. J. Harrison, *J. Chem. Physics.* **1992**, *96*, 6796–6806.

- [375] T. H. Dunning, *J. Chem. Phys.* **1989**, *90*, 1007–1023.
- [376] D. E. Woon, T. H. Dunning, *J. Chem. Phys.* **1995**, *103*, 4572–4585.
- [377] J. J. Philips, M. A. Hudspeth, P. M. Browne, J. E. Peralta, *Chem. Phys. Lett.* **2010**, *495*, 146–150.
- [378] C. Lee, W. Yang, R. G. Parr, *Phys. Rev. B* **1988**, *37*, 785–789.
- [379] P. J. Stephens, F. J. Devlin, C. F. Chabalowski, M. J. Frisch, *J. Phys. Chem.* **1994**, *98*, 11623–11627.
- [380] T. Yanai, D. P. Tew, N. C. Handy, *Chem. Phys. Lett.* **2004**, *393*, 51–57.
- [381] A. A. Meier, G. H. Wagnière, *Chem. Phys.* **1987**, *113*, 287–307.
- [382] J. P. Perdew, W. Yue, *Phys. Rev. B* **1986**, *33*, 8800–8802.
- [383] J. P. Perdew, Y. Wang, *Phys. Rev. B* **1992**, *45*, 13244–13249.
- [384] J. P. Perdew, K. Burke, M. Ernzerhof, *Phys. Rev. Lett.* **1996**, *77*, 3865–3868.
- [385] J. Tao, J. P. Perdew, V. N. Staroverov, G. E. Scuseria, *Phys. Rev. Lett.* **2003**, *91*, 146401.
- [386] N. Mardirossian, M. Head-Gordon, *J. Chem. Phys.* **2016**, *144*, 214110.
- [387] L. Pauling, *J. Chem. Soc., Chem. Commun.* **1980**, 688–689.
- [388] E. B. Guidez, C. M. Aikens, *J. Phys. Chem. C* **2013**, *117*, 21466–21475.
- [389] P. Sony, A. Shukla, *Phys. Rev. B* **2007**, *75*, 155208.
- [390] H. B. Klevens, J. R. Platt, *J. Chem. Phys.* **1949**, *17*, 470–481.
- [391] D. Biermann, W. Schmidt, *J. Am. Chem. Soc.* **1980**, *102*, 3163–3173.
- [392] A. Bree, L. E. Lyons, *J. Chem. Soc.* **1960**, 5206–5212.
- [393] W. Kutzelnigg, *Einführung in die Theoretische Chemie - Band 2: Die chemische Bindung*, 2nd ed., Wiley, New York, NY, USA, **1993**.
- [394] C. A. Coulson, I. Fischer, *Philos. Mag.* **1949**, *40*, 386–393.
- [395] D. Hait, A. Rettig, M. Head-Gordon, *Phys. Chem. Chem. Phys.* **2019**, *21*, 21761–21775.
- [396] M. A. Barstow, J. K. Barstow, S. L. Casewell, J. B. Holberg, I. Hubeny, *Mon. Not. R. Astron. Soc.* **2014**, *440*, 1607–1625.
- [397] S. O. Kepler, D. Koester, G. Ourique, *Science* **2016**, *352*, 67–69.
- [398] W. C. Stwalley, W. T. Zemke, *J. Phys. Chem. Ref. Data* **1993**, *22*, 87–112.

-
- [399] M. J. Pemberton, T. J. P. Irons, T. Helgaker, A. M. Teale, *J. Chem. Phys.* **2022**, *156*, 204113.
- [400] B. P. Pritchard, D. Altarawy, B. Didier, T. D. Gibson, T. L. Windus, *J. Chem. Inf. Model.* **2019**, *59*, 4814–4820.
- [401] M. Jeziorska, W. Cencek, K. Patkowski, B. Jeziorski, K. Szalewicz, *J. Chem. Phys.* **2007**, *127*, 124303.

List of Figures

4.7.1. Flow chart for magnetic point groups	40
6.2.1. Graphical illustration of A , B and C terms of MCD	72
8.1.1. Input for 2c calculations in magnetic fields	85
8.2.1. SCF procedure with additional functionalities	86
8.2.2. Construction of Coulomb and exchange potentials	89
8.3.1. Hessian consisting of internal coordinates in magnetic fields	98
9.2.1. Obara–Saika for overlap integrals	105
9.3.1. Calculation of kinetic energy integrals	108
9.4.1. Computation of complex Boys function	112
9.4.2. Obara–Saika for nuclear attraction integrals	115
9.5.1. Algorithm for derivatives of four-center integrals	122
10.2.1. Test set of 36 small molecules	127
10.2.2. Error of the RI- JK approximation	128
10.2.3. Error of the RI- J and RI- K approximations	129
10.2.4. Error of the RI approximation for electronic excitations	130
10.4.1. Assessment of efficiency for the OpenMP parallelization	134
11.1.1. Algorithm for calculation of Berry curvature tensor	137
11.2.1. Angular dependence of Berry charge distribution	141
12.1.1. Structures of p -benzoquinone and tetrachloro- p -benzoquinone	148
12.1.2. MCD spectrum of p -benzoquinone	149
12.1.3. MCD spectrum of tetrachloro- p -benzoquinone	150
12.2.1. Structure of the ZnDiNTAP molecule	151
12.2.2. MCD of ZnDiNTAP with different basis sets	152
12.2.3. MCD of ZnDiNTAP with different density functionals	153
12.2.4. Theoretical versus experimental MCD spectrum of ZnDiNTAP	155

13.1.1. Influence of magnetic field on electronic excitations	158
13.1.2. Excitation energies of pyrazine in magnetic field	160
13.2.1. Structure of tetracene	161
13.2.2. UV/Vis spectrum of tetracene in the absence of a field	164
13.2.3. Influence of magnetic field on electronic excitations of tetracene . .	165
13.2.4. Transition densities of tetracene	166
13.2.5. UV/Vis spectra of tetracene in magnetic fields	167
13.2.6. Color change of tetracene	168
14.2.1. Potential energy surface of H ₂ in magnetic fields	171
14.2.2. Potential energy barrier for rotation of H ₂ in magnetic fields . . .	172
14.2.3. Trajectories for rotational and librational motion of H ₂	173
14.2.4. Rovibrational spectrum of H ₂ in strong magnetic field	175
14.2.5. Canonical ensemble of rovibrational spectra for H ₂	176
14.3.1. Potential energy surface of LiH in magnetic fields	178
14.3.2. Potential energy barrier for rotation of LiH in magnetic fields . . .	179
14.3.3. Trajectories for rotational and librational motion of LiH	180
14.3.4. Rovibrational spectrum of LiH in strong magnetic field	181
14.3.5. Canonical ensemble of infrared spectra for LiH	182
14.3.6. Comparison between Berry and Mulliken approaches	183
15.1.1. Potential energy surface of He ₂ in strong magnetic field	186
15.1.2. PES of different spin states for He ₂ in magnetic field	188
15.2.1. Geometries of helium clusters with up to 19 atoms	190

List of Tables

4.7.1. Character table of the double group C_∞	41
4.7.2. Character table of the double group $C_{\infty h}$	42
5.2.1. Symmetry classification of Hartree–Fock wave functions	46
10.4.1. Timings for benchmark calculations on aromatic molecules	133
11.2.1. Charge distribution of LiH with perpendicular magnetic fields	139
11.2.2. Charge distribution of LiH with parallel magnetic fields	140
11.2.3. Isotropic average of charge distribution	142
11.2.4. Basis set dependence of Berry and Mulliken charges	143
13.2.1. Excitation energies of tetracene with optimized geometry	163
13.2.2. Excitation energies of tetracene with fixed geometry	164
15.1.1. Bond length and dissociation energy of He_2 in $ \mathbf{B} = 2.5 B_0$	187
15.1.2. Bond length and dissociation energy of He_2 in $ \mathbf{B} = 2 B_0$	188
15.2.1. Bond lengths of helium clusters with up to 19 atoms	190

Permissions to Print

This work contains material, which was previously published in scientific journals. The permissions to use this material in print and electronic form was obtained from the copyright-holders:

- Section 4.7, as well as figure 4.7.1 and tables 4.7.1, 4.7.2 contained therein. Reproduced with permission from *Molecular point groups and symmetry in external magnetic fields*, Ansgar Pausch, Melanie Gebele, Wim Klopper, J. Chem. Phys. 2021, 155, 201101. Copyright 2021 American Institute of Physics Publishing.
- Sections 5.2.4, 8.2.4, 9.4.2, 9.5.3, 10.4, figures 9.4.1, 10.4.1, table 10.4.1. Reproduced and adapted with permission from *Efficient evaluation of three-centre two-electron integrals over London orbitals*, A. Pausch, W. Klopper, Mol. Phys. 2020, 118, e1736675. Copyright 2020 Taylor & Francis.
- Sections 5.4, 6.1.4, 6.2.3, 10.2.3, 13.1, chapter 12, and figures 6.2.1, 10.2.4, 12.1.2, 12.1.3, 12.2.1, 12.2.2, 12.2.3 and 12.2.4. Reproduced and adapted with permission from *Efficient Calculation of Magnetic-Circular-Dichroism Spectra using Spin-Noncollinear Linear-Response Time-Dependent Density-Functional Theory in Finite Magnetic Fields*, A. Pausch, C. Holzer, W. Klopper, J. Chem. Theory Comput. 2022, 18, 3747–3758. Copyright 2022 American Chemical Society.
- Sections 5.4, 6.1.4, 13.1.3 and figure 13.1.2. Reproduced and adapted with permission from *Linear Response of Current-Dependent Density Functional Approximations in Magnetic Fields*, A. Pausch, C. Holzer, J. Phys. Chem. Lett. 2022, 13, 4335–4341. Copyright 2022 American Chemical Society.

- Sections 5.5, 6.1.5, 13.2.2, tables 13.2.1, 13.2.2, figures 13.2.3, 13.2.4, 13.2.5, 13.2.6. Reproduced and adapted with permission from *The GW/BSE Method in Magnetic Fields*, C. Holzer, A. Pausch, W. Klopper, *Front. Chem.* 2021, 9, 746162. Following CC BY 4.0.
- Sections 14.2 and 14.3, figures 14.2.2, 14.2.3, 14.2.4, 14.2.5, 14.3.1, 14.3.2, 14.3.3, 14.3.4, 14.3.5. Reproduced and adapted with permission from *Molecular dynamics of linear molecules in strong magnetic fields*, L. Monzel, A. Pausch, L. D. M. Peters, E. I. Tellgren, T. Helgaker, W. Klopper, *J. Chem. Phys.* 2022, 157, 054106. Copyright 2022 American Institute of Physics Publishing.

List of Publications

9. *Molecular Dynamics of Linear Molecules in Strong Magnetic Fields*
L. Monzel, **A. Pausch**, L. D. M. Peters, E. I. Tellgren, T. Helgaker, W. Klopper
J. Chem. Phys. **2022**, *157*, 054106.
DOI: 10.1063/5.0097800
8. *Linear Response of Current-Dependent Density Functional Approximations in Magnetic Fields*
A. Pausch, C. Holzer
J. Phys. Chem. Lett. **2022**, *13*, 4335–4341.
DOI: 10.1021/acs.jpcclett.2c01082
7. *Efficient Calculation of Magnetic-Circular-Dichroism Spectra using Spin-Noncollinear Linear-Response Time-Dependent Density-Functional Theory in Finite Magnetic Fields*
A. Pausch, C. Holzer, W. Klopper
J. Chem. Theory Comput. **2022**, *18*, 3747–3758.
DOI: 10.1021/acs.jctc.2c00232
6. *Molecular point groups and symmetry in external magnetic fields*
A. Pausch, M. Gebele, W. Klopper
J. Chem. Phys. **2021**, *155*, 201101.
DOI: 10.1063/5.0069859
5. *The GW/BSE Method in Magnetic Fields*
C. Holzer, **A. Pausch**, W. Klopper
Front. Chem. **2021**, *9*, 746162.
DOI: 10.3389/FCHEM.2021.746162

4. *Chiral Resolution of Spin-Crossover Active Iron(II) [2x2] Grid Complexes*
N. Suryadevara, **A. Pausch**, E. Moreno-Pineda, A. Mizuno, J. Bürck, A. Baksi,
T. Hochdörffer, I. Šalitroš, A. S. Ulrich, M. M. Kappes, V. Schünemann,
W. Klopper, M. Ruben
Chem. Eur. J. **2021**, *27*, 15172–15180.
DOI: 10.1002/CHEM.202101432
3. *Efficient evaluation of three-centre two-electron integrals over London orbitals*
A. Pausch, W. Klopper
Mol. Phys. **2020**, *118*, e1736675.
DOI: 10.1080/00268976.2020.1736675
2. *Computation of Electromagnetic Properties of Molecular Ensembles*
I. Fernandez-Corbaton, D. Beutel, C. Rockstuhl, **A. Pausch**, W. Klopper
ChemPhysChem **2020**, *21*, 878–887.
DOI: 10.1002/CPHC.202000072
1. *A Fast Electrochemical Quartz Crystal Microbalance, which Acquires Frequency and Bandwidth on Multiple Overtones*
J. Petri, S. Hochstädt, T. Nentwig, **A. Pausch**, A. Langhoff, D. Johannsmann
Electroanalysis **2017**, *29*, 806–813.
DOI: 10.1002/ELAN.201600580